Les cinétiques de dissolution et de précipitation de la magnésite aux conditions hydrothermales

Giuseppe Saldi

Université de Toulouse

THESE

En vue de l'obtention du

DOCTORAT DE L'UNIVERSITÉ DE TOULOUSE

Délivré par *l'Université Toulouse III - Paul Sabatier*
Discipline ou spécialité : *géochimie éxperimentale*

Présentée et soutenue par *Giuseppe Saldi*
Le *24 Septembre 2009*

Titre : *Les cinétiques de dissolution et précipitation de la magnésite aux conditions hydrothermales*

JURY

Jean-Louis Dandurand, professeur à l'Université Paul Sabatier, président
François Guyot, professeur à l'Université Denis Diderot-Paris 7, rapporteur
Manuel Prieto Rubio, professeur à l'Universidad de Oviedo, rapporteur
Eric H. Oelkers, directeur de recherche CNRS, directeur de thèse
Alain Baronnet, professeur à l'Université Paul Cézanne-Aix Marseille 3, invité
Jacques Schott, directeur de recherche CNRS, invité
Guntram Jordan, Ludwig Maximilians Universitat-Muenchen, invité

Ecole doctorale : *sciences de l'univers, de l'environnement et de l'espace*
Unité de recherche : *LMTG*
Directeur(s) de Thèse : *Dr. Eric H. Oelkers*
Rapporteurs : *Prof. François Guyot, Prof. Manuel Prieto Rubio*

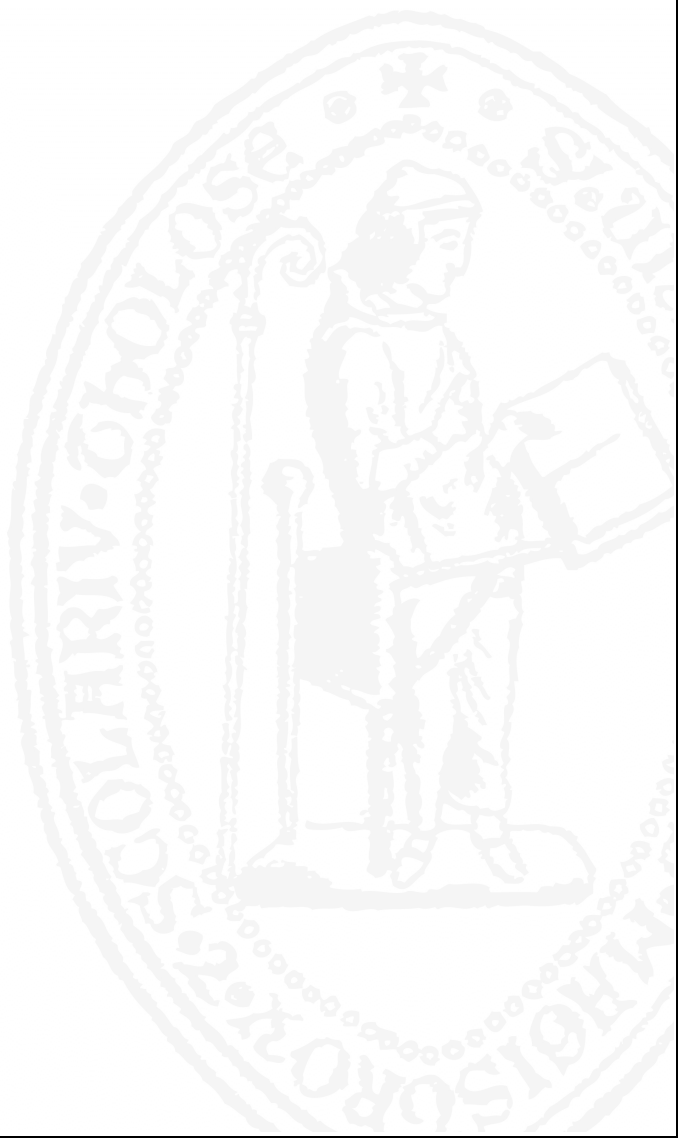

Abstract

Magnesite ($MgCO_3$) is the stable anhydrous member of a series of Mg-carbonates with different degrees of hydration. Despite its relative scarcity in the natural environments, it constitutes an important mineral phase for the permanent sequestration of CO_2 as carbonate minerals. Experimental determination of magnesite precipitation and dissolution rates at conditions representative of the storage sites is therefore fundamental for the assessment of magnesite sequestration potential in basaltic and ultramafic rocks and the optimization of the techniques of CO_2 storage.

Magnesite precipitation rates have been measured using mixed-flow and batch reactors as a function of temperature ($100 \leq T \leq 200$ °C), solution composition and CO_2 partial pressure (up to 30 bar). Rates were found to be independent of aqueous solution ionic strength at 0.1 M $< I <$ 1.1 M but decrease significantly with increasing aqueous CO_3^{2-} activity at pH > 8. All rates obtained from mixed flow reactor experiments were found to be consistent with the model of Pokrovsky et al. (1999) where magnesite precipitation rates are proportional to the concentration of the $>MgOH_2^+$ surface species. The study of magnesite crystallization using hydrothermal atomic force microscopy (HAFM) demonstrated the consistency of the rates derived from microscopic measurements with those obtained from bulk experiments and showed that these rates are also consistent with a spiral growth mechanism. According to AFM observations this mechanism controls magnesite growth over a wide range of temperatures and saturation states ($15 \leq \Omega \leq 200$ for $80 \leq T < 120$ °C). Precipitation rates dependence on solution composition recommends the use of relatively high pCO_2 to accelerate the rate of the overall carbonation process, avoiding the inhibiting effect of carbonate ions on magnesite precipitation and increasing the rates of Mg-silicate dissolution via acidification of reacting solutions.

Determination of magnesite dissolution rates by mixed flow reactor at 150 and 200 °C and at neutral to alkaline conditions allowed us to improve and extend to high temperatures the surface complexation model originally developed at 25 °C. The decrease of dissolution rates observed from 150 to 200 °C can be explained by the increasing carbonation and hydrolysis of the rate controlling $>MgOH_2^+$ sites. As a result of the decreasing rates of dissolution, the achievement of alkaline conditions and temperatures higher than 100 °C by CO_2-rich fluids represents a favorable condition for CO_2 sequestration as dissolved alkalinity in deep aquifers where carbonate minerals are major constituting phases.

The use of a hydrogen electrode concentration cell (HECC) corroborates the kinetic data obtained at close to equilibrium conditions by the precise determination of magnesite solubility product as a function of temperature (50-200°C). These measurements allowed generating the thermodynamic properties of this phase and comparing them with those obtained from calorimetric measurements and phase equilibria experiments.

The results of this study significantly improve our understanding of the kinetic behaviour of carbonate minerals in hydrothermal systems and provide an essential database for the future study of dissolution/precipitation reactions of carbonate minerals in complex systems. This work also provides important kinetic constraints for the geochemical modeling of CO_2 sequestration processes and will help the evaluation of impact and risks connected to a long-term storage.

Keywords: carbonate minerals; magnesite precipitation and dissolution rates; CO_2 sequestration; solubility product; hydrothermal conditions.

Résumé

La magnésite ($MgCO_3$) est la forme anhydre la plus stable d'une série de carbonates de magnésium qui présentent différents degrés d'hydratation. Malgré sa rareté dans les environnements naturels, elle constitue une phase minérale fondamentale pour le piégeage minéral permanent du CO_2. La détermination expérimentale des vitesses de précipitation et de dissolution de la magnésite dans des conditions représentatives de la séquestration géologique est donc fondamentale pour l'estimation du potentiel de séquestration de CO_2 par cette phase dans les basaltes et dans les roches ultrabasiques et pour l'optimisation des procédés de stockage du CO_2.

Nous avons mesuré les vitesses de précipitation de la magnésite en utilisant des réacteurs à circulation et des réacteurs fermés, en fonction de la température ($100 \leq T \leq 200$ °C), de la composition de la solution aqueuse et de la pression partielle de CO_2 (de 0 à 30 bar). Les vitesses mésurées sont indépendantes de la force ionique de la solution pour $0.1\ M < I < 1.1\ M$, mais elles diminuent significativement avec l'augmentation de l'activité des ions CO_3^{2-} pour des pH supérieures à 8. Les vitesses mesurées dans les réacteurs à circulation sont cohérentes avec le modèle de coordination chimique surfacique de Pokrovsky et al. (1999) selon lequel les vitesses de précipitation de la magnésite sont proportionnelles à la concentration des sites surfaciques $>MgOH_2^+$. L'étude des vitesses de cristallisation conduite par microscopie à force atomique hydrothermale (HAFM) a montré un bon accord entre les vitesses déduites de mesures microscopiques et les vitesses macroscopiques et a aussi démontré que la précipitation de la magnésite s'effectue selon un mécanisme de croissance spirale. Suivant les observations effectuées par AFM, ce mécanisme contrôle la vitesse de croissance de la magnésite dans un grand intervalle de température et d'indice de saturation ($15 \leq \Omega \leq 200$ pour $80 \leq T < 120$ °C). En raison de l'inhibition de la précipitation de la magnésite par les ions carbonates, il est recommandé d'opérer sous des pressions partielles de CO_2 assez élevées, ce qui présente en outre l'avantage d'accélérer la cinétique de dissolution des silicates magnésiens, grâce à l'acidification de la solution par le CO_2.

La détermination des vitesses de dissolution de la magnésite dans des réacteurs à circulation à 150 et 200 °C et en milieu neutre à alcalin nous a permis d'améliorer le modèle de complexation de surface et d'étendre son application aux températures considérées. La diminution des vitesses de dissolution observée de 150 à 200 °C peut être expliquée par l'augmentation, en fonction de la température, de la carbonatation et de l'hydrolyse des sites $>MgOH_2^+$ qui contrôlent la vitesse de dissolution de la magnésite. Des températures supérieures à 100 °C qui entrainent une diminution de la vitesse de dissolution de la magnésite et des autres carbonates sont donc favorables au stockage de CO_2 sous forme dissoute dans les aquifères profonds riches en minéraux carbonatés.

L'utilisation d'une cellule à électrodes d'hydrogène (HECC) nous a permis de préciser les données cinétiques à proximité de l'équilibre grâce à la détermination précise du produit de solubilité de la magnésite en fonction de la température (50-200 °C). De plus, ces mesures nous ont permis de générer les propriétés thermodynamiques de la magnésite et de les comparer à celles obtenues par mesures calorimétriques et par équilibres de phases.

Les résultats de cette étude représentent une importante contribution à la compréhension des cinétiques de réaction des minéraux carbonatés dans les systèmes hydrothermaux et permettent de proposer une base de données essentielle pour la quantification des réactions de dissolution/précipitation des carbonates dans les systèmes complexes. En outre, ce travail fournit des contraintes cinétiques pour la modélisation géochimique des processus de séquestration du CO_2 et sera utile à l'évaluation de l'impact et des risques liés au stockage de CO_2 à long terme.

Mots clés: minéraux carbonatés ; cinétiques de dissolution et précipitation de la magnésite; séquestration géologique du CO_2 ; produit de solubilité; conditions hydrothermales.

Remerciements

Ce travail a été réalisé dans le cadre du projet européen MIR-EST (Mineral Interface Reactivity — Early Stage Training Network, MEST-CT-2005-021120). Il a largement bénéficié de l'apport scientifique et de réunions de formation organisées par les leaders de groupes universitaires qui ont participé à ce réseau et au réseau européen MINGRO.

En premier lieu, je voudrais remercier mon directeur de thèse, Eric Oelkers, pour m'avoir permis de venir à Toulouse faire mon doctorat et pour avoir mis à ma disposition tout ce dont je pouvais avoir besoin pour compléter mon travail dans les meilleures conditions. Je tiens également à remercier Jacques Schott pour sa grande disponibilité, l'aide, le soutien et le grand intérêt montré envers mon travail. Un grand merci à Oleg Pokrovsky et Pascale Bénézeth pour leur collaboration et leur soutien et à Gleb Pokrovski pour ses conseils. Un merci tout particulier à Guntram Jordan pour m'avoir accueilli dans les murs du département de minéralogie et cristallographie de la Ludwig-Maximilians Universität de Munich, pour tout ce qu'il m'a appris et les discussions constructives que l'on a souvent eues devant un verre de bière.

J'exprime aussi ma reconnaissance à Alain Castillo et Jean-Claude Harrichoury pour leur expertise et leur constant support technique et même pour avoir rendu plus agréables les heures de travail passées dans les salles des réacteurs hydrothermaux du LMTG. Je remercie Carole Causserand pour sa disponibilité et sa présence pendant la partie analytique de ce travail.

Mes vifs remerciements vont aussi à Manolo Prieto et François Guyot pour avoir accepté d'être les rapporteurs de ce travail, à Jean-Louis Dandurand pour sa disponibilité et pour avoir lu et corrigé avec intérêt ce manuscrit et à Alain Baronnet pour avoir accepté avec enthousiasme et intérêt de faire partie du jury de thèse.

Mon séjour à Toulouse n'aurait pas été possible sans le support et l'encouragement extraordinaire de mes parents ainsi que de toute ma famille, auxquels j'adresse toute ma reconnaissance. Enfin, je garderai en mémoire toutes les personnes et les amis rencontrés à Toulouse pendant les quatre années de thèse ; leur présence m'a aidé dans les moments un peu difficiles et a contribué à rendre mon expérience plus riche et agréable.

TABLE DES MATIÈRES

Introduction

INTRODUCTION GENERALE

La réduction des émissions anthropogéniques de CO_2 est considérée comme essentielle pour la stabilisation des concentrations de ce gaz dans l'atmosphère, afin de réduire l'accroissement de la température à la surface de la Terre. La récupération et le stockage du CO_2 (CCS : « CO_2 capture and storage ») représentent une des options les plus prometteuses pour réduire le taux de CO_2 atmosphérique puisqu'elle permet de poursuivre l'utilisation raisonnée des combustibles fossiles tout en diminuant le taux de gaz à effet serre (cf. Pacala and Socolow, 2004). En outre, le « CCS » est un processus économiquement réalisable car met en œuvre des technologies déjà existantes, qui ont été développées et appliquées par les industries pétrolières.

Le processus de capture et séquestration du CO_2 consiste à capturer le carbone émis par les centrales électriques et les autres procédés industriels, le transporter vers un site de séquestration, l'injecter et le stocker en profondeur dans des formations géologiques ou sous les couches de sédiments au marins.

Les sites potentiels pour le stockage du CO_2 sont les réservoirs de pétrole et de gaz naturel épuisés, les aquifères salins profonds et les mines de charbon qui ne sont plus en exploitation (Hitchon et al., 1999; Bachu, 2000; IPCC 2005; Oelkers et Cole, 2008). Selon le contexte géologique, l'anhydride carbonique peut être retenu sous forme de gaz ou de fluide supercritique sous un toit imperméable (cap rock), tel qu' une formation argileuse, sous forme dissoute (CO_2 dissous, HCO_3^-, CO_3^{2-}) dans les fluides de bassins sédimentaires, ou adsorbé sur la matière organique (e. g., charbon et argiles noires), ou bien encore piégé sous forme solide grâce à sa précipitation minérale (Oelkers et Schott, 2005; Wilson et Gerard, 2007; Benson et Cole, 2008). Une autre solution est aussi sa séquestration sous forme d'hydrate dans l'océan profond (voir Adams et Caldeira, 2008).

Quel que soit le type du stockage, son efficacité repose sur la combinaison de plusieurs mécanismes de piégeage qui peuvent se développer dans un contexte donné. Néanmoins, parmi tous les mécanismes envisageables, le plus efficace à long terme est assurément la fixation minérale du CO_2. Ce processus, connu aussi sous le nom de carbonatation minérale, consiste en la précipitation de carbonates stables comme la calcite ($CaCO_3$), la dolomite [$CaMg(CO_3)_2$], la sidérite ($FeCO_3$), la magnésite ($MgCO_3$) et la dawsonite [$NaAlCO_3(OH)_2$],

résultant de la dissolution de minéraux silicatés de la roche encaissante qui fournissent les ions divalents nécessaires à la fixation du CO_2 sous forme solide (Seifritz, 1990; Lackner et al., 1995, Kojima et al., 1997). La précipitation des ces minéraux carbonatés, résultat de l'interaction eau-roche, représente un stockage de CO_2 permanent, puisque ces phases sont généralement stable à l'échelle des temps géologiques.

La carbonatation minérale peut être réalisée *ex situ*, c'est-à-dire en extrayant les matériaux bruts nécessaires au processus, ou *in situ*, par l'injection directe de CO_2 dans des formations rocheuses appropriées pour sa mise en œuvre. Le matériel brut requis pour la séquestration *ex situ* de l'anhydride carbonique est principalement constitué par les silicates de calcium et surtout de magnésium. Ces derniers sont, en effet, relativement abondants dans les formations basiques et ultrabasiques et leur quantité serait largement suffisante pour lier le CO_2 émis par les centrales thermiques de la planète (Lackner et al., 1995). Péridotites et serpentinites contiennent entre 30 et 50 % en poids de MgO situé dans les principaux silicates de magnésium (olivine, serpentine, pyroxène). Ces minéraux constituent une source de cations divalents (Mg, Ca, Fe,...) qui est en général plus abondante que dans les silicates calciques (il y a seulement 10-15 % de CaO dans les formations rocheuses). La réaction des silicates magnésiens avec le CO_2 conduit principalement à la formation de magnésite. La formation de magnésite lors de l'altération des roches ultramafiques est un processus observé dans la nature, qui s'effectue, cependant, avec des cinétiques très lentes. Des expériences récentes de carbonatation de serpentine [$Mg_3Si_2O_5(OH)_4$] et de forstérite ($Mg_2Si_2O_4$) ont démontré que la libération de magnésium peut être limitée par la précipitation de silice ou le développement à la surface des silicates magnésiens d'une couche altérée riche en silice (ex. O' Connor et al., 2000; Béarat et al., 2006; Gerdemann et al., 2007). La vitesse de la réaction peut être accélérée grâce à un prétraitement du matériau silicaté, par exemple, par l'augmentation de sa surface, un traitement thermique ou une activation chimique (Maroto-Valer et al., 2005; Gerdemann et al., 2007). Cependant, les coûts d'extraction, de broyage ou de traitement préalable de la matière première, de transport et de stockage du matériau, ainsi que les conditions requises pour rendre la réaction de carbonatation plus efficace (température et pression partielle de CO_2 élevées) rendent le processus ex-situ non envisageable économiquement (Oelkers et al., 2008). Au contraire, l'injection directe de fluides enrichis en CO_2 dans des formations rocheuses appropriées évite la plupart de ces inconvénients et fournit une solution plus économique. Celle-ci peut être particulièrement efficace, non seulement dans des roches ultramafiques, mais aussi dans les grandes formations basaltiques,

en raison de leurs volumes considérables et de leurs relatives abondances en cations divalents par rapport à la silice (McGrail et al., 2006; Matter et al., 2007; Oelkers et al., 2008).

Afin d'évaluer le potentiel de séquestration de ces systèmes géologiques et d'analyser la faisabilité du processus, il est essentiel de connaitre avec précision les vitesses de carbonatation. Les vitesses de précipitation de la plupart des minéraux sont encore mal connues et elles ne peuvent pas être facilement déduites de vitesses de dissolution correspondantes (cf. Steefel et Van Cappellen, 1990). Pour ces raisons, il est indispensable de réaliser des études expérimentales visant à mesurer directement les vitesses de cristallisation des phases pertinentes, afin d'obtenir les données nécessaires à l'optimisation du processus de séquestration et à son application dans des environnements variés.

Afin de contribuer à l'établissement d'une base de données cinétiques sur la précipitation des minéraux carbonatés, nous avons mesuré les vitesses de précipitation du minéral-clef qu'est la magnésite, en fonction des paramètres importants qui contrôlent sa vitesse de cristallisation, comme la température, la composition chimique de la solution aqueuse et la pression partielle de CO_2. Cette étude a été menée à l'aide d'expériences en réacteurs à circulation et en réacteurs fermés permettant l'analyse chimique des solutions. L'interprétation des données ainsi acquises a été réalisée avec le modèle de complexation surfacique (SCM : surface complexation model) développé par Van Cappellen et al. (1993) et Pokrovsky et al. (1999a, b) dans le cadre de la théorie de l'état transitoire. A cette fin, nous avons étendu jusqu'à 200 °C l'application de ce modèle, initialement développé pour la température ambiante. Une deuxième partie du travail a été consacrée à l'étude des processus microscopiques qui se produisent à la surface de la magnésite lors de sa croissance cristalline et qui contrôlent sa formation dans les environnements naturels. Cette étude a été possible grâce à l'utilisation de la microscopie à force atomique hydrothermale (HAFM) disponible au Département de Cristallographie de l'Université Ludwig Maximilians de Munich (Allemagne). Elle a permis pour la première fois l'observation et la caractérisation des processus de nucléation et croissance de la magnésite à l'échelle atomique et leurs quantification et extrapolation à l'échelle macroscopique. L'ensemble des données sera précieuse pour l'optimisation des procédés de carbonatation minérale *in situ* aussi bien que *ex situ*.

En complément de cette étude et des récents travaux consacrés à la dissolution des minéraux carbonatés à hautes température et pression partielle de CO_2 (e. g. Pokrovsky et al.,

2009), nous avons mesuré la vitesse de dissolution de la magnésite à 150 et 200 °C en solutions neutres et alcalines en fonction de la concentration des espèces carbonatées, du pH et de l'affinité chimique de la réaction de dissolution. En effet, l'injection de CO_2 dans les grés et dans les aquifères carbonatés a été proposée et étudiée comme solution potentielle pour le stockage du CO_2. C'est pourquoi la connaissance des cinétiques de dissolution de la magnésite et des autres phases carbonatées dans des conditions de temperature, pression de CO_2 et compositions chimiques des solutions pertinentes pour le stockage géologique fourniront des informations complémentaires concernant la réactivité et la stabilité des réservoirs confinés dans des formations carbonatées, supposées garantir la stabilité du CO_2 piégé sous forme dissoute. Finalement, le produit de solubilité de la magnésite et ses propriétés thermodynamiques ont été déterminés à l'aide d'une cellule à concentration d'hydrogène (HECC) récemment construite au LMTG (cf. Bénézeth et al., 2009). Les propriétés thermodynamiques des carbonates, disponibles dans la littérature, ont été essentiellement obtenues à partir de mesures calorimétriques et d'expériences de transformation de phase à température et pression élevées. Le dispositif employé nous a permis une détermination précise du produit de solubilité de la magnésite en utilisant des mesures traditionnelles de solubilité, ainsi qu'une réévaluation des propriétés thermodynamiques dont les valeurs proposées par la littérature sont souvent discordantes. La connaissance exacte des produits de solubilité et des vitesses de dissolution et précipitation est une condition fondamentale pour l'estimation du potentiel de séquestration du CO_2 par les minéraux carbonatés et pour modéliser et optimiser les stratégies du piégeage minéral dans différents scénarios et à des échelles variées. Le travail présenté dans cette thèse fournit une caractérisation complète des propriétés thermodynamiques et cinétiques de la magnésite en réponse à cette demande, mais elle améliore aussi la compréhension générale des cinétiques de réaction dans les systèmes dominés par les carbonates.

CHAPITRE 1

Méthodes expérimentales

Méthodes expérimentales

1. Matériaux : minéraux

Différents types d'échantillons de magnésite ont été utilisés en fonction des expériences réalisées. Pour les mesures des vitesses de dissolution et précipitation en réacteur ouvert ou fermé, nous avons utilisé des échantillons naturels et des poudres synthétisées en laboratoire. Une poudre synthétique a aussi été utilisée pour la détermination du produit de solubilité de la magnésite dans la cellule à hydrogène. L'étude par microscopie à force atomique de la croissance cristalline de ce minéral a été menée, quant à elle, avec des monocristaux obtenus par clivage d'un macro cristal naturel.

1.1 Echantillons naturels

L'échantillon de magnésite naturel que nous avons préparé pour notre étude cinétique provient du gisement de Huaziyu, situé dans la province orientale de Liaonig, en Chine. La géochimie et la géologie de cette minéralisation massive ont été récemment décrites par Jiang et al. (2004). Des grains de taille variable (2-5 mm) ont été triés manuellement pour éliminer les éventuelles impuretés, puis broyés afin d'obtenir la fraction granulométrique souhaitée. Le broyage a été réalisé en plusieurs étapes : pour une taille d'échantillon > 10 mm, nous avons effectué un concassage préliminaire à l'aide d'un marteau en prenant soin d'envelopper l'échantillon dans du papier pour limiter les risques de contamination et éviter la perte d'échantillon. Les grains de taille < 10 mm ainsi obtenus ont ensuite été broyés dans un mortier manuel en agate. Cette opération a été alternée avec des séquences de séparation granulométrique effectuées par tamisage à sec avec des tamis à mailles en nylon pour séparer les grains ayant une taille comprise entre 50 et 100 μm. Cette dernière fraction a été conservée pour notre étude expérimentale.

Le broyage des échantillons produit des fines particules susceptibles d'adhérer à la surface des grains ainsi que des défauts de surface tels que des zones de très faible rayon de courbure. La présence de fines particules et de surfaces perturbées est souvent à l'origine d'une augmentation de la solubilité, mais aussi des vitesses de dissolution (Rimstidt et Barnes, 1980 ; Schott et al., 1981 ; Gautier, 1999). La plupart des fines particules a été

éliminée par traitement aux ultrasons dans de l'éthanol et par rinçages successifs dans de l'eau déminéralisée jusqu'à l'obtention d'un surnageant clair. A l'issue de ce traitement, il ne reste aucune fine particule visible sur la surface des grains de magnésite, comme le montre l'analyse au microscope électronique à balayage (Fig. 1). Les poudres de magnésite ainsi traitées ont ensuite été séchées dans une étuve à 60 °C pendant deux à trois jours.

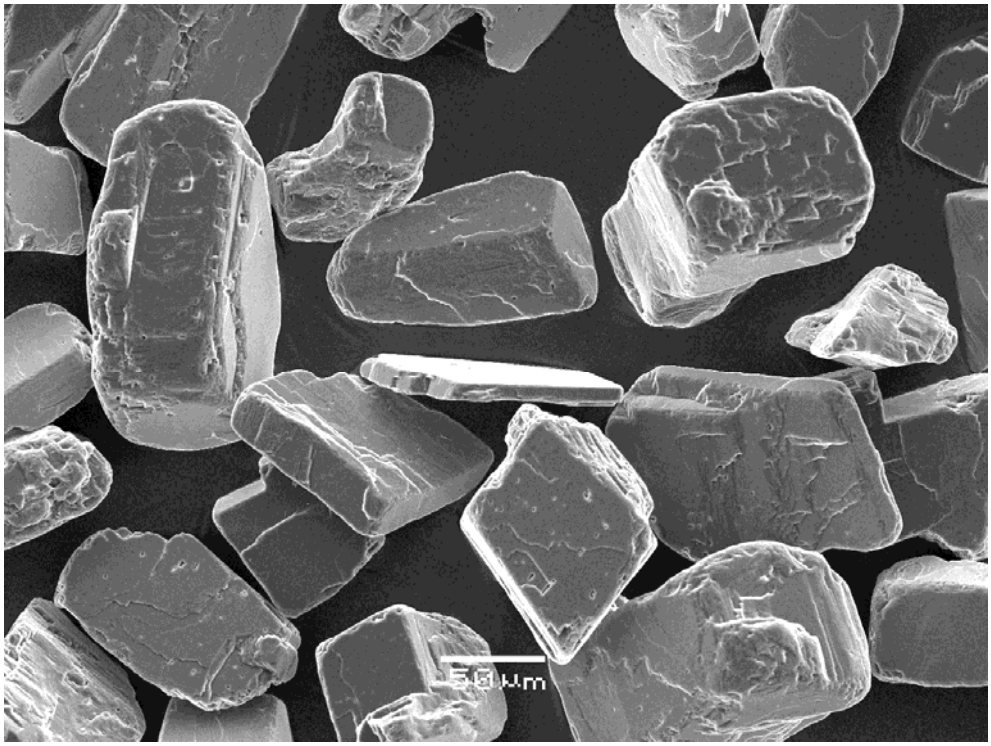

Fgure 1. Image MEB des grains de magnésite provenant du gisement de Huaziyu prêts à être utilisés dans nos expériences.

1.2 Synthèse des échantillons de magnésite

Plusieurs échantillons de magnésite ont été synthétisés à partir de carbonate de Mg hydraté ($MgCO_3$ Prolabo Rhône-Poulenc). Pour chaque expérience de synthèse environ 20 g de ce réactif ont été placés dans un autoclave en titane de 400 ml en présence de 250 ml d'eau déminéralisée et de 15-20 g de carboglace (CO_2 solide) pour obtenir une pression partielle de CO_2 de 35 bars dans l'autoclave voisine de la température ambiante. La température de l'autoclave a ensuite été augmentée jusqu'à 200 à 250 °C pour accélérer la réaction de formation de la magnésite. Après trois à quatre semaines le chauffage de l'autoclave a été arrêté, tandis que la solution aqueuse était immédiatement évacuée en ouvrant la vanne placée

sur une extrémité de l'autoclave, afin d'éviter toute réaction de la poudre avec la solution lors du refroidissement. La présence à la sortie de l'autoclave d'un fritté en titane d'une porosité de 2 μm évite le passage de cristaux de magnésite à travers la vanne. La poudre de magnésite ainsi produite est constituée de cristaux de forme rhomboédrique à pseudo-cubique, de taille généralement comprise entre quelques micromètres et 40 μm. Aucune séparation granulométrique n'a été effectuée par la suite sur ces échantillons synthétiques. Une image de la poudre synthétique produite selon cette procédure est reproduite dans la Figure 2.

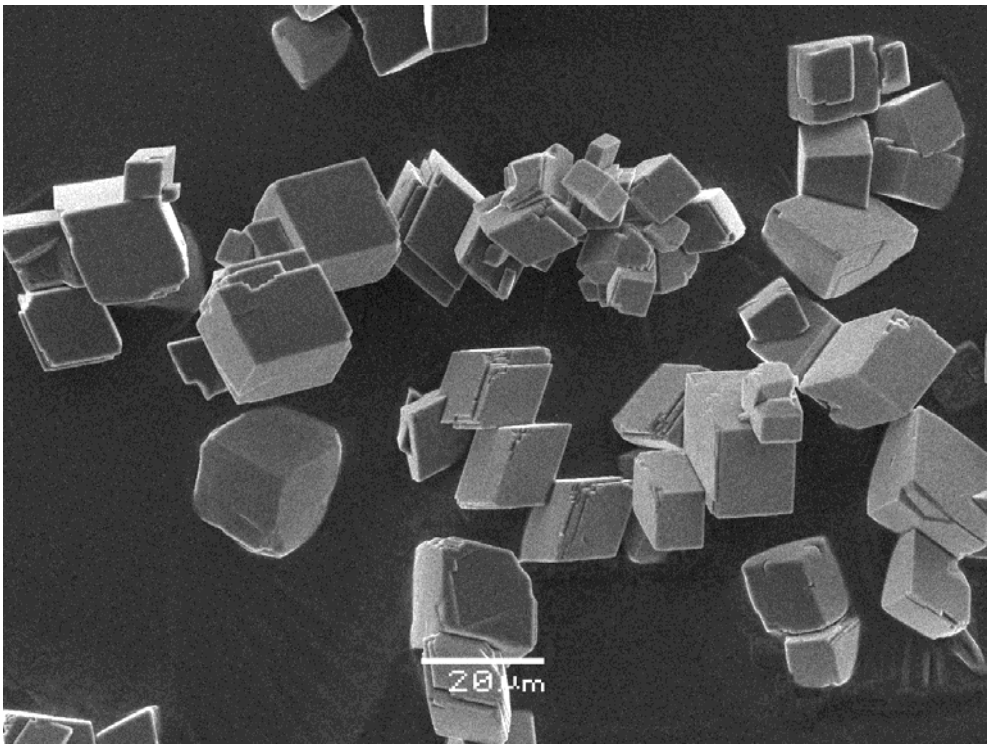

Figure 2. Image MEB des cristaux de magnésite synthétique utilisée pour la mesure de la solubilité et des cinétiques de dissolution/précipitation.

1.3 Caractérisation des solides

1.3.1 Analyse chimique

La composition chimique et minéralogique des solides utilisés dans notre travail a été déterminée par microsonde électronique, par diffraction des rayons X et par LA-ICP-MS. Les analyses à la microsonde ont permis de déterminer la composition moyenne de la magnésite naturelle provenant du gisement de Huaziyu, alors que l'analyse des éléments en trace

contenus dans cet échantillon a été conduite par ablation laser couplée à un spectromètre de masse à plasma inductif (LA-ICP-MS). Les résultats de ces analyses sont reportés dans le Tableau 1. L'analyse par diffraction des rayons X (radiation CuKα de longueur d'onde $\lambda = 1.789 \cdot 10^{-10}$ m), n'a mis en évidence aucune raie étrangère à celles de la magnésite pour les différents échantillons utilisés au cours de ce travail. Un exemple de spectre DRX caractéristique de la magnésite synthétique est reporté sur la Figure 3.

Tableau 1. Composition chimique de la magnésite de Huaziyu utilisée dans cette étude.

Composition en oxydes[a] (poids %)		Elements en trace[b] (ppm)	
MgO	47.32	Na	33.5
CaO	0.32	Si	288.4
MnO	0.02	Cl	307.0
FeO	0.10	P	220.9
SrO	–	K	25.7
BaO	–	Cr	3.2
CO_2	51.7		

[a]Déterminée par microsonde électronique (moyenne de 20 points)
[b]Déterminés par LA-ICP-MS, (moyenne de 7 analyses ponctuelles)

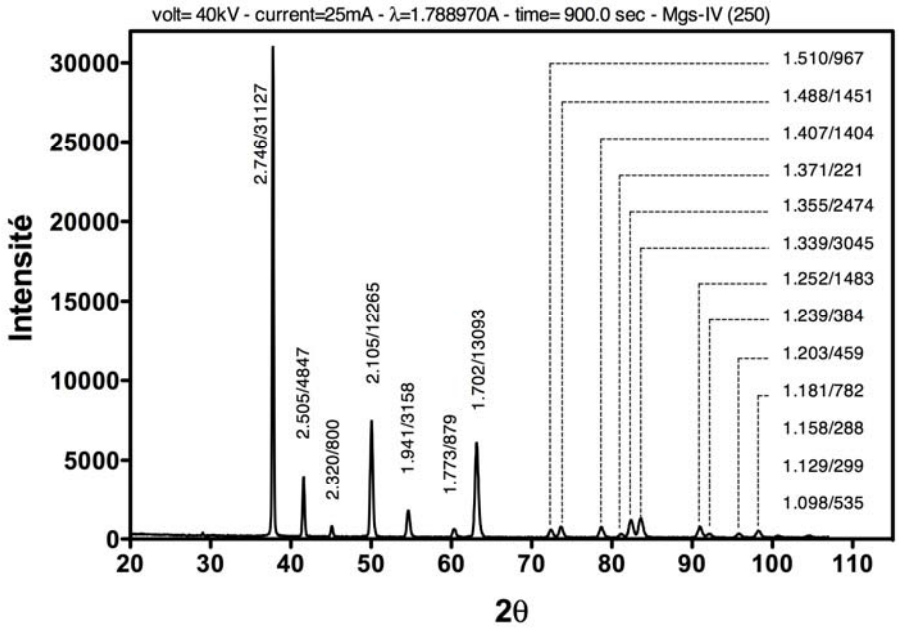

Figure 3. Exemple de spectre DRX caractéristique de la magnésite obtenu lors de l'analyse d'un des échantillons synthétiques (Mgs-IV) utilisés dans cette étude (distance réticulaire/intensité).

1.3.2 Détermination des surfaces spécifiques

Les surfaces spécifiques des poudres de magnésite avant expérience ont été mesurées par la méthode BET (Brunauer, Emmett et Teller, 1938) appliquée à l'isotherme d'adsorption partielle du krypton à la température de l'azote liquide (63 K < T < 77.2 K à la pression atmosphérique). L'erreur sur les mesures BET, liée en partie à la calibration de l'appareil (AUTOSORB 1, Quantachrome instruments) est estimée à 10%, alors que la reproductibilité des mesures est de l'ordre de 2%. L'estimation des valeurs des surfaces géométriques a été aussi faite pour les poudres de magnésite synthétique sur la base des analyses granulométriques effectuées sur les mêmes échantillons. Le calcul de la surface géométrique utilise la valeur médiane de la distribution granulométrique et suppose une géométrie cubique des grains:

$$S_{GEO} = 6/\rho \cdot d_m \,, \qquad (1)$$

où d_m représente le diamètre médian de la poudre analysée et ρ la densité de la magnésite (3.01 g/cm^3). Les valeurs des surfaces spécifiques BET et géométriques sont reportées dans le Tableau 2. On note que la surface BET mesurée sur les échantillons synthétiques est de 2 à 3

fois plus grande que la surface géométrique. Le rapport S_{BET}/S_{GEO} représente le facteur de rugosité de la surface (Anbeek, 1992). La proximité des valeurs de surface géométrique et BET implique que les grains synthétiques ne présentent pas une forte rugosité, ni d'importante microporosité interne, comme le confirment les observations par microscopie électronique à balayage.

Tableau 2. Surfaces spécifiques BET et géométriques des échantillons naturels (Huaziyu et Satka) et synthétiques de magnésite utilisés dans notre étude.

$MgCO_3$	S_{BET} (cm^2/g)	S_{GEO} (cm^2/g)	S_{BET}/S_{GEO}
Huaziyu A	1281	-	-
Huaziyu B	971	-	-
Satka	1260	-	-
Mgs-1	2882	-	-
Mgs-I	2241	822	2.7
Mgs-II	1723	643	2.7
Mgs-III	1610	772	2.1
Mgs-IV	2153	636	3.4
Mgs-V	1791	844	2.1
Mgs-VI	1474	782	1.9
Mgs-VII	1826	992	1.8
Mgs-VIII	2007	669	3

2. Dispositifs expérimentaux utilisés pour les études cinétiques et de solubilité

La plupart des vitesses de dissolution et précipitation présentées dans cette étude ont été déduites d'expériences conduites dans des réacteurs hydrothermaux à circulation. Seules quelques mesures vitesses de précipitation ont été determinées en utilisant un réacteur fermé et une cellule potentiométrique utilisant des électrodes à hydrogène. Ces deux derniers dispositifs ont été utilisés principalement pour la détermination du produit de solubilité de la magnésite en fonction de la température.

2.1 Réacteur à circulation (mixed flow reactor)

Ce type de réacteur a été utilisé avec succès depuis plus que vingt ans pour déterminer les vitesses de dissolution et précipitation de nombreux mineraux (Chou et Wollast, 1984 ; Rimstidt et Dove, 1986 ; Dove et Crerar, 1990 ; Berger et al., 1994 ; Devidal et al., 1997 ; Gautier, 1999). Par rapport au réacteur fermé, le reacteur à circulation présente le grand avantage de permettre la détermination directe de la vitesse de dissolution ou précipitation à l'état stationnaire, sans avoir à suivre l'évolution des concentrations des espèces dissoutes au cours du temps et à intégrer les données, comme dans le cas des études menées en réacteur fermé, dans lequel l'écart à l'équilibre varie en fonction du temps. Ainsi, l'utilisation des réacteurs à circulation permet d'opérer sous des conditions physico-chimiques choisies et constantes (composition chimique de la solution aqueuse et affinité chimique de la réaction) et de les faire varier par simple ajustement du débit et/ou changement de la composition chimique de la solution injectée dans le réacteur.

Le réacteur de type « mixed flow » est un système ouvert de volume fixé à travers lequel circule un fluide à débit constant ; le fluide est parfaitement mélangé de sorte que température et composition chimique sont identiques en tout point du réacteur. Par conséquent, le fluide contenu dans le réacteur et celui prélevé à la sortie de ce dernier ont la même composition.

L'équation de conservation de la masse, appliquée à un traceur *i* injecté dans un réacteur à circulation parfaitement mélangé, s'écrit :

$$\frac{dC_i}{dt} = \frac{q}{V}\left[(C_{ie} - C_i(t)\right], \qquad (2)$$

où $C_i(t)$ représente la concentration du traceur *i* à l'instant t dans le réacteur, *V* est le volume utile du réacteur, *q* le débit du fluide et C_{ie} représente la concentration du traceur à l'entrée du réacteur. En supposant qu'à l'instant t=0 on a $C_i(t)=0$, l'intégration de l'équation (2) donne :

$$C_i(t) = C_{ie}\left[1 - \exp\left(-t/\tau\right)\right], \qquad (3)$$

où $\tau = V/q$ représente le temps moyen de résidence d'un élément de fluide dans le réacteur.

Pour $t >> \tau$, $C_i(t) \approx C_{ie}$ = constante et on dira qu'on est en régime stationnaire. La résolution de l'équation (3) montre, en particulier, que l'état stationnaire est atteint au bout d'un temps $t_{stat}=4.6\times\tau$. A l'état stationnaire on peut donc calculer la vitesse de la réaction de dissolution/précipitation à partir de la concentration de l'élément *i* dans l'effluent, du débit de la solution et de la surface interfaciale solide/solution, suivant :

$$\boldsymbol{r}_i = \frac{q \cdot \left[C_{is} - C_{ie}\right]}{S \cdot m \cdot \upsilon_i} , \qquad (4)$$

où C_{is} et C_{ie} représentent les concentrations en élément *i* respectivement à la sortie et à l'entrée du réacteur (mol/kg), *q* est le débit de la solution (kg/s), S est la surface specifique du matériau (cm^2/g), *m* la masse de matériau introduite dans le réacteur (g) et υ_i est le coefficient stœchiométrique de l'élément *i* dans le minéral ; $\boldsymbol{r}_i$ s'éxprime en mol/(cm^2·s).

Lors de ce travail chaque essai a été poursuivi jusqu'à 3 à 4 fois le temps de residence après l'atteinte de l'état stationnaire mécanique (correspondant à $t_{stat}=4.6\times\tau$), ce qui est généralement suffisant pour observer une concentration constante des éléments dissous dans l'effluent. La vitesse moyenne de dissolution/précipitation est calculée lorsque trois prélèvements successifs donnent la même concentration de *i* dans l'effluent. Tous nos essais ont été conduits entre 100 et 200 °C dans des réacteurs Parr de volumes 200 et 300 ml, modifiés pour opérer en système ouvert. Un schéma des réacteurs utilisés lors de nos essais est représenté sur la Figure 4. Toutes les parties du réacteur en contact avec la solution à haute température sont en titane pour éviter tout risque de contamination des solutions et des solides étudiés. La température du four qui entoure le réacteur est contrôlée par un régulateur électronique avec une précision de ± 1 °C. Le fluide est injecté dans le réacteur à l'aide d'une pompe HPLC qui permet le contrôle du débit de 0.1 à 10 ml/min. Le fluide en sortie est filtré à travers un fritté en titane dont les pores ont un diamètre de 2 μm, puis refroidi à la température ambiante par un circuit d'eau froide enveloppant le tuyau de sortie. Un régulateur de pression à membrane maintient la pression dans le réacteur au dessus de la pression saturante de la vapeur de la solution. La solution dans le réacteur est mélangée à l'aide d'une hélice fixée à une tige qui tourne à une vitesse constante par entrainement magnétique à l'aide d'un moteur extérieur.

Avant chaque expérience une solution acide de rinçage ($HCl+HNO_3$ à pH = 2) puis de l'eau déionizée est mise en circulation pendant au moins 24 heures dans le réacteur et des échantillons témoins sont prélevés pour s'assurer de l'absence de pollution dans le dispositif expérimental.

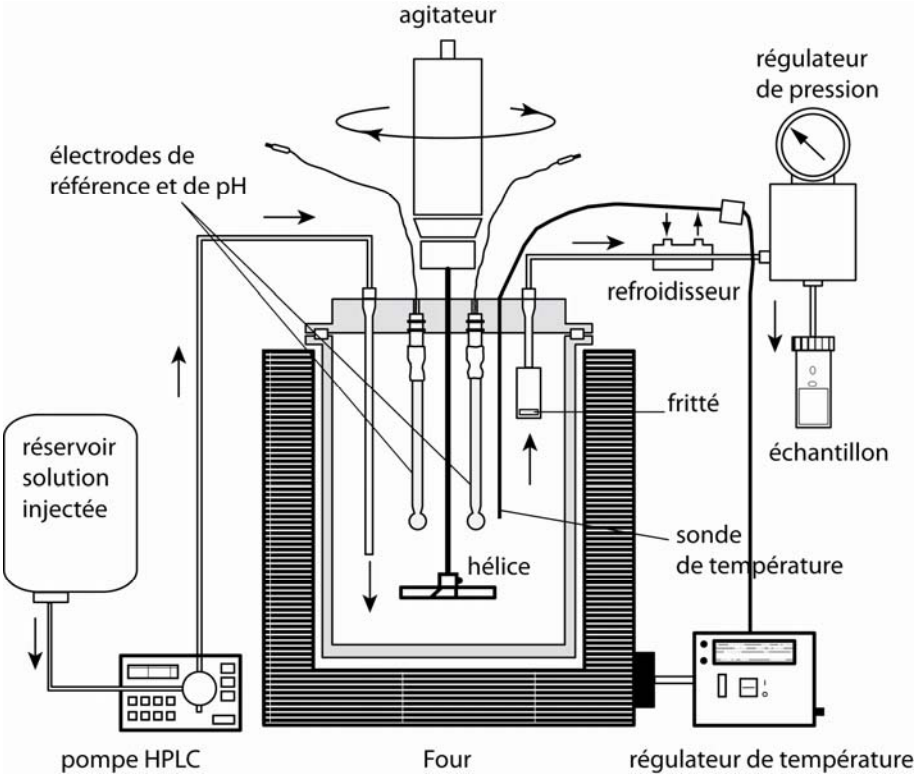

Figure 4. Représentation schématique d'un réacteur à circulation hydrothermal (mixed flow) utilisé pour les mesures des vitesses de dissolution et précipitation de la magnésite (voir le texte pour la description).

Les expériences de dissolution et précipitation sont réalisées en présence d'une quantité initiale connue (entre 0.3 et 3g) de poudre de magnésite placée dans le réacteur. Le récipient est ensuite rempli avec la solution réactive de départ, fermé avec la tête du réacteur et connecté au réservoir de solution réactive et au tuyau de sortie. La solution est soumise à agitation et le système chauffé jusqu'à la température fixée. Lorsque la température de consigne est atteinte, la pompe est mise en action afin de faire circuler la solution dans le réacteur avec le débit choisi. Des prélèvements réguliers sont effectués au cours du temps et pH, alcalinité et concentration en magnésium sont mesurés dans les effluents jusqu'à l'atteinte de l'état stationnaire. De nouvelles conditions expérimentales peuvent alors être sélectionnées, sans démonter le dispositif, en choisissant un débit différent ou en changeant la solution réactive qui circule à travers le réacteur.

2.2 Réacteur fermé (batch reactor)

Les expériences de précipitation et de solubilité en système fermé ont été réalisées dans un réacteur en titane de 400 ml qui a été modifié pour pouvoir effectuer des mesures de pH in situ et mesurer en continu les valeurs de la pression de CO_2 dans le réacteur grâce à un transducteur de pression. Le système d'agitation est le même que pour les réacteurs à circulation. Dans ces essais, une masse précise de poudre de magnésite (7-9 g) est mise en contact avec un volume de solution NaCl 0.1 M correspondant à un taux de remplissage variable entre 85 et 95 % selon la température de l'essai. Le système est chauffé jusqu'à 120 ou 150 °C et une pression de CO_2 d'environ 15 ou 30 bar est imposée lorsque l'équilibre thermique est atteint. Des prélèvements réguliers sont effectués pour suivre l'évolution chimique de la solution jusqu' à l'atteinte de l'équilibre chimique entre solide et solution. Les prélèvements sont réalisés grâce à une vanne et un tube en titane muni à son extrémité d'un fritté en titane de 2 μm de diamètre qui plonge dans la solution. Pour chaque échantillonnage, environ 2.5-3 ml de solution ont été prélevés et acidifiés par une solution d'acide concentré (HNO_3 15 M) afin de mesurer la concentration en magnésium. A cause de la forte pression de CO_2 appliquée et de l'important dégazage de la solution lors du prélèvement, aucune mesure précise de l'alcalinité n'a pu être effectuée. Par conséquent, dans les calculs de spéciation et d'indice de saturation on a utilisé les valeurs de pH mesurées in situ et on a fait l'hypothèse que la solution était en équilibre avec la pression partielle de CO_2 mesurée dans le réacteur pour déterminer la concentration de carbonate total dissous et la spéciation des espèces carbonatées. Lorsque l'équilibre chimique est atteint, la temperature est augmentée de 120 à 150 °C ou bien de 150 à 200 °C ; en raison de la solubilité rétrograde de la magnésite, la solution qui était à l'équilibre avec la magnésite devient sursaturée par rapport à ce minéral dont la précipitation s'amorce. Les prélèvements fréquents d'échantillons de solution nous permettent de suivre au cours du temps la concentration en magnésium dissous dans le réacteur et de calculer la vitesse de précipitation de la magnésite en fonction de l'indice de saturation. Les détails des calculs des vitesses de précipitation sont donnés dans le chapitre 2 (p. 30 et 51).

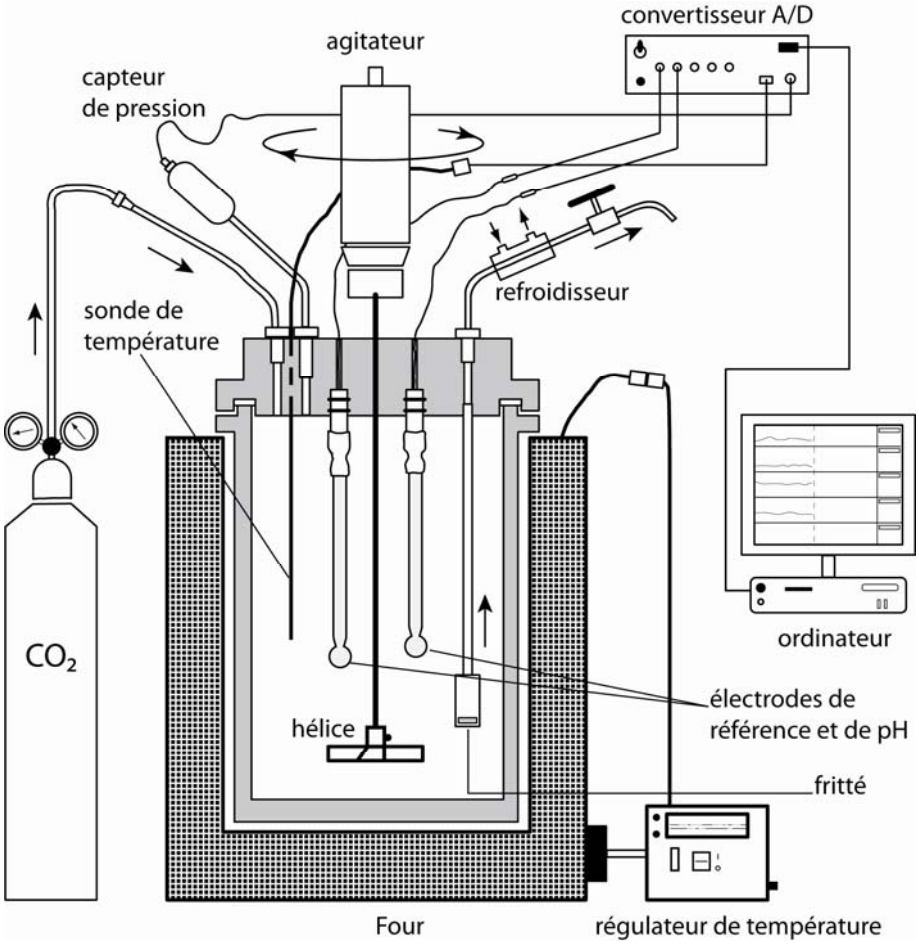

Figure 5. Schéma du réacteur fermé (batch) utilisé pour les mesures de solubilité et pour l'étude des cinétiques de précipitation de la magnésite sous fortes pressions de CO_2. Les valeurs de la pression totale (bars), la température et du potentiel d'électrode (pH in situ, mV) sont mesurées en continu et enregistrées sur un ordinateur.

2.3 Cellule potentiomètrique- électrodes à hydrogène

La cellule à hydrogène utilisée dans cette étude a été récemment construite au LMTG (voir Bénézeth et al., 2009). Le principal avantage de cette cellule est de permettre la mesure «in situ» du pH jusqu'à des températures d'environ 290°C et des pressions de 100 bars. Le pH est, en effet, un paramètre particulièrement important dans les calculs thermodynamiques concernant les systèmes carbonatés et son évolution permet de suivre la cinétique d'un grand nombre de réactions, en particulier de précipitation des minéraux carbonatés. Cette cellule permet ainsi d'étudier de manière très précise toute réaction mettant en jeu des protons, aussi bien du point de vue de l'équilibre que de la cinétique. Brièvement, cette cellule potentiométrique, schématisée sur la Figure 6, utilise deux électrodes en platine (electroplatinisées) plongeant respectivement dans une solution de référence et la solution

d'essai contenant une suspension de magnésite (de 1 à 3 g de solide selon les expériences, pour 100-110 ml de solution). Afin que les électrodes puissent répondre efficacement à la réaction d'électrode: $H_2 = 2H^+ + 2e^-$, la cellule est au préalable purgée avec de l'hydrogène pur. Une fois la purge réalisée, une pression d'hydrogène est fixée à ~10 bar à température ambiante.

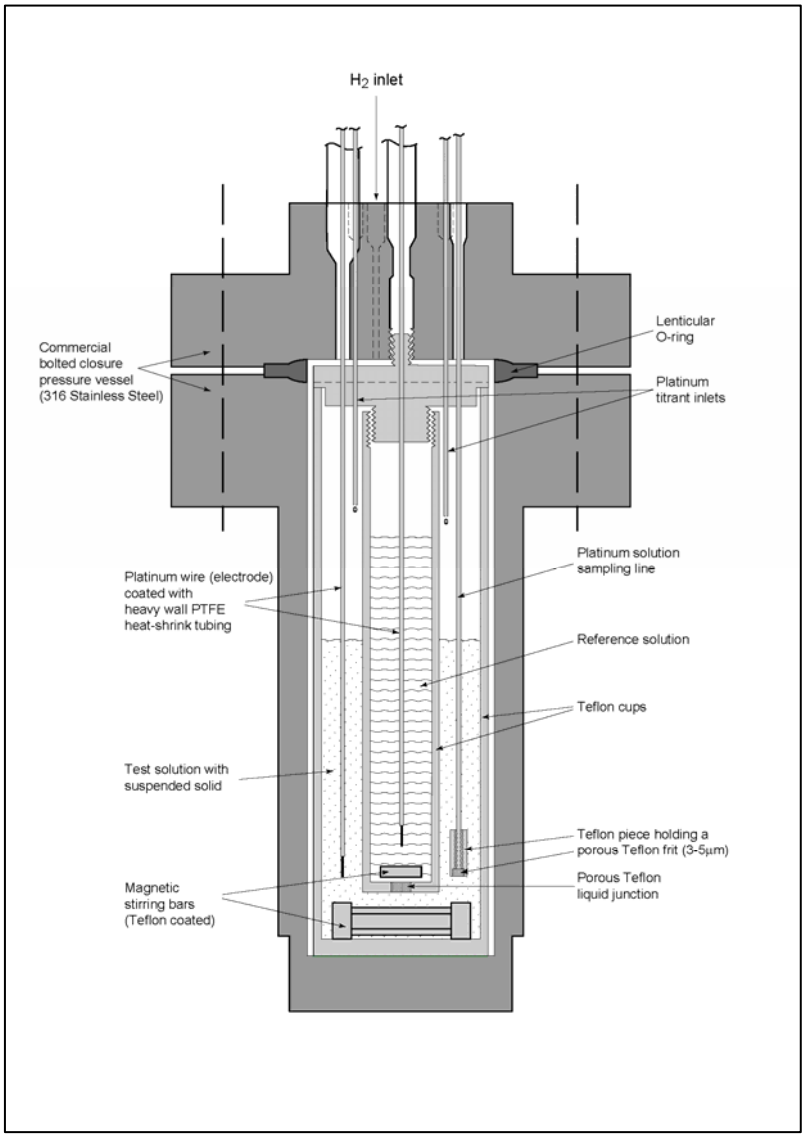

Figure 6. Schéma de la cellule potentiométrique-électrodes à hydrogène construite au LMTG (Bénézeth et al., 2009), utilisée pour les mesures de solubilité de la magnésite.

La configuration de la cellule dans un système typique de mesure de solubilité est représentée par :

$$H_2, Pt \mid NaCl(m_1), HCl\ (m_2), MgCO_{3(s)} \parallel NaCl(m_1), HCl\ (m_3) \mid Pt, H_2$$

Solution d'essai solution de référence

Les concentration de NaCl (électrolyte inerte), égales dans les deux solutions (NaCl, m_1), doit être au moins 10 fois supérieures à celle de la concentration en proton (m_2) afin de minimiser le potentiel de jonction liquide (E_{lj}), paramètre crucial dans la mesure du pH in situ, ainsi que de rendre égal à l'unité le rapport des coefficients d'activité de l'ion hydrogène dans les deux demi cellules. La concentration en ion hydrogène dans la solution d'essai ($[H^+]_{essai}$) peut ainsi être calculée avec une précision de 0,002 unité pH à partir de la différence de potentiel (E) entre la solution de référence (de concentration en ion hydrogène connue, $[H^+]_{ref}$) et la solution d'essai, selon la loi de Nernst :

$$pH = -\log [H^+]_{essai} = -\log [H^+]_{ref} + F(E+E_{lj})/2.3026RT,$$

où F est la constante de Faraday, R est la constante des gaz parfaits et T la température.

3. Méthode d'étude à l'échelle microscopique : le microscope à force atomique (AFM)

L'AFM (atomic force microscopy) consitue la technique de microscopie à champ proche (SPM, scanning probe microscopy) la plus versatile et la plus couramment utilisée pour l'étude et la caractérisation physique des surfaces aux échelles micro- et nanométrique.

Cette technique est indispensable dans les études de croissance cristalline, car elle permet non seulement de visualiser la morphologie et la distribution de différents paramètres de la surface, comme la forme et l'interdistance des marches et terrasses élémentaires, mais aussi d'observer et de mesurer en temps réel le mouvement de ces paramètres pendant les réactions de dissolution et précipitation du solide.

Le premier microscope à force atomique fut développé par Binnig et collaborateurs en 1986. Les premiers AFM commerciaux ont fait leur apparition au début des années quatre-vingt-dix et ont connu, depuis, plusieurs améliorations ; ils présentent un domaine d'application de plus en plus important.

En principe, l'AFM est constitué par une pointe sondeuse montée sur l'extrémité d'un microlevier qui scanne la surface de l'échantillon que l'on veut observer (Fig. 7).

L'enregistrement du déplacement relatif de la sonde par rapport à la surface balayée, déterminé par la force d'interaction entre la pointe et les atomes surfaciques, fournit l'image topographique de l'échantillon. La pointe sondeuse, généralement en silicium ou nitrure de silicium (Si_3N_4), est extrêmement fine (elle a un rayon de courbure de quelques nm jusqu'à quelques dizaines de nm) et sa finesse détermine le pouvoir de résolution du microscope. La force s'exerçant entre la pointe et la surface balayée est donnée par la loi de Hooke ($F = -k \cdot x$) et varie du µN au nN ; le microlevier est doté d'une constante de rappel (k) très faible (0.01-1 $N \cdot m^{-1}$) afin de permettre au microscope de contrôler la force entre la pointe et l'échantillon avec une grande précision.

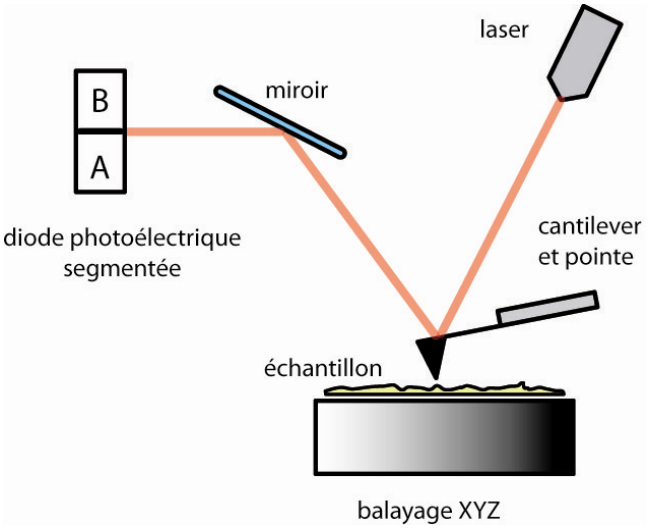

Figure 7. Principe de fonctionnement de la microscopIe à force atomique (AFM). L'échantillon de surface est scanné par une sonde constituée par une pointe miniature fixée à l'extrémité d'un micro levier (cantilever) ; le déplacement relatif de la pointe par rapport à l'échantillon placé sur la platine de balayage est mesuré au moyen d'un faisceau laser qui est réfléchi du cantilever sur un détecteur photoélectrique et restitue la microtopographie de la surface.

Le balayage de la surface est réalisé par un transducteur piézoélectrique qui se détend ou se contracte en réponse au voltage appliqué. L'élément piézoélectrique positionne et déplace la pointe sur l'échantillon (ou l'échantillon sous la pointe) avec des mouvements très précis et reproductibles qui peuvent être de l'ordre des dimensions atomiques. Dans la configuration que nous avons utilisée pendant notre étude, l'échantillon est monté sur l'extrémité supérieure d'un tube piézoélectrique dont on contrôle le mouvement selon les directions orthogonales x, y et z par un dispositif électronique connecté à un ordinateur.

La mesure de la déflection verticale du microlevier est généralement effectuée au moyen d'un rayon laser qui est réfléchit par l'extrémité du levier vers un détecteur photoélectrique (PSD, position sensitive detector). Le photodétecteur est constitué par un cadran de 4 photodiodes. Lors de la déflection du levier, en réponse à la topographie de l'échantillon balayé, le rayon laser dévie de sa position initiale sur le détecteur et la mesure de l'intensité relative du faisceau sur chaque photodiode sera proportionnelle au déplacement vertical et horizontal de la pointe.

Selon l'application et le type de forces mesurées, on distingue trois modes principaux d'utilisation de l'AFM : le mode contact (statique), le mode non-contact et le mode contact intermittent (dit de «tapping »). Le mode contact est le premier mode d'utilisation qui a été développé et il est encore le plus utilisé dans l'étude des surfaces minérales. Dans ce mode, la pointe sondeuse est en contact direct avec la surface et les forces d'interaction qui se développent sont de nature répulsive. Les variations topographiques de la surface sondée provoquent une déflection du microlevier puisque la force entre la pointe sondeuse et la surface change. La déflection est maintenue à un niveau constant prédéfini par une boucle d'asservissement qui déplace l'échantillon (ou la pointe) dans une direction appropriée à chaque point (x,y) de mesure. De cette manière la force entre la pointe et l'échantillon reste constante et les déplacements le long des directions x, y et z sont enregistrés pour fournir une image en 3D de la surface étudiée. La mesure de la déviation par le laser permet aussi d'accéder aux forces de frottement entre sonde et échantillon et d'avoir ainsi des informations relatives à la nature chimique de la surface.

La résolution latérale de l'AFM correspond en première approximation au rayon de courbure de la pointe sondeuse et elle est de l'ordre de quelques dizaines de nanomètres alors que la résolution verticale est principalement déterminée par la résolution du déplacement vertical du système de balayage, qui est de l'ordre de 1 Å et qui permet de distinguer les marches de dimensions atomiques.

3.1 L'AFM hydrothermale

Une des principales limites des AFM commerciaux est la gamme réduite des températures auxquelles cette technique peut être appliquée dans un milieu aqueux. A la température ambiante, la magnésite et la plupart des oxydes et des minéraux silicatés ont en

effet des vitesses de dissolution et précipitation faibles par rapport au temps de mesure normalement accessible en AFM. Pour appliquer la technique AFM à l'étude cinétique des réactions de ces minéraux en solution il est indispensable d'augmenter sensiblement la température. Cependant, l'augmentation de la température impose des modifications importantes du dispositif expérimental, car de nombreux facteurs comme le dégazage de la solution aqueuse, la présence de matériaux de faible stabilité thermique et l'absence de système de pressurisation, peuvent empêcher le fonctionnement correct du microscope et interférer avec l'acquisition des images à des températures élevées.

Le premier modèle de microscope AFM hydrothermal (HAFM), capable d'opérer jusqu'à 150 °C sous une pression de ~6 atm et avec une résolution comparable à celle d'un AFM normal, a été développé par Higgins et al. (1998). L'HAFM que nous avons utilisé pour l'étude de la cinétique de croissance cristalline de la magnésite est une amélioration de ce premier prototype.

Le dispositif que nous avons utilisé est équipé d'un système de pressurisation du fluide qui permet de travailler à des températures supérieures au point d'ébullition de l'eau tout en prévenant la formation de bulles et le dégazage de la solution. Une même pression d'azote est appliquée à tout le dispositif expérimental de sorte qu'aucune pression différentielle n'existe entre les différents composants du microscope. La solution réactive est contenue dans des réservoirs compressibles en Viton placés à un niveau plus élevé que la cellule du microscope. De cette manière, la solution peut circuler par gravité à travers la cellule de l'AFM sans détériorer l'acquisition et la résolution des images. La présence de trois différents réservoirs permet de changer la solution d'entrée dans la cellule AFM et de mélanger deux ou trois solutions avant l'entrée dans la cellule. La solution qui sort de la cellule est collectée dans un récipient en acier inoxydable doté d'un robinet de vidange. Le flux peut être alternativement dévié par une vanne dans un cylindre échantillonneur contenant des tubes en PC pour la récolte des échantillons à analyser. La circulation du fluide du réservoir à la cellule et de la cellule au point de prélevement utilise des tuyaux en téflon et la régulation du débit de la solution est réalisée grâce à un régulateur manuel à vis.

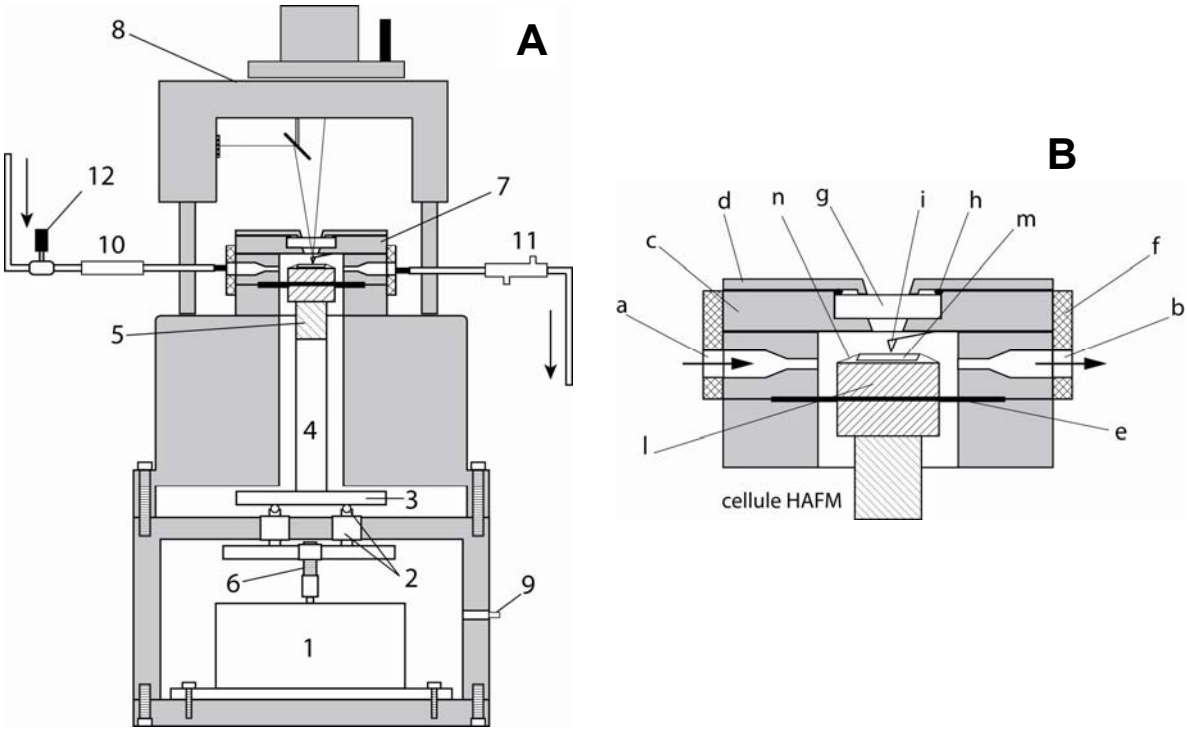

Figure 8. (**A**) Représentation schématique du microscope à force atomique hydrothermal: 1) moteur pas à pas ; 2) roulement à billes ; 3) platine en acier ; 4) tube piézoélectrique ; 5) entretoise thermique ; 6) vis principale du mécanisme de roulement ; 7) cellule contenant le fluide ; 8) tête optique avec source laser, miroir et photodiode ; 9) entrée pour le gaz ; 10) préchauffage ; 11) refroidisseur du fluide qui circule ; 12) vanne de régulation du débit. (**B**) Détail de la cellule: a) entrée du fluide ; b) sortie du fluide ; c) couverture en titane ; d) couvercle supérieur ; e) membrane de Kalrez^{TM} ; f) bague chauffante ; g) verre en saphir ; h) joint en viton; i) levier et pointe ; l) porte-échantillon ; m) échantillon; n) fil fixe-échantillon en titane.

Le modèle de la cellule AFM hydrothermale est le même que celui de la cellule construite par Higgins et al. (1998) et est représentée sur la Figure 8. La base du microscope, qui accueille le moteur pas à pas avec le scanner piézoélectrique, est séparée de la partie supérieure, la cellule à fluide, au moyen d'une membrane flexible inerte. La cellule qui contient le fluide a un volume d'environ 500 µl et toutes ses pièces en contact avec le fluide (à part la membrane, le microlevier en Si, et la fenêtre optique en saphir) ont été construites en titane afin de résister à la corrosion. L'échantillon à étudier est monté sur le support en continuité avec le tube piézoélectrique et est fixé à l'aide d'un fil en titane. L'élément piézoélectrique scanne ainsi en mode contact la surface de l'échantillon sous la pointe du microlevier installé avec une pince à vis sur la partie inférieure du couvercle de la cellule. La couvercle de la cellule, portant la fenêtre optique, est fixée hermétiquement à la partie

inférieure de la cellule avec un joint circulaire et des vis et il est surmonté par une platine en acier qui doit assurer l'immobilité du saphir de la fenêtre optique et participer à la parfaite étanchéité de la cellule. La cellule est chauffée à l'aide d'un élément chauffant circulaire qui l'entoure et la température est régulée par un thermocouple ; le fluide peut être préchauffé avant de circuler à travers le microscope, par une thermorésistance située le long du tuyau d'entrée. L'effluent est refroidi par un circuit d'eau froide autour du tuyau de sortie.

L'acquisition du signal de déflection est réalisée grâce à une tête optique sur laquelle sont montés la source du faisceau laser, le miroir et la photodiode. La tête optique repose sur un trépied qui permet le positionnement précis du système de relevé au-dessus de la fenêtre optique. La transformation du signal des photodiodes et du voltage de la boucle d'asservissement, effectuée par l'ordinateur, fournit une représentation tridimensionnelle de la topographie de la surface. L'analyse des séquences d'images ainsi acquises permet d'étudier la cinématique des processus de dissolution et de croissance cristalline à l'interface solution aqueuse/minéral.

4. Méthodes d'analyse des solutions

4.1 Analyse du magnésium

La mesure de la concentration du magnésium a été effectuée par spectrométrie d'absorption atomique (SAA) à la flamme en utilisant un spectrophotomètre Perkin-Elmer AAnalyst 400. Dans cet appareil, l'échantillon de solution à analyser est pulvérisé dans une flamme air-acétylène et transformé en vapeur atomique. Une radiation correspondant à la raie de résonance du magnésium est générée par une lampe à cathode creuse (contenant le même élément) et dirigée sur la vapeur. Une partie de la radiation est ainsi absorbée par les atomes de magnésium, qui passent de l'état fondamental à l'état excité. La quantité de photons absorbés par l'échantillon de solution produit un signal d'absorbance [$A=\log_{10}(I_0/I_1)$] qui est proportionnel à la concentration de l'élément dosé. La concentration du magnésium dans la solution aqueuse est donc déterminée par comparaison avec des étalons de concentrations connues, analysés dans les mêmes conditions.

Avant tout dosage les échantillons ont été amenés à un pH acide (pH ≈ 2) par ajout de HNO_3 15 N et une quantité d'oxyde de lanthane, égale à 30 µl par 10 ml d'échantillon, a été aussi ajouté pour éliminer de possibles interférences. Les étalons (gamme 0.1-0.6 ppm) ont

été préparés dans la même matrice que les solutions expérimentales (ex. 0.1 mol/kg de NaCl) à partir d'une solution de référence contenant 1000 ppm de magnésium (Merck $Mg(NO_3)_2$ dans HNO_3 0.5 mol/kg). La limite de détection de la concentration en magnésium est de l'ordre de 0.020 ppm avec une incertitude de ± 1%.

4.2 Détermination de l'alcalinité

La mesure de l'alcalinité des solutions expérimentales a été effectuée immédiatement après échantillonnage par titrage acidimétrique traditionnel, soit à l'aide d'un titreur volumétrique automatique (Schott TA 10plus), soit manuellement suivant la méthode de Gran (voir par exemple Stumm et Morgan, 1996). Pour les titrages nous avons utilisé de l'HCl avec une concentration variable entre 0.001 et 0.1 M, en fonction du pH et de la concentration en carbonate total dissous. L'erreur pour chaque détermination est d'environ ± 1% avec une limite de détection de l'ordre de 5×10^{-5} eq/l.

CHAPITRE 2

Cinétiques de précipitation de la magnésite aux conditions hydrothermales

Résumé en français de l'article :

"Experimental study of magnesite precipitation kinetics as a function of temperature, CO_2 partial pressure and solution chemistry"

1. Introduction

La détermination des vitesses de précipitation de phases carbonatées, comme la calcite ($CaCO_3$), la dolomite [$CaMg(CO_3)_2$], la dawsonite [$NaAlCO_3(OH_2)$], la sidérite ($FeCO_3$) et la magnésite ($MgCO_3$) est fondamentale pour l'optimisation des procédés de séquestration in situ et ex situ de l'anhydride carbonique. En particulier, le fort intérêt actuel pour la magnésite et ses mécanismes et vitesses de précipitation est motivé par la possibilité de piéger le CO_2 dans des roches ultrabasiques et basaltiques, qui, en raison de leur abondance et de leur teneur en magnésium, présentent un potentiel élevé pour le stockage de ce gaz. Plusieurs études ont déjà abordé ce sujet, mais elles se sont surtout focalisées sur le processus contrôlant la disponibilité des ions Mg^{2+} (notamment la dissolution des silicates de Mg) indispensables à la précipitation de la magnésite (ex. O'Connor et al., 2000; Giammar et al, 2005 ; Maroto-Valer et al., 2005; Béarat et al., 2006 ; Gerdemann et al., 2007). De fait, aucune étude détaillée de la vitesse de précipitation de cette phase n'a été réalisée à ce jour, alors que la compréhension du processus couplé, dissolution des silicates magnésiens et précipitation de la magnésite, est nécessaire à l'optimisation des procédés de séquestration du CO_2 par minéralisation.

L'objectif de notre étude est donc la quantification des vitesses de précipitation de la magnésite en fonction de la température, de la pression partielle de CO_2 et de la composition chimique des solutions réactives, dans une gamme de conditions pertinentes à l'application industrielle des processus de carbonatation. Les résultats de ce travail peuvent, en outre, contribuer à une meilleure compréhension des mécanismes élémentaires qui contrôlent et limitent la formation de la magnésite, comme d'autres minéraux, dans les environnements naturels.

2. Considérations théoriques

Dans l'approche classique de l'étude des cinétiques de réaction des phases carbonatées, les vitesses de précipitation sont analysées dans le cadre du modèle mécanistique construit par

Plummer et al. (1978). Selon ce modèle la vitesse de précipitation (r_p) est seulement fonction de l'indice de saturation (Ω) par rapport à la phase susceptible de précipiter :

$$r_p = k(\Omega\text{-}1)^n , \qquad (1)$$

où k représente une constante de vitesse tandis que la valeur de l'ordre de réaction n est indicatif du mécanisme de croissance. Même si l'équation (1) constitue une description fonctionnelle des vitesses de précipitation en fonction de l'écart à l'équilibre, elle ne fournit aucune information sur les réactions qui ont lieu à l'interface solution aqueuse/minéral. Les modèles de chimie de coordination surfacique récemment développés (Van Cappellen et al., 1993 ; Pokrovsky et al., 1999a) fournissent, en revanche, une base théorique plus rigureuse et puissante pour l'interprétation des vitesses de précipitation, car ils permettent de reconnaitre les réactions élémentaires qui se produisent à la surface du minéral et qui sont responsables de la précipitation.

Si on suppose, en accord avec le principe de microréversibilité, que le complexe précurseur du complexe activé est le même pour la dissolution et la précipitation, l'utilisation du modèle de complexation surfacique, développé dans le cas de la dissolution de la magnésite à 25 °C par Pokrovsky et al. (1999a), permet d'établir la relation suivante, qui peut être utilisée pour interpréter nos résultats et vérifier l'applicabilité de ce modèle à la précipitation de la magnésite :

$$r_p = k^-_{Mg} \left\{ > MgOH_2^+ \right\}^n \left(\Omega^n - 1 \right). \qquad (2)$$

Dans l'équation (2) k^-_{Mg} est une constante de vitesse, $\left\{ > MgOH_2^+ \right\}$ répresente la concentration surfacique du complexe précurseur $>MgOH_2^+$, Ω identifie l'indice de saturation de la solution, et n l'ordre de la réaction de précipitation.

Dans les solutions carbonatées (riches en espèce CO_3^{2-}), une partie des sites $>MgOH_2^+$ peut être remplacée par le complexe surfacique $>MgCO_3^-$ et on peut répresenter la formation des sites $>MgOH_2^+$ à partir de sites $>MgCO_3^-$ par la relation:

$$>MgCO_3^- + H_2O = >MgOH_2^+ + CO_3^{2-}, \qquad (3)$$

dont la constante d'équilibre est donnée par :

$$K_{CO3} = \frac{\left\{ > MgOH_2^+ \right\} a_{CO_3^{2-}}}{\left\{ > MgCO_3^- \right\}} . \qquad (\text{avec } a_{H_2O} = 1) \qquad (4)$$

Dans les conditions où la chimie de surface de la magnésite est dominée par les complexes $>MgCO_3^-$ et $>MgOH_2^+$, c'est-à-dire dans des solutions faiblement alcalines et en l'absence de ligands organiques et inorganiques, la combinaison des équations (2) et (4) mène à la relation suivante :

$$\boldsymbol{r}_p = \boldsymbol{k}_{Mg}^{-} \left(\frac{K_{CO3}}{K_{CO3} + \boldsymbol{a}_{CO_3^{2-}}} \right)^{\boldsymbol{n}} \left(\Omega^{\boldsymbol{n}} - 1 \right) , \qquad (5)$$

qui permet de décrire la vitesse de précipitation en fonction de Ω et de l'activité des ions carbonates ($\boldsymbol{a}_{CO_3^{2-}}$).

3. Méthodes expérimentales

Notre étude expérimentale a été conduite dans des réacteurs à circulation et des réacteurs fermés, à quatre températures différentes (100, 120, 150, 200 °C) et en utilisant des poudres synthétiques de magnésite, à la surface desquelles se produit la croissance cristalline de ce minéral (Fig. 1 de l'article). Les réacteurs fermés nous ont permis de mesurer les vitesses de cristallisation de $MgCO_3$ sous de fortes pressions de CO_2 et dans des conditions proche de l'équilibre. Les solutions expérimentales utilisées pour les expériences ont été préparées à partir de NaCl, $NaHCO_3$, $MgCl_2$, HCl et NaOH et de l'eau ultra pure, en variant la proportion de ces réactifs pour obtenir différents degrés de sursaturation et teneurs en espèces carbonatées à des forces ioniques variables entre 0.1 et 1 M (voir Tableau 2, article).

Pour les essais réalisées dans des réacteurs à circulation, les vitesses de précipitation ($\boldsymbol{r}_p$) à une température donnée ont été calculées à partir de la variation de la concentration en Mg entre la solution à l'entrée et à la sortie du réacteur ($\Delta[Mg]_{tot}$), du débit de la solution (q) et de la surface totale de magnésite présente dans le réacteur ($\boldsymbol{S}$) suivant:

$$\boldsymbol{r}_p = -q \cdot \Delta[Mg]_{tot}/\boldsymbol{S} \qquad (6)$$

Lors des essais en réacteur fermé la précipitation a été provoquée par une rapide augmentation de la température d'une solution aqueuse initialement en équilibre avec une poudre de magnésite. La vitesse de précipitation a été calculée en suivant l'évolution temporelle de la concentration en Mg dissous lors de l'approche de l'équilibre thermodynamique à la nouvelle

température. L'analyse de la cinétique de relaxation (Eigen and de Maeyer 1963), déjà utilisées dans des études antérieures (par exemple, Pines and Huppert, 1983; Prabhananda et al., 1987; Bénézeth et al., 2008), nous a ainsi permis de décrire la variation, en fonction du temps, de la concentration en magnésium ($\partial C/\partial t$) à l'aide de l'équation :

$$\partial C / \partial t = \frac{-\left[(C_{eq})_1 - (C_{eq})_2\right]}{\tau} e^{-t/\tau}, \qquad (7)$$

où $(C_{eq})_1$ and $(C_{eq})_2$ représentent les concentrations en Mg à l' équilibre avant et après le saut de température et τ représente le temps de relaxation, qui est une fonction de la constante de vitesse de la réaction de précipitation ($\boldsymbol{k}$) suivant :

$$\tau = \frac{C(t) - (C_{eq})_2}{\boldsymbol{k}(\Omega^{\boldsymbol{n}} - 1)\boldsymbol{S}} \qquad (8)$$

4. Résultats principaux de l'étude

Sur la Figure 4 (article) nous avons reporté le logarithme des vitesses de précipitation de la magnésite mesurées en réacteur à circulation, en fonction du logarithme de l'indice de saturation de la solution pour différentes activités de CO_3^{2-} à 100, 150 et 200 °C. Ces diagrammes montrent que les vitesses de précipitation mesurées diminuent avec l'augmentation de l'activité de CO_3^{2-}. Malgré la dispersion des données, qui est due à l'imparfaite reproductibilité des résultats expérimentaux, les lignes en tirets montrent aussi que les vitesses de précipitation sont en général cohérentes avec un ordre de réaction $\boldsymbol{n}$ = 2. Cette valeur de l'ordre de réaction est représentative d'un mécanisme de croissance en spirale, en accord avec l'étude par microscopie AFM effectuée dans le cadre de ce travail (voir chapitre 2) et des études antérieures sur la cristallisation de la calcite (Shiraki et Brantley, 1995 ; Teng et al., 1998, 2000). Ces observations suggèrent que l'équation (5) ci-dessus peut être utilisée pour décrire la vitesse de précipitation de la magnésite en fonction de la composition de la solution et de son degré de sursaturation par rapport à ce minéral. L'équation (5) permet de déterminer la constante de vitesse ($\boldsymbol{k}_{Mg}^{-}$) et la constante K_{CO3}. Ces déterminations ont été faites à chaque température par simple interpolation des données expérimentales (voir la Fig. 5 de l'article): les valeurs attribuées à $\boldsymbol{k}_{Mg}^{-}$ correspondent aux intercepts des courbes décrites par l'équation (5) avec l'axe des ordonnées, alors que les

valeurs moyennes de K_{CO3} ont été choisies afin de fournir la meilleure description de la diminution des vitesses de précipitation en fonction de $\boldsymbol{a}_{CO_3^{2-}}$. Les valeurs de $\boldsymbol{k}_{Mg}^{-}$ et K_{CO3} obtenues par cette méthode sont listées dans le Tableau 7 (article). On peut noter que les valeurs de K_{CO3} augmentent quand la température diminue, ce qui reflète un accroissement de la complexation des ions carbonates avec les sites magnésiens et donc une augmentation de l'inhibition par CO_3^{2-} lorsque la température augmente. Les diagrammes de la Figure 5a et 5b montrent qu'il existe un accord satisfaisant entre les vitesses expérimentales et celles prévues par le modèle, en fonction de $\boldsymbol{a}_{CO_3^{2-}}$ et de la température.

Les vitesses de précipitation de la magnésite mesurées en réacteur fermé ne sont pas compatibles avec un mécanisme de croissance spirale. Les conditions très proches de l'équilibre et l'ordre de la réaction proches de 1 (Fig. 9 et 10, article) témoignent plutôt d'une croissance linéaire des cristaux de magnésite, probablement facilitée par la formation d'hétérogénéités surfaciques durant la phase de dissolution des cristaux précédant la phase de précipitation. En outre, les faibles pH (5.1-5.6) mesurés au cours de nos essais, réalisés sous des fortes pressions de CO_2 (15-30 bars), limitent la concentration de CO_3^{2-} à des valeurs très faibles et évitent ainsi l'effet d'inhibition observé aux pH basiques où la proportion de cette espèce est beaucoup plus importante.

La détermination des constantes de vitesse $\boldsymbol{k}_{Mg}^{-}$ en fonction de la température nous a permis, à l'aide du diagramme d'Arrhenius, de déterminer la valeur de l'énergie d'activation apparente ($\boldsymbol{E}_a$) de la réaction de précipitation et ainsi d'extrapoler les valeurs des constantes de vitesse à plus basse température (Fig. 6, article). L'extrapolation de ces vitesses avec l'énergie d'activation déterminée dans cette étude (64 kJ/mol) donne $\boldsymbol{k}_{Mg}^{-} = 4.1\times10^{-18}$ mol/cm^2/s à 25 °C. Cette valeur de constante de vitesse est environ 6.5 ordres de grandeur plus faible que celle déterminée pour la calcite à la même température par Yeghicheyan (1996), dans des conditions où le même mécanisme est supposé contrôler les vitesses de précipitation. Cette très faible valeur de la constante cinétique explique la grande difficulté à précipiter de la magnésite à température ambiante et la formation préférentielle de carbonates magnésiens hydratés moins stables. La difficulté, par rapport à la calcite, de formation de la magnésite à température ambiante par précipitation directe à partir de solutions sursaturées peut être mise en relation avec la stabilité beaucoup plus grande de la liaison Mg-O par rapport à Ca-O, dont témoignent les très lentes vitesses d'échange entre les molécules d'eau

de la solution aqueuse et la sphère d'hydratation du Mg, comme l'ont déjà souligné Pokrovsky et Schott (2002).

5. Implications pour le stockage géologique du CO_2

Les données expérimentales issues de ce travail suggèrent la faisabilité du processus de carbonatation minérale *ex situ* sous fortes pressions de CO_2, c'est-à-dire dans des conditions qui induisent des pH des solutions faiblement acides ou proches de la neutralité et ainsi permettent d'accélérer les vitesses de dissolution des silicates magnésiens, tout en évitant l'inhibition de la précipitation de la magnésite par les ions CO_3^{2-}. Cependant, dans le cas d'injection de fluides enrichis en CO_2 dans des roches basiques et ultrabasiques (carbonatation minérale *in situ*), l'augmentation du pH des solutions, induite par la dissolution des roches, augmente la teneur en CO_3^{2-} et ainsi ralentit notablement la vitesse du processus global de carbonatation. En outre, à cause de la complexité chimique et minéralogique des sites potentiels de stockage et des faibles vitesses de précipitation des carbonates magnésiens, la formation de magnésite ou de carbonates de magnésium hydratés, peut être défavorisée par la nucléation de phases secondaires porteuses de magnésium comme les smectites et les zéolites (Marini, 2007 ; Gisy and Stefánsson, 2008; Andreani et al., 2009).

Experimental study of magnesite precipitation kinetics as a function of temperature CO_2 pressure and solution chemistry

Giuseppe D. Saldi*, Jacques Schott, Oleg S. Pokrovsky, Quentin Gautier

and Eric H. Oelkers

Géochimie et Biogéochimie Expérimentale, LMTG – CNRS – OMP – Université de Toulouse, 14, Avenue Edouard Belin, 31400 Toulouse, France

***Corresponding author:**

Tel.: +33 5 61 33 26 32; fax: +33 5 61 33 25 60

E-mail addresses: saldi@lmtg.obs-mip.fr, oelkers@lmtg.obs-mip.fr

Prepared for submission to *Geochimica et Cosmochimica Acta*

Keywords: magnesite, precipitation kinetics, CO_2 sequestration, mineral carbonation

Abstract

Magnesite precipitation rates were measured from 100 to 200 °C and 6.9 < pH < 9.3 as a function of solution saturation state and composition, and CO_2 partial pressure using mixed flow and batch reactors. Rates were found to be independent of aqueous solution ionic strength at 0.1 M < I < 1.1 M but decrease significantly with increasing aqueous CO_3^{2-} activity at pH > 8. All rates obtained from mixed flow reactor experiments were found to be consistent with the model of Pokrovsky et al. (1999a) where magnesite precipitation rates are proportional to the concentration of the >$MgOH_2^+$ surface species. The inhibitory effect of aqueous CO_3^{2-} stems from its tendency to form stable >$MgCO_3^-$ surface complexes from >$MgOH_2^+$. Consistent with this model magnesite precipitation rates can be described using:

$$r_p = k_{Mg}^{-}\left(\frac{K_{CO3}}{K_{CO3} + a_{CO_3^{2-}}}\right)^2 \left(\Omega^2 - 1\right) ,$$

where k_{Mg}^{-} represents a rate constant, K_{CO3} is the formation constant of the rate controlling surface species (>$MgOH_2^+$) via desorption of CO_3^{2-} ions from >$MgCO_3^-$ sites; and Ω is the saturation state of the aqueous solution. The variation of the rate constant is described by the relation $k_{Mg}^{-} = A_a \exp(-E_a / RT)$, where A_a is a pre-exponential factor equal to 7.1×10^{-7} mol/cm^2/s, E_a designates an activation energy equal to 64 kJ/mol, R represents the gas constant and T is the absolute temperature. The effect of aqueous CO_3^{2-} on rates decreases with decreasing temperature. This decrease is interpreted to stem from a decreasing stability of >$MgCO_3^-$ on the magnesite surface at lower temperatures.

Unlike rates measured in mixed flow reactor, magnesite precipitation rates determined in batch reactor at 150 and 200 °C exhibit a linear dependence with magnesite saturation state, consistently with generally lower degrees of supersaturation of the precipitating solutions and a different surface morphology of magnesite seeds which were significantly dissolved before precipitation reaction began.

1. Introduction

The recent and ongoing debate on global warming and the need for a drastic reduction of atmospheric greenhouse content have spurred renewed interest in the study of carbonate mineral stability and precipitation kinetics. This interest is motivated by the possibility of mineral sequestration of CO_2. The goal of this mineral sequestration is to form stable carbonate minerals such as calcite ($CaCO_3$), dolomite [$CaMg(CO_3)_2$], siderite ($FeCO_3$), and magnesite ($MgCO_3$) from a combination of silicate mineral dissolution, which liberates divalent metal cations, coupled to carbonate precipitation (cf. Berner et al., 1983; Oelkers and Schott, 2005; Oelkers et al., 2008). Both ultramafic and basaltic rocks are among the most abundant and economically available source of divalent cations needed to precipitate solid carbonates (Lackner et al., 1995, 1997; Goldberg et al., 2001; McGrail et al., 2006). Ultramafic rocks, in particular, can contain between 30 and 50 % of MgO by weight in Mg-silicates and, being also relatively poor in silica, represent the feedstock material with the highest potential for CO_2 mineral sequestration (Wolff-Boenisch et al., 2006). Mg carbonation can occur via the following reactions:

$$Mg_2SiO_{4(s)} + 2CO_{2(g)} + 2H_2O = 2MgCO_{3(s)} + H_4SiO_{4(aq)} \quad (1)$$

Forsterite Magnesite

$$Mg_3Si_2O_5(OH)_{4(s)} + 3CO_{2(g)} + 2H_2O = 3MgCO_{3(s)} + 2H_4SiO_{4(aq)} \quad (2)$$

Serpentine Magnesite

where dissolved silica may eventually precipitate as quartz, amorphous silica, or other silicates. Knowledge of magnesite precipitation rates are therefore fundamental for the development and optimization of economically viable in situ and ex-situ CO_2 mineral sequestration.

Several studies have attempted to provide insight into the coupled Mg-silicate dissolution/magnesite precipitation process as a possible industrial application (e.g. Wolf et al., 2004; Giammar et al., 2005; Chen et al., 2006; Gerdemann et al., 2007; Oelkers et al., 2008; Andreani et al., 2009). Some of these studies quantified the effect of physico-chemical parameters which affect the efficiency of this coupled process. For example, it was shown that mineral carbonation proceeds relatively faster and more efficiently when using forsterite (Mg_2SiO_4) instead of serpentine [$(Mg_3Si_2O_5(OH)_4$] (Gerdemann et al., 2007). However, the use of serpentine would be preferable because this mineral is much more abundant and

accessible than olivine, but it requires either physical pretreatment or chemical activation to enhance its reactivity (O'Connor et al., 2000; Maroto-Valer et al., 2005; Alexander et al., 2007). As the dissolution rates of silicate minerals are generally slow at room temperature, it is necessary to increase *T* above 100°C to make the overall process practical. Optimum carbonation conditions for processes employing Mg-silicates (serpentine and olivine), as reported by Gerdermann et al. (2007), are achieved at temperatures of 155-185 °C and pCO_2 between 115 and 150 bar in solutions of 1 M NaCl and ~0.06 M $NaHCO_3$. The dissolution rates of various Mg-silicates have been reported in the literature (e.g. Luce et al., 1972; Lin and Clemency, 1981; Schott et al., 1981, 1983; Wogelius and Walther, 1991; Rosso and Rimstidt, 2000; Pokrovsky and Schott, 2000; Oelkers, 2001; Oelkers and Schott, 2001; Hänchen et al., 2006, Saldi et al., 2007). While these studies provide the basis for estimating Mg release rates into solution from silicate dissolution, little corresponding work has been done on Mg-carbonate precipitation kinetics.

Magnesite formation at near Earth surface conditions is strongly hindered by its slow kinetics and formation of metastable hydrous Mg-carbonate phases, such as nesquehonite ($MgCO_3 \cdot 3H_2O$), hydromagnesite [$MgCO_3Mg(OH)_2 \cdot 4H_2O$] and less commonly artinite and dypingite (Christ and Hostetler, 1970; Lippmann, 1973; Hänchen et al., 2008, Saldi et al., 2009). Slow magnesite crystallization rates and its scarcity in surficial environments are traditionally attributed to the high hydration energy of the Mg^{2+}ion and the strength of Mg-O bonds compared to Ca-O bonds (see Lippmann (1973) for an extensive discussion). Magnesite formation in natural environments sometimes results from the dehydration of hydromagnesite; this transformation is favored at high salinities, elevated CO_2 partial pressure, and high *T* (cf. Christ and Hostetler, 1970). The enhancing effect of pCO_2 and ionic strength on $MgCO_3$ crystallization rates was also pointed out by Sayles and Fyfe (1973), who quantified the transformation rates of hydromagnesite into magnesite in aqueous solution at 126° C. The catalytic effect of CO_2 partial pressure on magnesite formation had also been reported by Baron and Favre (1958). Nonetheless a substantial degree of supersaturation is required to initiate magnesite heterogeneous nucleation even at most favorable conditions (Giammar et al, 2005; Hänchen et al. 2008; Saldi et al., 2009).

The main objective of this work is to quantify magnesite precipitation rates as a function of saturation state, temperature, CO_2 partial pressure, and solution chemistry. These rates will aid in the fundamental understanding of the elementary mechanisms which control

magnesite formation during both natural and industrial processes. Such results will also allow for an improved description of Mg carbonation as a CO_2 sequestration method using reactive transport models.

2. Theoretical considerations

According to the classic model of Plummer et al. (1978) and Wollast (1990), the dissolution kinetics of magnesite is controlled by two parallel reactions:

$$MgCO_{3(cr)} + H^+ = >HMgCO_3^+ \rightarrow Mg^{2+} + HCO_3^- \quad (3)$$

$$MgCO_{3(cr)} + nH_2O = >MgCO_3 \cdot nH_2O \rightarrow Mg^{2+} + CO_3^{2-} \quad (4)$$

which correspond to a protonation and hydration mechanism, respectively. The middle term of each reaction, which was not specifically mentioned by the original authors, corresponds to the rate controlling precursor complex of each mechanism. Reactions (3) and (4) dominate under acidic and alkaline conditions, respectively. Far from equilibrium magnesite dissolution rates can be described using

$$r_+ = k_{H^+} \cdot a_{H^+} + k_{H_2O} \quad (5)$$

where k_{H^+} and k_{H_2O} refer to the rate constant of reaction (3) and (4) and a_{H^+} represents the activity of proton. It should be noted that a third parallel reaction, surface carbonation by H_2CO_3, was envisaged by Plummer et al . (1978), but it was recently dismissed by Pokrovsky et al. (2005) and Schott et al. (2009), who demonstrated that, at a given ionic strength, H_2CO_3 has no specific effect on carbonate dissolution rates and that measured increased dissolution rates as a function of carbonic acid concentration can be accounted for by solution acidification rather than the presence of H_2CO_3.

Within the Plummer et al. (1978) model, precipitation occurs via the reverse of reaction (4). At neutral to basic conditions, where magnesite can precipitate, this leads to the following equation describing magnesite dissolution and precipitation rates:

$$r = k_{H_2O}(1-\Omega), \quad (6)$$

where Ω defines the saturation state of the aqueous solution, equal to the ratio of the ion activity product of dissolved mineral components (Q) to the thermodynamic solubility product (K_{sp}). For magnesite, the saturation state is defined by

$$\Omega = \frac{Q}{K_{sp}} = \frac{\boldsymbol{a}_{Mg^{2+}} \boldsymbol{a}_{CO_3^{2-}}}{K_{MgCO_3}} \ , \qquad (7)$$

where $\boldsymbol{a}_i$ refers to the activity of the subscripted aqueous species. Following this approach carbonate precipitation rates have been commonly described by means of the empirical rate equation:

$$\boldsymbol{r}_p = \boldsymbol{k} (\Omega\text{-}1)^{\boldsymbol{n}} \ , \qquad (8)$$

where $\boldsymbol{r}_p$ stands for the surface area normalized precipitation rate, $\boldsymbol{k}$ refers to an empirical rate constant, and $\boldsymbol{n}$ designates a reaction order, which is indicative of the growth mechanism. This rate equation was used to fit experimental precipitation data of calcite (Nancollas and Reddy, 1971; Reddy et al., 1981; Mucci and Morse, 1983; Inskeep and Bloom, 1985; Busenberg and Plummer, 1986; Shiraki and Brantley, 1995), Mg-calcite (Mucci, 1986) and dolomite (Arvidson and Mackenzie, 1999). Such fits provide a good representation of carbonate minerals precipitation in aqueous solution at various conditions, but do not usually provide much insight into processes occurring at the mineral/water interface.

An improved description of carbonate dissolution and precipitation rates can be made using surface speciation models (SCM) (Van Cappellen et al., 1993; Pokrovsky et al., 1999a, 1999b). Within these models the forward rate is assumed to be equal to the concentration of a rate controlling species on the mineral surface. Surface speciation models assume the existence of two primary hydration sites at the carbonate-solution interface, >MeOH° and >CO_3H°, whose protonation/hydration and reaction with various ligands control mineral reactivity. Within this approach, proton-promoted dissolution at pH < 5 is attributed to the protonation of surface carbonate groups (>CO_3H°), whereas fully hydrated metal centers (>$MeOH_2^+$) govern the H_2O-promoted dissolution at pH>6 (Pokrovsky and Schott, 2001, 2002). Thus, within the context of the surface coordination chemistry model, magnesite dissolution rates at far from equilibrium conditions can be expressed as:

$$\boldsymbol{r}_+ = \boldsymbol{r}_{+H^+} + \boldsymbol{r}_{+H_2O} = \ \boldsymbol{k}_H \left\{> CO_3H°\right\}^{\boldsymbol{n}_H} + \boldsymbol{k}_{H_2O} \left\{> MgOH_2^+\right\}^{\boldsymbol{n}_{H_2O}} \qquad (9)$$

where k_H and k_{H_2O} designate the rate constant relative to proton-promoted and H_2O-promoted dissolution, respectively, and n_H and n_{H_2O} represent the reaction orders with respect to surface protonated carbonate and hydrated Mg-centers.

Assuming, in accord with the principle of detailed balancing, that the precursor complex is the same both for dissolution and precipitation, the following expression for magnesite overall reaction rate can be derived for neutral to alkaline solutions, where close to equilibrium conditions are readily achieved:

$$r = k_{H_2O} \left\{ > MgOH_2^+ \right\}^{n_{H_2O}} \left(1 - \Omega^{n_{H_2O}} \right), \quad (10)$$

The rate controlling $>MgOH_2^+$ complex on the magnesite surface can be formed by the following reactions:

$$>MgOH° + H_2O = >MgOH_2^+ + OH^- \quad , \quad (11)$$

$$>MgCO_3^- + H_2O = >MgOH_2^+ + CO_3^{2-} \quad , \quad (12)$$

$$>MgHCO_3° + H_2O = >MgOH_2^+ + HCO_3^- \quad , \quad (13)$$

for which the corresponding values of the intrinsic stability constants are given by K_{OH}, K_{CO3}, and K_{HCO3}. Values for these stability constants at 25 °C were reported by Pokrovsky et al. (1999a). Assuming that the concentrations of >MgOH° and $>MgHCO_3°$ are negligible, the mass balance on Mg surface sites can be expressed as

$$1 = X_{>MgOH_2^+} + X_{>MgCO_3^-} \quad (14)$$

Combining the law of mass action for reaction (12) with (14) and as $a_{H_2O} \approx 1$, the concentration of $>MgOH_2^+$ can be expressed as a function of CO_3^{2-} activity by:

$$X_{>MgOH_2^+} = \frac{K_{CO3}}{K_{CO3} + a_{CO_3^{2-}}} \quad . \quad (15)$$

Which can be combined with Eqn. (10) to give:

$$r_d = k_{Mg}^+ \left(\frac{K_{CO3}}{K_{CO3} \cdot + a_{CO_3^{2-}}} \right)^{n_{H2O}} \cdot \left(1 - \Omega^{n_{H_2O}} \right) \quad (16)$$

Eqn. (16) suggests an inhibiting effect of CO_3^{2-} ions on magnesite dissolution and precipitation rates. Eqn. (16) provides the means to describe magnesite precipitation kinetics

as a function of saturation state and surface chemistry, which itself depends on the chemical composition of the aqueous solution. This equation will be used below to interpret and describe measured magnesite precipitation rates.

3. Experimental methods

3.1 Magnesite samples

Eight different synthetic magnesite samples were used for the experiments. Synthetic magnesite was synthetized from analytical grade hydromagnesite ($MgCO_3$ Prolabo Rhône-Poulenc) . This solid was placed in a 400 ml rocking autoclaves at temperatures of 200 and 250 °C for three weeks at an average pCO_2 of 50 bar. The resulting magnesite powders consisted of < 40 μm rhombohedral crystals. A representative SEM photomicrograph of produced synthetic magnesite powder is shown in Figure 1a; XRD and EDS analyses demonstrate a high degree of purity for all the samples. The specific surface area of magnesite powders was determined by multipoint krypton adsorption using the BET (Brunauer et al., 1938) method. Resulting BET surface areas ranged from 1474 to 2241 cm^2/g. The uncertainty of these measurements is estimated to be ± 10%. The geometric surface areas of these powders were also determined on the basis of granulometric analysis: calculations were made assuming that the crystals have a rhombohedral shape. A summary of the geometric and BET specific surface areas of all powders is reported in Table 1. Resulting geometric surface areas ranged from 600 to 1000 cm^2/g.

3.2 Preparation and analyses of solutions

All reactive fluids were prepared by adding reagent and analytical grade NaCl, $MgCl_2$, $NaHCO_3$, HCl, and NaOH to high purity deionized water. The relative concentration of these compounds was changed to obtain various aqueous Mg^{2+}/CO_3^{2-} activity ratios and different degrees of supersaturation with respect to magnesite. Experiments were performed at ionic strengths ranging from 0.1 to 1M. The compositions of the reactive fluids used in the present study are listed in Table 2.

Reactive fluids sampled both before and during each experiment were analysed for magnesium concentration and alkalinity. Mg was measured by flame atomic absorption

spectroscopy (AAS) with an uncertainty of ± 1% and a detection limit of 6×10^{-7} M, whereas the alkalinity was determined by standard HCl titration with an uncertainty of ± 1% and a detection limit of 5×10^{-5} M. Reactive fluid pH was measured at 25 °C using a standard glass electrode. pH of fluid samples obtained during the experiments was measured immediately after sampling. Saturation state and solution speciation were calculated using the PHREEQC code (Parkhurst and Appelo, 1999) together with its llnl thermodynamic database, after adding formation constants for the aqueous $MgOH^+$ complex, taken from Shock et al. (1997).

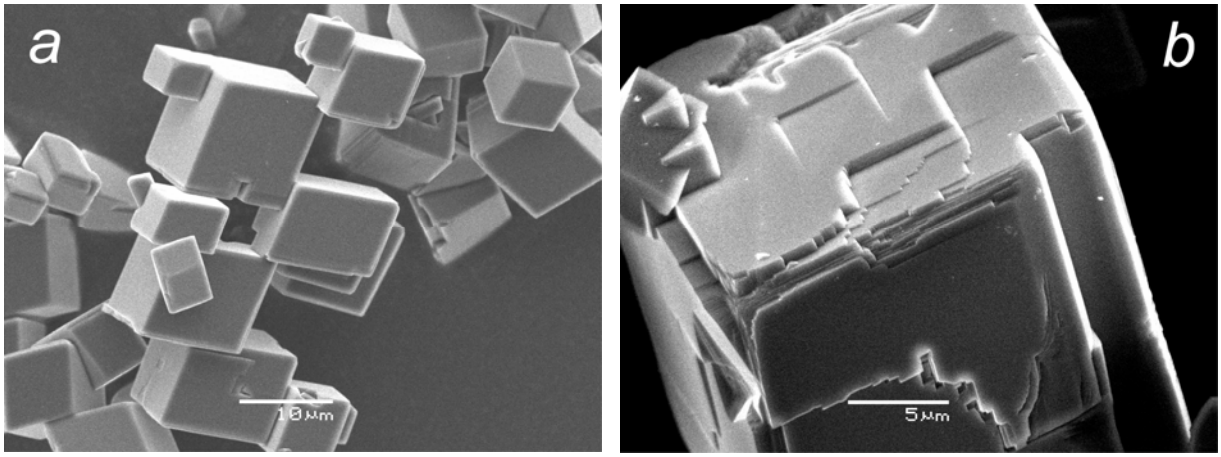

Figure 1. SEM photomicrographs of synthetic $MgCO_3$ used for batch and mixed-flow reactor experiments: an example of magnesite powder after synthesis at 250 °C and CO_2 pressure of 50 bar (***a***); a detail of a $MgCO_3$ crystal after a precipitation experiment in mixed flow reactor (***b***).

Table 1. Values of specific surface area for the magnesite powders used in this study as detemined by krypton adsorption (S_{BET}) and by granulometric analysis (S_{GEO}).

$MgCO_3$ powders	S_{BET} (cm^2/g)	S_{GEO} (cm^2/g)
Mgs-I	2241	822
Mgs-II	1723	643
Mgs-III	1610	772
Mgs-IV	2153	636
Mgs-V	1791	844
Mgs-VI	1474	782
Mgs-VII	1826	992
Mgs-VIII	2007	669

Table 2. Composition of experimental solutions used for magnesite precipitation experiments in the present study.

Exp. Sol.	exp. *T* (°C)	pH (25°C)	NaCl [mol/kg]	$MgCl_2$ [mol/kg]	HCl [mol/kg]	NaOH [mol/kg]	$NaHCO_3$ [mol/kg]
PM6	200	8.11	0.1	1.653E-04	0	0	0.01
PM6B	200	8.08	0.1	1.698E-04	0	0	0.01
PM7	200	8.26	0.1	9.308E-05	0	0	0.02
PM7C	200	8.24	0.1	9.420E-05	0	0	0.02
PM8	200	8.36	0.1	5.253E-05	0	0	0.04
PM9	200	7.15	0.1	1.712E-04	0	0	0.01
PM9B	200	7.20	0.1	1.692E-04	0	0	0.01
PM12	200	6.62	0.1	2.260E-04	2.02E-02	0	0.04
PM12B	200	6.45	0.1	1.313E-04	5.20E-03	0	0.01
PM13	200	6.12	0.1	1.842E-04	6.50E-03	0	0.01
PM21	200	6.55	0.5	2.684E-04	9.75E-03	0	0.02
PM21E	200	6.28	0.5	2.729E-04	9.75E-03	0	0.02
PM24	200	6.22	1.00	3.841E-04	9.22E-03	0	0.02
PM27	200	6.22	1.00	3.513E-04	9.27E-03	0	0.02
PM29	200	6.13	0.10	2.657E-04	6.68E-03	0	0.01
PM30	200	7.78	0.10	5.503E-05	2.19E-03	0	0.06
PM33	200	6.25	1.00	3.708E-04	9.27E-03	0	0.02
PM33B	200	6.22	1.00	3.570E-04	9.27E-03	0	0.02
PM35	200	7.82	0.10	5.669E-05	2.19E-03	0	0.06
PM35B	200	7.86	0.10	5.600E-05	2.19E-03	0	0.06
PM37	200	8.83	0.10	1.653E-05	0.00E+00	0	0.08
PM41	200	8.71	0.10	2.023E-05	0.00E+00	4.00E-04	0.01
PM14	150	7.49	0.08	2.944E-04	4.48E-03	0	0.04
PM16	150	7.92	0.1	3.174E-04	1.60E-03	0	0.01
PM17	150	7.07	0.1	3.729E-04	2.79E-03	0	0.02
PM17A	150	7.21	0.1	3.930E-04	2.79E-03	0	0.02
PM18	150	7.48	0.1	3.174E-04	4.39E-03	0	0.04
PM18C	150	7.48	0.1	3.155E-04	4.39E-03	0	0.04
PM19	150	6.68	0.1	6.578E-04	1.21E-03	0	0.006
PM19A	150	6.51	0.1	6.679E-04	1.21E-03	0	0.006
PM19D	150	6.60	0.1	6.560E-04	1.21E-03	0	0.006
PM20	150	7.46	0.1	2.983E-04	5.73E-03	0	0.06
PM20B	150	7.60	0.1	2.922E-04	5.73E-03	0	0.06
PM20D	150	7.38	0.1	2.913E-04	5.73E-03	0	0.06
PM22	150	6.90	0.5	5.591E-04	3.30E-03	0	0.02
PM23	150	7.15	0.5	5.560E-04	3.30E-03	0	0.02
PM23B	150	6.93	0.5	5.526E-04	3.30E-03	0	0.02
PM25	120	7.22	0.1	6.716E-04	2.00E-03	0	0.02
PM26	120	7.19	0.1	6.669E-04	1.40E-03	0	0.02
PM26A	120	7.38	0.1	6.689E-04	7.30E-04	0	0.02
PM28	120	7.66	0.1	6.674E-04	6.95E-04	0	0.02
PM28B	120	7.66	0.1	6.537E-04	6.95E-04	0	0.02
PM31	120	7.64	0.1	3.876E-04	7.33E-04	0	0.02
PM31B	100	7.47	0.1	8.281E-04	0	0	0.02
PM32	100	7.79	0.1	8.430E-04	0	8.00E-04	0.02

Exp. Sol.	exp. *T* (°C)	pH (25°C)	NaCl [mol/kg]	$MgCl_2$ [mol/kg]	HCl [mol/kg]	NaOH [mol/kg]	$NaHCO_3$ [mol/kg]
PM34	100	7.87	0.1	8.634E-04	0	8.00E-04	0.02
PM34B	100	7.74	0.1	8.286E-04	0	8.00E-04	0.02
PM36	100	8.27	0.1	3.851E-04	0	8.00E-04	0.02
PM36B	100	8.43	0.1	2.322E-04	0	8.00E-04	0.02
PM38	100	8.32	0.1	4.166E-03	0	9.30E-03	0.01
PM39	100	8.75	0.06	1.193E-04	0	2.72E-03	0.06
PM39B	100	8.70	0.06	1.176E-04	0	2.72E-03	0.06
QM1	100	8.90	0.1	3.752E-04	0	0.0101	0.04
QM2	100	9.120	0.04	6.512E-05	0	0.0101	0.08
QM2A	100	9.200	0.04	6.832E-05	0	0.0101	0.08
QM3A	100	9.448	0.01	3.234E-05	0	0.019	0.090

Table 3. Summary of magnesite precipitation experiments performed in this study at 100 °C in open system reactor.

Run #	Ω	pH	I M	Alk [mol/kg]	Δ [Mg] [mol/kg]	$a(CO_3^{2-})$	BET s. area [cm^2/g]	$MgCO_3$ mass [g]	FFR [g/min]	r_p [$mol/cm^2/s$]
PM31B	30.0	7.63	0.12	1.79E-02	-5.18E-05	4.52E-05	1723	1.753	0.602	1.72E-13
PM32	32.9	7.66	0.12	1.87E-02	-5.82E-05	4.96E-05	1723	1.753	1.197	3.84E-13
PM32A	34.5	7.68	0.12	1.87E-02	-5.45E-05	5.20E-05	1723	1.753	1.689	5.08E-13
PM32B	39.8	7.74	0.12	1.87E-02	-4.25E-05	5.95E-05	1723	1.753	2.378	5.57E-13
PM32C	39.1	7.72	0.12	1.87E-02	-3.32E-05	5.77E-05	1723	1.753	3.367	6.16E-13
PM34	33.3	7.70	0.12	1.85E-02	-1.44E-04	5.50E-05	2007	2.825	0.597	2.52E-13
PM34A	43.8	7.81	0.12	1.86E-02	-1.10E-04	7.02E-05	2007	2.825	0.984	3.18E-13
PM34B	33.9	7.68	0.12	1.85E-02	-4.84E-05	5.15E-05	2007	2.825	1.481	2.11E-13
PM34C	38.5	7.74	0.12	1.86E-02	-4.93E-05	5.90E-05	2007	2.825	2.156	3.12E-13
PM36	25.1	7.98	0.12	1.95E-02	-9.31E-05	1.08E-04	2007	1.599	0.491	2.37E-13
PM36A	31.2	8.04	0.12	1.96E-02	-5.82E-05	1.22E-04	2007	1.599	1.085	3.28E-13
PM36B	20.1	8.12	0.12	1.99E-02	-5.53E-05	1.48E-04	2007	1.599	0.396	1.14E-13
PM36C	23.9	8.12	0.12	1.99E-02	-2.35E-05	1.50E-04	2007	1.599	0.987	1.20E-13
PM38*	29.6	7.34	0.12	7.68E-03	-8.57E-04	9.47E-06	1791	1.803	0.581	2.57E-12
PM38A*	42.8	7.45	0.12	8.16E-03	-6.09E-04	1.28E-05	1791	1.803	1.103	3.47E-12
PM39*	16.7	8.42	0.12	6.18E-02	-7.32E-05	8.83E-04	1791	1.803	0.593	2.24E-13
PM39A*	26.5	8.41	0.12	6.19E-02	-4.54E-05	8.67E-04	1791	1.803	1.107	2.60E-13
PM39B*	22.4	8.43	0.12	6.18E-02	-5.65E-05	8.99E-04	1791	1.803	1.602	4.68E-13
QM1*	18.0	8.00	0.14	3.88E-02	-2.48E-04	2.22E-04	1791	1.780	1.198	1.55E-12
QM2*	20.3	8.87	0.14	9.03E-02	-3.17E-05	2.98E-03	1791	1.780	0.584	9.68E-14
QM2A*	20.1	8.86	0.14	8.89E-02	-2.40E-05	2.90E-03	1791	1.780	1.084	1.36E-13
QM2B*	20.1	8.86	0.14	8.90E-02	-1.95E-05	2.90E-03	1791	1.780	1.506	1.53E-13
QM3A*	19.5	9.09	0.14	1.09E-01	-4.42E-06	5.22E-03	1791	1.712	0.500	1.20E-14
QM3B*	21.9	9.25	0.14	1.09E-01	-2.61E-06	6.38E-03	1791	1.712	0.900	1.28E-14

* Experiments performed with the powder Mgs-V

Table 4. Summary of magnesite precipitation experiments performed in this study at 120 °C in open system reactor.

Run #	Ω	pH	I M	Alk [mol/kg]	Δ [Mg] [mol/kg]	$a(CO_3^{2-})$	BET s. area [cm^2/g]	$MgCO_3$ mass [g]	FFR [g/min]	r_p [$mol/cm^2/s$]
PM25	30.7	7.46	0.12	1.62E-02	-8.13E-05	2.66E-05	1723	0.806	0.990	9.66E-13
PM26	29.0	7.51	0.12	1.67E-02	-1.78E-04	3.06E-05	1723	0.795	0.590	1.28E-12
PM26A	34.7	7.52	0.12	1.75E-02	-1.13E-04	3.25E-05	1723	0.795	1.484	2.04E-12
PM26B	40.8	7.59	0.12	1.75E-02	-1.01E-04	3.78E-05	1723	0.795	1.874	2.30E-12
PM26C	43.3	7.63	0.12	1.74E-02	-1.17E-04	4.14E-05	1723	0.795	2.371	3.36E-12
PM26D	44.8	7.61	0.12	1.75E-02	-7.23E-05	3.96E-05	1723	0.795	3.526	3.10E-12
PM28	30.7	7.61	0.12	1.73E-02	-2.60E-04	3.96E-05	1723	0.761	0.493	1.63E-12
PM28A	46.0	7.68	0.12	1.75E-02	-1.43E-04	4.67E-05	1723	0.761	1.780	3.24E-12
PM28B	36.9	7.53	0.12	1.76E-02	-7.60E-05	3.33E-05	1723	0.761	2.390	2.31E-12
PM28C	38.3	7.53	0.12	1.77E-02	-5.44E-05	3.34E-05	1723	0.761	3.973	2.75E-12
PM28D	46.8	7.63	0.12	1.76E-02	-5.99E-05	4.17E-05	1723	0.761	2.994	2.28E-12
PM28E	44.7	7.59	0.12	1.76E-02	-4.34E-05	3.86E-05	1723	0.761	5.487	3.02E-12
PM31	25.1	7.66	0.12	1.81E-02	-9.55E-05	4.60E-05	1723	1.753	1.183	6.23E-13
PM31A	24.2	7.78	0.12	1.80E-02	-1.67E-04	5.98E-05	1723	1.753	0.587	5.42E-13
PM25	30.7	7.46	0.12	1.62E-02	-8.13E-05	2.66E-05	1723	0.806	0.990	9.66E-13
PM26	29.0	7.51	0.12	1.67E-02	-1.78E-04	3.06E-05	1723	0.795	0.590	1.28E-12
PM26A	34.7	7.52	0.12	1.75E-02	-1.13E-04	3.25E-05	1723	0.795	1.484	2.04E-12
PM26B	40.8	7.59	0.12	1.75E-02	-1.01E-04	3.78E-05	1723	0.795	1.874	2.30E-12
PM26C	43.3	7.63	0.12	1.74E-02	-1.17E-04	4.14E-05	1723	0.795	2.371	3.36E-12
PM26D	44.8	7.61	0.12	1.75E-02	-7.23E-05	3.96E-05	1723	0.795	3.526	3.10E-12
PM28	30.7	7.61	0.12	1.73E-02	-2.60E-04	3.96E-05	1723	0.761	0.493	1.63E-12
PM28A	46.0	7.68	0.12	1.75E-02	-1.43E-04	4.67E-05	1723	0.761	1.780	3.24E-12
PM28B	36.9	7.53	0.12	1.76E-02	-7.60E-05	3.33E-05	1723	0.761	2.390	2.31E-12
PM28C	38.3	7.53	0.12	1.77E-02	-5.44E-05	3.34E-05	1723	0.761	3.973	2.75E-12
PM28D	46.8	7.63	0.12	1.76E-02	-5.99E-05	4.17E-05	1723	0.761	2.994	2.28E-12
PM28E	44.7	7.59	0.12	1.76E-02	-4.34E-05	3.86E-05	1723	0.761	5.487	3.02E-12
PM31	25.1	7.66	0.12	1.81E-02	-9.55E-05	4.60E-05	1723	1.753	1.183	6.23E-13
PM31A	24.2	7.78	0.12	1.80E-02	-1.67E-04	5.98E-05	1723	1.753	0.587	5.42E-13

3.3 In-situ pH measurements

Both in the batch and mixed-flow reactors pH was also measured during several experiments using an innovative in-situ electrochemical potential measurement system, consisting of a solid contact Li-Sn alloy commercial electrode (Potential®, St. Petersburg, Russia) coupled to a Na-selective glass reference electrode, which provides a constant potential in Na^+ rich solutions (typically 0.1 M NaCl). A detailed description of this type of electrode is provided by Pokrovski et al. (1995). The electrochemical cell is thus:

Sn-Cu, Li-Sn alloy | H-selective glass | Na-bearing buffer solution | Na-selective glass | Sn-Cu, Li-Sn alloy.

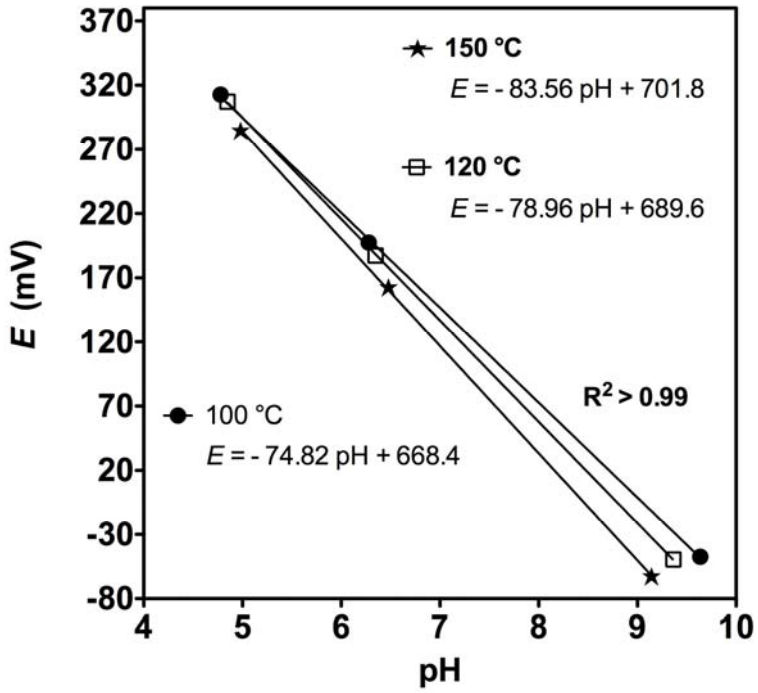

Figure 2. Examples of calibration using a solid contact pH electrode coupled with a Na-selective reference electrode at 100, 120 and 150 °C in 0.1 M NaCl medium.

The electromotive force of the cell is described by the Nernst equation:

$$E = E° + (2.3\boldsymbol{R}T/F)\,[\mathrm{Log}\ \boldsymbol{a}_{H^+} + \mathrm{Log}\ \boldsymbol{a}_{Na^+}]\,, \qquad (17)$$

where E stands for the measured electrical potential of the system, $E°$ denotes the standard potential determined from the calibration curve, $\boldsymbol{R}$ represents the gas constant, T corresponds to the absolute temperature, F symbolizes the Faraday constant, and $\boldsymbol{a}_{H^+}$ and $\boldsymbol{a}_{Na^+}$ designate the activity of the H^+ and Na^+ ions in solution. The pH-electrode inserted into the reactor was calibrated using $NaCl/Na_2CO_3$, $NaCl/B(OH)_3/NaOH$ and $NaCl/CH_3COONa/HCl$ solutions at 100, 120 and 150 °C. The pH of the buffer solutions were determined from calculations made with PHREEQC (Parkhurst and Appelo, 1999) and the HCh (GIBBS) software package (Shavrov, 1999; Shvarov and Bastrakov, 1999) using the $NaB(OH)_4°$ association constant reported by Pokrovski et al. (1995). These electrodes were not used at 200 °C due to poor stability. The prepared buffer solutions were standardized against NIST buffers at 25 °C (pH 4.01, 6.86 and 9.18) using a standard pH glass combination electrode and were found to be in close agreement with their theoretical values. An example of a high temperature electrode

calibration in 0.1 M Na bearing solutions at 100, 120, and 150 °C is illustrated in Figure 2: the slopes of the calibration lines are close to the corresponding Nernst slopes. Electrode potentials exhibited high stability at temperatures up to 150° C over time periods of several days with an accuracy of 0.02 pH units. The electrodes required only a weekly pH calibration to correct for drift from the original calibration.

Table 5. Summary of magnesite precipitation experiments performed in this study at 150 °C in open system reactor.

Run #	Ω	pH	I M	Alk [mol/kg]	Δ [Mg] [mol/kg]	$a(CO_3^{2-})$	BET s. area [cm^2/g]	$MgCO_3$ mass [g]	FFR [g/min]	r_p [$mol/cm^2/s$]
PM14A	38.5	7.80	0.12	3.41E-02	-2.07E-04	9.53E-05	1610	0.629	1.593	5.42E-12
PM14B	52.3	7.75	0.12	3.40E-02	-1.65E-04	8.60E-05	1610	0.629	5.392	1.47E-11
PM14C	46.4	7.85	0.12	3.40E-02	-1.99E-04	1.08E-04	1610	0.629	2.728	8.94E-12
PM16	13.4	7.32	0.11	7.43E-03	-8.03E-05	7.04E-06	1723	0.407	0.445	8.49E-13
PM16A	17.1	7.41	0.11	7.47E-03	-6.63E-05	8.58E-06	1723	0.407	0.896	1.41E-12
PM16B	19.3	7.43	0.11	7.49E-03	-4.60E-05	8.97E-06	1723	0.407	1.592	1.74E-12
PM16C	20.2	7.43	0.11	7.51E-03	-3.29E-05	8.99E-06	1723	0.407	3.189	2.50E-12
PM16D	19.1	7.45	0.11	7.47E-03	-5.97E-05	9.42E-06	1723	0.407	1.598	2.27E-12
PM16E	26.8	7.55	0.11	7.53E-03	-2.35E-05	1.18E-05	1723	0.407	4.998	2.79E-12
PM17	35.5	7.50	0.12	1.59E-02	-1.34E-04	2.26E-05	1723	0.591	2.195	4.82E-12
PM17A	27.3	7.48	0.12	1.59E-02	-2.01E-04	2.16E-05	1723	0.591	1.490	4.91E-12
PM17B	20.3	7.56	0.12	1.59E-02	-2.72E-04	2.58E-05	1723	0.591	0.604	2.69E-12
PM17C	27.8	7.67	0.12	1.59E-02	-2.59E-04	3.28E-05	1723	0.591	1.105	4.68E-12
PM17D	43.6	7.66	0.12	1.59E-02	-1.82E-04	3.27E-05	1723	0.591	3.960	1.18E-11
PM18	34.5	7.63	0.14	3.41E-02	-2.05E-04	6.46E-05	1723	0.405	0.886	4.34E-12
PM18A	27.3	7.73	0.14	3.41E-02	-2.44E-04	8.09E-05	1723	0.405	0.444	2.59E-12
PM18B	67.1	7.76	0.14	3.42E-02	-1.45E-04	8.52E-05	1723	0.405	3.193	1.11E-11
PM18C	57.9	7.85	0.14	3.41E-02	-1.91E-04	1.06E-04	1723	0.405	1.588	7.24E-12
PM18D	74.1	7.79	0.14	3.42E-02	-1.36E-04	9.11E-05	1723	0.405	3.998	1.30E-11
PM19	10.3	7.14	0.11	3.28E-03	-8.97E-05	2.02E-06	1723	0.592	0.500	7.33E-13
PM19A	8.3	7.00	0.11	3.32E-03	-5.50E-05	1.50E-06	1723	0.592	0.903	8.11E-13
PM19B	9.2	7.05	0.11	3.30E-03	-5.75E-05	1.68E-06	1723	0.592	1.496	1.40E-12
PM19C	11.7	7.15	0.11	3.30E-03	-4.30E-05	2.10E-06	1723	0.592	2.179	1.53E-12
PM19D	6.9	6.90	0.11	3.33E-03	-1.45E-05	1.20E-06	1723	0.592	3.649	8.66E-13
PM20	25.3	7.80	0.16	5.19E-02	-2.49E-04	1.42E-04	1723	0.417	0.391	2.25E-12
PM20A	50.1	7.79	0.16	5.20E-02	-1.97E-04	1.37E-04	1723	0.417	1.590	7.28E-12
PM20B	41.6	7.79	0.16	5.20E-02	-2.10E-04	1.39E-04	1723	0.417	0.891	4.33E-12
PM20C	54.6	7.74	0.16	5.20E-02	-1.72E-04	1.24E-04	1723	0.417	1.992	7.97E-12
PM20D	56.4	7.64	0.16	5.20E-02	-1.41E-04	9.85E-05	1723	0.417	3.208	1.05E-11
PM20E	47.6	7.74	0.16	5.20E-02	-1.87E-04	1.24E-04	1723	0.417	1.385	6.00E-12
PM20F	67.2	7.68	0.16	5.20E-02	-1.25E-04	1.07E-04	1723	0.417	4.512	1.31E-11
PM20G	66.6	7.79	0.16	5.20E-02	-1.59E-04	1.39E-04	1723	0.417	2.493	9.16E-12
PM22	28.4	7.42	0.52	1.49E-02	-1.34E-04	1.49E-05	1723	0.595	2.352	5.11E-12
PM22A	25.6	7.35	0.52	1.49E-02	-1.05E-04	1.25E-05	1723	0.595	4.453	7.59E-12
PM22B	23.8	7.42	0.52	1.48E-02	-1.96E-04	1.46E-05	1723	0.595	1.614	5.14E-12
PM22C	18.2	7.62	0.52	1.49E-02	-3.79E-04	2.31E-05	1723	0.595	0.711	4.38E-12
PM23	28.5	7.52	0.52	1.49E-02	-2.09E-04	1.85E-05	1723	0.598	1.094	3.70E-12
PM23A	28.7	7.44	0.52	1.49E-02	-1.45E-04	1.56E-05	1723	0.598	3.604	8.44E-12
PM23B	32.2	7.52	0.52	1.49E-02	-1.58E-04	1.84E-05	1723	0.596	1.989	5.08E-12
PM23C	27.5	7.37	0.52	1.49E-02	-9.42E-05	1.33E-05	1723	0.596	4.988	7.62E-12

Table 6. Summary of magnesite precipitation experiments performed in this study at 200 °C in open system reactor.

Run #	Ω	pH	I M	Alk [mol/kg]	Δ [Mg] [mol/kg]	$a(CO_3^{2-})$	BET s. area [cm^2/g]	$MgCO_3$ mass [g]	FFR [g/min]	r_p [$mol/cm^2/s$]
PM6A	11.4	7.96	0.11	9.13E-03	-1.48E-04	1.69E-05	2241	0.306	1.798	6.47E-12
PM6B	14.1	7.96	0.11	9.12E-03	-1.48E-04	1.69E-05	2241	0.306	2.500	9.01E-12
PM6C	17.1	7.93	0.11	9.15E-03	-1.43E-04	1.61E-05	2241	0.306	4.007	1.39E-11
PM6D	7.6	7.92	0.11	9.09E-03	-1.58E-04	1.56E-05	2241	0.306	1.497	5.74E-12
PM6E	19.5	7.92	0.11	9.12E-03	-1.39E-04	1.56E-05	2241	0.306	7.521	2.54E-11
PM7A	6.5	8.14	0.12	1.91E-02	-9.15E-05	4.84E-05	2241	0.305	0.691	1.54E-12
PM7B	9.4	8.14	0.12	1.91E-02	-8.83E-05	5.39E-05	2241	0.305	1.796	3.87E-12
PM7C	7.6	8.13	0.12	1.91E-02	-8.62E-05	5.42E-05	2241	0.305	2.499	5.26E-12
PM7D	13.2	8.15	0.12	1.89E-02	-8.85E-05	5.22E-05	2241	0.305	1.999	4.32E-12
PM7E	18.9	8.16	0.12	1.92E-02	-8.45E-05	5.48E-05	2241	0.305	4.004	8.26E-12
PM8	6.2	8.25	0.14	1.92E-02	-8.06E-05	5.64E-05	2241	0.305	7.515	1.48E-11
PM8A	8.0	8.26	0.14	3.90E-02	-4.98E-05	1.41E-04	2241	0.303	1.197	1.46E-12
PM8B	8.6	8.26	0.14	3.90E-02	-4.90E-05	1.44E-04	2241	0.303	1.793	2.16E-12
PM8C	6.1	8.24	0.14	3.90E-02	-4.88E-05	1.45E-04	2241	0.303	2.501	2.99E-12
PM8D	11.7	8.29	0.14	3.90E-02	-4.98E-05	1.39E-04	2241	0.303	1.000	1.22E-12
PM8E	14.3	8.31	0.14	3.90E-02	-4.76E-05	1.54E-04	2241	0.303	4.017	4.69E-12
PM9	6.7	7.44	0.11	3.90E-02	-4.66E-05	1.59E-04	2241	0.303	7.508	8.58E-12
PM9A	6.0	7.64	0.11	6.45E-03	-1.43E-04	3.88E-06	2241	0.305	0.697	2.43E-12
PM9B	4.0	7.47	0.11	6.58E-03	-1.53E-04	6.09E-06	2241	0.305	0.401	1.50E-12
PM12	12.9	7.36	0.14	1.90E-02	-1.94E-04	9.41E-06	1610	0.429	0.700	3.27E-12
PM12A	20.2	7.29	0.14	1.90E-02	-1.55E-04	5.75E-06	1610	0.429	3.509	1.31E-11
PM12B	6.3	7.37	0.11	4.49E-03	-8.02E-05	1.74E-06	1610	0.429	1.502	2.91E-12
PM12C	11.4	7.47	0.11	4.43E-03	-6.86E-05	2.78E-06	1610	0.429	3.004	4.97E-12
PM12D	14.5	7.53	0.11	4.42E-03	-5.80E-05	3.15E-06	1610	0.429	5.516	7.72E-12
PM13	6.3	7.04	0.11	3.15E-03	-8.12E-05	7.63E-07	1610	0.422	0.699	1.39E-12
PM13A	6.9	6.96	0.11	3.12E-03	-4.94E-05	6.25E-07	1610	0.422	3.700	4.48E-12
PM13B	7.1	7.05	0.11	3.15E-03	-7.06E-05	7.76E-07	1610	0.422	1.499	2.59E-12
PM13C	9.3	7.10	0.11	3.12E-03	-4.49E-05	8.42E-07	1610	0.422	6.015	6.62E-12
PM13D	9.7	7.10	0.11	3.14E-03	-4.02E-05	8.49E-07	1610	0.422	8.013	7.90E-12
PM13E	9.8	7.24	0.11	3.09E-03	-7.19E-05	1.15E-06	1610	0.422	2.501	4.41E-12
PM29	8.5	6.93	0.11	2.75E-03	-6.54E-05	5.08E-07	1723	0.407	1.902	2.96E-12
PM29A	8.6	6.89	0.11	2.78E-03	-5.06E-05	4.71E-07	1723	0.407	4.012	4.83E-12
PM29B	9.0	6.89	0.11	2.82E-03	-4.10E-05	4.78E-07	1723	0.407	6.961	6.78E-12
PM30	21.8	8.20	0.16	5.53E-02	-4.63E-05	1.78E-04	1723	0.407	1.810	1.99E-12
PM30A	26.1	8.23	0.16	5.52E-02	-4.49E-05	1.89E-04	1723	0.407	4.015	4.28E-12
PM30B	29.1	8.21	0.16	5.52E-02	-4.34E-05	1.80E-04	1723	0.407	7.511	7.75E-12
PM35	16.6	8.23	1.02	9.54E-03	-2.14E-04	3.07E-06	1723	0.456	0.566	2.57E-12
PM35A	22.7	8.24	1.02	9.41E-03	-1.99E-04	3.60E-06	1723	0.456	1.128	4.76E-12
PM35B	17.3	8.24	1.02	9.49E-03	-1.38E-04	2.07E-06	1723	0.456	1.545	4.52E-12
PM35C	18.5	8.21	1.02	9.45E-03	-1.28E-04	2.66E-06	1723	0.456	2.098	5.68E-12
PM35D	13.8	8.26	1.02	9.49E-03	-1.02E-04	2.77E-06	1723	0.456	2.798	6.05E-12
PM35E	19.5	8.22	1.02	9.49E-03	-9.79E-05	3.44E-06	1723	0.456	3.527	7.32E-12
PM35F	11.4	8.27	1.02	9.50E-03	-8.99E-05	3.27E-06	1723	0.456	4.355	8.30E-12
PM37	14.9	8.63	0.16	5.68E-02	-5.03E-05	1.94E-04	1723	0.456	0.598	6.39E-13
PM37A	21.8	8.64	0.16	5.69E-02	-4.80E-05	1.98E-04	1723	0.456	1.198	1.22E-12
PM37B	25.0	8.62	0.16	5.69E-02	-4.94E-05	1.98E-04	1723	0.456	1.600	1.68E-12
PM37C	27.2	8.61	0.16	5.69E-02	-4.88E-05	1.88E-04	1723	0.456	2.196	2.27E-12
PM41	3.4	8.10	0.16	5.69E-02	-5.08E-05	2.06E-04	1723	0.456	0.400	4.32E-13
PM41A	4.9	8.10	0.16	5.69E-02	-4.85E-05	1.92E-04	1723	0.456	2.796	2.88E-12
PM21	11.9	7.39	0.52	9.23E-03	-1.83E-04	4.09E-06	1723	0.398	0.608	2.70E-12
PM21A	15.6	7.43	0.52	9.25E-03	-1.64E-04	4.45E-06	1723	0.398	1.220	4.86E-12
PM21B	22.0	7.47	0.52	9.30E-03	-1.33E-04	4.90E-06	1723	0.402	4.266	1.36E-11

Run #	**Ω**	**pH**	**I M**	**Alk** [mol/kg]	**Δ [Mg]** [mol/kg]	***a*(CO_3^{2-})**	**BET s. area** [cm^2/g]	**$MgCO_3$ mass** [g]	**FFR** [g/min]	r_p [mol/cm^2/s]
PM21C	18.5	7.58	0.52	9.24E-03	-1.75E-04	6.16E-06	1723	0.402	1.826	7.67E-12
PM21D	20.7	7.60	0.52	9.21E-03	-1.67E-04	6.42E-06	1723	0.402	2.539	1.02E-11
PM21E	10.7	7.42	0.52	9.34E-03	-2.01E-04	4.44E-06	1723	0.402	0.405	1.95E-12
PM21F	17.3	7.51	0.52	9.24E-03	-1.74E-04	5.34E-06	1723	0.402	1.421	5.94E-12
PM24	19.5	7.36	1.02	9.33E-03	-1.74E-04	3.62E-06	1723	0.401	1.441	6.04E-12
PM24A	17.5	7.23	1.02	9.35E-03	-1.38E-04	2.73E-06	1723	0.401	3.925	1.31E-11
PM24B	20.4	7.40	1.02	9.29E-03	-1.78E-04	3.90E-06	1723	0.401	1.855	7.98E-12
PM24C	17.2	7.26	1.02	9.37E-03	-1.56E-04	2.89E-06	1723	0.401	2.794	1.05E-11
PM24D	15.5	7.40	1.02	9.22E-03	-2.27E-04	3.87E-06	1723	0.401	1.236	6.77E-12
PM24E	13.0	7.53	1.02	9.24E-03	-2.83E-04	5.19E-06	1723	0.401	0.621	4.23E-12
PM27	15.6	7.25	1.02	9.49E-03	-1.43E-04	2.89E-06	1723	0.413	1.449	4.88E-12
PM27A	12.3	7.40	1.02	9.56E-03	-2.32E-04	4.05E-06	1723	0.413	0.517	2.81E-12
PM33	12.5	7.28	1.03	9.54E-03	-2.14E-04	3.07E-06	1723	0.456	0.566	2.57E-12
PM33A	15.9	7.35	1.03	9.41E-03	-1.99E-04	3.60E-06	1723	0.456	1.128	4.76E-12
PM33B	12.0	7.10	1.03	9.49E-03	-1.38E-04	2.07E-06	1723	0.456	1.545	4.52E-12
PM33C	15.9	7.22	1.03	9.45E-03	-1.28E-04	2.66E-06	1723	0.456	2.098	5.68E-12
PM33D	18.4	7.23	1.03	9.49E-03	-1.02E-04	2.77E-06	1723	0.456	2.798	6.05E-12
PM33E	22.9	7.33	1.03	9.49E-03	-9.79E-05	3.44E-06	1723	0.456	3.527	7.32E-12
PM33F	22.5	7.31	1.03	9.50E-03	-8.99E-05	3.27E-06	1723	0.456	4.355	8.30E-12

3.4 Mixed-flow reactor experiments

Seeded magnesite precipitation experiments were performed in 200 and 300 ml titanium reactors similar to that described by Dove and Crerar (1990) and Gautier et al. (1994). Inlet solutions were stored in compressible polyethylene containers and injected into the reactor through a 2 μm titanium filter by a HPLC pump allowing flow rates ranging from 0.1 to 10 ml/min. Fluids inside the reactor were stirred at a constant rate by a Parr magnetically driven stirrer and kept at constant temperature ± 1 °C by a Parr controlled furnace. The fluid left the reactor through a 2 μm titanium filter and was cooled before reaching a back-pressure regulator that maintained a constant pressure throughout the system.

Mixed-flow reactor experiments were run as series of several experiments on a single magnesite powder sample. The initial experiment of a series was begun by placing the magnesite powder in the reactor and selecting the initial temperature. A reactive fluid of known compositon was passed through the reactor at constant flow rate until a steady-state outlet fluid composition was observed. A steady-state was assumed when the outlet fluid composition did not change within analytic uncertainity for more than 7 residence times. The residence time is equal to the reactor volume divided by the fluid flow rate. Once steady-state

was attained, a new experiment was begun by changing the flow rate and/or the inlet fluid composition. Each experimental series is noted by a distinct prefix in the list of experiments of Tables 3-6, which report the physico-chemical parameters and the rates of precipitation for all the experiments performed.

3.5 Batch reactor experiments

$MgCO_3$ precipitation experiments were also performed in a 400 ml Ti batch reactor at 15 and 30 bars of CO_2 partial pressures and at temperatures of 150 and 200 °C. These experiments took advantage of the retrograde solubility of magnesite to perturb the saturation state via temperature increases. When the equilibrium is perturbed by a sudden temperature, pH, or pressure change, the system relaxes to its new chemical equilibrium condition. The kinetic analysis of such behavior effects is known as relaxation kinetics and was originally developed by Eigen and de Maeyer (1963).

When the displacement from equilibrium is slight and for relatively fast reactions, the progress of the system towards the new equilibrium state can be described by the first-order law given by:

$$\left[C_t - (C_{eq})_2 \right] = \left[(C_{eq})_1 - (C_{eq})_2 \right] \cdot e^{-t/\tau} \tag{18}$$

whose derivative with respect to time is given by:

$$\partial C / \partial t = \frac{-\left[(C_{eq})_1 - (C_{eq})_2 \right]}{\tau} e^{-t/\tau} \tag{19}$$

where $(C_{eq})_1$ and $(C_{eq})_2$ are the equilibrium concentrations of one of the characteristic chemical species involved in the reaction before and after the temperature change, C_t is the concentration at the time t, and τ represents a time parameter known as relaxation time, which is a function of the rate constant. These equations have been used to interpret solution compositions stemming from pH-jumps (Pines and Huppert, 1983; Bénézeth et al., 2008), pressure-jumps (Dangles et al., 1994; Torrent et al., 2006) and temperature-jumps (Prabahananda et al., 1987; Castaing et al., 1991). Closed system experiments performed in the present study were initiated by dissolving between 7 and 9 g of magnesite at 120 and 150 °C and a CO_2 partial pressure of 15-30 bar in 0.1 M NaCl solutions. Once magnesite equilibrium was attained, the temperature was increased either from 120 to 150 °C or from

150 to 200 °C. As a consequence the solution originally at equilibrium became supersaturated with respect to $MgCO_3$ and precipitation began. The typical duration of this type of experiments was of 2-3 weeks, allowing the determination of the precipitation rates at close to equilibrium conditons.

4. Experimental Results

4.1 Open system reactor experiments

All open system experiments were run until a steady state outlet concentration of Mg was attained. An example of attainment of steady state is shown in Figure 3. The plot shows that mechanical and chemical steady states do not coincide, the chemical steady state being attained later. Mechanical steady state is equal to 4.6 times the residence time of the fluid in the reactor. Steady state precipitation rates ($\boldsymbol{r}_p$), were calculated using

$$\boldsymbol{r}_p = -q \cdot \Delta[Mg]_{tot}/\boldsymbol{S} \qquad (20)$$

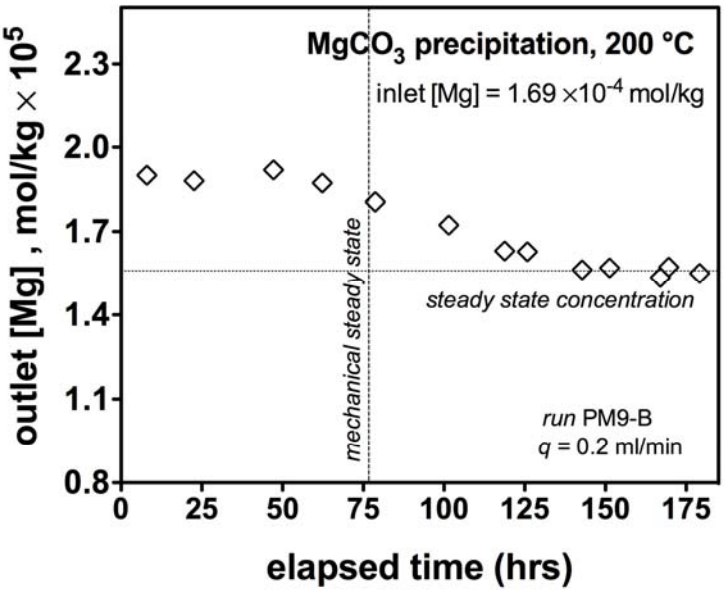

Figure 3. Evolution of Mg concentration in the outlet solution as a function of time during experiment PM9, performed in mixed flow reactor. Note that the chemical and mechanical steady states do not coincide.

where q represents the fluid flow rate, $\Delta[Mg]_{tot}$ stands for the difference between the outlet and inlet solution Mg concentration (in mol/kg) and ***S*** refers to the total mineral surface area. The surface area used to calculate the rates was the BET surface area of unreacted powders. To verify that surface area did not significantly change during the experimental series, the initial experimental conditions were sometimes reproduced at the end of the series. No significant difference was observed in the reproduced experiments.

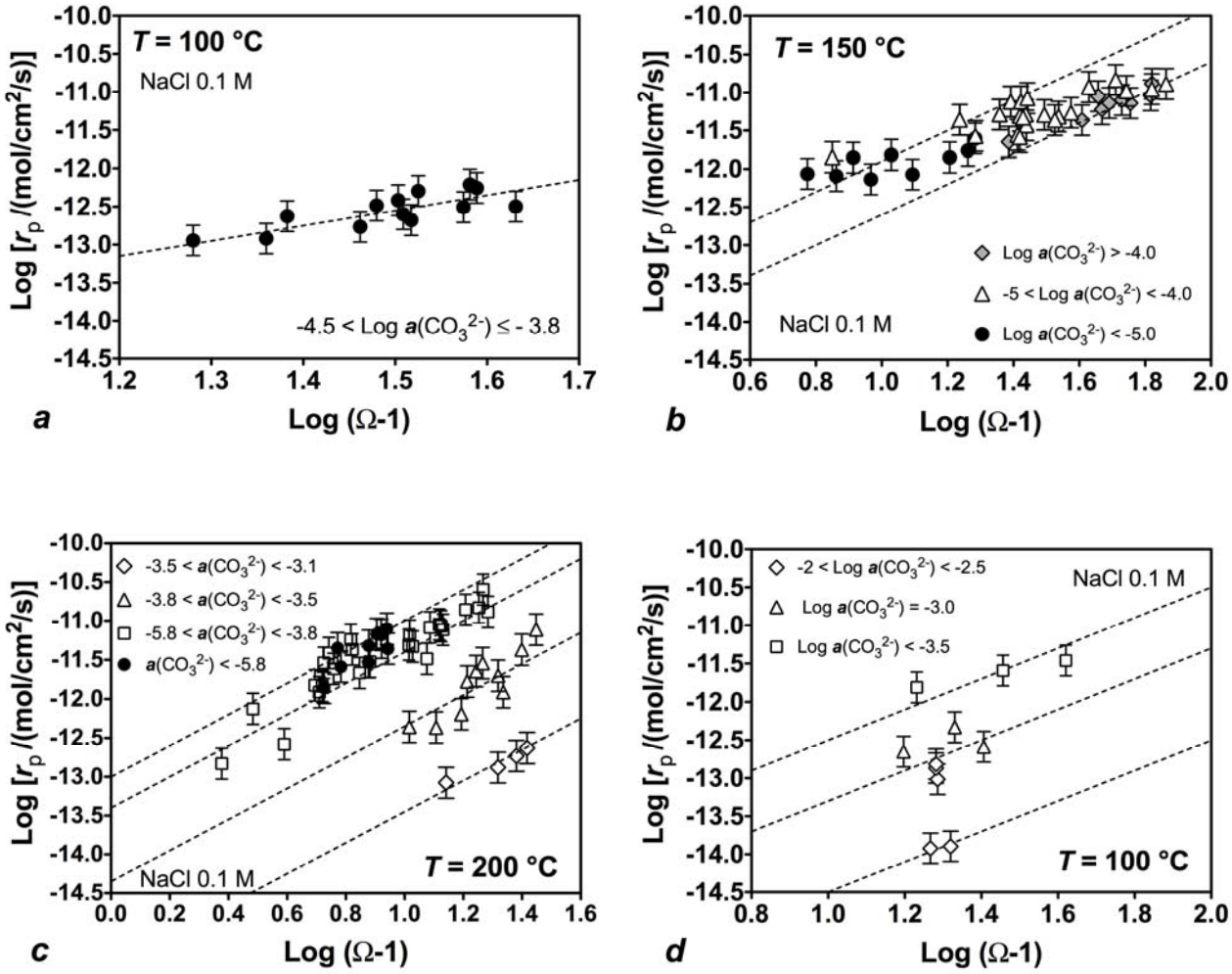

Figure 4. Logarithmic plots of the precipitation rates measured at 100 (***a***,***d***), 150 (***b***) and 200 °C (***c***) versus the relative degree of supersaturation (Ω-1) and for different CO_3^{2-} activities and at a constant concentration of NaCl = 0.1 M. Dashed lines represent the best fits to Eqn. (8) with slope corresponding to ***n*** = 2. In ***a*** to ***c*** symbols identify experiments performed using any powder sample except Mgs-V, whereas symbols on plot ***d*** refer to experiments performed with the only specimen Mgs-V. Error bars correspond to an uncertainty of ± 0.2 logarithmic units.

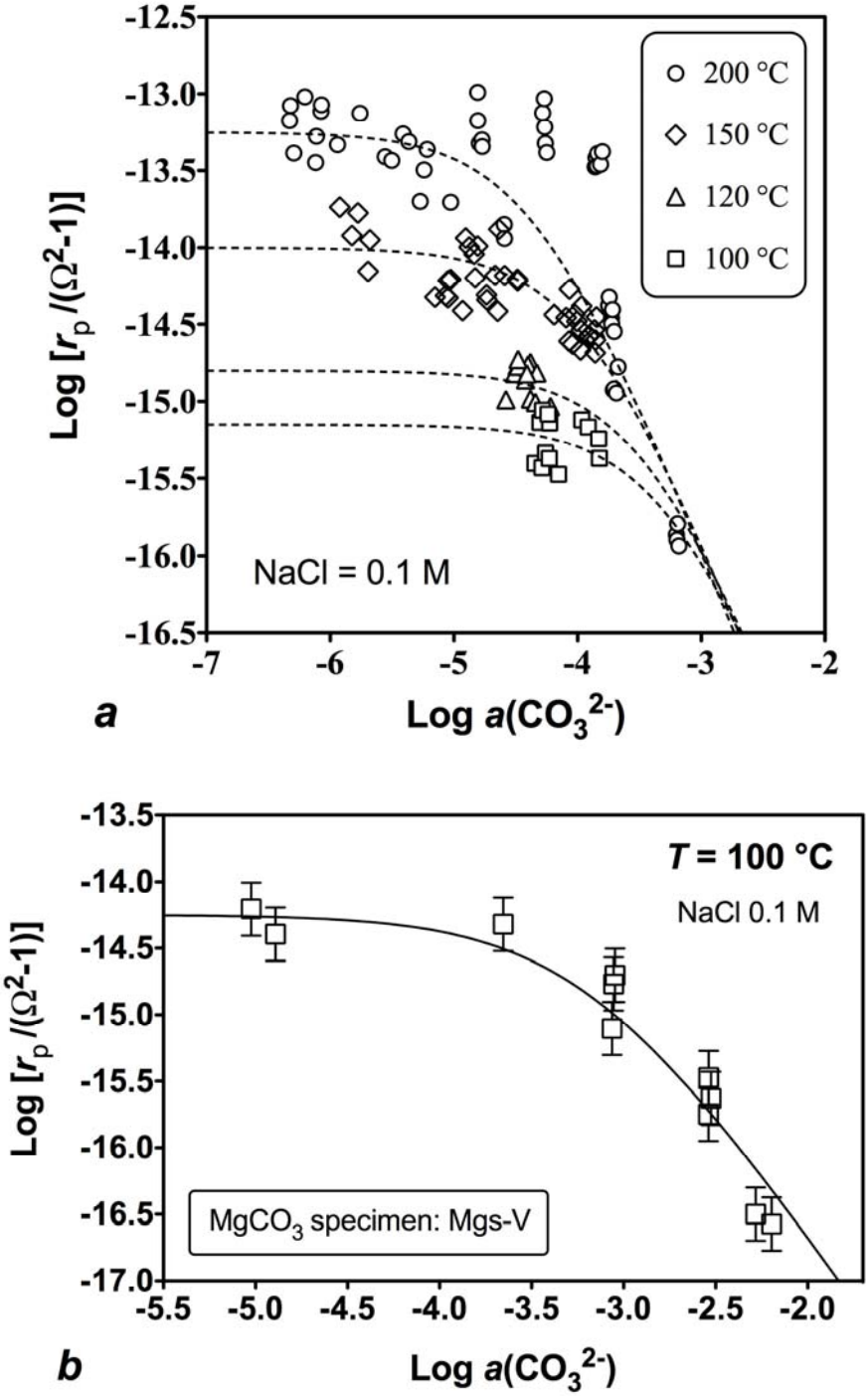

Figure 5. Magnesite precipitation rates as a function of CO_3^{2-} activity in solution from 100 to 200 °C (***a***) and at 100 °C for magnesite Mgs-V-type (***b***). Symbols represent experimental data, dashed and solid lines are the best fit of the data obtained using Eqn. 16.

A summary of all steady-state precipitation rate measurements performed in this study is listed in Tables 3-6 for experiments carried out at 100, 120, 150, and 200 °C, respectively.

As mentioned above, Table 2 provides the composition of all the starting solution used during the experiments.

Precipitation rates measured in 0.1 M NaCl solutions on all magnesite powders other than Mgs-V are plotted as a function of the corresponding fluid saturation state in Figures 4a-c at 100, 150, and 200° C, respectively. Rates obtained at various aqueous CO_3^{2-} activity are distinguished by different symbols. Correspondingly, magnesite rates obtained from experiments performed on magnesite powder Mgs-V are plotted in Fig. 4d. In general, magnesite precipitation rates decrease at constant saturation state with increasing aqueous CO_3^{2-} activity consistent with the magnesite rate equation described above (Eqn. 16). The lines drawn through the symbols in Fig. 4, which are consistent with the general trend of the data for each set of magnesite precipitation rates, have a slope of 2. This slope is consistent with a value of n=2 in Eqn. (8) and consistent with a spiral growth mechanism dominating magnesite precipitation rates (cf. Teng et al., 2000). Previous AFM studies have shown that magnesite growth is dominated by spiral growth at these conditions (Saldi et al., 2009 (see chapter 3)). The intercept of these straight lines shown in Figs 4a – d (i.e. when log (Ω-1) = 0) corresponds to the logarithm of the term $k_{Mg}^{+}\left(\frac{K_{co3}}{K_{co3}\cdot + a_{co_3^{2-}}}\right)^{n_{H2O}}$ in Eqn. (16). Regression of the data shown in Figure 4c relative to the experiments at 200 °C suggests that this logarithm decreases from -13.0 to -15.5 when $a_{CO_3^{2-}}$ is increased from 10^{-6} to 10^{-3}. Despite some scatter, the same effect is evident for experiments performed at 150 and 100 °C, but the effect of $a_{CO_3^{2-}}$ becomes less strong as temperature decreases. At 150 °C (Fig. 4b) the apparent rate constant roughly decreases from $10^{-13.9}$ to $10^{-14.6}$ mol/cm^2/s when $a_{CO_3^{2-}}$ is increased by one order of magnitude from ~10^{-5} to ≥10^{-4}. At 100 °C, rates obtained from experiments performed on powder Mgs-V, as shown in Fig. 4d, also exhibit a clear decrease with increasing $a_{CO_3^{2-}}$, but these experiments resulted in rates that are on average 0.9 orders of magnitude higher than those obtained from experiments performed with the other magnesite powders.

The variation of magnesite precipitation rates with $a_{CO_3^{2-}}$ can be further assessed in Fig 5. Fig. 5a illustrates the logarithm of all rates obtained in 0.1 M NaCl solutions on magnesite powders other than Mgs-V divided by (Ω^2-1) versus Log $a_{CO_3^{2-}}$. A corresponding plot for rates obtained from powder Mgs-V is shown in Fig. 5b. The curves drawn through the symbols correspond to a regression of the rate data at each temperature consistent with Eqn. (16). This regression yields directly the values of k_{Mg}^{-} (the corresponding rate constant for the precipitation reaction) and K_{CO3} listed in Table 7. Both of these values vary systematically with temperature; K_{CO3} decreases with increasing temperature consistently with a corresponding increase in the effect of $a_{CO_3^{2-}}$ on rates at elevated temperature. The variation of the rate constant k_{Mg}^{-} with temperature is illustrated on the Arrhenius plot shown in Figure 6. These rate constants exhibit a linear dependence on reciprocal temperature consistent with an activation energy of 64±13 kJ/mol.

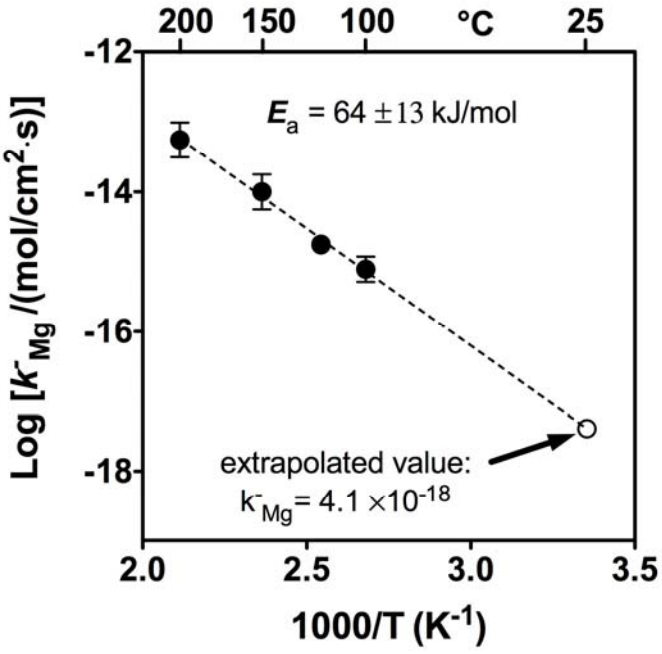

Figure 6. Apparent activation energy for $MgCO_3$ precipitation obtained through linear least square fit of the rate constant determined at 100, 120, 150 and 200 °C from mixed flow reactor experiments (full symbols). The empty circle identifies the value of the rate constant extrapolated at 25 °C according to the extracted value of E_a (64 kJ/mol).

The effect of ionic strength on magnesite precipitation rates can be assessed with the aid of Figure 7, where rates obtained in 0.1, 0.5, and 1.0 M NaCl solutions at 200 °C are plotted as a function of fluid saturation state in logarithmic scale. Even if the rates obtained in 0.1 M NaCl tend to plot slightly higher than the rates measured in 0.5 and 1M solutions, considering the uncertainty of the experimental measurements and the thermodynamic calculation done at 200 °C, no clear effect of changing aqueous solution NaCl concentration is observable.

Table 7. Values of the rate constant (k_{Mg}^{-}) and of the constant of desorption of CO_3^{2-} (K_{CO3}) determined in this study as a function of *T*.

T (°C)	Log k_{Mg}^{-} (mol/cm^2/s)	Log K_{CO3}
100	-15.1±0.2	-3.2 ±0.2
120	-14.75±0.1	-3.45
150	-14.0±0.25	-3.9±0.2
200	-13.25±0.25	-4.35±0.15
100*	-14.25 ±0.15*	-3.2 ±0.2*

*values obtained from magnesite powder Mgs-V

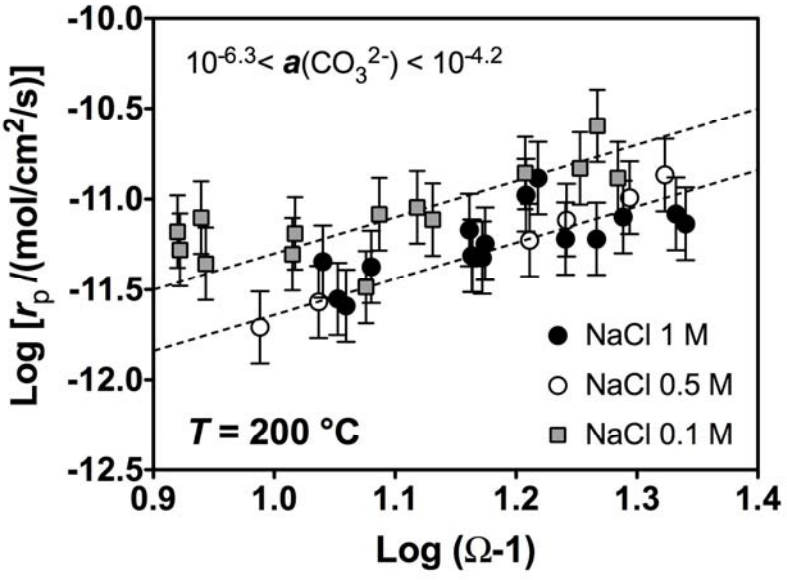

Figure 7. Logarithmic plots of the precipitation rates measured at 200 °C as a function of the realtive degree of supersaturation and the ionic strength (NaCl 0.1-1M). Error bars correspond to a 0.2 log units uncertainty in measured rates.

4.2 Closed system reactor experiments

Further experiments were performed in a batch reactor to allow determination of magnesite precipitation rates at elevated CO_2 pressures. An example of the fluid Mg concentration during a closed system experiment is shown in Figure 8. Precipitation rates have been determined using the *relaxation kinetics* approach described in section 3.5, by integration of Eqn. (8) with Eqn. (18) and (19). Four different experiments were performed, at 150 and 200 °C, applying a CO_2 partial pressure of 15 and 30 bar at both temperatures. Presence of constant high pCO_2 kept the pH at values ranging between 4.9 and 5.6, preventing the possible precipitation of brucite and hydromagnesite along with magnesite. The summary of the experimental conditions of these experiments is reported in Table 8.

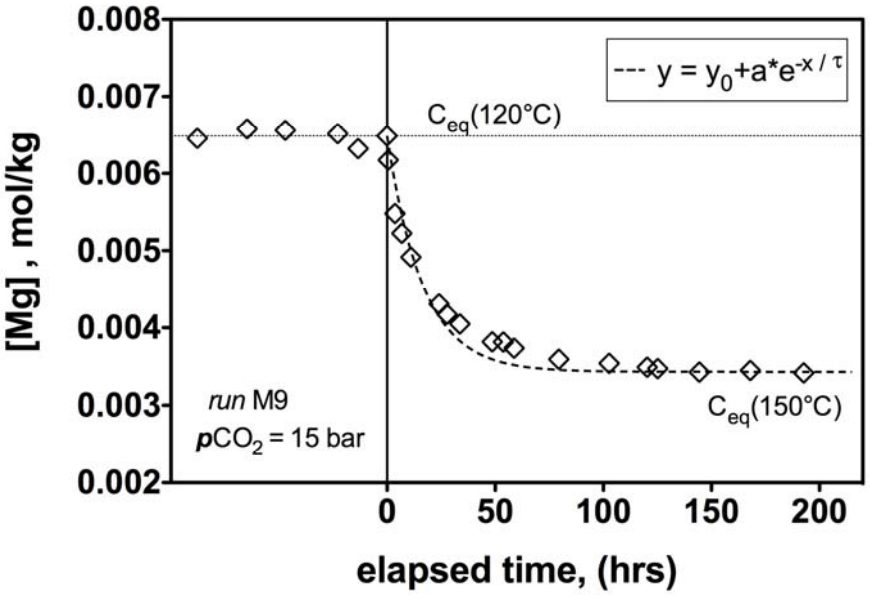

Figure 8. Example of $MgCO_3$ precipitation induced by a *T*-jump in closed system. In this case *T* was rapidly increased from 120 to 150 °C at a constant CO_2 partial pressure of 15 bar. As a consequence the Mg concentration of the system starts to decrease until the new equilibrium with respect to $MgCO_3$ is achieved.

For each experiment, after the determination the relaxation time τ from the curve describing the time variation of Mg concentration in the system between the onset of precipitation (t = 0) and the new state of apparent equilibrium, rates were calculated according to Eqn. (19) and compared with the corresponding state of saturation of the precipitating

solution. The dependence of precipitation rates upon saturation state can be assessed with the aid of logarithmic plots such as the one reported in Figure 9 for experiment M9, where precipitation rates are reported as a function of the relative degree of supersaturation (Ω-1). In this plot we can observe that rates are consistent with an order of reaction $\boldsymbol{n} = 1$ for values of Log(Ω-1) > - 0.1, corresponding to Ω > 1.8. The y-axis intercept of the regression line drawn through the symbols with a slope equal to 1 thus represents the rate constant for the precipitation reaction under the distinctive experimental conditions ($=10^{-12.7}$ mol/cm^2·s). Below Ω≈1.8 the order of the precipitation rates with respect to Ω-1 is >> 1. This is likely to be an artifact due to the log-log data plot at very near to equilibrium conditions, for which Mg concentration variation as a function of time and thus magnesite precipitation rates cannot be accurately measured (see discussion below). Magnesite precipitation rates deduced from the closed system experiments at 150 and 200 °C are plotted against solution saturation state in Figure 10. It can be seen that measured magnesite crystallization rates are consistent with a pseudo-linear dependence on the solution saturation state and that the increase of CO_2 partial pressure (from 15 to 30 bar) does not appreciably affect the rates determined at 150 °C but seems to slightly inhibit precipitation at 200 °C. The crystallization rate constant $\boldsymbol{k}$ extracted from these linear regressions is found to be equal to $10^{-12.7}$ at 150 °C (Fig. 9 and 10a) and to decrease from $10^{-12.3}$ to $10^{-12.85}$ when pCO_2 is increased from 15 to 30 bar at 200 °C (Fig. 10b).

Table 8. Summary of the experimental conditions of batch reactor precipitation experiments performed at 150 and 200 °C. The rate constants refer to a linear dependence of the precipitation rates on the relative degree of supersaturation (Ω-1).

Run #	***T*** (°C)	***I*** M	***p*CO$_2$** (bar)	**pH range**	***a*(CO$_3^{2-}$) range**	**BET s. area** [cm^2/g]	**MgCO$_3$ mass** [g]	Log $\boldsymbol{k}_{Mg}^{-}$ [mol/cm^2/s]
M7	150	0.1	30.0	5.24-5.12	$10^{-7.0}$-$10^{-7.3}$	2007	9.058	-12.7±0.1
M9	150	0.1	15	5.49-5.30	$10^{-6.8}$-$10^{-7.2}$	1826	7.127	-12.7±0.1
M5	200	0.1	30	*5.58-5.17	$10^{-7.4}$-$10^{-8.2}$	2153	7.890	-12.85±0.1
M8	200	0.1	15	*5.41-5.29	$10^{-7.2}$-$10^{-7.9}$	1474	6.056	-12.3±0.1

*calculated pH values

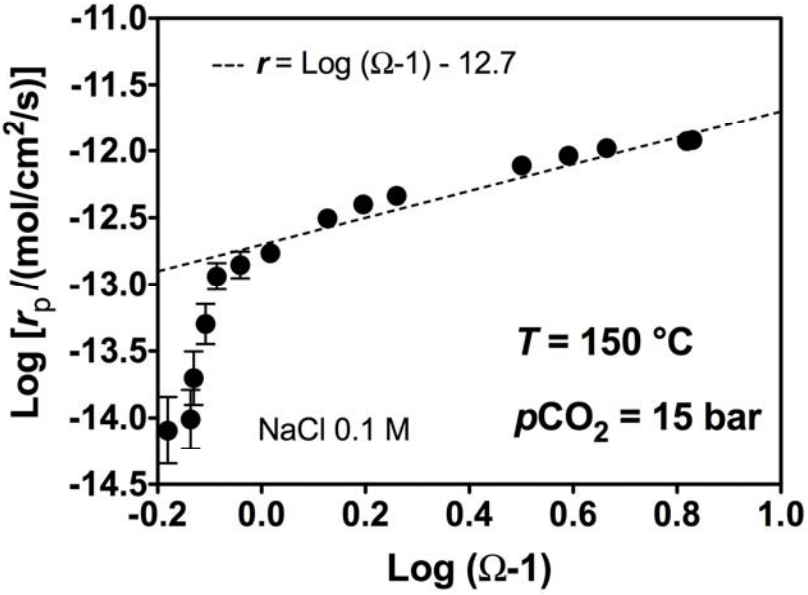

Figure 9. Logarithmic plots of the precipitation rates measured at 150 °C and pCO_2 of 15 bar during a closed system experiment. The straight dashed line represent the fit of experimental rates at Ω >1.8. Measured rates are consistent with a linear growth (***n*** = 1).

5. Discussion

5.1 Open system reactor experiments

As shown in Figure 5, despite some scatter of datapoints, magnesite precipitation rates obtained from mixed-flow reactor experiments are satisfactorily described by the rate model of Eqn. (16). The scatter of the precipitation data, also discernible in the diagrams of Fig. 4, generally reflects uncertainties associated with aqueous speciation and Ω calculations, especially at 200 °C where in situ pH measurements could not be performed and calculations rely on alkalinity and pH measurements at 25 °C. Some scatter may also arise from the heterogeneity of synthetic powders used in the experiments regarding their surface properties. For example, it is likely that slightly different synthesis conditions (e.g. lower pCO_2) resulting in higher concentration of defects favorable to precipitation at the surface of the powder samples used for the eleven Mgs-V runs performed at 100 °C, could explain the higher precipitation rates (by about 0.9 orders of magnitude) obtained in these runs (see also discussion below for batch reactor experiments).

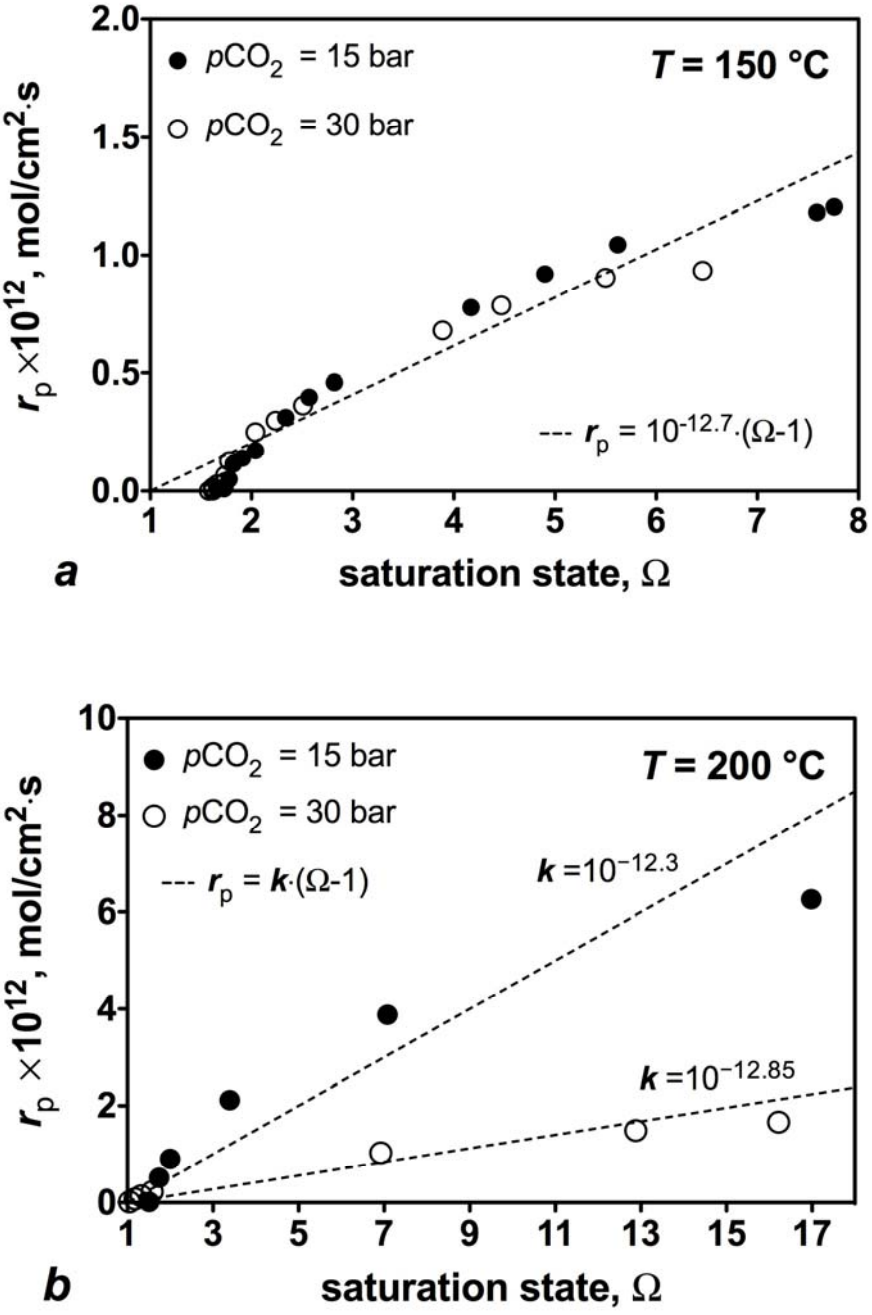

Figure 10. Precipitation rates measured after batch reactor experiments at pCO_2 of 15 and 30 bar plotted against the corresponding saturation state. (***a***) 150 °C ; (***b***) 200°C. A direct effect of pCO_2 on the kinetics cannot be inferred.

The equation used to describe the rates precipitation (Eqn. 16) represents a Langmuir-type adsorption isotherm (Langmuir, 1918) which provides a quantitative description of the kinetic effect of aqueous CO_3^{2-} on $MgCO_3$ precipitation. Besides magnesite, the same form of

equation was used to describe the inhibitory effect of aqueous carbonate on dolomite dissolution (Pokrovsky and Schott, 2001), but also to model the inhibitory action of different ions on dissolution and precipitation kinetics of other mineral phases (e.g. Christoffersen and Christoffersen,1981; Van Cappellen and Berner, 1991). The fit provided by Eqn. (16) shows how the carbonate effect starts to be significant for activities of the anion > 10^{-5} and 10^{-3} at 200 and 100 °C respectively. This results from the increase of the constant of reaction (12), K_{CO3}, which was found to increase from 4.5×10^{-5} to 5.5×10^{-4} when temperature decreases from 200 to 100 °C.

In deriving the rate equation used to describe the precipitation rates we have only taken into account the formation of $>MgOH_2^+$ and $>MgCO_3^-$ surface sites. However it should be noticed that the increase of temperature and solution pH can also favor the formation of >MgOH° as described by reaction (11). An assessment of the influence of the formation of >MgOH° on magnesite precipitation kinetics is difficult because there are not realiable data on aqueous magnesium hydrolysis and thus on the stability of >MgOH° sites as a function of temperature. However, using available Mg^{2+} hydrolysis constants and assuming, as a first approximation, equal stability of MgOH+ and >MgOH° (cf. Schlinder and Stumm, 1987; Schott et al., 2009), it can be deduced that the formation of >MgOH° is neglible in most of our experiments at 100 and 150°C, but that it can be significant at 200°C, pH > 8 and ∑CO2 < 0.1M where >MgOH° could represent up to 80% of Mg surface sites (for example for the runs PM7 and PM8) as suggested by Saldi et al. (2009, see chapter 3). However, it is believed that for the large majority of investigated experimental conditions, Equation (16) can accurately describe magnesite precipitation rates as illustrated by the good agreement observed in Figure 5a between measured and calculated rates.

5.2 Batch reactor experiments

Unlike experiments in mixed flow reactors, the run performed in the batch reactor allowed investigation of magnesite precipitation at close to equilibrium conditions (Ω < 10). As shown in the plots of Figures 9 and 10 magnesite growth rates determined at 150 and 200 °C and at 15 < pCO_2 < 30 exhibit a linear dependence on solution saturation index ($\boldsymbol{n}$ = 1) for Ω > 2. This order of reaction is consistent with a growth process taking place at grain surface features (e.g. steps and kink sites) which were generated during the initial magnesite dissolution stage before the increase of temperature and subsequent precipitation reaction. As

already emphasized, the very low precipitation rates obtained at $\Omega < 2$ are affected by high uncertainties stemming from the difficuty to interpret Mg-concentration profiles and to determine exact Mg concentration at equilibrium. As a result, these few reaction rates and their dependence on solution saturation index will not be further analysed.

6. Comparison of magnesite precipitation mechanisms in batch and mixed flow reactors

Magnesite precipitation rates determined in mixed flow reactors at high values of solution saturation indexes ($10 < \Omega < 75$) are proportional to square of solution saturation index ($\boldsymbol{n} = 2$) and consistent with a spiral growth mechanism driven by screw dislocations. These rate data and growth mechanism are in excellent agreement with our previous AFM study of magnesite crystal growth between at 80 to 120 °C and Ω values ranging from 25 to 220 (Saldi et al., 2009 (see chapter 3)).

In contrast magnesite precipitation rates measured in batch reactors at 150 and 200°C and lower Ω values ($2 < \Omega < 15$) are linear functions of solution saturation index ($\boldsymbol{n} = 1$) which is consistent with a precipitation mechanism driven by the attachment of growth units to steps and kinks present at the magnesite surface. The different growth mechanism likely arise from i) closer to equilibrium conditions (smaller values of Ω) in batch experiments and ii) different history of magnesite powders used as seed for precipitation in batch and open reactors. Indeed, in batch reactor, magnesite powder underwent, prior to precipitation, a significant dissolution stage which is likely to have produce surface features (i. e. steps) which allow simple attachment of growth units to the surface, consistent with a linear growth mechanism. Similar impact of the history of powder treatment (like the degree of powder dissolution) on growth mechanism has been already observed by Gautier (1999) for quartz precipitation rates. One can understand that linear growth was less likely to occur in mixed flow experiments which were performed using undissolved magnesite powders exhibiting mostly flat surfaces which requires a mechanism of step generation to grow.

7. Dependence of magnesite precipitation rates on temperature

The Arrhenius plot of precipitation rates measured in mixed flow reactor allows to determine the activation energy of magnesite precipitation rate constant and thus to extrapolate precipitation rates to ambient temperature (Figure 6). The linear regression of the rate constants determined between 100 and 200 °C and plotted in Figure 6 yields a rate constant $k_{Mg}^{-} = 4.1\times10^{-18}$ mol/cm^2/s at 25 °C. For seeded calcite growth at 25 °C, Yeghicheyan (1996) determined a rate constant of 1.3×10^{-11} mol/cm^2/s, with a dependence of reaction rate on solution saturation index of 1.9, in good agreement with the observations of previous studies (e.g. Reddy and Gaillard, 1981). This enormous difference between magnesite and calcite precipitation rate constants (~6.5 orders of magnitude) can be further illustrated by the times needed to precipitate a given amount of corresponding carbonates from a solution equally supersaturated with respect to the two minerals. Considering for example two aqueous solution having $\Omega = 3$ with respect to calcite and magnesite at 25 °C, we can calculate that it will take 60 hours and 23000 years to precipitate 10 g of calcite and magnesite, respectively, on 1 m^2 of corresponding carbonate surface. At 60°C, the same amount of magnesite would instead precipitate in 1500 years. According to the experimental measurements of Pokrovsky and Schott (2001) about 100 years would be necessary to precipitate the same number of moles of dolomite at 25°C. The slow kinetics of these reactions is confirmed by the estimates made by Usdowski (1989), who studied the transformation of aragonite into dolomite and magnesite at 60 °C and estimated that between 100 and 1000 years would be required for the completion of these reactions at ambient temperature. Note that a similar difference between magnesite and calcite precipitation kinetics is also found at 100 °C as magnesite precipition rate constant measured in this study (7.9×10^{-16} mol/cm^2/s) is about 6 orders of magnitude lower that calcite rate constant (1×10^{-9} mol/cm^2/s) determined by Shiraki and Brantley (1995) while the precipitation of both minerals is lead by a spiral growth mechanism.

The difficulty in precipitating magnesite from supersaturated solutions compared to calcite is likely related to the much stronger strength of Mg-O bonds than Ca-O bonds as illustrated by the rates of exchange of water molecules from Mg and Ca ions coordination sphere. As noted by Pokrovsky and Schott (2002), the 4.5 orders of magnitude difference between magnesite and calcite H_2O-promoted dissolution rates perfectly matches the difference of rate of exchange of water molecules between the solvent and Ca and Mg spheres reported by Lincoln and Merbach (1995). Carbonate mineral precipitation is controlled by the

exchange in metal coordination sphere of one water molecule with incoming carbonate or bicarbonate ions thus leading to the formation of a carbonate complex in solution or at the solid surface (Di Tommaso and de Leeuw, 2009). Thus, like for dissolution, carbonate precipitation rates should be proportional to the rate of exchange of water molecules in the coordination sphere of corresponding metal constituting carbonate. Moreover, it is interesting to note that whereas exchange of water molecules in Ca coordination sphere proceeds via an associatively activated mechanism (the rate controlling step is the creation of a new bond between the metal and incoming ligand), the exchange of water molecules in Mg (and Fe, Co, Ni) sphere proceeds via a dissociatevely activated mechanism (the rate controlling step is the breaking of a Mg-O bond) (Lincoln and Merbach, 1995). This dissociative mechanism likely accounts for the much lower precipitation rates of magnesite, siderite, and dolomite compared to calcite, and the reluctance of Mg, Fe, Ni, Co to form the anhydrous carbonates at ambient temperature in aquatic environments (Schott et al., 2009).

It is well known that the substitution in a metal aqueous ion coordination sphere of one or several water molecules for organic or inorganic ligands - that polarize Me-O bonds – increases the rate of exchange of water molecules. As demonstrated by recent measurements of magnesite precipitation rates in the presence of oxalate ions (Gautier et al., 2009), organic ligands with negatively charged oxygen donors may enhance the precipitation rate of magnesite and dolomite and account for their biomineralisation in surface environments (Vasconcelos et al., 1995).

We have seen in this study that experiments performed in batch experiments in which preliminary dissolution step has generated active surface sites for precipitation yield magnesite precipitation rate constants almost one order of magnitude higher than those perfomed using unreacted synthetic powders. This is consistent with an experimental study of Deelman (1999) showing that both magnesite and dolomite nucleation were favored at low temperature (40 °C) by successive large fluctuations in the chemical composition of the aqueous solution, consisting of alternating steps of dissolution and precipitation. This evidence might explain, according to this author, the large variety of chemical conditions of the environments where recent formation of dolomite and magnesite is found (Deelman, 2003). Following the evidence provided by Pokrovsky and Schott (2004) and cited references for mineral dissolution, it is likely that significant pH variations and subsequent dissolution phases could induce a regeneration of precipitation-active surface sites and accelerate the

rates of exchange of water molecules in Mg ion coordination sphere, thus resulting in a transient acceleration of the precipitation rates.

8. Concluding remarks and implications for CO_2 mineral sequestration

Magnesite precipitation rates were measured both in mixed flow and batch reactors as a function of temperature, saturation state, pCO_2 and aqueous CO_2 speciation. Rates measured in mixed flow reactors can be described by the surface complexation model developed by Pokrovsky et al. (1999a) with inhibition by carbonate ions for $a_{CO_3^{2-}} > 10^{-5}$, and are proportional to the square of the solution saturation index Ω, consistent with spiral growth at screw dislocations. In contrast, rates determined in closed system experiments under elevated pCO_2 follow a linear dependence on the saturation state reflecting sorption of reactants on steps and kinks. The linear rate law observed in batch experiments likely results from lower values of Ω and higher concentration of active sites for crystal growth like steps and kinks produced by the powder dissolution stage preceding each precipitation run.

The precipitation rate constants obtained from batch experiments at 150 and 200 °C are almost one order of magnitude higher than the corresponding rate constants extracted from mixed flow experiments and are consistent with an activation energy of ~ 30 kJ/mol compared to 64 kJ/mol in flow experiments. Using this activation energy to extrapolate magnesite linear growth rate constant at 25 °C shows that magnesite precipitation rates at ambient temperature may be three orders of magnitude higher than the rates predicted from mixed flow reactors measurements. As a consequence, magnesite precipitation rates obtained from mixed flow reactor experiments and extrapolated to ambient temperature must be considered as the lowest growth rates measured experimentally. It is likely that the surface morphology and especially the density of surface features favorable to crystal growth (e.g. etch pits, steps and kinks) exert a critical control on magnesite growth mechanisms and rates.

Magnesite much slower precipitation rates, compared to calcite, can be accounted for by much lower rates of water molecules exchange between the solvent and the inner sphere of hydration of Mg-ions. Investigation of the impact of various ligands on the exchange kinetics of water molecules and on magnesite (dolomite) precipitation rate is therefore fundamental to better characterize the mechanisms and rates of Mg-carbonates inorganic and biogenic precipitation in surficial aquatic environments.

The experimental results presented in this study should allow a better understanding and modeling of mineral carbonation processes via the dissolution of Mg-silicates (e.g. forsterite, pyroxenes and serpentine minerals) and associated magnesite formation. Although the limiting step for the all process is thought to be the slow release rate of Mg-ions, which is also slackened by the rapid development of a silica-rich layer (Pokrovsky and Schott, 2000; Béarat et al., 2006), rates of magnesite precipitation at conditions where the extent of the carbonation reaction reaches its optimum (high CO_2 partial pressure, 150-200 °C) can be relatively slow compared to the bulk rates measured for forsterite dissolution and extrapolated at higher *T* (cf. Hänchen et al., 2006). Use of elevated pCO_2 and corresponding slightly acidic pH (pH~5) is though essential not only to accelerate the rates of Mg-silicates dissolution but also to avoid the inhibiting effect of dissolved CO_3^{2-} on magnesite precipitation as well as on Mg-silicate dissolution (cf. Wogelius and Walther, 1991; Pokrovsky and Schott, 2000; Hänchen et al., 2006). At alkaline conditions, the surface/aqueous complexation of significant amounts of dissolved Mg by increasing concentration of dissolved counterions (HCO_3^-, CO_3^{2-} and OH^-) would further inhibit the rate of the overall carbonation process. Moreover, in the case of injection of CO_2-enriched fluids into basaltic or peridotitic rocks, the process of in situ mineral carbonation is complicated by the inherent chemical and mineralogical complexity of those systems in that Mg-carbonate formation is hindered by the competing formation of other secondary Mg-bearing phases such as smectites, zeolites and sepiolite (Marini, 2007; Gisy and Stefánsson, 2008; Andreani et al., 2009).

Acknowledgements

We would like to thank Jean-Claude Harrichoury and Alain Castillo for their scrupulous technical assistance throughout the duration of the experimental work, and Carole Causserand for her generous assistance during the analytical part of the work. We thank also Alain Pages for performing granulometric analyses, and express our gratitude Andrey Bychkov for his indispensable expertise in developing and improving the system of pH measurement in situ. We are also grateful to Pascale Bénézeth, and Jean-Louis Dandurand for helpful discussions during the course of this study. Support from Centre National de la Recherche Scientifique, and the European Community through the MIR Early Stage Training Network (MEST-CT-2005-021120) is gratefully acknowledged.

9. *References*

Alexander, G., Maroto-Valer, M. M., and Gafarova-Aksoy, P. (2007). Evaluation of reaction variables in the dissolution of serpentine for mineral carbonation. *Fuel* **86**, 273-281.

Andreani, M., Luquot, L., Gouze, P., Godard, M., Hoise, E., and Gibert, B. (2009). Experimental study of carbon sequestration reactions controlled by the percolation of CO_2-rich brine through peridotites. *Environ. Sci. Technol.* **43**, 1226-1231.

Arvidson, R. S. and Mackenzie, F. T., 1999. The dolomite problem: Control of precipitation kinetics by temperature and saturation state. *Am. J. Sci.* **299**, 257-288.

Baron G. and Favre I. (1958). État actuel des recherché en direction de la synthèse de la dolomie. *Revue de l'Institut Français du Petrole* **XIII** n. 7-8, 1067-1085.

Béarat, H., McKelvy, M. J., Chizmeshya, A. V. G., Gormley, D., Nunez, R., Carpenter, R. W., Squires, K., and Wolf, G. H. (2006). Carbon sequestration via aqueous olivine mineral carbonation: Role of passivating layer formation. *Environ. Sci. Technol.* **40**, 4802-4808.

Bénézeth, P., Palmer, D. A., and Wesolowski, D. J. (2008). Dissolution/precipitation kinetics of boehmite and gibbsite: Application of a pH-relaxation technique to study near-equilibrium rates. *Geochim. Cosmochim. Acta* **72**, 2429-2453.

Berner, R. A., Lasaga, A. C., and Garrels, R. M. (1983). The carbonate-silicate geochemical cycle and its effect on atmospheric carbon-dioxide over the past 100 million years. *Am. J. Sci.* **283**, 641-683.

Brunauer S., Emmet P. H., and Teller E. (1938). Adsorption of gases in multimolecular layers. *J. Am. Chem. Soc.*, **60**, 309-319.

Busenberg, E., and Plummer, L. N. (1986). A comparative study of the dissolution and crystal growth kinetics of calcite and aragonite, *in* Mumpton, F. A., editor, Studies in Diagenesis: U. S. Geological Survey Bulletin B 1578, pp. 139–168.

Castaing M., Kraus J.-L., Beaufils P. and Ricard J. (1991). Temperature-jump method for studying the fast transport of Na^+ by (221)C10-crptand across lipid membranes. *Biophys. Chem.* **41**, 203–215.

Chen, Z. Y., O'Connor, W. K., and Gerdemann, S. J. (2006). Chemistry of aqueous mineral carbonation for carbon sequestration and explanation of experimental results. *Environ. Prog.* **25**, 161-166.

Chou, L., Garrels, R.M., Wollast, R. (1989). Comparative study of the kinetics and mechanisms of dissolution of carbonate minerals. *Chem. Geo.* **78**, 269-282.

Christ C. L. and Hostetler P. B. (1970). Studies in the system MgO-SiO_2-CO_2-H_2O (II): the activity product constant of magnesite. *Am. J. Sci.* **268**, 439-453.

Christoffersen, J. and Christoffersen, M. R., 1981. Kinetics of dissolution of calcium hydroxyapatite : IV. The effect of some biologically important inhibitors. *Journal of Crystal Growth* **53**, 42-54.

Dangles O., Elhabiri M. and Brouillard R. (1994) Kinetic and thermodynamic investigation of the aluminum–anthocyanin complexation in aqueous solution. *J. Chem. Soc. Perkin Trans.* **2**, 2587-2596.

Deelman, J. C. (1999). Low temperature nucleation of magnesite and dolomite. *N. Jb. Miner. Mh.* **7**, 289-302.

Deelman, J. C. (2003). Note on magnesite formation (studies on irreversible geochemical reactions **9**). *Carnets de Géologie/Notebooks on Geology*, Maintenon, Letter 2003/03.

Di Tommaso D. and de Leeuw N. H. (2009). Theoretical study of the dimerization of calcium carbonate in aqueous solution under natural water conditions. *Geochim. Cosmochim. Acta* **In Press** (doi:10.1016/j.gca.2009.06.003).

Dove P.M. and Crerar D.A. (1990). Kinetics of quartz dissolution in electrolyte solution using a hydrothermal mixed flow reactor. *Geochim. Cosmochim. Acta* **54**, 955-969.

Duckworth, O. W. and Martin, S. T., (2003). Connections between surface complexation and geometric models of mineral dissolution investigated for rhodochrosite. *Geochim. Cosmochim. Acta* **67**, 1787-1801.

Eigen M. and de Maeyer L. (1963). In "Thechnique of Organic Chemistry" vol. VIIIb. A. Weissenberger Ed.; Wiley, New York, pp. 895

Eyring, H. (1935). The activated complex in chemical reactions. *J. Chem. Phys.* **3,** 107-115.

Gautelier, M., Schott, J., and Oelkers, E. H., 2007. An experimental study of dolomite dissolution rates at 80 degrees C as a function of chemical affinity and solution composition. *Chem. Geo.* **242**, 509-517.

Gautier J.-M. (1999). Etude experimental et modelisation de la cinetique de dissolution et de cristallisation des silicates en milieu hydrothermal: cas du quartz et du feldspath potassique. PhD thesis.

Gautier, J.-M., Oelkers, E. H., and Schott, J., 1994. Experimental study of K-feldspar dissolution rates as a function of chemical affinity at 150°C and pH 9. *Geochim. Cosmochim. Acta* **58**, 4549-4560.

Gautier, J.-M., Oelkers, E. H., and Schott, J., 2001. Are quartz dissolution rates proportional to B.E.T. surface areas? *Geochim. Cosmochim. Acta* **65**, 1059-1070.

Gautier Q., Saldi G. D., Bénézeth P., Oelkers E. H. and Schott J. (2009). Effects of organic ligands on magnesite precipitation rates. *Geochim. Cosmochim. Acta* **73** (13), A419.

Gerdemann, S. J., O'Connor, W. K., Dahlin, D. C., Penner, L. R., and Rush, H. (2007). Ex situ aqueous mineral carbonation. *Environ. Sci. Technol.* **41**, 2587-2593.

Giammar D.E., Bruant R.G. and Peters, C.A. (2005). Forsterite dissolution and magnesite precipitation at conditions relevent for deep saline aquifer storage and sequestration of carbon-dioxide. *Chem. Geo.* **217,** 257-276.

Goldberg P., Chen Z-Y, O'Connor W., Walters R., and Ziock H. (2001). CO_2 Mineral Sequestration Studies in U.S.. *Presented at the First National Conference on Carbon Sequestration,* Washington, DC, May 14-17 2001.

Goldberg P., Chen Z.-Y., O' Connor W., Walters R., and Ziock H. (2001). CO_2 mineral sequestration studies in U. S.. *Presented at the First National Conference on Carbon Sequestration*. Washington DC, May 14-17, 2001.

Gratz A. J., Hillner P. E., and Hansma P. K. (1993) Step dynamics and spiral growth on calcite. *Geochim. Cosmochim. Acta* **57**, 491–495.

Gysi, A. P. and Stefánsson, A. (2008). Numerical modeling of CO_2-water-basalt interaction. *Mineralogical Magazine* **72**, 55-59.

Hänchen, M., Prigiobbe, V., Baciocchi, R., and Mazzotti, M. 2008. Precipitation in the Mg-carbonate system – effects of temperature and CO_2 pressure. *Chem. Eng. Sci.,* **63,** 1012-1028.

Hänchen, M., Prigiobbe, V., Storti, G., Seward, T. M., and Mazzotti, M. (2006). Dissolution kinetics of fosteritic olivine at 90-150 °C including effects of the presence of CO2. *Geochim. Cosmochim. Acta* **70**, 4403-4416.

Hribar, B., Southall, N. T., Vlachy, V., and Dill, K. A. (2002). How ions affect the structure of water. *Journal of the American Chemical Society* **124**, 12302-12311.

Inskeep, W. P. and Bloom, P. R., 1985. An evaluation of rate equations for calcite precipitation kinetics at pCO2 less than 0.01 atm and pH greater than 8. *Geochim. Cosmochim. Acta* **49**, 2165-2180.

Lackner, K. S., Butt, D. P., and Wendt, C. H. (1997). Progress on binding CO2 in mineral substrates. *Energy Conversion and Management* **38**, S259-S264.

Lackner, K. S., Wendt, C. H., Butt, D. P., Joyce, E. L., and Sharp, D. H. (1995). Carbon dioxide disposal in carbonate minerals. *Energy* **20**, 1153-1170.

Langmuir, I. (1918). The adsorption of gases on plane surfaces of glass, mica and platinum. *Journal of the American Chemical Society* **40**, 1361-1403.

Lin F.-C., and Cemency C. V. (1981) The dissolution kinetics of brucite, antigorite, talc and phlogopite at room temperature and pressure. *Am. Min.* **66**, 801–806.

Lincoln S. F. and Merbach A. E. (1995). Substitution reactions of solvated metal cations. In *Advances in inorganic chemistry*, vol. 42, pp. 1-88. Academic Press.

Lippmann F. (1973). Sedimentary Carbonate minerals. Springer-Verlag eds., pp. 229.

Luce R. W., Bartlett W. B., and Parks G. A. (1972). Dissolution kinetics of magnesium silicates. *Geochim. Cosmochim. Acta* **36**, 35–50.

Marini L. (2007). Geological sequestration of carbon dioxide: Thrmodynamics, kinetics and reaction path modeling. *Developments in Geochemistry* **11**. Elsevier, pp. 470.

Maroto-Valer, M. M., Fauth, D. J., Kuchta, M. E., Zhang, Y., and Andresen, J. M. (2005). Activation of magnesium rich minerals as carbonation feedstock materials for CO2 sequestration. *Fuel Processing Technology* **86**, 1627-1645.

McGrail, B. P., Schaef, H. T., Ho, A. M., Chien, Y. J., Dooley, J. J., and Davidson, C. L. (2006). Potential for carbon dioxide sequestration in flood basalts. *J. Geophys. Res.-Solid Earth* **111**, 13.

Möller P. (1989). Magnesite: geology, mineralogy, geochemistry, formation of Mg-carbonates. *Monograph series on Mineral Deposits*, n. 28, pp. 300, ed. By P. Möller. Gebrüder Borntraeger, Berlin-Stuttgart.

Morse, J.W., Arvidson, R.S. and Luttge, A. (2007). Calcite formation and dissolution. *Chem. Revs.* **107,** 342-381.

Mucci, A. and Morse, J. W. (1983). The incorporation of Mg^{2+} and Sr^{2+} into calcite overgrowths: influences of growth rate and solution composition. *Geochim. Cosmochim. Acta* **47**, 217-233.

Mucci, A. (1986). Growth kinetics and composition of magnesian calcite overgrowths precipitated from seawater: Quantitative influence of orthophosphate ions. *Geochim. Cosmochim. Acta* **50**, 2255-2265.

Nancollas, G. H. and Reddy, M. M. (1971). The crystallization of calcium carbonate. II. Calcite growth mechanism. *Journal of Colloid and Interface Science* **37**, 824-830.

O'Connor W.K., Dahlin D.C., Nilsen D.N., Rush G.E., Walters R.P., and Turner P.C. (2000). CO_2 Storage in Solid Form: A study of direct mineral carbonation. *Fifth International Conference on Greenhouse Gas Control Technologies,* Cairns, Australia, August 13 - August 16, 2000.

Oelkers E. H. (2001). An experimental study of forsterite dissolution rates as a function of temperature and aqueous Mg and Si concentrations. *Chem. Geo.* **175**, 485-494.

Oelkers E.H. and Cole D.R. (2008). Carbon dioxide sequestration: A solution to a global problem. *Elements* **4**, 305-310.

Oelkers E. H. and Schott J. (2001). An experimental study of enstatite dissolution rates as a function of pH, temperature, and aqueous Mg and Si concentration, and the mechanism of pyroxene/pyroxenoid dissolution. *Geochim. Cosmochim. Acta* **65**, 1219-1231.

Oelkers E.H. and Schott J. (2005). Geochemical Aspects of CO_2 Sequestration. *Chem. Geo.* **217,** 183-186.

Oelkers E.H., Gislason S.R. and Matter, J. (2008) Mineral carbonation of CO_2. *Elements* **4**, 333-337.

Parkhurst D. L. and Appelo C. A. J. (1999).User's guide to PHREEQC (version 2) - a computer program for speciation, batch-reaction,one-dimensional transport, and inverse geochemical calculations. U.S. Geological Survey Water-resources Investigation Report 99-4259, pp. 312.

Piana, S., Jones, F., and Gale, J. D. (2006). Assisted desolvation as a key kinetic step for crystal growth. *J. American Chemical Society* **128**, 13568-13574.

Pines E. and Huppert D. (1983). pH jump: a relaxation approach. *J. Phys. Chem.* **87**, 4471-4478.

Plummer, L. N., Wigley, T. M. L., and Parkhurst, D. L. (1978). Kinetics of calcite dissolution in CO_2-water system at 5 °C to 60 °C and 0.0 to 1.0 atm CO_2. *Am. J. Sci.* **278**, 179-216.

Pokrovski, G. S., Schott, J., and Sergeyev, A. S. (1995). Experimental determination of the stability constants of NaSO4- and NaB (OH)40 in hydrothermal solutions using a new high-temperature sodium-selective glass electrode -- Implications for boron isotopic fractionation. *Chem. Geo.* **124**, 253-265.

Pokrovsky O.S. and Schott J. (1999). Processes at the magnesium-bearing carbonates solution interface. II Kinetics and mechanism of magnesite dissolution. *Geochim. Cosmochim. Acta* **63**, 881-897.

Pokrovsky O. S., Schott J., and Thomas F. (1999a). Processes at the magnesium-bearing carbonates/solution interface. I. A surface speciation model for magnesite. *Geochim. Cosmochim. Acta* **63**, 863-880.

Pokrovsky O. S., Schott J., and Thomas F. (1999b). Dolomite surface speciation and reactivity in aquatic systems. *Geochim. Cosmochim. Acta* **63**, 3133-3143.

Pokrovsky O. S. and Schott J. (2000). Kinetics and mechanism of forsterite dissolution at 25°C and pH from 1 to 12. *Geochim. Cosmochim. Acta* **64**, 3313-3325.

Pokrovsky O. S. and Schott J. (2001). Kinetics and mechanism of dolomite dissolution in neutral to alkaline solutions revisited. *Am. J. Sci.* **301**, 597-626.

Pokrovsky O. S. and Schott J. (2002). Surface chemistry and dissolution kinetics of divalent metal carbonates. *Environ. Sci. Technol.* **36**, 426-432.

Pokrovsky O.S. and Schott J. (2004). Experimental study of brucite dissolution and precipitation in aqueous solution: surface speciation and chemical affinity control. *Geochim. Cosmochim. Acta* **68**, 31-45.

Pokrovsky O. S., Golubev S. V., and Schott J. (2005). Dissolution kinetics of calcite, dolomite and magnesite at 25 °C and 0 to 50 atm pCO2. *Chem. Geo.* **217**, 239-255.

Prabhananda B. S., Rittger E. and Grell E. (1987). Kinetics and mechanism of anionic ligand binding to carbonic anhydrase. *Biophys. Chem.* **26**, 217-224.

Prigogine I. (1967). Introduction to Thermodynamics of Irreversible Processes. Wiley, New York, pp. 147.

Reddy, M. M. and Gaillard, W. D. (1981). Kinetics of calcium carbonate (calcite)-seeded crystallization: Influence of solid/solution ratio on the reaction rate constant. *Journal of Colloid and Interface Science* **80**, 171-178.

Reddy, M. M., Plummer, L. N., and Busenberg, E. (1981). Crystal growth of calcite from calcium bicarbonate solutions at constant PCO_2 and 25 °C: a test of calcite dissolution model. *Geochim. Cosmochim. Acta* **45**, 1281-1289.

Rosso, J. J. and Rimstidt, J. D. (2000). A high resolution study of forsterite dissolution rates. *Geochim. Cosmochim. Acta* **64**, 797-811.

Saldi, G. D. (2009). An experimental study of $MgCO_3$ reactivity and stability for CO_2 sequestration. Ph.D. Thesis.

Saldi G. D. , Jordan G., Oelkers E. H. and Schott J. (2009). Magnesite growth rates as a function of saturation state and temperature. *Geochim. Cosmochim. Acta*. **Accepted.**

Saldi, G. D., Köhler, S. J., Marty, N., and Oelkers, E. H. (2007). Dissolution rates of talc as a function of solution composition, pH and temperature. *Geochim. Cosmochim. Acta* **71**, 3446-3457.

Sayles, F. L. and Fyfe, W. S. (1973). The crystallization of magnesite from aqueous solution. *Geochim. Cosmochim. Acta* **37**, 87-99.

Shiraki, R. and Brantley, S. L. (1995). Kinetics of near-equilibrium calcite precipitation at 100°C: An evaluation of elementary reaction-based and affinity-based rate laws. *Geochim. Cosmochim. Acta* **59**, 1457-1471.

Schlinder P. W. and Stumm W. (1987). The surface chemistry of oxides, hydroxides and oxide minerals. *In*: Aquatic surface chemistry. Stumm W. (ed.) John Wiley, New York, p. 83-110.

Schott J., Pokrovsky O. S., and Oelkers E. H. (2009). The link between mineral dissolution/precipitation kinetics and solution chemistry. In "Thermodynamics and kinetics of water-rock interaction", *Rev. Min.***70**, 207-258.

Schott J. and Berner R. A. (1983). X-ray photoelectron studiesof the mechanism of iron silicate dissolution during weathering. *Geochim. Cosmochim. Acta* **47**, 2233-2240.

Schott J., Berner R. A., and Sjoberg E. L. (1981). Mechanism of pyroxene and amphibole weathering —I. Experimental studies of iron-free minerals. *Geochim. Cosmochim. Acta* **45**, 2123-2135.

Shock, E. L., Sassani, D. C., Willis, M., and Sverjensky, D. A. (1997). Inorganic species in geologic fluids: Correlations among standard molal thermodynamic properties of aqueous ions and hydroxide complexes. *Geochim. Cosmochim. Acta* **61**, 907-950.

Shvarov, Y. V. (1999). Algorithmization of the numerical equilibrium modelling of dynamic geochemical processes. *Geochemistry International* **37**, 571-576.

Shvarov, Y., Bastrakov, E. (1999). A software package for geochemical equilibrium modeling. User's Guide. Australian Geological Survey Organization, Department of Industry, Science and Resources.

Stipp, S. L. and Hochella, M. F. (1991). Structure and bonding environments at the calcite surface as observed with X-ray photoelectron spectroscopy (XPS) and low energy electron diffraction (LEED). *Geochim. Cosmochim. Acta* **55**, 1723-1736.

Teng, H. H., Dove, P. M., and De Yoreo, J. J. (2000). Kinetics of calcite growth: surface processes and relationships to macroscopic rate laws. *Geochim. Cosmochim. Acta* **64**, 2255-2266.

Torrent, J., Font, J., Herberhold, H., Marchal, S., Ribó, M., Ruan, K., Winter, R., Vilanova, M., and Lange, R. (2006). The use of pressure-jump relaxation kinetics to study protein folding landscapes. *Biochim. Biophys. Acta (BBA) - Proteins & Proteomics* **1764**, 489-496.

Usdowski E. (1989). Synthesis of dolomite and magnesite at 60 °C in the system Ca^{2+}-Mg^{2+}-CO_3^{2-} -Cl_2^2-H_2O. *Naturwissenschaften* **76**, 374-375.

Van Cappellen, P. and Berner, R. A., (1991). Fluorapatite crystal growth from modified seawater solutions. *Geochim. Cosmochim. Acta* **55**, 1219-1234.

Van Cappellen, P., Charlet, L., Stumm, W., and Wersin, P. (1993). A surface complexation model of the carbonate mineral-aqueous solution interface. *Geochim. Cosmochim. Acta* **57**, 3505-3518.

Vasconcelos C., McKenzie J. A., Bernasconi S., Grujic D., and Tien A. J. (1995). Microbial mediation as a possible mechanism for natural dolomite formationat low temperatures: *Nature* **377**, 220–222.

Wogelius, R. A. and Walther, J. V. (1991). Olivine dissolution at 25 °C: effects of pH, CO_2 and organic acids. *Geochim. Cosmochim. Acta* **55**, 943-954.

Wolf, G.H., Chizmeshya A.V.G., Diefenbacher, J., and McKelvy, M.J., (2004). In-situ observationof CO_2 sequestration reactions using a novel microreaction system. *Env. Sci. Tech.,* **38,** 932-936.

Wolff-Boenisch, D., Gislason, S. R., and Oelkers, E. H. (2006). The effect of crystallinity on dissolution rates and CO_2 consumption capacity of silicates. *Geochim. Cosmochim. Acta* **70**, 858-870.

Wollast, R., (1990). Rate and mechanism of dissolution of carbonates in the system $CaCO_3$ – $MgCO_3$, *in* Stumm, W., editor, Aquatic Chemical Kinetics: Reaction Rates of Processes in Natural Waters: New York, J. Wiley & Sons, p. 431-445.

Yeghicheyan, D. (1996). Etude expérimentale du partage des terres rares entre carbonates de calcium et solutions aqueuses: influence de la cinétique de cristallisation et de la spéciation des terres rares en solution. *PhD Thesis*, Université Paul Sabatier, pp. 167.

CHAPITRE 3

Etude AFM des vitesses de nucléation et croissance cristalline de la magnésite

Résumé en français de l'article :

"Magnesite growth rates as a function of temperature and saturation state"

1. Introduction

Cette étude a été menée avec le but principal de déterminer les processus microscopiques qui contrôlent les vitesses de précipitation de la magnésite et donc sa formation dans différents environnements naturels. La magnésite est aussi un exemple de minéraux qui, comme le quartz, n'arrive pas à précipiter directement d'une solution sursaturée à température ambiante (Lippmann, 1973; Pokrovsky et Schott, 1999; Giammar et al., 2005). C'est pourquoi l'étude microscopique ici présentée a des implications plus générales et peut apporter des éléments nouveaux utiles à la compréhension des phénomènes qui empêchent la précipitation de certaines minéraux à basse température. En outre, en considération de la possibilité de piéger le CO_2 sous forme minérale, la précipitation de cette phase a suscité un grand intérêt dans la communauté scientifique (cf. Kaszuba et al., 2003; Oelkers et Schott, 2005; Hänchen et al., 2008; Oelkers et al., 2008), et par conséquent la détermination précise des vitesses et des mécanismes élémentaires de croissance ont une importance fondamentale pour le développement de techniques de séquestration efficaces et économiquement possibles.

2. Méthodes Experimentales

Les vitesse de nucléation et croissance de la magnésite ont pu être mesurées en utilisant la microscopie à force atomique hydrothermale (HAFM) (voir Higgins et al., 1998). Cette technique permet de calculer ces vitesses en fonction de l'évolution temporelle de la morphologie d'un échantillon de surface étudié. Il est ainsi possible de comparer les vitesses de précipitation dérivées de mesure effectuées par AFM avec celle déduites de l'étude macroscopique en réacteur à circulation ou fermé. Cette comparaison permet de mieux contraindre la signification des observations microscopique et de fournir une quantification plus précise du processus global.

Les expériences de croissance ont été menées sur la surface de clivage (104) d'un échantillon de magnésite naturelle, en utilisant comme milieux réactifs des solutions sursaturées par rapport à cette phase. Les solutions ont été préparées à partir de $MgCl_2$, $NaHCO_3$, HCl, NaOH, NaCl et H_2O ultra pure, en fixant la force ionique à environ 0.1 M (voir tableau 1). Les processus de nucléation et croissance ont été étudié en fonction de la température ($80 \leq T \leq 120$ °C), de l'indice de saturation de la solution ($6 \leq \Omega < 820$) et du rapport d'activité $\boldsymbol{a}(Mg^{2+})/\boldsymbol{a}(CO_3^{2-})$.

3. Résultats et observations expérimentales

Les vitesses d'avancement des marches et les fréquences de nucléation ont étés mesurés systématiquement entre 80 et 105 °C. Dans cet intervalle de température la génération de nouvelles couches élémentaires de hauteur 2.74 Å se produit par un mécanisme de croissance spirale qui est responsable de la génération d'ilots de croissance caractérisées par une forte anisotropie (schéma Fig. 2), où les marches obtuses (G_o) avancent environ un ordre de grandeur plus rapidement que les marches aiguës (G_a) et reproduisent la même anisotropie observée par Jordan et al. (2001) dans le cas de la formation de puits de corrosion durant la dissolution de ce minéral. Les vitesses d'avancement des marches augmentent de manière linéaire avec l'indice de saturation à toute température au delà d'une valeur critique (Ω_c) correspondant à l'intercepte des corrélations linéaires entre vitesses de marches et indice de saturation (Fig. 7a-b). Au dessous de ces valeurs critiques de sursaturation il n'y a pas de données disponibles, mais on peut en déduire que la dépendance de l'indice de saturation devient non-linéaire en raison de la faible densité de kinks (Chernov et Rashkovic, 1987 ; Higgins et al., 2000), ou à cause de l'effet d'impuretés présentes dans les solutions expérimentales, comme observé par des études effectuées sur la croissance de la calcite (Teng et al., 1999; Davis et al., 2000; Wasylenki et al. 2005).

Nous avons aussi observé un changement de morphologie des ilot de croissance en réponse à la variation de température et de l'état de saturation de la solution (Fig. 3): dès qu'on approche l'équilibre, soit par une diminution de la température, soit par une diminution de l'état de sursaturation de la solution, l'angle compris entre le deux marches obtuses s'élargit vers la valeur (~103°) typique du rhombe délimité par les directions cristallographiques $[48\bar{1}]$ et $[\bar{4}41]$.

En ce qui concerne le mécanisme de formation de nouvelles couches élémentaires, comme déjà anticipé, il s'agit généralement d'une croissance spirale (Fig. 4). Ce mécanisme de croissance n'a pas toujours été facile à mettre en évidence à cause de la forte anisotropie de vitesse entre marches lentes et marches rapides : la haute densité de marches aiguës empêche souvent l'individuation du type de dislocation. Les dislocations qui sont responsables de la génération de nouvelles couches sont souvent associées à des importantes structures (gradins) auprès des quelle on retrouve la concentration la plus élevée de défauts linéaires (Fig. 5). Un changement de mécanisme caractérisé par une nucléation bidimensionnelle aléatoire a été vérifié seulement dans des conditions extrêmes (T > 100 °C and Ω > ~200) mais dans ces cas les vitesses de croissance n'ont pu être quantifié à cause de la forte distorsion et l'absence de points de référence entre images successives dues aux vitesses de croissance élevées par rapport aux vitesses de scansion de la surface du cristal.

La vitesse d'avancement des marches en fonction de la température est décrite par la relation d'Arrhenius (Sangwal, 1998) :

$$\boldsymbol{k}_v = \boldsymbol{A} \exp(-\boldsymbol{E}_a/\boldsymbol{R}T), \qquad (1)$$

où $\boldsymbol{k}_v$ designe le coefficient cinétique des marche qui correspond à la pente des lignes d'interpolation représentées sur les Fig. 7a et 7c de l'article, $\boldsymbol{A}$ represente un facteur pre-exponentiel, $\boldsymbol{R}$ est la constante des gaz parfaits, et $\boldsymbol{E}_a$ correspond à l'énergie d'activation. Sur la base de cette relation les vitesses des marches mesurées entre 80 et 100 °C déterminent une énergie d'activation de 159 kJ/mol (Fig. 7b). Des vitesses de précipitation peuvent être extrapolées à partir des observations faites par AFM en utilisant l'expression suivante (Higgins et al., 2002) :

$$\boldsymbol{r} = I \cdot h / V_M , \qquad (2)$$

où $\boldsymbol{r}$ représente la vitesse de précipitation, I désigne la fréquence de nucléation des couches de hauteur h (= 2.74 Å) et V_M corresponde au volume molaire de la magnésite (28.1 cm^3/mol). Les fréquences de génération de nouvelles couches mesurées sur le plan cristallographique (104) sont reportées dans le tableau 3 en fonction de Ω et T et plotées en fonction de l'indice de saturation en Fig.6 (article).

La comparaison entre les vitesses mesurées dans le réacteur à circulation, normalisées à la surface géométrique et réunies dans le tableau 2, et celles dérivées des observations AFM à

100 °C (Fig. 9, article) montrent que les deux ensembles de données sont en très bon accord entre eux et cohérents avec des vitesses de précipitation contrôlées par un mécanisme de croissance spirale, selon l'équation (Nielsen, 1984 ; Shiraki and Brantley, 1995):

$$\boldsymbol{r} = \boldsymbol{k} \cdot (\Omega\text{-}1)^2. \qquad (3)$$

Cette conclusion est par ailleurs corroborée par les images AFM obtenues au cours de cette étude.

L'énergie d'activation relative aux vitesses d'avancement des marches, égale à 159 kJ/mol, est beaucoup plus élevée que celle déduite de l'étude macroscopique des vitesses de précipitation (~64 kJ/mol) et relative au processus global (nucléation plus croissance). Ceci implique que les vitesses d'avancement des marches diminuent plus rapidement que les fréquences de génération de nouvelles marches en réponse à la diminution de température. Si, en effet, on prend en compte l'énergie d'activation déduite des mesures de vitesses des marches obtuses on trouverait un coefficient cinétique ($\boldsymbol{k}_v$) égal à 2.7×10^{-14} cm/s à 25 °C, et une valeur de $\boldsymbol{k}_v$ d'environ 2.2×10^{-15} cm/s pour le marches aiguës, compte tenu de la relation existante entre le deux types de marches (Fig. 8). Avec de telles valeurs de coefficients cinétiques et pour un indice de saturation égal à 10, les marches aiguës avanceraient de 10 nm en 1.5 ans en prohibant, de fait, l'atteinte de la longueur critique nécessaire à la spirale pour tourner et ainsi alimenter la croissance cristalline qui est contrôlée par ce mécanisme. Ces contraintes cinétiques expliquent bien la difficulté à précipiter la magnésite à basse température, malgré sa stabilité, et par conséquent la tendance à former de phases hydratées moins stable.

Magnesite growth rates as a function of temperature and saturation state

Giuseppe D. Saldi[1,]*, Guntram Jordan[2], Jacques Schott[1], and Eric H. Oelkers[1]

[1]*Géochimie et Biogéochimie Expérimentale, LMTG – CNRS – OMP – Université de Toulouse, 14, Avenue Edouard Belin, 31400 Toulouse, France*
[2]*Department für Geo- und Umweltwissenschaften, Ludwig-Maximilians-Universität München, Theresienstr. 41, 80333 München, Germany*

*Corresponding author:

Tel.: +33 5 61 33 26 32; fax: +33 5 61 33 25 60

E-mail address: saldi@lmtg.obs-mip.fr; oelkers@lmtg.obs-mip.fr

Accepted for publication on *Geochimica et Cosmochimica Acta*

Keywords: magnesite, precipitation kinetics, nucleation and growth mechanisms, CO_2 sequestration, hydrothermal AFM

Abstract

Magnesite growth rates and step velocities have been measured systematically as a function of temperature from 80 to 105 °C and saturation state in 0.1 M NaCl solutions using hydrothermal atomic force microscopy (HAFM). The observations indicate that at these conditions magnesite precipitation is dominated by the coupling of step generation via spiral growth at screw dislocations and step advancement away from these dislocations. As these two processes occur in series the slowest of these dominates precipitation rates. At 100 °C magnesite growth rates (***r***) determined by HAFM are consistent with

$$\boldsymbol{r} = \boldsymbol{k}(\Omega - 1)^{\boldsymbol{2}}$$

where ***k*** is a constant equal to 6.5×10^{-16} mol/cm^2/s and Ω is the saturation index with respect to magnesite. This equation is consistent with spiral growth step generation controlling magnesite precipitation rates. Corresponding magnesite precipitation rates measured using mixed flow reactors are shown to be consistent with both the rates measured by HAFM and the spiral growth theory, confirming the rate limiting mechanism. Step advancement, however, is observed to slow by far faster than step generation with decreasing temperature; the activation energy for step advancement is 159 kJ/mol whereas step generation rates have an estimated activation energy of ~60 kJ/mol. As such, it seems likely that at ambient temperatures magnesite growth is controlled by very slow step advancement rates.

1. Introduction

The kinetics of mineral precipitation is among the poorest understood processes in low-temperature geochemistry. Whereas all minerals dissolve when exposed to an undersaturated fluid, many minerals do not precipitate from supersaturated fluids at ambient conditions. Moreover, there lacks an accurate geochemical model for predicting at which conditions a supersaturated fluid will begin to precipitate a particular secondary phase. For example, many surface waters are strongly supersaturated with respect to quartz (e.g. Arnorsson et al., 2002). Quartz, however, precipitates rarely, if at all, at Earth surface conditions (Dove and Rimstidt 1994; Gislason et al., 1996). In contrast, quartz readily precipitates in sedimentary

basins at temperatures in excess of ~ 80 °C (Bjorlykke and Egeberg, 1993; Oelkers et al., 1996).

The carbonate minerals provide an interesting case study in the low-temperature inhibition of mineral precipitation. Calcite ($CaCO_3$) precipitates readily at ambient conditions (c.f. Morse et al., 2007), but magnesite ($MgCO_3$) and dolomite ($CaMg(CO_3)_2$) observed to precipitate slowly if at all at low temperatures (Lippmann, 1973; Pokrovsky and Schott, 1999; Giammar et al., 2005). Magnesite ($MgCO_3$) formation at Earth surface conditions has been reported to be hampered by the slow kinetics of desolvation of Mg-ions from aqueous solution stemming from the high dehydration free energy of Mg^{2+} compared to Ca^{2+} (Christ and Hostetler, 1970; Sayles and Fyfe, 1973, see also Kowacz et al., 2007). This high dehydration energy favors the formation of less stable hydrated Mg-carbonates including nesquehonite and hydromagnesite at low temperature (Christ and Hostetler, 1970; Lippmann, 1973; Hänchen et al., 2008). Direct formation of magnesite from supersaturated aqueous solution or by transition from a hydrous phase is favored at high salinities (e.g. lower H_2O activities), by increasing CO_2 partial pressure, or by an increase of temperature (Möller, 1989).

Magnesite precipitation has aroused much interest in the scientific community due to its potential as a possible safe long-term CO_2 storage host (c.f. Kaszuba et al., 2003; Wolf et al., 2004; Oelkers and Schott, 2005; Hänchen et al., 2008; Oelkers and Cole, 2008; Oelkers et al., 2008). For example, magnesite precipitation can be provoked by the interaction of CO_2 charged waters with forsterite at temperatures of 95 °C (Giammar et al., 2005). The improved understanding of magnesite precipitation kinetics may prove instrumental in the development of efficient carbon sequestration techniques.

The overall goals of the present study are: 1) to determine the microscopic processes controlling magnesite precipitation in natural environments; and 2) to illuminate the reasons why many minerals fail to precipitate from supersaturated solutions at ambient conditions. Towards this goal the nucleation and growth rates of magnesite have been measured using both flow-through hydrothermal atomic force microscopy and traditional mixed-flow reactors as a function of temperature and saturation state.

AFM techniques enable the direct observation of the processes occurring at the mineral/water interface (e.g. Gratz et al., 1993; Bosbach et al., 1998; Pina et al., 2000;

Astilleros et al., 2002; Sánchez-Pastor, 2005; Aldushin et al., 2007; Vavouraki et al., 2008). By observing the temporal evolution of mineral surface morphology, microscopic growth rates can be obtained that are directly comparable with those measured on the bulk mineral (c.f. Brandt et al., 2003; Aldushin et al., 2006). Previous AFM studies on magnesite reactivity focused in its dissolution behavior in acidic solutions (Jordan et al., 2001; Higgins et al., 2002), and in presence of different organic ligands at near neutral to basic pH (Jordan et al., 2007). The present study is the first to our knowledge to apply directly atomic force microscopy to characterizing the rates and mechanism of magnesite nucleation and growth.

2. Theoretical considerations

Magnesite dissolution and precipitation can be described by:

$$MgCO_{3(s)} = Mg^{2+} + CO_3^{2-} \quad (1)$$

The law of mass action for this reaction is given by

$$K_{MgCO_3} = a_{Mg^{2+}} a_{CO_3^{2-}} \quad (2)$$

where a_i refers to the activity of the subscripted aqueous species and K_{MgCO_3} designates the equilibrium constant for reaction (1). The saturation state of reactive solutions with respect to magnesite is defined by:

$$\Omega = \frac{a_{Mg^{2+}} a_{CO_3^{2-}}}{K_{MgCO_3}} \quad . \quad (3)$$

The standard state adopted in this study is that of unit activity for pure minerals and H_2O at any temperature and pressure. For all other aqueous species the standard state is defined by unit activity in a hypothetical 1 molal solution referenced to infinite dilution at any temperature and pressure. All saturation states, ion activities and solution speciation calculations reported in this study were determined using PHREEQC (Pakhurst and Appelo, 1999). These calculations were performed using the llnl thermodynamic database after adding equilibrium constants for the $MgOH^+$ formation reaction taken from Shock et al. (1997).

One formalism for quantifying mineral nucleation and growth stems from BCF growth theory (Burton et al. 1951). This theory assumes that crystals grow by the addition of material at steps which acts as sinks. In accord with this theory, the velocity of step growing on a crystal surface will be proportional to the driving force of the reaction such that

$$\boldsymbol{v} = \boldsymbol{k}_{\mathrm{v}} (\Omega\text{-}1) \qquad (4)$$

where $\boldsymbol{k}_{\boldsymbol{v}}$ stands for a kinetic constant and $\boldsymbol{v}$ refers to the step velocity on the growing crystal surface. Building upon BCF-formalism, Nielsen (1984) and Zhang and Nancollas (1998). showed that mineral growth from solutions should be consistent with

$$\boldsymbol{r} = \boldsymbol{k}(\Omega - 1)^{\boldsymbol{n}} \qquad (5)$$

where $\boldsymbol{r}$ refers to the mineral growth rate, $\boldsymbol{k}$ stands for a rate constant and $\boldsymbol{n}$ signifies a coefficient that depends on the growth mechanism, where $\boldsymbol{n}$ = 1 for transport or adsorption controlled growth and $\boldsymbol{n}$ = 2 for spiral growth (c.f. Shiraki and Brantley, 1995). If growth is controlled by surface nucleation, rates are quantified via an exponential function of saturation state. A summary of various models describing mineral nucleation and growth is presented by Ohara and Reid (1973). A number of studies, however, have noted that although step velocities increase linearly with saturation state in strongly supersaturated conditions, this linear behavior is not observed at close to equilibrium conditions (Teng et al., 1999; Davis et al., 2000). This behavior has been attributed to either the presence of trace impurities in the reactive fluid or the effects of kink density on step advance rates (Teng et al., 1999; Davis et al., 2000; Higgins et al., 2000; Vekilov, 2007). In such circumstances step velocities at high degrees of saturation can be described using

$$\boldsymbol{v} = \boldsymbol{k}_{\mathrm{v}} (\Omega - \Omega_{\mathrm{c}}) \qquad (6)$$

where Ω_{c} represents the saturation state at which linear correlations between step velocities and saturation state cross the $\boldsymbol{v}$ = 0 axis.

The variation of the rate constant $\boldsymbol{k}_{\mathrm{v}}$ with temperature can be described using an Arrhenius-type relation such as

$$\boldsymbol{k}_{\mathrm{v}} = \boldsymbol{A} \exp(\boldsymbol{-E_a/RT}) , \qquad (7)$$

where A defines a pre-exponential factor, R stands for the gas constant and E_a represents an activation energy (e.g. Sangwal, 1998). Equations (1) to (7) are used below to aid in the interpretation of magnesite precipitation rates as a function of saturation state and temperature.

3. Experimental methods

All growth experiments were performed in aqueous solutions that were supersaturated with respect to magnesite. Supersaturated solutions were prepared by adding reagent grade NaCl, $MgCl_2$, $NaHCO_3$, HCl and NaOH to high purity deionized water (resistivity 18 MΩ cm). The relative concentration of these compounds was adjusted to obtain 0.1 M NaCl concentration to assure a close to constant ionic strength in all experiments at various supersaturation states and various aqueous Mg^{2+}/CO_3^{2-} activity ratios. The compositions of all solutions used for HAFM experiments are summarized in Table 1.

Reactive solutions of all experiments were regularly analyzed for magnesium concentration and alkalinity. Mg was measured by flame atomic absorption spectroscopy (AAS) with an uncertainty of ± 1% and a detection limit of 6×10^{-7} M, whereas the alkalinity was determined by standard HCl titration with an uncertainty of ± 1% and a detection limit of 5×10^{-5} M. pH of inlet solutions and outlet solutions were measured at 25 °C immediately after sampling using a standard glass electrode.

3.1 HAFM experiments

HAFM experiments were performed using transparent monocrystals from Brumado, Brazil. The experiments were performed on the (104) cleavage surfaces obtained by cleaving the crystal with a scalpel prior to each experiment. The surface areas of the samples used were 0.1–0.5 cm^2. A previously reported chemical analysis, in mole percent, of this magnesite by electron microprobe yielded O = 60.04%, C = 20.07%, Mg = 19.75%, Ca = 0.08%, Fe = 0.03% (Jordan et al., 2001). This analysis is consistent with the magnesite formula: $(Mg_{0.987}Ca_{0.004}Fe_{0.001})C_{1.002}O_3$. The content of Mn, Cu and Zn of this magnesite was less than 0.01% mole percent.

Table 1. Composition of the solutions used for magnesite growth experiments performed by HAFM.

Exp. Sol.	pH (25°C)	NaCl [mol/kg]	$MgCl_2$ [mol/kg]	HCl [mol/kg]	NaOH [mol/kg]	$NaHCO_3$ [mol/kg]	Alkalinity [mol/kg]
mg1311-A	7.95	0.1	4.143E-04	1.71E-04	0	0.01	0.0992
mg1411-A	8.04	0.1	8.321E-04	1.36E-04	0	0.01	0.0998
mg1203-A	8.2	0.1	7.380E-03	0	0	0.02	0.0199
mg1303-B	8.51	0.1	8.775E-03	0	0	0.02	0.0202
mg1403-B	8.34	0.1	1.292E-02	0	0	0.02	0.0198
mg0503-A	8.24	0.1	2.657E-03	0	0	0.02	0.0201
mg1803-A	8.55	0.1	1.809E-03	0	1.90E-03	0.06	0.0607
mg0204-A	8.24	0.1	4.129E-03	0	0	0.02	0.0198
mg0204-B	8.27	0.1	2.590E-03	0	0	0.02	0.0198
mg1004-A	8.21	0.1	5.166E-03	0	0	0.02	0.0207
mg1104-B	8.27	0.1	1.302E-03	0	0	0.02	0.0202
mg2104-A	7.92	0.1	4.414E-04	7.41E-04	0	0.02	0.0191
mg2104-B	7.92	0.1	6.383E-04	6.95E-04	0	0.02	0.0189
mg2904-B	8.26	0.1	2.613E-03	0	0	0.01	0.0098
mg2904-A	8.31	0.1	7.256E-04	0	0	0.04	0.0404
mg0205-A	8.24	0.1	2.595E-03	0	0	0.01	0.0098
mg0205-B	8.32	0.1	7.228E-04	0	0	0.04	0.0391
mg0205-C	8.88	0.1	2.494E-04	0	4.20E-03	0.06	0.0626
mg1505-C	8.76	0.1	2.227E-04	0	3.40E-03	0.06	0.0639
mg1505-A	8.08	0.1	2.616E-03	1.22E-04	0	0.01	0.0098
mg1605-A	8.08	0.1	2.616E-03	1.22E-04	0	0.01	0.0098
mg1605-B	8.31	0.1	6.385E-04	0	0	0.035	0.0347
mg2005-A	8.28	0.1	6.660E-04	0	0	0.035	0.0351
mg2005-B	8.28	0.1	5.573E-04	0	0	0.033	0.0330
mg2205-A	8.33	0.1	6.654E-04	0	0	0.035	0.0338
mg2205-B	8.33	0.1	5.561E-04	0	0	0.033	0.0319
mg2205-C	8.34	0.1	5.016E-04	0	0	0.03	0.0304
mg0306-A	8.35	0.1	4.660E-04	0	0	0.0275	0.0270
mg0306-B	8.35	0.1	3.972E-04	0	0	0.024	0.0241
mg0306-C	8.37	0.1	3.258E-04	0	0	0.02	0.0201
mg1306-A	8.05	0.1	2.356E-03	2.14E-04	0	0.01	0.0097
mg1406-B	8.37	0.1	5.077E-04	0	0	0.029	0.0293
mg1606-A	8.01	0.1	2.357E-03	2.14E-04	0	0.01	0.0097
mg1606-B	8.35	0.1	5.187E-04	0	0	0.029	0.0288
mg1606-C	8.79	0.1	1.440E-04	0	2.90E-03	0.06	0.0614
mg1706-A	8.36	0.1	4.277E-04	0	0	0.0275	0.0268
mg1706-B	8.34	0.1	4.048E-04	0	0	0.024	0.0242

AFM experiments were conducted using a self-constructed hydrothermal atomic force microscope (HAFM) working in contact mode (cf. Higgins et al., 1998), which allows a continuous flow of solution to interact with the solid substrate. The instrument can be pressurized enabling the investigation of the solid-liquid interface at temperatures above 100 °C. The magnesite crystals were mechanically fixed within the HAFM fluid cell using a titanium wire. After fixing the sample and sealing the cell, fluid flow of the prepared

aqueous solution through the cell (volume approximately 500 µl) was established at a constant rate of 10-25 µl/s. Experiments were run at temperatures from 80 to 120 °C, and at pressures ranging from 1 to 2.5 bar.

Magnesite growth rates can be derived from the HAFM image sequences by measuring speeds and densities of step advancement normalized to the scan field area. Alternatively, growth rates can be determined by measuring the frequency of steps passing a fixed reference point on the mineral surface. This latter method is equivalent to measuring the formation frequency of elementary layers at a given position on the surface per unit time (Higgins et al., 2002; Pina and Jordan, 2009). In the present study this latter method was adopted and magnesite growth rates (***r***) were obtained from the product of the measured steady-state frequencies I and the elementary layer thickness h (equal to $d_{(104)}$ = 2.74 Å) divided by the magnesite molar volume V_M (28.1 cm^3/mol) in accord with:

$$\boldsymbol{r} = I \cdot h / V_M \tag{8}$$

Note that as h and V_M are constants, I varies with the saturation state in accord with

$$I = \frac{\boldsymbol{k} V_M}{h} (\Omega - 1)^{\boldsymbol{n}} \tag{9}$$

The use of Eqn. (8) to derive precipitation rates implies that the effective area over which I was measured is representative of the entire magnesite surface. If so, ***r*** obtained from AFM analysis is directly comparable to macroscopic rates obtained by solution chemistry analysis from mixed-flow reactor experiments (see below). Although the HAFM cell is a single pass flow reactor, magnesite precipitation rates could not be obtained from the difference between the inlet and outlet fluid composition; due to the small surface area of crystals this compositional difference lies within the range of analytical error.

3.2 Mixed-Flow Reactor experiments

Macroscopic magnesite growth experiments were performed in titanium mixed-flow reactors in the presence of synthetic magnesite seed crystals. Magnesite seed crystals were synthesized in rocking autoclaves at 250 °C and a CO_2 partial pressure of 50 bar starting from analytical grade hydromagnesite. Three different samples of synthetic magnesite powders

were used in these experiments, for which both BET and geometric surface area were determined. Geometric surface area was obtained from granulometric analysis assuming all grains were rhombohedral in shape, whereas the BET specific surface was measured by multipoint krypton adsorption according to the BET method (Brunauer et al., 1938). Values of BET and geometric surface areas are reported in Table 2 for corresponding experiments.

Application of mixed flow reactors to measure mineral dissolution rates have been described in detail by Dove and Crerar (1990), Berger et al. (1994), and Oelkers and Schott (1995, 1999). A Gilson high precision/high pressure liquid chromatography pump provided continuous fluid flow ranging from 0.6 to 4 g/min during the experiments. The precision of the fluid flow rates was ± 4 percent. The volume of the titanium reactor was 300 ml. The solution within the reactor was mixed by a Paar magnetically driven stirrer and kept at a constant temperature using a Paar furnace. The elevated pressure was maintained using a back pressure regulator. A solid contact pH electrode coupled to a Na-selective glass reference electrode was mounted within the reactor to measure the pH *in situ* and to monitor the saturation state of solution during the experiments. A detailed description of the electrode system is provided by Saldi (2009).

Table 2. Macroscopic magnesite growth rates (r_{MFR}) determined by mixed-flow reactor experiments at 100 °C. Growth measurements were performed in the presence of synthetic magnesite seeds. Rates are normalized to their geometric surface area (see text for description).

Run n.	Ω	pH	$NaHCO_3$ [mol/kg]	Alkal. [mol/kg]	BET s. area [cm^2/g]	geom. s. area [cm^2/g]	$MgCO_3$ mass [g]	inlet [Mg] [mol/kg]	outlet [Mg] [mol/kg]	Fluid Flow Rate [g/min]	r_{MFR} [mol/cm^2/s]
1-1	30.0	7.63	0.02	1.79E-02	1723	643	1.753	8.28E-04	7.76E-04	0.602	4.61E-13
2-1	32.9	7.65	0.02	1.87E-02	1723	643	1.753	8.43E-04	7.85E-04	1.197	1.03E-12
2-2	34.5	7.67	0.02	1.87E-02	1723	643	1.753	8.43E-04	7.89E-04	1.689	1.36E-12
2-3	39.8	7.73	0.02	1.87E-02	1723	643	1.753	8.43E-04	8.01E-04	2.378	1.49E-12
2-4	39.1	7.72	0.02	1.87E-02	1723	643	1.753	8.43E-04	8.10E-04	3.367	1.65E-12
3-1	33.3	7.70	0.02	1.85E-02	2007	669	2.825	8.63E-04	7.20E-04	0.597	7.56E-13
3-2	43.8	7.81	0.02	1.86E-02	2007	669	2.825	8.63E-04	7.53E-04	0.984	6.42E-13
3-3	33.9	7.67	0.02	1.86E-02	2007	669	2.825	8.29E-04	7.80E-04	1.481	6.33E-13
3-4	38.5	7.73	0.02	1.86E-02	2007	669	2.825	8.29E-04	7.79E-04	2.156	9.37E-13
4-1	25.1	7.98	0.02	1.95E-02	2007	669	1.599	3.85E-04	2.92E-04	0.491	7.13E-13
4-2	31.2	8.03	0.02	1.96E-02	2007	669	2.825	3.85E-04	3.27E-04	1.085	9.84E-13
4-3	20.1	8.12	0.02	1.99E-02	2007	669	2.825	2.32E-04	1.77E-04	0.396	3.41E-13
4-4	23.9	8.12	0.02	1.99E-02	2007	669	2.825	2.32E-04	2.09E-04	0.987	3.61E-13
6-2	26.5	8.41	0.06	6.19E-02	1791	844	1.780	1.19E-04	7.39E-05	1.107	5.51E-13

Mixed-flow experiments were run in series; each series consisted of several different experiments performed on a single magnesite powder. Each experimental series is noted by a distinct prefix on the experiment numbers listed in Table 2. At the beginning of each experimental series the reactor was dismantled at ambient conditions. A specific mass of synthetic magnesite was placed in the reactor. The reactor was filled with the first solution, closed, and placed in the furnace. Temperature, pressure, flow, and stirring rate were adjusted to desired settings. Fluid flow rates and outlet solution compositions were measured regularly. Steady-state outlet concentrations were obtained after an elapsed time ranging from 7 hours to 3 days, depending on the flow rate. Steady-state was verified with a minimum of three constant Mg concentrations of the outlet fluid samples taken over several residence times[1]. Finally, after all data at a given set of conditions had been obtained, inlet fluid composition, and/or fluid flow rate were changed to the next desired experimental conditions.

4. Results

4.1 Step morphology

An example of magnesite growth observed by AFM is presented in Figure 1. The magnesite surface consists of 2.7 Å high monomolecular steps separated by atomically flat terraces. Magnesite growth proceeds by the propagation of these steps. The step advancement rate is nonequivalent for opposing obtuse steps G_o and acute steps G_a (Fig. 2), which are approximately parallel to the $[48\bar{1}]$ and $[\bar{4}41]$ directions. At the conditions of the experiments performed in the present study, step advancement at obtuse steps is by far faster than at acute steps. A similar rate anisotropy has been reported for magnesite dissolution by Jordan et al. (2001). The contrasting growth behavior of acute and obtuse steps has been related to the crystal structure and reflects the different geometry and coordination of kink-sites where the incorporation of growth units takes place (Staudt, 1994; Paquette and Reeder, 1995; Reeder, 1996).

[1] The residence time is defined as the volume of the reactor divided by the reactive fluid flow rate.

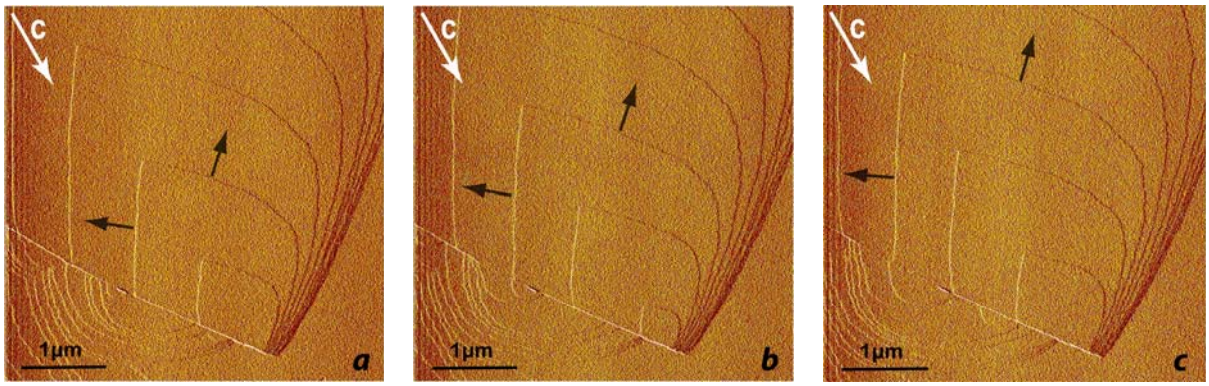

Figure 1. HAFM images of a growing magnesite surface at 80 °C and a saturation index (Ω) of 208. A hillock can be seen nucleating at a macrostep on the magnesite surface. The three images were taken in sequence at 202 seconds from each other. During that time frame a new magnesite monolayer is generated. The black arrows indicate the directions of the two obtuse steps advancing at a faster rate; the white arrow represents the projection of the c-axis which enters downward into the plan of the page.

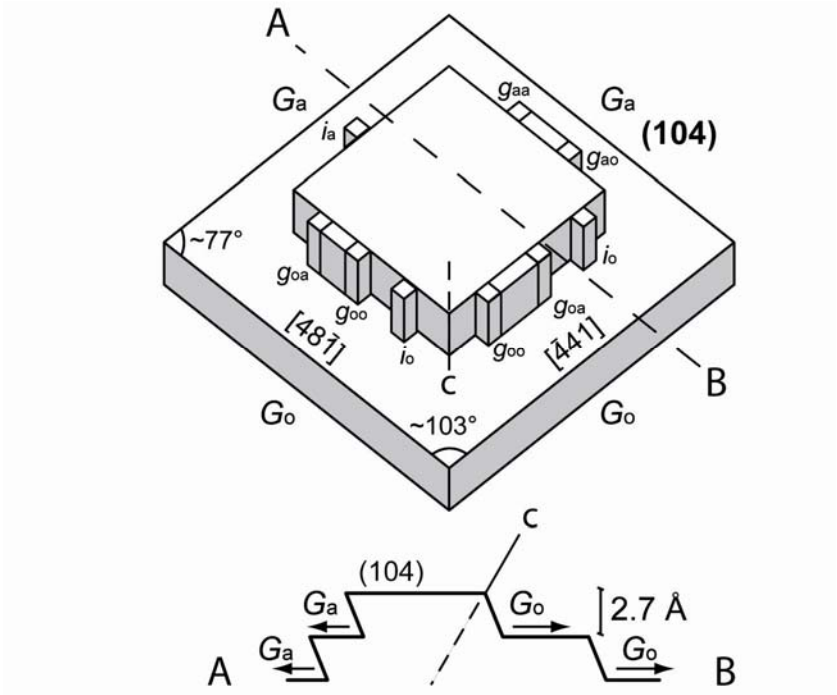

Figure 2. Sketches of a magnesite growth hillock on the (104) surface. Abbreviations: *G* = step; g = kink site; i = kink-nucleation site; o = obtuse; a = acute; *c* = [001]. Obtuse and acute monolayer steps are formed as a result of crystal symmetry, with obtuse steps (G_o) advancing at a rate which is roughly one order of magnitude higher than that of acute steps (G_a). The angle between the step riser of acute and obtuse step and the underlying terrace is of ~ 68° and ~ 112° respectively.

4.2 Step generation

As a consequence of the step rate anisotropy, the step density at the acute step side of growth hillocks is in cases so high that individual steps could not be resolved by the AFM tip. In these cases, it cannot be determined whether the steps form closed circles or a spiral around the step source, i.e. whether edge dislocations or screw dislocations generate the observed steps. Where individual steps were resolved, a spiral growth mechanism was detected. An example of a spiral is shown in Figure 4. The observed growth spirals appeared to be

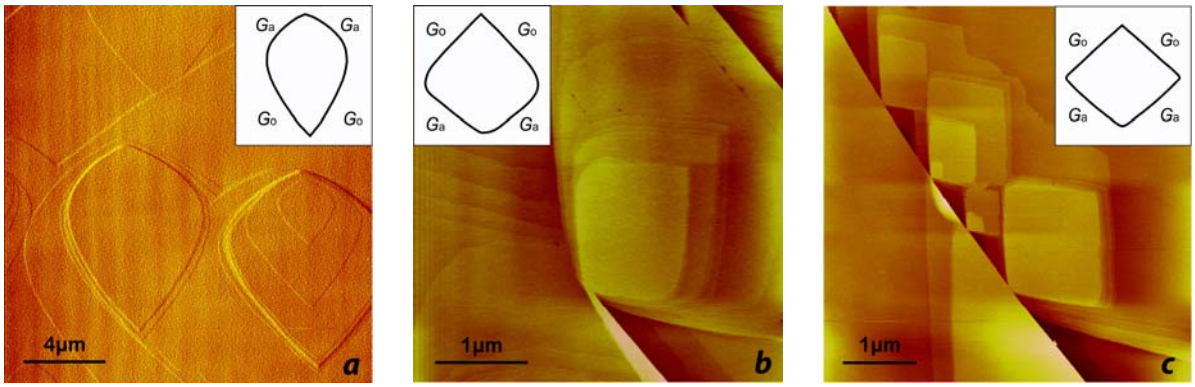

Figure 3. A series of HAFM images showing the effect of supersaturation state and temperature on the shape of growth islands and relative orientation of steps on the magnesite (104) surface. The temperature and supersaturation state of the three experiments shown in this figure are: a) Ω = 382.6, T = 80 °C; b) Ω = 59.5, T = 100 °C; d) Ω = 27.4, T = 85 °C.

associated with large cleavage steps on the magnesite surface such as shown in Figure 5. Thus either the screw dislocations were induced by cleaving or the cleavage was following pre-existing defects. At the lowest temperature and supersaturation considered (mg1311-A and mg1411-A), spiral growth was not observed within the time frame of experiments. At the highest temperatures and degrees of supersaturation (mg1303-B and mg2904-A) generation of steps via random two-dimensional nucleation was observed. At such conditions, growth rates were very fast relative to the scan rate. As a consequence, most AFM images taken at these conditions were distorted and reference points between successive images were not evident. Both factors precluded the quantification of rates at these conditions.

4.3 Layer formation frequencies and step advancement rates

Spiral growth induces a layer formation at a point on the surface. Layer formation frequencies and step advancement rates were obtained from AFM images sequences. The results are listed in Table 3 and the layer formation frequencies are plotted as a function of saturation state in Figure 6. Despite the scatter, these frequencies increase systematically with increasing saturation state. The curve through these data represent a regression of the 100° C rates with Eqn. (5) and $\boldsymbol{n} = 2$. The scatter of the data reflects the variable nature of the step generation process and precludes quantitative assessment of the temperature dependence of layer generation frequencies.

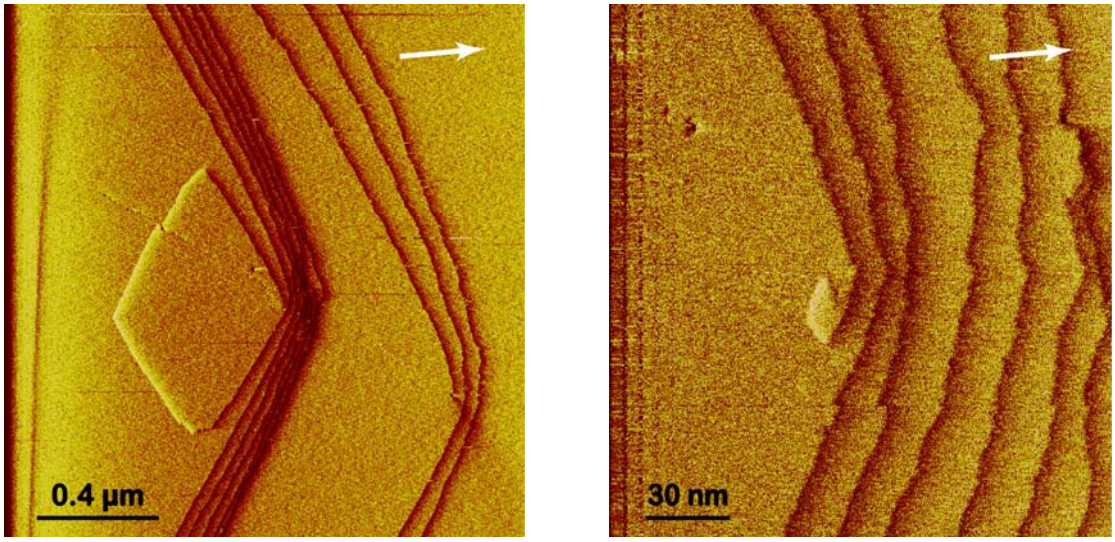

Figure 4. HAFM image showing spiral growth lead by screw dislocations on a growing magnesite surface. The image on the right is the detail of one of the centre of nucleation of the image on the left. Experimental conditions: T = 100 °C, Ω = 47.3. White arrows represent the projection of the c-axis which enters downward into the plane of the page.

Magnesite obtuse step advancement rates are plotted as a function of saturation state in Figure 7a, c, and d. The ± uncertainties on the step advancement rates listed in table 3 correspond to the standard deviation of ~12 measured rates at each temperature. One temperature and saturation state condition was reproduced (Experiments mg1505-A and mg1506-A); step advancement rates of the reproduced experiment matched within uncertainty that obtained from the original. Velocities obtained at constant temperature/constant reactive fluid Mg^{2+}/CO_3^{2-}activity ratio rates appear to increase linearly with saturation state. This

observation is in close agreement with crystal growth theory (Burton et al., 1951; Chernov, 1961) and with the results of several experimental growth studies (e.g. Gratz et al., 1993; Higgins et al., 2000; Teng et al., 2000). The curves in Fig. 7a correspond to linear fits of obtuse step advancement rates obtained at 90, 95 and 100 °C in solutions having a Mg^{2+}/CO_3^{2-} activity ratio of 0.7. However, the linear correlations do not pass through the origin. The slopes of these linear regressions are plotted as a function of reciprocal temperature in Fig. 7b and reveal an Arrhenius behavior, which yields an activation energy of 159±17 kJ/mol. An extrapolation of these slopes to 80 and 85 ºC is shown in this figure. The 80 ºC slope is shown to be consistent with the corresponding step velocity data as shown in Figure 7c.

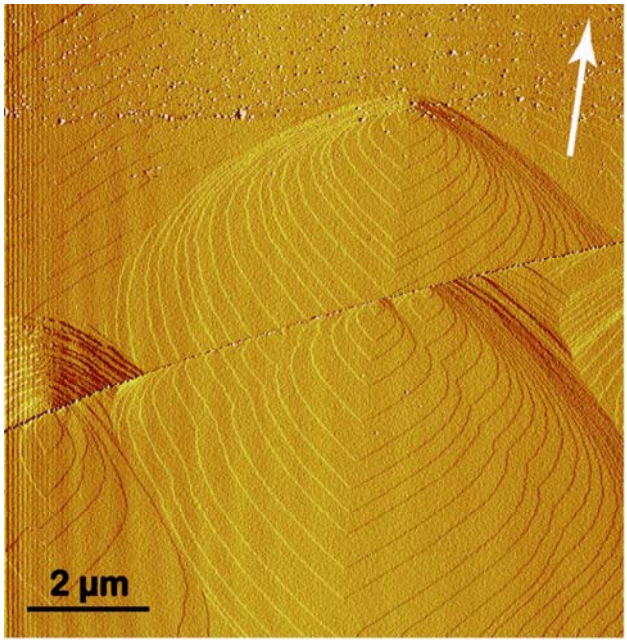

Figure 5. HAFM image of magnesite monolayers in close proximity of macrosteps on a growing magnesite (104) surface at 105 °C and Ω =134. The white arrow indicates the orientation of the c-axis which enters downward into the plane of the page.

The variation of obtuse step advancement rates with the aqueous Mg^{2+}/CO_3^{2-}activity ratio of the reactive fluid can be assessed with the aid of Fig 7d. No clear effect of this activity ratio on the step advancement rates is apparent. The deviation of some Mg-rich solutions from the quasi-stoichimetric line, reported on the plot for a Mg^{2+}/CO_3^{2-}activity ratio of ~0.7, is small and within the uncertainty of the experimental measurements. At supersaturation higher than 95, data dispersion precludes assessment of any possible effect of Mg^{2+}/CO_3^{2-}activity ratio of the step advancement rates.

Fewer acute step advancement rates were measurable due to their relatively slow velocity. Measured acute step advancement rates are plotted as a function of their corresponding obtuse step velocities in Fig. 8. Although there is some scatter visible in this figure, acute step advancement rates are found to be on average 11.8 times slower than corresponding obtuse step advancement rates.

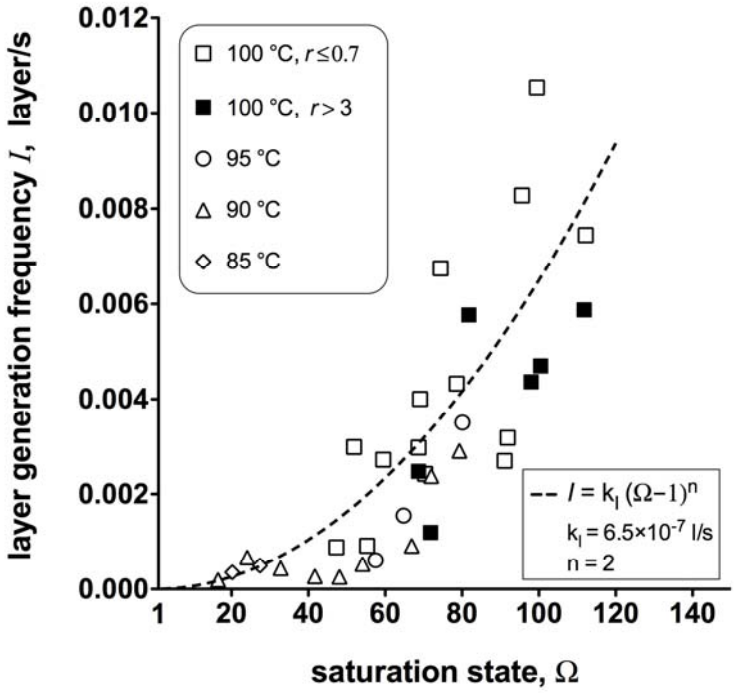

Figure 6. Dependence of the layer generation frequency *I* on the saturation state Ω, between 85 and 100 °C. The dashed line drawn through the symbols represent an exponential function describing the dependence of monolayer formation frequencies on Ω at 100°C. The frequency of generation of new layers is consistent with a parabolic dependence on the saturation index (***n*** = 2). For such a type of function the kinetic constant k_l is found to vary between 4×10^{-7} and 9×10^{-7} l/s ; on the plot an average value of 6.5×10^{-7} l/s has been considered.

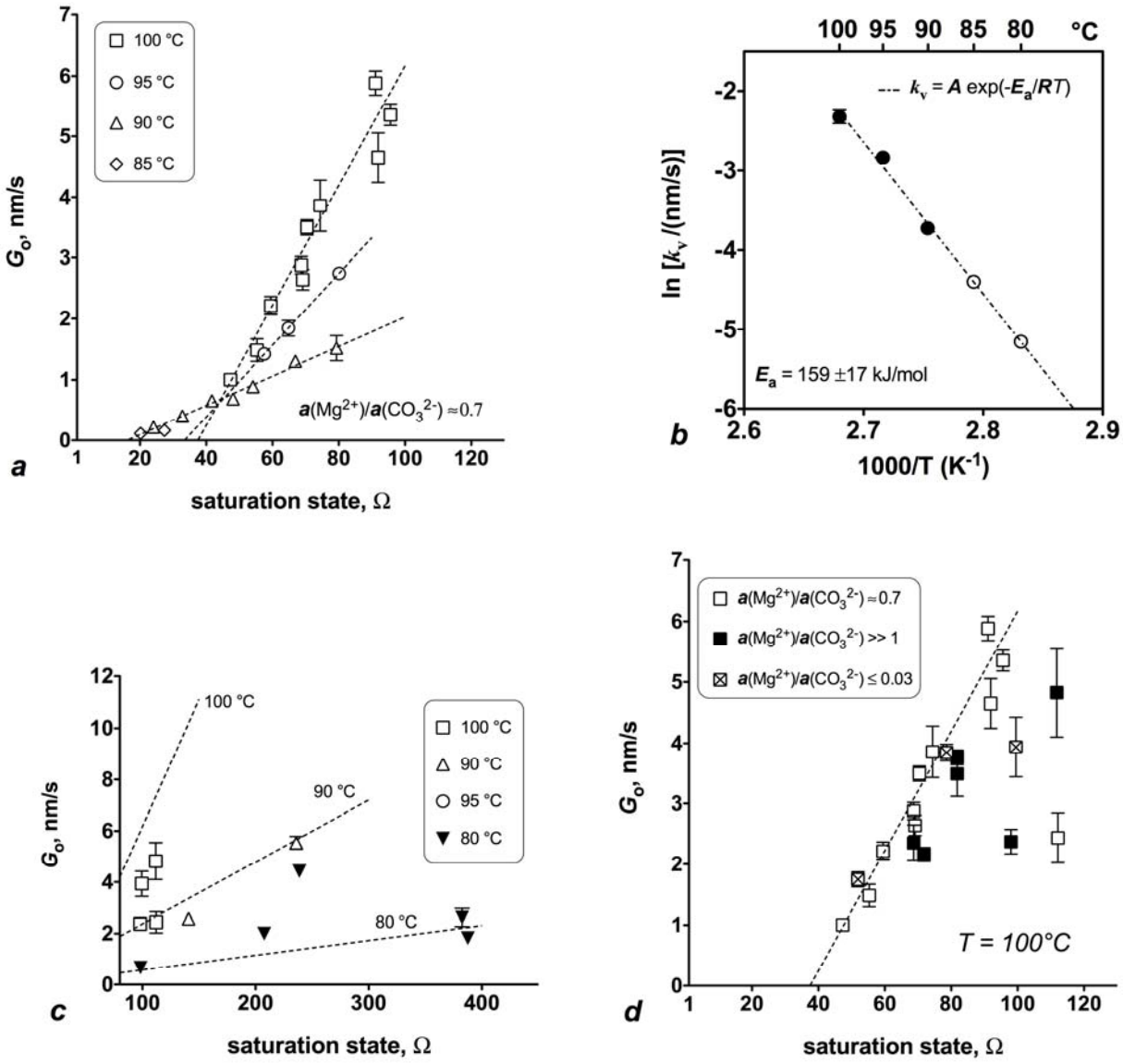

Figure 7. a) Dependence of obtuse step advancement rates (G_o) as a function of saturation state (Ω) at various T for a Mg^{2+}/CO_3^{2-} ion activity ratio of ~ 0.7. Measured step advancement rates are fitted with linear correlations for T = 90, 95 and 100 °C. **b)** The apparent kinetic constants, equal to the slope of the lines in (a), are represented in an Arrhenius plot yielding an apparent activation energy E_a of 159 kJ/mol. **c)** obtuse step advancement rates measured at Ω > 80. Dashed lines represent the linear fits of fig. a) extrapolated at higher supersaturations (90 and 100 °C) and the linear fit of data at 80°C consistent with the activation energy previously determined. **d)** obtuse step advancement rates at 100 °C plotted against Ω for different values of Mg^{2+}/CO_3^{2-} ion activity ratio.

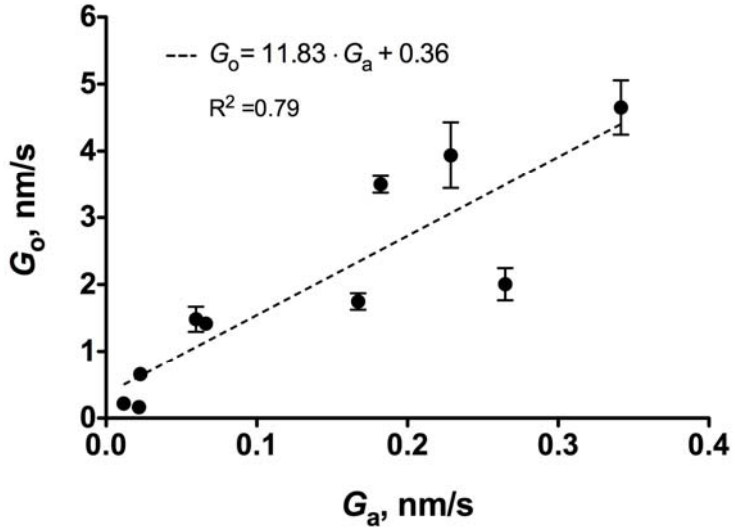

Figure 8. Relation between obtuse (G_o) and acute (G_a) step velocities on the (104) surface. Obtuse steps advancement rates are roughly twelve times faster than acute steps.

4.4 Bulk magnesite precipitation rates from mixed-flow reactor experiments

Magnesite precipitation rates obtained from mixed-flow reactors and normalized to the geometric surface area are listed in Table 2. The logarithm of these rates is depicted as a function of log (Ω-1) in Fig. 9 together with corresponding rates obtained from layer formation frequencies using Eqn. (8). A linear fit of both datasets shows the rates obtained with the two experimental methods are in close agreement and consistent with a slope equal to 2. The slope of this regression line is thus consistent with magnesite precipitation being dominated by a spiral growth mechanism.

5. Discussion

5.1 Magnesite growth mechanisms

The results presented above suggest that magnesite growth at T = 80-120 °C and Ω = ~20-100 is dominated by a spiral growth mechanism. This mechanism is supported by AFM observations revealing active spiral growth and by the observation that both AFM rates and mixed-flow reactor rates are proportional to $(\Omega\text{-}1)^2$. This behavior is similar to that observed on calcite at 25 °C as reported by Gratz et al. (1993), Dove and Hochella (1993), and Teng et

al. (1999, 2000). As mentioned above owing to the high step density of acute steps, growth spirals could not always be identified by AFM. Nevertheless, the variation of magnesite precipitation rates with saturation state is consistent with the dominance of a spiral growth mechanism (see below).

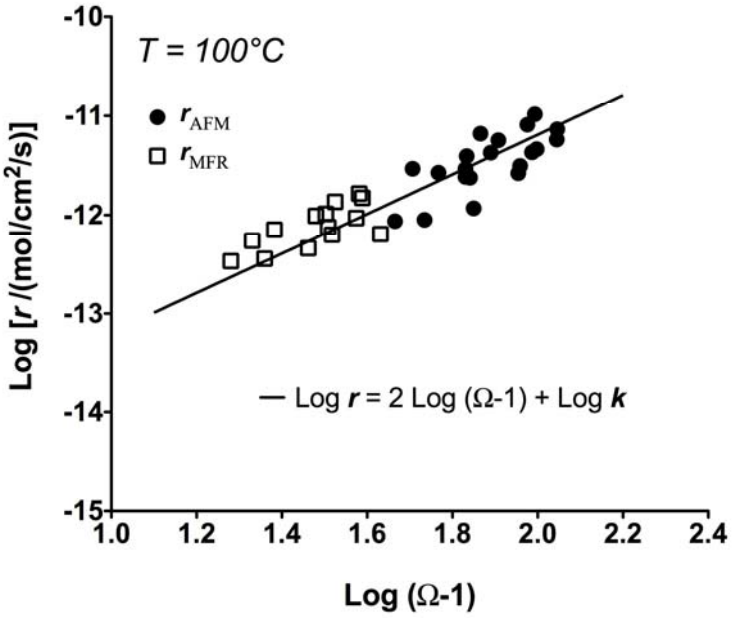

Figure 9. Comparison between microscopic growth rates (r_{AFM}) and macroscopic growth rates (r_{MFR}), determined by mixed-flow reactor solution analysis, at 100°C. Microscopic and macroscopic overall growth rates are in good agreement and consistent with an order of reaction n = 2 and an apparent kinetic constant k of~ 6.5×10^{-16} mol/cm^2/s, according to the rate equation: $r = k\,(\Omega\text{-}1)^n$.

In contrast to the measured precipitation rates, which closely match crystal growth theory, step advance rates as shown in Fig. 7a are consistent with $G_o \propto (\Omega\text{-}1)$ only above a certain saturation state; linear correlations between G_o and (Ω-1) intersect the abscissa at Ω > 1 (see Fig. 7a). The non-linear behavior below the threshold supersaturation has been attributed to either a supersaturation dependent kink density at the step edges (e.g., Chernov and Rashkovich, 1987; Higgins et al., 2000) or to the presence of trace impurities in the reactive fluid consistent with Eqn. (6) (Teng et al., 1999; Davis et al., 2000; Wasylenki et al., 2005). The first effect, the saturation dependent kink density, might be favored by the strong Mg-O bond energy (c.f., Georgiou and Vekilov, 2006; Vekilov, 2007). The second effect, the influences of minute impurities, might be favored by the presence of impurities in the present

study. Analysis before and after AFM experiments revealed the presence of as much as 1 ppm of Ca in addition to the 0.1 M of NaCl background electrolyte. Such impurities could affect step velocities through their adsorption onto the mineral surface slowing step movement (Cabrera and Vermileya, 1958; Voronkov and Rashkovich, 1992; Potapenko, 1993; Kubota and Mullin, 1995; van Enckevort and van den Berg, 1998). However, the degree to which the presence of these dissolved species affected magnesite step velocities is still unclear.

5.2 What inhibits magnesite precipitation at 25° C?

As mentioned in the introduction, many minerals, including magnesite appear to be unable to precipitate at low temperatures. In the Mg-CO_3-H_2O system, metastable hydrous Mg-carbonates, such as nesquehonite ($MgCO_3 \cdot 3H_2O$) and hydromagnesite [$(MgCO_3)_4 \cdot Mg(OH)_2 \cdot 4H_2O$] rather than the more stable magnesite are observed to precipitate. Insight into factors limiting magnesite precipitation and growth at low temperatures can be obtained from the results presented above.

Bulk magnesite precipitation rates are found to match closely the precipitation rates derived from layer formation frequencies obtained by AFM. At 100° C and pH ≈ 8 these rates are consistent with Eqn. (5), $\boldsymbol{n} = 2$ and $\boldsymbol{k} = 6.5 \times 10^{-16}$ mol/cm^2/s leading to a precipitation rate of 5.3×10^{-14} mol/cm^2/s at $\Omega = 10$. Saldi (2009) reported the activation energy of magnesite precipitation from bulk magnesite precipitation experiments at 100-200 °C to be 64 kJ/mol. Taking into account this activation energy, a rate constant ($\boldsymbol{k}$) of 4.1×10^{-18} mol/cm^2/s would be found for 25 °C. This value is 6 orders of magnitude less than the respective value for calcite and leads to a magnesite growth rate of 3.3×10^{-16} mol/cm^2/s at $\Omega = 10$. At this rate it would take approximately 340,000 years to precipitate a 1 mm layer of magnesite.

Although this estimated magnesite growth rate is slow, the AFM observations presented above suggest that magnesite precipitation rates at 25 °C may be even lower than this estimate. From the linear range of obtuse step advancement rates at 100 °C and Eqn. (6) a value for $\boldsymbol{k_v}$ of 9.9×10^{-9}cm/s is found. The activation energy for this reaction is relatively high and equals 159 kJ/mol. This activation energy suggests that step advancement rates slow faster with decreasing temperature than spiral growth step generation. As pointed out by Pina et al. (1998) step generation at screw dislocations could be limited by an ever tightening spiral

due to decreasing step advancement rates. Taking into account the activation energy for obtuse step advancement, one can estimate k_v = 2.7x10^{-14}cm/s at 25 °C. Assuming $G_o/G_a \approx$ 12 is temperature independent, one obtains $k_v \approx$ 2.2 x10^{-15} cm/s for acute step advancement at 25 °C. These k_v values suggest that obtuse and acute steps will advance at most 2.4x10^{-13} and 2.0 x10^{-14} cm/s, respectively, at Ω = 10 and 25 °C. Teng et al. (1998) derived the critical length required for a step to rotate around a screw dislocation from AFM observations on calcite as a function of fluid saturation state. The authors found a critical length of ~10 nm at Ω = 10 and 25° C. Using this value for magnesite and bearing in mind the problems of such a procedure (Higgins and Hu, 2006), it would take ~1.5 years for the acute steps to advance 10 nm, effectively arresting the magnesite spiral growth/step advancement mechanism.

Table 3. Summary of the physico-chemical parameters of all magnesite HAFM growth experiments performed in the present study. Reported parameters include step velocities (G_o), layer generation frequencies (I) and calculated microscopic growth rates (r_{AFM}). Ion activities listed in this table were calculated from solution chemistry data provided in Table 1 using PHREEQC (Pakhurst and Appelo, 1999) together with its llnl thermodynamic database.

Exp. Sol.	T (°C)	Ω	pH	$a_{Mg^{2+}}$	$a_{CO_3^{2-}}$	$\frac{a_{Mg^{2+}}}{a_{CO_3^{2-}}}$	I [layer/s]	G_o [nm/s]	r_{AFM} [mol/cm^2/s]
mg1311-A	80	6.0	7.78	1.452E-04	3.459E-05	4.19	n.d.[1]	n.d.[1]	n.d.[1]
mg1411-A	80	13.5	7.83	2.897E-04	3.899E-05	7.43	n.d.[1]	n.d.[1]	n.d.[1]
mg0503-A	80	98.3	7.96	8.151E-04	1.009E-04	8.08	n.d.[2]	0.67±0.04	n.d.[2]
mg1203-A	80	207.7	7.87	2.274E-03	7.645E-05	29.74	1.59E-03	2.00±0.24	1.56E-12
mg1803-A	80	238.7	8.26	3.525E-04	5.669E-04	0.62	9.79E-03	4.42 ±0.20	9.61E-12
mg1403-B	80	382.6	7.93	3.905E-03	8.200E-05	47.62	1.30E-03	2.62±0.35	1.28E-12
mg1303-B	80	387.6	8.10	2.607E-03	1.244E-04	20.96	n.d.[2]	1.83±0.11	n.d.[2]
mg0306-C	85	20.2	8.10	9.530E-05	1.425E-04	0.67	3.53E-04	0.11±0.02	3.46E-13
mg0306-B	85	27.4	8.09	1.113E-04	1.657E-04	0.67	4.94E-04	0.16±0.02	4.85E-13
mg2104-A	90	16.5	7.77	1.340E-04	6.663E-05	2.01	1.95E-04	0.23±0.02	1.92E-13
mg2104-B	90	23.4	7.77	1.942E-04	6.512E-05	2.98	n.d.[2]	0.38±0.02	n.d.[2]
mg0306-C	90	24.1	8.09	9.268E-05	1.410E-04	0.66	6.70E-04	0.22±0.01	6.58E-13
mg0306-B	90	32.8	8.08	1.080E-04	1.643E-04	0.66	4.41E-04	0.40±0.02	4.33E-13
mg0306-A	90	41.7	8.08	1.226E-04	1.840E-04	0.67	2.67E-04	0.66±0.05	2.62E-13
mg2205-C	90	48.1	8.07	1.273E-04	2.044E-04	0.62	2.59E-04	0.69±0.07	2.54E-13
mg2205-B	90	54.1	8.07	1.393E-04	2.103E-04	0.66	5.29E-04	0.89±0.05	5.19E-13
mg2205-A	90	66.9	8.06	1.635E-04	2.216E-04	0.74	9.17E-04	1.30±0.07	9.00E-13
mg2904-B	90	72.0	7.91	8.640E-04	4.510E-05	19.16	2.38E-03	0.77±0.10	2.34E-12
mg2904-A	90	79.3	8.05	1.679E-04	2.556E-04	0.66	2.91E-03	1.52±0.21	2.85E-12
mg0204-B	90	140.8	7.96	7.579E-04	1.005E-04	7.54	n.d.[2]	2.57±0.17	n.d.[2]
mg1004-A	90	236.0	7.87	1.510E-03	8.455E-05	17.86	1.44E-02	5.54±0.25	1.41E-11
mg2205-C	95	57.5	8.07	1.229E-04	2.029E-04	0.61	6.10E-04	1.42±0.06	5.99E-13
mg2205-B	95	64.8	8.06	1.344E-04	2.089E-04	0.64	1.55E-03	1.84±0.13	1.52E-12
mg2205-A	95	80.1	8.06	1.576E-04	2.201E-04	0.72	3.51E-03	2.75±0.07	3.44E-12
mg0204-A	95	235.6	7.90	1.184E-03	8.624E-05	13.73	n.d.[3]	3.98±0.88	n.d.[3]
mg1706-B	100	47.3	8.06	1.031E-04	1.587E-04	0.65	8.85E-04	1.00±0.04	8.69E-13
mg1606-C	100	51.9	8.46	1.965E-05	9.139E-04	0.02	2.99E-03	1.75±0.12	2.94E-12
mg1706-A	100	55.3	8.08	1.049E-04	1.824E-04	0.57	9.14E-04	1.48±0.19	8.97E-13
mg0306-A	100	59.5	8.07	1.143E-04	1.803E-04	0.63	2.72E-03	2.22±0.15	2.67E-12
mg2205-C	100	68.7	8.07	1.183E-04	2.010E-04	0.59	2.98E-03	2.88±0.14	2.93E-12
mg1606-A	100	68.7	7.75	7.582E-04	3.138E-05	24.17	2.48E-03	2.35±0.30	2.43E-12
mg1606-B	100	69.1	8.07	1.245E-04	1.921E-04	0.65	4.01E-03	2.64±0.17	3.93E-12
mg1406-B	100	70.4	8.08	1.205E-04	2.022E-04	0.60	2.43E-03	3.50±0.13	2.38E-12
mg1306-A	100	71.8	7.77	7.563E-04	3.286E-05	23.01	1.20E-03	2.16±0.11	1.17E-12
mg2005-B	100	74.4	8.02	1.295E-04	1.988E-04	0.65	6.75E-03	3.86±0.42	6.63E-12
mg1505-C	100	78.6	8.43	3.036E-05	8.960E-04	0.03	4.33E-03	3.85±0.14	4.25E-12
mg1505-A	100	81.8	7.78	8.373E-04	3.385E-05	24.74	5.77E-03	3.49±0.37	5.67E-12
mg1605-A	100	81.8	7.78	8.373E-04	3.385E-05	24.74	n.d.[2]	3.77±0.12	n.d.[2]
mg1605-B	100	91.1	8.04	1.447E-04	2.179E-04	0.66	2.70E-03	5.89±0.20	2.65E-12
mg2005-A	100	91.9	8.02	1.514E-04	2.101E-04	0.72	3.19E-03	4.65±0.41	3.13E-12
mg2205-A	100	95.6	8.06	1.516E-04	2.183E-04	0.69	8.28E-03	5.35±017	8.13E-12
mg0205-A	100	98.0	7.87	8.232E-04	4.121E-05	19.98	4.37E-03	2.37±0.20	4.29E-12

Exp. Sol.	T (°C)	Ω	pH	$a_{Mg^{2+}}$	$a_{CO_3^{2-}}$	$\frac{a_{Mg^{2+}}}{a_{CO_3^{2-}}}$	I [layer/s]	G_o [nm/s]	r_{AFM} [mol/cm^2/s]
mg0205-C	100	99.5	8.54	3.149E-05	1.094E-03	0.03	1.05E-02	3.94±0.49	1.04E-11
mg2904-B	100	100.48	7.88	8.281E-04	4.201E-05	19.71	4.70E-03	n.d.[2]	4.62E-12
mg1104-B	100	111.8	7.97	3.565E-04	1.086E-04	3.28	5.88E-03	4.83±0.72	5.77E-12
mg0205-B	100	112.2	8.05	1.559E-04	2.491E-04	0.63	7.45E-03	2.44±0.41	7.32E-12
mg0205-C	105	114.8	8.53	2.972E-05	1.067E-05	0.03	n.d.[2]	n.d.[2]	n.d.[2]
mg2904-A	105	134.4	8.05	1.479E-04	2.506E-04	0.59	1.41E-02	n.d.[3]	1.39E-11
mg1303-B	105	812.8	7.99	2.307E 03	9.616E-5	23.99	n.d.[3]	n.d.[3]	n.d.[3]
mg2904-A	110	158.5	8.05	1.409E-04	2.477E 04	0.57	n.d.[3]	n.d.[3]	n.d.[3]
mg2904-A	120	223.9	8.05	1.262E-04	2.410E-04	0.52	n.d.[3]	n.d.[3]	n.d.[3]

n.d.[1]= not determined for limited scan numbers (step growth and/or layer generation are too slow to be measured; absence of step generation process)
n.d.[2]= not determined for limited observations due unfavorable morphologic conditions or limited number of images.
n.d.[3]= not determined for limited scan rate (i.e. growth rates and/or layer generation are too fast to be quantified).

6. Concluding remarks

The results presented above indicate that magnesite readily precipitates at temperatures from 80 to 120° via a spiral growth mechanism. The interpretation of AFM and mixed flow reactor experiments yields a growth rate equation that can be used to describe the rates as a function of solution saturation state at 100°. Such rates may be used to assess and optimize the mineral sequestration of CO_2 in response to dissolution of magnesium-rich silicate rocks.

Observations suggest that magnesite precipitation at ambient temperature is limited by the slow step propagation, which limits the step generation by spiral growth on the magnesite surface. The activation energy for step propagation is 159 kJ/mol, which is by far larger than that of many other surface reactions such as mineral dissolution. As hydrated magnesium carbonates readily precipitate at ambient temperatures it seems likely that this high activation energy and slow step advancement rates at ambient temperature stems from the slow dehydration rates of aqueous magnesium. It follows that aqueous metal dehydration kinetics may play a critical role in determining if a mineral can precipitate in natural environments at ambient temperature.

Acknowledgements

We would like to thank Casjen Merkel and Nuria Sánchez-Pastor for help and assistance during experiments at HAFM in München. We are also grateful to Chris Pearce, Teresa Roncal-Herrero, Oleg Pokrovsky, Pascale Bénézeth, Jean-Louis Dandurand, Robert Gout, and Stacey Callahan for helpful discussions during the course of this study. Alain Castillo, Jean-Claude Harrichoury and Carole Causserand provided technical assistance during the experimental work in Toulouse. Support from Centre National de la Recherche Scientifique, and the European Community through the MIR Early Stage Training Network (MEST-CT-2005-021120) is gratefully acknowledged. This manuscript benefited from insightful review comments provided by Steven Higgins and José Manuel Astilleros. We thank Chen Zhu for his editorial expertise.

7. References

Aldushin, K., Jordan, G., Aldushina, E. & Schmahl, W.W. (2007) On the kinetics of ion-exchange in phlogopite - an in-situ AFM study. *Clays and Clay Minerals* **55**, 339-347.

Aldushin, K., Jordan, G. & Schmahl, W.W. (2006) Basal plane reactivity of phyllosilicates studied in-situ by hydrothermal atomic force microscopy (HAFM). *Geochim. Cosmochim. Acta.* **70**, 4380-4391.

Arnorsson S.N., Gunnarsson, I., Stefansson, A., and Sveinbjornsdottir A.E. (2002) Major element chemistry of surface and ground waters in basaltic terrain, N-ICeland. I. Primary mineral saturation. *Geochim. Cosmochim. Acta* **66**, 4015-4046.

Astilleros, J. M., Pina, C. M., Fernndez-Diaz, L., and Putnis, A., (2002) Molecular-scale surface processes during the growth of calcite in the presence of manganese. *Geochim. Cosmochim. Acta* **66**, 3177-3189.

Berger G., Cadore E., Schott J., and Dove P.M. (1994) Dissolution rate of quartz in lead and sodium electrolyte solutions between 25 and 300 °C: effect of the nature of surface complexes and reaction affinity. *Geochim. Cosmochim. Acta* **58**, 541-551.

Bjorlykke, K. and Egeberg, P.K. (1993) Quartz cementation in sedimentary basins. *AAPG Bull.* **77**, 1538-1546.

Bosbach, D., Hall, C., and Putnis, A. (1998) Mineral precipitation and dissolution in aqueous solution: in-situ microscopic observations on barite (001) with atomic force microscopy. *Chem. Geo.* **151**, 143-160.

Brandt, F., Bosbach, D., Krawczyk-Barsch, E., Arnold, T., and Bernhard. G. (2003) Chlorite dissolution in the acid pH-range: A combined microscopoc and macroscopic approach. *Geochim. Cosmochim. Acta* **67**, 1451-1461.

Brunauer S., Emmet P. H., and Teller E. (1938) Adsorption of gases in multimolecular layers. *J. Am. Chem. Soc.*, **60**, 309-319.

Burton W. K., Cabrera N., and Frank F. C. (1951) The growth of crystals and the equilibrium structure of their surfaces. *Phil. Trans. Royal Soc. London* **A243**, 299–358.

Cabrera N. and Vermilyea D. A. (1958) The growth of crystals from solution. In *Growth and Perfection of Crystals* (ed. R. H. Doremus, B. W. Roberts, and D. Turnbull), pp. 393–410. John Wiley & Sons.

Chernov A. A. (1961) The spiral growth of crystals. *Soviet Phys. Usp.* **4**, 116–148.

Chernov, A. A. and Rashkovich, L. N. (1987) Spiral crystal growth with nonlinear dependence of step growth rate on supersaturation; the {110} faces of KH2PO4 crystals in aqueous solution. *Journal of Crystal Growth* **84**, 389-393.

Christ C. L. and Hostetler P. B. (1970) Studies in the system MgO-SiO_2-CO_2-H_2O (II): the activity product constant of magnesite. *Am. J. Sci.* **268**, 439-453.

Davis K. J., Dove P. M., and De Joreo J. J. (2000) The role of Mg^{2+} as an impurity in calcite growth. *Science* **290**, 1134-1137.

Dove P.M. and Crerar D.A. (1990) Kinetics of quartz dissolution in electrolyte solution using a hydrothermal mixed flow reactor. *Geochim. Cosmochim. Acta* **54**, 955-969.

Dove, P. M. and Hochella Jr, M. F., (1993) Calcite precipitation mechanisms and inhibition by orthophosphate: In situ observations by Scanning Force Microscopy. *Geochim. Cosmochim. Acta* **57**, 705-714.

Dove P. M. and Rimstidt D. J. (1994) Silica - Water Interactions. *Rev. Min.* **29,** 259-308.

Georgiou, D. K. and Vekilov, P. G. (2006) A fast response mechanism for insulin storage in crystals may involve kink generation by association of 2D clusters. *Proc. Natl. Acad. Sci. U. S. A.* **103**, 1681-1686.

Giammar D.E., Bruant R.G. and Peters, C.A. (2005) Forsterite dissolution and magnesite precipitation at conditions relevent for deep saline aquifer storage and sequestration of carbon-dioxide. *Chem. Geo.* **217,** 257-276.

Gislason, S.R., Arnórsson, S., and Ármannsson, H. (1996) Chemical weathering of basalt in Southwest Iceland: Effects of runoff, age of rocks and vegetative/glacial cover. *Am. J. Sci.* **296,** 837-907.

Gratz A. J., Hillner P. E., and Hansma P. K. (1993) Step dynamics and spiral growth on calcite. *Geochim. Cosmochim. Acta* **57**, 491–495.

Hänchen, M., Prigiobbe, V., Baciocchi, R., and Mazzotti, M. (2008) Precipitation in the Mg-carbonate system – effects of temperature and CO_2 pressure. *Chem. Eng. Sci.,* **63,** 1012-1028.

Higgins S. R., Eggleston C. M., Knauss K. G., and Boro C. O. (1998) A hydrothermal atomic force microscope for imaging in aqueous solution up to 150°C. *Rev. Sci. Instrum.* **69,** 2994–2998.

Higgins S. R., Bosbach D., Eggleston C. M., and Knauss K. (2000) Kink dynamics and step growth on barium sulfate (001): a hydrothermal scanning probe microscopy study. *J. Phys. Chem. B* **104**, 6978-6982.

Higgins, S. R., Jordan, G., and Eggleston, C. M. (2002) Dissolution kinetics of magnesite in acidic aqueous solution: a hydrothermal atomic force microscopy study assessing step kinetics and dissolution flux. *Geochim. Cosmochim. Acta* **66**, 3201-3210.

Higgins S.R. and Hu X. (2006) Near molecular-scale growth of natural minerals: Experimental methods and errors in length-dependent step speeds with scanning probe microscopy. *Journal of Electron Spectroscopy and Related Phenomena* **150**, 235–247.

Jordan, G., Higgins, S. R., Eggleston, C. M., Knauss, K. G., and Schmahl, W. W. (2001) Dissolution kinetics of magnesite in acidic aqueous solution, a hydrothermal atomic force microscopy (HAFM) study: step orientation and kink dynamics. *Geochim. Cosmochim. Acta* **65**, 4257-4266.

Jordan, G., Pokrovsky, O. S., Guichet, X., and Schmahl, W. W. (2007) Organic and inorganic ligand effects on magnesite dissolution at 100 °C and pH = 5 to 10. *Chem. Geo.* **242**, 484-496.

Kaszuba J.P., Janecky, D.R., and Snow, M.G. (2003) Carbon dioxide reaction process in a model brine aquifer at 200º C and 200 bars: Implications for geologic sequestration of carbon. *App. Geochem.,* **18,** 1065-1080.

Kowacz, M., Putnis, C., and Putnis, A. (2007). The effect of cation : anion ratio in solution on the mechanism of barite growth at constant supersaturation: Role of the desolvation process on the growth kinetics. *Geochim. Cosmochim. Acta* **71**, 5168-5179.

Kubota, N. and Mullin, J. W. (1995) A kinetic model for crystal growth from aqueous solution in the presence of impurity. *J. Crystal Growth* **152**, 203-208.

Lippmann F. (1973) Sedimentary Carbonate minerals. Springer-Verlag, pp. 229.

Möller P. (1989) Magnesite: geology, mineralogy, geochemistry, formation of Mg-carbonates. *Monograph series on Mineral Deposits*, n. 28, pp. 300. Gebrüder Borntraeger, Berlin-Stuttgart.

Morse, J.W., Arvidson, R.S. and Luttge, A. (2007) Calcite formation and dissolution. *Chem. Revs.* **107,** 342-381.

Nielsen A. E. (1984) Electrolyte crystal growth mechanism. *J. Crystal Growth* **67**, 289-310.

Oelkers E.H., Bjorkum, P.A., and Murphy W.M. (1996) A petrographic and computational investigation of quartz cementation and porosity reduction in North Sea sandstones. *Am. J. Sci.,* **296,** 420-452.

Oelkers E.H., and Cole D.R. (2008) Carbon dioxide sequestration: A solution to a global problem. *Elements* **4**, 305-310.

Oelkers, E.H., Gislason, S.R., and Matter, J. (2008) Mineral carbonation of CO_2. *Elements* **4**, 333-337.

Oelkers, E. H. and Schott, J. (1995) Experimental study of anorthite dissolution rates and the relative mechanism of feldspar hydrolysis. *Geochim. Cosmochim. Acta* **59**, 5039-5053.

Oelkers, E. H. and Schott, J. (1999) Experimental study of kyanite dissolution rates as a function of chemical affinity and solution composition. *Geochim. Cosmochim. Acta* **63**, 785-797.

Oelkers E.H., Schott J. (2005) Geochemical Aspects of CO_2 Sequestration. *Chem. Geo.* **217,** 183-186.

Ohara M. and Reid R.C. (1973) Modeling crystal growth rates from solution. Prentice Hall, Inc., London, pp. 272.

Paquette, J. and Reeder, R. J. (1995) Relationship between surface structure, growth mechanism, and trace element incorporation in calcite. *Geochim. Cosmochim. Acta* **59**, 735-749.

Parkhurst D. L. and Appelo C. A. J. (1999) User's guide to PHREEQC (version 2) - a computer program for speciation, batch-reaction,one-dimensional transport, and inverse geochemical calculations. U.S. Geological Survey Water-resources Investigation Report 99-4259, pp. 312

Pina, C. M., Fernández-Díaz, L., Prieto, M., and Putnis, A. (2000). In situ atomic force microscope observations of a dissolution-crystallisation reaction: the phosgenite-cerussite transformation. *Geochim. Cosmochim. Acta* **64**, 215-221.

Pina, C. M., Becker, U., Risthaus, P., Bosbach, D., and Putnis, A. (1998) Molecular-scale mechanisms of crystal growth in barite. *Nature* **395**, 483-486.

Pina C. M. and Jordan G. (2009) Reactivity of mineral surfaces at nano-scale: kinetics and mechanisms of growth and dissolution. EMU-notes in Mineralogy 8, accepted.

Pokrovsky, O.S. and Schott, J. (1999) Processes at the magnesium-bearing carbonates solution interface. II Kinetics and mechanism of magnesite dissolution. *Geochim. Cosmochim. Acta* **63**, 881-897.

Potapenko, S. Y. (1993) Moving of step through impurity fence. *J. Crystal Growth* **133**, 147-154.

Reeder, R. J. (1996) Interaction of divalent cobalt, zinc, cadmium, and barium with the calcite surface during layer growth. *Geochim. Cosmochim. Acta* **60**, 1543-1552.

Saldi, G.D. (2009) Les cinétiques de dissolution et précipitation de la magnesite aux conditions hydrothermales. Thèse de l'Université Paul-Sabatier, Toulouse, 184 p.

Sánchez-Pastor, N., Pina, C. M., Astilleros, J. M., Fernandez-Diaz, L., and Putnis, A. (2005) Epitaxial growth of celestite on barite (001) face at a molecular scale. *Surf. Sci.* **581**, 225-235.

Sangwal, K. (1998) Growth kinetics and surface morphology of crystals grown from solutions: Recent observations and their interpretations. *Progress in Crystal Growth and Characterization of Materials* **36**, 163-248.

Sayles, F. L. and Fyfe, W. S. (1973) The crystallization of magnesite from aqueous solution. *Geochim. Cosmochim. Acta* **37**, 87-99.

Shiraki, R. and Brantley, S. L. (1995) Kinetics of near-equilibrium calcite precipitation at 100°C: An evaluation of elementary reaction-based and affinity-based rate laws. *Geochim. Cosmochim. Acta* **59**, 1457-1471.

Shock, E. L., Sassani, D. C., Willis, M., and Sverjensky, D. A. (1997) Inorganic species in geologic fluids: Correlations among standard molal thermodynamic properties of aqueous ions and hydroxide complexes. *Geochim. Cosmochim. Acta* **61**, 907-950.

Staudt, W. J., Reeder, R. J., and Schoonen, M. A. A. (1994) Surface structural controls on compositional zoning of SO_2^{-4} and SeO_2^{-4} in synthetic calcite single crystals. *Geochim. Cosmochim. Acta* **58**, 2087-2098.

Teng, H. H., Dove, P. M., and De Yoreo, J. J. (2000) Kinetics of calcite growth: surface processes and relationships to macroscopic rate laws. *Geochim. Cosmochim. Acta* **64**, 2255-2266.

Teng, H. H., Dove, P. M., and DeYoreo, J. J. (1999) Reversed calcite morphologies induced by microscopic growth kinetics: insight into biomineralization. *Geochim. Cosmochim. Acta* **63**, 2507-2512.

Teng H. H., Dove P. M., Orme C. A., and De Yoreo, J. J. (1998) The thermodynamics of calcite growth: A baseline for understanding biomineral formation. *Science* **282,** 724–727.

van Enckevort, W. J. P. and van den Berg, A. C. J. F. (1998) Impurity blocking of crystal growth: a Monte Carlo study. *J. Crystal Growth* **183**, 441-455.

Vavouraki, A. I., Putnis, C. V., Putnis, A., and Koutsoukos, P. G. (2008) An Atomic Force Microscopy study of the growth of calcite in the presence of sodium sulfate. *Chem. Geo.* **253**, 243-251.

Vekilov, P. G. (2007) What determines the rate of growth of crystals from solution? *Cryst. Growth Des.* **7**, 2796-2810.

Voronkov V. V. and Rashkovich L. N. (1992) Influence of a mobile adsorbed impurity on the motion of steps. *Sov. Phys. Crystallogr.* **37(3)**, 289–295.

Wasylenki, L. E., Dove, P. M., Wilson, D. S., and De Yoreo, J. J. (2005) Nanoscale effects of strontium on calcite growth: An in situ AFM study in the absence of vital effects. *Geochim. Cosmochim. Acta* **69**, 3017-3027.

Wolf, G.H., Chizmeshya A.V.G., Diefenbacher, J., and McKelvy, M.J., (2004) In-situ observationof CO_2 sequestration reactions using a novel microreaction system. *Env. Sci. Tech.,* **38,** 932-936.

Zhang, J. and Nancollas, G. H. (1998) Kink Density and Rate of Step Movement during Growth and Dissolution of an ABCrystal in a Nonstoichiometric Solution. *Journal of Colloid and Interface Science* **200**, 131-145.

CHAPITRE 4

Vitesses de dissolution de la magnésite en milieu neutre et alcalin à 150 et 200°C

Résumé en français de l'article :

« Magnesite dissolution rates at 150 and 200 °C at neutral to alkaline conditions»

1. Introduction

Les mécanismes et les cinétiques de dissolution des minéraux carbonatés dans les environnements naturels ont fait l'objet d'études détaillées depuis plus de quarante ans. Cependant, ce n'est que récemment que l'intérêt pour la réactivité des ces minéraux s'est déplacé vers les températures et les pressions super ambiantes. Cet intérêt résulte de la nécessité de connaitre la stabilité et la cinétique de dissolution des minéraux carbonatés aux conditions pertinentes au stockage de CO_2 dans des aquifères salins (Talman et al., 1990; Zhang et al., 2007; Jordan et al. 2007; Pokrovsky et al., 2009; Pokrovsky et al., 2009a).

Le but de ce travail est de fournir des données sur la cinétique de la dissolution de la magnésite, aux conditions de température (150-200 °C) et d'affinité chimique ($0 < A < 25$ kJ/mol) représentatives de celles rencontrées dans les formations sédimentaires profondes. Les résultats issus de ce travail apporteront des informations précieuses sur la stabilité des carbonates de magnésium dans ces formations où elles constituent le réservoir géologique ou peuvent précipiter, facilitant ainsi le stockage du CO_2.

2. Cadre théorique et méthodes expérimentales

La présente étude a été conduite avec des échantillons naturels et synthétiques de poudre de magnésite. Les échantillons naturels ont deux origines différentes : le premier provient de la région de Satka (Oural, Russie) et avait été caractérisé par Pokrovsky et al. (1999a) ; le deuxième provient du gisement de Huaziyu, dans la province de Liaoning (Chine); la composition chimique moyenne de cet échantillon (déterminée par microsonde électronique et

LA-ICP-MS) est reportée dans le Tableau 1. Un troisième échantillon de magnésite a été synthétisé a partir de carbonate de magnésium hydraté et de glace carbonique à 200 °C. Les échantillons naturels et synthétiques de magnésite ont aussi été caractérisés par diffraction aux rayons-X et microscopie électronique à balayage (MEB), dont deux images sont reportées sur la Figure 1 pour une poudre naturelle et une synthétique.

Nous avons déterminé les vitesses de dissolution de la magnésite à l'état stationnaire dans des réacteurs à circulation, à partir de l'analyse chimique des solutions en entrée et en sortie du dispositif expérimental dans lequel la magnésite a été dissoute ; ces vitesses ont été normalisées à la valeur de la surface spécifique de la poudre utilisée dans chaque expérience (voir Tableau 2). Nous avons conduit ce travail à des pH neutres et alcalins et pour différentes valeurs de l'indice de saturation correspondant à des conditions proches à éloignées de l'équilibre thermodynamique avec la phase solide ; les compositions des solutions utilisées sont reportées dans les Tableaux 3 et 4. Nous avons ensuite calculé la spéciation chimique et les valeurs de l'indice de saturation correspondant à chaque essai à l'aide du code de calcul PHREEQC et en utilisant la base de données llnl.

Le cadre théorique utilisé pour l'interprétation des résultats expérimentaux est fourni par le model de complexation surfacique développé par Pokrovsky et al. (1999a) en conjonction avec la théorie de l'état transitoire, qui décrivent la vitesse de dissolution de la magnésite selon la relation :

$$r_d = [\, k_{CO_3} \{>CO_3H°\}^m + k^+_{Mg} \{>MgOH_2^+\}^n] \cdot \left[1 - \left(\frac{Q}{K_{MgCO3}} \right)^n \right], \qquad (1)$$

où k_{CO_3} et k^+_{Mg} représentent des constants de vitesse, m et n sont les ordres de réaction par rapport à la protonation des sites surfaciques $>CO_3^-$ et à l'hydratation des sites >MgOH° respectivement, Q représente le produit d'activité ionique ($a_{Mg} \cdot a_{CO_3^{2-}}$), K_{MgCO3} correspond au produit de solubilité de la magnésite, R est la constante des gaz parfaits et T la température absolue. Pokrovsky et Schott (1999) ont démontré que pour la magnésite les valeurs de m comme de n sont égales à 4, ce qui signifie que la réaction élémentaire de dissolution implique la protonation / hydratation complète des 4 sites de surface autour du site où la rupture des liaisons Mg-O se produit. Aux conditions neutres et alcalines, la dissolution est contrôlée par l'hydratation des sites métalliques (deuxième terme de l'équation 1) et toute

réaction qui réduit la concentration en sites $>MgOH_2^+$ à la surface du minéral aura un effet inhibiteur sur la vitesse de dissolution. En particulier, dans les solutions basiques ou enrichies en espèces carbonatées la dissolution peut être ralentie par la carbonatation et l'hydrolyse des sites magnésiens qui contrôlent la dissolution suivant les réactions :

$$>MgCO_3^- + H_2O \Leftarrow >MgOH_2^+ + CO_3^{2-}, \quad (2)$$

$$>MgOH^\circ + H_2O \Leftarrow >MgOH_2^+ + OH^-, \quad (3)$$

dont les constante d'équilibre sont respectivement exprimées par :

$$\boldsymbol{K}_{CO3} = \frac{\{> MgOH_2^+\}\boldsymbol{a}_{CO_3^{2-}}}{\{> MgCO_3^{2-}\}} \quad (4) \qquad \text{et} \qquad \boldsymbol{K}_{OH} = \frac{\{> MgOH_2^+\}\boldsymbol{a}_{OH^-}}{\{> MgOH^\circ\}}. \quad (5)$$

Les réactions (2) et (3) montrent que les vitesses de dissolution de la magnésite diminuent lorsque l'activité de CO_3^{2-} et OH^- augmentent et, par conséquent, la détermination des valeurs des constantes K_{CO3} et K_{OH} est indispensable à la quantification de ces effets d'inhibition sur les vitesses de dissolution.

La combinaison de l'équation (1) avec l'expression des constantes K_{OH} et K_{CO3} et celle qui décrit l'expression qui décrit la conservation des sites métalliques :

$$\boldsymbol{s} = \{>MgOH_2^+\} + \{>MgCO_3^-\} + \{>MgOH^\circ\}, \quad (6)$$

nous permet d'exprimer la vitesse de dissolution de la magnésite loin de l'équilibre en fonction de $\boldsymbol{a}_{CO_3^{2-}}$ et du pH de la solution en utilisant l'expression :

$$\boldsymbol{r}_+ = \boldsymbol{k'}_{Mg}\left(\frac{K_{CO3}K_{OH}\boldsymbol{a}_{H^+}}{K_{CO3} + K_{CO3}K_{OH}\boldsymbol{a}_{H^+} + K_{OH}\boldsymbol{a}_{H^+}\boldsymbol{a}_{CO_3^{2-}}}\right)^4, \quad (7)$$

où la concentration totale des sites Mg ($\boldsymbol{s}$) est inclue dans la constante de vitesse $\boldsymbol{k'}_{Mg}$.

3. Résultats expérimentaux et leur interprétation

Les vitesses de dissolution de la magnésite mesurées à 150 et 200 °C sont reportées dans les tableaux 4 et 5 et représentées en fonction du pH et de l'activité de CO_3^{2-} dans les diagrammes de la Figure 3. Ces graphiques montrent que les vitesse de dissolution diminuent

rapidement avec l'augmentation de $a_{CO_3^{2-}}$ ou du pH. Dans la gamme des conditions étudiées les vitesses mesurées diminuent d'environ 3 ordres de grandeur avec une influence du pH qui apparaît plus marquée que celle de $a_{CO_3^{2-}}$, comme le montrent les droites de corrélation tracées pour les données à 200 °C sur les diagrammes des Figures 3b et 3d. Cependant, pour les plus fortes concentrations du carbonate et les pH les plus basiques il faut aussi prendre en compte l'effet de l'affinité chimique, car les solutions réactives sont proches de l'équilibre (voir l'échelle de l'indice de saturation sur l'axe supérieur des graphiques). Pour distinguer les effets des concentrations de CO_3^{2-} et OH^- de celui de l'affinité chimique, nous avons calculé les vitesses de dissolution loin de l'équilibre (r_+) à partir de vitesses mesurées (r_d) à l'aide de l'expression :

$$r_+ = r_d / \left[1 - \exp\left(\frac{-nA}{RT}\right)\right], \qquad (8)$$

avec n=4, en supposant donc que l'ordre de réaction par rapport aux sites $>MgOH_2^+$ ne change pas avec la température (Pokrovsky and Schott, 1999, Pokrovsky et al., 2009). Les vitesses de dissolution ainsi obtenues, qui sont représentées pour une force ionique égale à 0.1 M dans les diagrammes de Figure 4, confirment l'important effet d'inhibition de CO_3^{2-} et OH^-.

Les graphiques de figures 3 et 4 montrent aussi que les vitesses de dissolution mesurées à 200 °C sont égales ou inférieures à celles obtenues à 150 °C. Ce résultat implique une valeur négative ou proche de 0 pour l'énergie apparente d'activation de la réaction de dissolution dans cet intervalle de température.

Afin de modéliser les vitesses de dissolution en fonction de la température et de la composition de la solution aqueuse à l'aide de l'équation (7), il est indispensable de connaître les constantes d'équilibre et les enthalpies des réactions (2) et (3) dans les conditions de nos essais. Les valeurs de K_{OH} et K_{CO3} à 25 °C ont été déduites de mesures de potentiel Zeta et titrations de surface réalisées par Pokrovsky et al. (1999a). Les valeurs de K_{CO3} ont été calculées à 150 et à 200 °C grâce à l'approximation de l'enthalpie de la réaction correspondante [$\Delta H_{r(CO3)}$] à partir des vitesses de précipitation de la magnésite présentées au chapitre 2. La valeur de la constante de vitesse k_{Mg}^+ à 200 °C a été déduites de vitesses de dissolution mesurées au cours de cette étude à 150 °C entre pH 4 et 6 à l'aide de l'équation

d'Arrhenius avec une énergie d'activation de 46 kJ/mol (Pokrovsky et al., 2009). La valeur de K_{OH}, seule variable de modélisation, a été déduite des données expérimentales à l'aide de l'équation (7). Les valeurs de $\boldsymbol{k}^{+}_{Mg}$, K_{CO3} et K_{OH} à 150 et 200 °C sont reportées dans le Tableau 6. On peut voir sur le graphiques de la Figure 4 que les vitesses de dissolution prédites par l'équation (7), représentées par une ligne continue, sont en bon accord avec les vitesses expérimentales. Les Figures 5 et 6 mettent aussi en évidence le rôle primaire joué par la composition chimique de la solution dans la détermination des vitesses de dissolution en milieu neutre et basique en fonction de l'affinité chimique. Cet effet résulte de l'important impact de la composition de la solution sur les sites qui contrôlent la dissolution (voir la Figure 5).

La légère diminution de vitesse observée avec l'augmentation de la température de 150 à 200 °C peut être expliquée par la diminution correspondante des constantes K_{CO3} et K_{OH} dans cet intervalle de température, qui provoque une augmentation de la carbonatation et de l'hydrolyse des sites $>MgOH_2^+$.

Cette étude expérimentale de la vitesse de dissolution de la magnésite nous a permis d'étendre l'application du modèle de complexation de surface aux températures super ambiantes et d'y introduire l'effet du pH de la solution qui devient de plus en plus important au fur et à mesure que la température augmente. Nos observations suggèrent en particulier que l'alcalinisation des fluides enrichis en CO_2 suite aux interactions eau-roche, crée des conditions favorables à la stabilité des réservoirs sédimentaires calcaires destinés à accueillir le CO_2 sous forme dissoute. La diminution de la vitesse de dissolution avec l'augmentation de température au delà de 100°C, déjà notée par Pokrovsky et al. (2009), rend ce domaine de température plus efficace pour une séquestration fiable du CO_2 sous forme dissoute.

Magnesite dissolution rates at 150 and 200 °C at neutral to alkaline conditions

Giuseppe D. Saldi*, Jacques Schott, Oleg S. Pokrovsky and Eric H. Oelkers

Géochimie et Biogéochimie Expérimentale, LMTG – CNRS – OMP – Université de Toulouse, 14, Avenue Edouard Belin, 31400 Toulouse, France

***Corresponding author:**

Tel.: +33 5 61 33 26 32; fax: +33 5 61 33 25 60

E-mail addresses: saldi@lmtg.obs-mip.fr, oelkers@lmtg.obs-mip.fr

Prepared for submission to *Chemical Geology*

Keywords: magnesite dissolution rates, CO_2 sequestration, negative activation energy

Abstract

Magnesite dissolution rates were measured in mixed flow reactor at 150 and 200 °C at neutral to basic conditions (6 < pH < 9), as a function of ionic strength (0.001 M ≤ I ≤ 1M) and departure from equilibrium. They were found to increase with increasing ionic strength, but to diminish with increasing temperature from 150 to 200 °C in alkaline conditions as a result of the enhanced inhibition by OH^- and CO_3^{2-}. Measured rates have been interpreted within the framework of the surface complexation model developed by Pokrovsky et al. (1999a) in conjunction with the transition state theory (Eyring, 1935). Within this formalism, magnesite overall dissolution rates have been found to be consistent with the following rate equation:

$$r_d = k^+_{Mg} \cdot \left(\frac{K_{CO3} K_{OH} a_{H^+}}{K_{CO3} + K_{CO3} K_{OH} a_{H^+} + K_{OH} a_{H^+} a_{CO_3^{2-}}} \right)^4 \cdot \left[1 - \exp\left(-\frac{4A}{RT} \right) \right],$$

where r_d represents the dissolution rate normalized to the BET surface area of the mineral, k^+_{Mg} designates a rate constant, K_{CO3} and K_{OH} correspond to thermodynamic constants describing the formation of rate controlling magnesium surface sites as a function of CO_3^{2-} and OH^- activity respectively, a_i stands for the activity of the subscripted aqueous species, and A refers to the chemical affinity of the overall reaction. Values of K_{CO3} and K_{OH} as a function of temperature have been assessed from the equilibrium constants and enthalpies of the corresponding reactions in solution.

The present study shows that increasing temperature above 100 °C in neutral to alkaline CO_2-rich solutions, which significantly inhibit magnesite (and other Ca-Mg carbonates) dissolution, is likely to favor carbon dioxide sequestration in deep carbonate sedimentary basins.

1. Introduction

The present work is part of a systematic study aimed at a complete characterization of major carbonate minerals reactivity in natural environments at a wide variety of physico-chemical conditions, representative of Earth surface, deep sea sedimentary environments as well as hydrothermal systems. The dissolution behavior of Mg and Ca-carbonates has been the object of dedicated studies for more than 40 years (see Morse and Ardvison (2002) for a review of old and recent laboratory studies), but only recently the interest in their mechanisms and kinetics of dissolution has moved towards relatively high temperatures and elevated CO_2 partial pressures, mainly in response to the need for determining the reactivity of these minerals at conditions relevant to CO_2 sequestration in deep saline aquifers (Talman et al., 1990; Zhang et al., 2007; Jordan et al. 2007; Pokrovsky et al., 2009; Pokrovsky et al., 2009a).

Magnesite dissolution rates were determined under a large range of pH and solution compositions at 25 °C (Chou et al. 1989; Pokrovsky and Schott, 1999; Pokrovsky et al. 2005). At higher temperature the dissolution kinetics was investigated only at acidic to near neutral conditions by means of batch and mixed flow reactor under high pCO_2 (Pokrovsky et al., 2009) and in presence of various organic ligands (Pokrovsky et al., 2009a). Magnesite mechanisms and dissolution kinetics were also investigated by atomic force microscopy between 60 and 100 °C (Jordan et al., 2001; Higgins et al., 2002; Jordan et al., 2007) but a systematic study of the rates of dissolution of this carbonate at $T > 100$ °C and for conditions close to thermodynamic equilibrium has not been performed yet.

In the present study $MgCO_3$ dissolution kinetics has been investigated at 150 and 200 °C, in the neutral to alkaline pH region, as a function of ΣCO_2 concentration and ionic strength and from relatively far to very close to equilibrium conditions. The results obtained from this experimental work will enlarge the picture provided by previous studies on carbonate minerals dissolution, supplying more information about the stability of Mg-carbonate minerals in deep sedimentary formations where they constitute reservoir confining phases or where their precipitation is expected to trap CO_2.

2. Theoretical considerations

Metal carbonate dissolution has been usually described by three parallel reactions occurring at the mineral/water interface (Plummer et al., 1978; Chou et al., 1989; Wollast, 1990):

$$MeCO_3 + H^+ \xrightarrow{k_1} Me^{2+} + HCO_3^- \quad (1)$$

$$MeCO_3 + H_2CO_3^* \xrightarrow{k_2} Me^{2+} + 2HCO_3^- \quad (2)$$

$$MeCO_3 \underset{k_{-3}}{\overset{k_3}{\leftrightarrow}} Me^{2+} + CO_3^{2-} \quad (3)$$

where Me = Ca, Mg. Assuming that carbonate minerals crystallization is described by Eqn. 3, their overall dissolution rate can be expressed by:

$$r_d = k_1 \cdot a_{H^+}^n + k_2 \cdot a_{H_2CO_3^*}^p + k_3 - k_{-3} \cdot a_{Me^{2+}} \cdot a_{CO_3^{2-}} \quad (4)$$

where k_i are the rate constants of Eqns. (1) to (3), and a_i stands for the activity of the aqueous species. The value of exponent *n* is equal to 1 for calcite (Plummer et al., 1978; Alkattan et al., 1998) and varies from 0.5 (Busenberg and Plummer, 1982) to 0.75 (Chou et al., 1989) for dolomite, whereas *p* was found to be equal to 1 (Busenberg and Plummer, 1982). Within this mechanistic scheme, the first term in Eqn. 4 corresponds to solid surface protonation, the second to surface interaction with carbonic acid, the third to surface hydration, and the fourth term accounts for the precipitation reaction. The existence of reaction (2) has been recently dismissed by Pokrovsky et al. (2009) who demonstrated that, at constant ionic strength, H_2CO_3 has no specific effect on carbonates dissolution rates and that measured increased rates as a function of carbonic acid concentration can be accounted for by solution acidification resulting from CO_2 dissolution. Consequently Eqn. (4) describing carbonate overall reaction rate simplifies to:

$$r_d = k_1 \cdot a_{H^+}^n + k_3 - k_{-3} \cdot a_{Me^{2+}} \cdot a_{CO_3^{2-}} \quad (5)$$

A more predictive analysis of carbonate dissolution kinetics can be obtained using the surface complexation models (SCM) developed by Van Cappellen et al. (1993) and Pokrovsky et al. (1999a,b). These models are based on Zeta-potential and surface titration measurements, molecular dynamic simulations and state-of-the-art spectroscopic techniques (see their review in Pokrovsky et al., 2001; Villegas-Jiménez et al., 2009). The SCM assumes

the existence of two primary hydration sites at carbonate mineral-solution interface, >MeOH° and >CO_3H°, whose subsequent hydration and reaction with mineral constituting ions lead to the formation of the following surface species: >$MeOH_2^+$, >MeOH°, >MeO^-, >$MeHCO_3$°, >$MeCO_3^-$, >CO_3^-, >CO_3H° and >CO_3Mg^+. Within this approach, proton-promoted dissolution at pH < 5 can be explained by the protonation of surface carbonate groups (>CO_3H°) whereas the fully hydrated metal centers (>$MgOH_2^+$) govern the H_2O-promoted dissolution at pH > 6 (Pokrovsky and Schott,1999, 2002). Following this formalism, magnesite overall dissolution rate equation can be described within the framework of the transition state theory by (Pokrovsky and Schott, 1999):

$$\boldsymbol{r}_{\mathrm{d}} = [\,\boldsymbol{k}_{\mathrm{CO_3}}\,\{>\mathrm{CO_3H}°\}^{\boldsymbol{m}} + \boldsymbol{k}^{+}_{\mathrm{Mg}}\,\{>\mathrm{MgOH_2}^{+}\}^{\boldsymbol{n}}]\cdot\left[1-\left(\frac{Q}{K_{MgCO3}}\right)^{\boldsymbol{n}}\right], \qquad (6)$$

which can be also expressed as in terms of far from equilibrium dissolution rate $\boldsymbol{r}_+$ (cf. Lasaga, 1981; Aagaard and Helgeson, 1982; Oelkers et al., 1994):

$$\boldsymbol{r}_{\mathrm{d}} = \boldsymbol{r}_+\cdot\left[1-\left(\frac{Q}{K_{MgCO3}}\right)^{\boldsymbol{n}}\right] = \boldsymbol{r}_+\cdot\left[1-\exp\left(\frac{-\boldsymbol{n}A}{\boldsymbol{R}T}\right)\right]. \qquad (7)$$

In the two equation (6) and (7) $\boldsymbol{k}_{\mathrm{CO_3}}$ and $\boldsymbol{k}^{+}_{\mathrm{Mg}}$ represent rate constants, $\boldsymbol{m}$ and $\boldsymbol{n}$ indicate the reaction orders with respect to surface protonated carbonate and hydrated metal centers, respectively, Q represents the ion activity product ($\boldsymbol{a}_{\mathrm{Mg}}\cdot\boldsymbol{a}_{\mathrm{CO_3^{2-}}}$), K_{MgCO3} stands for the magnesite solubility product, $\boldsymbol{R}$ represents the gas constant T stands for the absolute temperature and A defines the chemical affinity of the dissolution reaction. The ratio between Q and K_{MgCO3} represents the saturation state of aqueous solution with respect to the solid phase and it is usually designated with Ω.

The study of magnesite dissolution rates at 25 °C (Pokrovsky and Schott, 1999) showed that the values of both $\boldsymbol{n}$ and $\boldsymbol{m}$ are approximately equal to 4, indicating that magnesite dissolution requires full protonation/hydration of all four surface sites around the site where the breaking of Mg-O bonds occurs. At near neutral to basic conditions magnesite dissolution is controlled by the hydration of surface metal sites (second term of Eqn. 6). In carbonate-rich solutions magnesite dissolution is inhibited by the formation of >$MgCO_3^-$ to the detriment of rate controlling >$MgOH_2^+$ according to:

$$>MgCO_3^- + H_2O = >MgOH_2^+ + CO_3^{2-}, \quad (8)$$

whose equilibrium constant is expressed by:

$$K_{CO3} = \frac{\{> MgOH_2^+\} a_{CO_3^{2-}}}{\{> MgCO_3^-\}} \quad (9)$$

Combination of Eqn. (6) and (9) yields, at far from equilibrium conditions (Pokrovsky and Schott, 1999):

$$r_+ = k_{Mg}^+ \cdot \left(\frac{K_{CO3}}{K_{CO3} + a_{CO_3^{2-}}} \right)^n \quad (10)$$

The temperature dependence of mineral dissolution rate (r_+) is generally interpreted within the framework of the Arrhenius equation:

$$r_+ = A_a \cdot e^{-E_a/RT} \quad (11)$$

where A_a is a pre-exponential factor and E_a represents the activation energy of the dissolution reaction. As shown by Pokrovsky et al. (2009), experimental characterization of E_a requires separating the overall rate dependence on temperature into two parts: a) contribution of the enthalpy of formation of the rate controlling surface sites (i.e. $>CO_3H°$ and $>MgOH_2^+$), and b) the activation energy of the dissolution rate constant (i.e. the activated complex). As such, attempts to estimate the activation energy from plots of rates (i.e. r_+) versus $1/T$ yield a combination of the activation energy and the enthalpy of the formation reaction of rate controlling sites. Activation energies generated in this way, commonly referred to as apparent activation energies, can exhibit negative values, as recently shown by Pokrovsky et al. (2009) and Schott et al. (2009) in the case of carbonate minerals proton-promoted dissolution.

3. Experimental methods

3.1 Magnesite samples

Magnesite samples of both natural and synthetic origin were used during the course of this study. Synthetic magnesite was produced in rocking autoclaves starting from analytical grade hydrated Mg-carbonate. About 20 g of this reagent were put in a 400 ml Ti-vessel with 250 ml of deionized water and 15-20 g of solid CO_2. The autoclave was sealed and

temperature was increased to 200 °C. After three weeks of reaction, the powder was recovered and stored in a stove at 60°C. The synthesized magnesite powders consist of crystals displaying a cubic to rhombohedral shape and size of few μm to 40 μm. A SEM photomicrograph of a synthetic magnesite sample used for the dissolution experiments is shown in Figure 1a; XRD and EDS analyses proved that the powder synthesized was pure magnesite. Natural $MgCO_3$ samples used in this study were of two different origins: a first specimen was from Satka (Russia) and was previously characterized by Pokrovsky et al. (1999a); the second natural magnesite specimen originated in the Huaziyu deposit (Liaoning province, China). XRD and EDS analyses of this sample did not detect any mineral phase other than magnesite. Electron microprobe and LA-ICP-MS analyses performed on this sample provided the results shown in Table 1. Description, chemical composition and origin of magnesite ore deposits in the Liaoning province were discussed by Jiang et al. (2004).

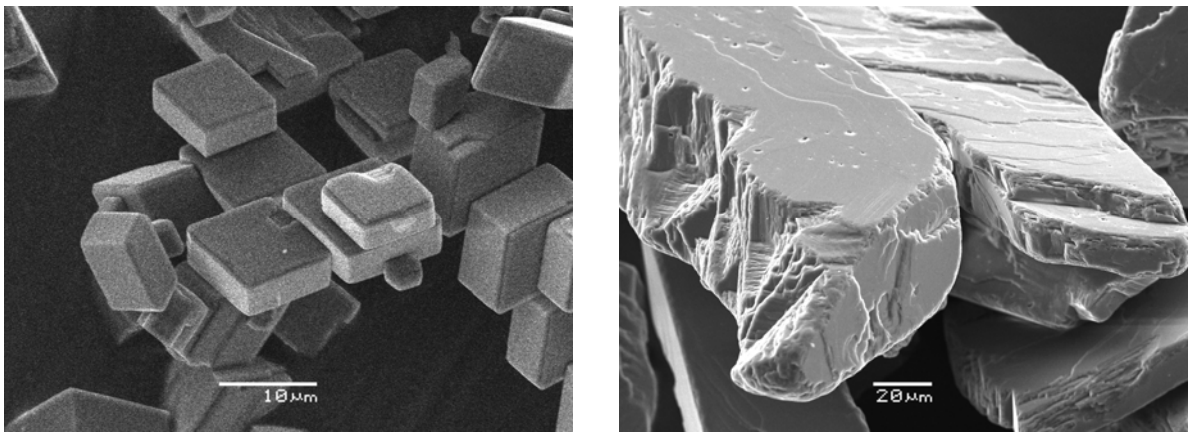

Figure 1. SEM photomicrographs of magnesite samples used during dissolution experiments: magnesite sample of synthetic origin (left); magnesite powder of natural origin from the Huaziyu deposit (right).

Natural magnesite samples were ground in agate mortar with a pestle and sieved. The size fraction between 50 and 100 μm was retained for the experiments, ultrasonically cleaned in alcohol to remove the fine particles, rinsed repeatedly with deionized water and dried for a few days at 60 °C. A SEM image of the Huaziyu $MgCO_3$ powder is reported in Figure 1b, showing the absence of fine particles at the surface of the grains.

The specific surface areas of the powders used in the present study were determined by multi-point krypton adsorption according to the BET method (Brunauer et al., 1938) and are reported for each sample in Table 2.

Table 1. Chemical composition of the Huaziyu magnesite used in this study

Major carbonate oxides[a] (weight %)		Trace elements[b] (ppm)	
MgO	47.32	Na	33.5
CaO	0.32	Si	288.4
MnO	0.02	Cl	307.0
FeO	0.10	P	220.9
SrO	–	K	25.7
BaO	–	Cr	3.2
CO_2	51.7		

[a]Determined by EMPA, average of 20 points
[b]Determined by LA-ICP-MS, average of 7 punctual analyses

Table 2. Specific surface area of the magnesite samples dissolved in this study, as determined by krypton adsorption (S_{BET})

$MgCO_3$ powders	S_{BET} (cm^2/g)
Huaziyu A	1281
Huaziyu B	971
Satka	1260
Mgs-1	2882
Mgs-2	2241
Mgs-II	1723
Mgs-V	1791
Mgs-VIII	2007

3.2 Experiments, solution analyses and thermodynamic calculations

Magnesite steady-state dissolution rates were determined by mixed-flow reactor experiments, using 200 and 300 ml high *T* titanium vessels, already described by Dove and Crerar (1990), Gautier et al. (1994) and Devidal et al. (1997). Inlet solutions were stored in compressible polyethylene containers and injected into the reactor through a 2 µm titanium filter by a HPLC pump allowing flow rates ranging from 0.1 to 10 ml/min. Solution inside the

reactor was stirred at a constant rate by a Parr magnetically driven stirrer and kept at constant temperature ± 1 °C by a Parr controlled furnace. The fluid left the reactor through a 2 μm titanium filter and was cooled down before reaching a back-pressure regulator that maintained a constant pressure throughout the system.

The reacting solutions were prepared with high purity deionized H_2O (18.2 MΩ·cm) and reagent grade NaCl, Na-Acetate, $NaHCO_3$, HCl, NaOH and $MgCl_2$ titrisol. Na-Acetate was used only in few experiments to buffer the solution pH at circumneutral values. Experiments were performed at ionic strengths varying from 0.001 to 1M NaCl/$NaHCO_3$. The compositions of starting experimental solutions used in our experiments are summarized in Table 3 (150 °C) and 4 (200 °C). All solutions were analyzed for magnesium concentration and alkalinity. Mg was measured by flame atomic absorption spectroscopy (AAS) with an uncertainty of ± 1% and a detection limit of 6×10^{-7} M, whereas the alkalinity was determined by standard HCl titration with an uncertainty of ± 1% and a detection limit of 5×10^{-5} M. Measurements of solution pH were performed at 25 °C for inlet solutions as well as for outlet solutions immediately after sampling by means of a standard glass electrode, previously calibrated with 4.01, 6.86 and 9.18 NIST pH buffers. Solutions pH was also measured in the course of the experiments performed at 150 °C using a solid contact Li-Sn alloy commercial pH electrode coupled with either a home-made Ag/AgCl reference electrode which provides a constant potential in Cl^- rich solutions, as described by Pokrovsky et al. (2005, 2009), or a Na-selective glass electrode providing a constant potential in Na^+-rich solution. The former reference electrode was employed successfully for Cl^- concentration ≈ 0.01 M; for Cl^- concentration ≥ 0.1 M its very low stability allowed pH measurements for the duration of only one or two experiments after the usual calibration, and in its place was adopted the latter type of reference electrode. The description of the potentiometric measurement using the Na-selective electrode has been provided by Saldi (2009). Potentials measured with both systems, under their reported selected conditions, proved to be sufficiently stable over the duration of several experiments, giving pH values affected by an uncertainty not higher than 0.02 to 0.05 pH units.

The standard state adopted in this study is that of unit activity for pure minerals and pure H_2O at any temperature and pressure. For other aqueous species the standard state is of unit activity in hypothetical 1 molal solution referenced to infinite dilution at any temperature and pressure. Aqueous solution speciation and saturation indexes with respect to different

solid phases were calculated by means of the PHREEQC code (Pakhurst and Appelo, 1999) using its llnl thermodynamic database and the Debye-Huckel equation for the calculation of the activity coefficients of dissolved species. The constants of formation of $MgOH^+$ aqueous complex as a function of *T* (Shock et al., 1997) were added to this database.

Table 3. Chemical composition of starting experimental solutions used at 150 °C.

Exp. Sol.	pH	NaCl [mol/kg]	$MgCl_2$ [mol/kg]	HCl [mol/kg]	NaOH [mol/kg]	$NaHCO_3$ [mol/kg]	NaAcetate [mol/kg]
H1	8.11	0	0	0	0	1.0E-02	0
H2A	7.59	0	0	0	0	1.0E-03	0
H3A	7.31	0	1.045E-04	0	0	1.0E-03	0
H4	8.09	0	0	0	0	1.0E-02	0
H4A	8.09	0	1.009E-05	0	0	1.0E-02	0
H4B	8.09	0	1.009E-05	0	0	1.0E-02	0
H5	7.22	0	1.015E-04	0	0	1.0E-03	0
H6	8.34	0	0	0	0	1.0E-01	0
H7A	7.54	0	2.134E-05	0	0	1.0E-03	0
H7B	7.56	0	1.531E-05	0	0	1.0E-03	0
H8	8.12	0	1.911E-06	0	0	1.0E-02	0
H8A	8.14	0	1.911E-06	0	0	1.0E-02	0
H8B	8.11	0	3.057E-06	0	0	1.0E-02	0
H9	7.40	0.1	0	0	0	0	0
H9A	7.46	0.1	0	0	0	2.0E-04	0
H9B	7.55	0.1	0	0	0	1.0E-03	0
H9C	7.88	0.1	0	0	0	5.0E-03	0
H10	7.22	0.1	0	5.0E-05	0	0	0
H11	6.73	0.1	0	1.0E-04	0	0	0
H17	7.97	0.01	0	0	0	5.0E-03	0
H17A	7.55	0.01	0	0	0	1.0E-03	0
H17B	7.30	0.01	0	0	0	2.0E-04	0
H17C	7.32	0.01	0	0	0	0	0
H25	7.32	0.01	0	5.0E-05	0	0	0
H25A	7.07	0.01	0	1.0E-04	0	0	0
H25B	7.33	0.01	0	6.0E-05	0	0	0
H28	7.73	1	0	0	0	5.0E-03	0
H29	6.78	0.01	0	1.6E-04	0	0	0
H29A	6.92	0.01	0	1.6E-04	0	0	0
H30	6.44	0.1	0	1.6E-04	0	0	0
H30A	6.71	0.1	0	1.6E-04	0	0	0
H31	7.55	1	0	0	0	1.0E-03	0
H32	7.51	1	0	0	0	2.0E-04	0
H32A	7.55	1	0	0	0	0	0
H34	7.51	1	0	5.0E-05	0	0	0
H34A	7.43	1	0	5.0E-05	0	0	0
H35	7.34	1	0	1.0E-04	0	0	0
H35A	7.39	1	0	1.0E-04	0	0	0
H36	7.08	1	0	1.5E-04	0	0	0
H36A	7.23	1	0	1.5E-04	0	0	0
H37	7.29	0.1	0	1.6E-04	0	0	0
H37A	7.17	0.1	0	2.0E-04	0	0	0

Exp. Sol.	**pH**	**NaCl** [mol/kg]	**$MgCl_2$** [mol/kg]	**HCl** [mol/kg]	**NaOH** [mol/kg]	**$NaHCO_3$** [mol/kg]	**NaAcetate** [mol/kg]
H38	7.19	1	0	2.0E-04	0	0	0
H38A	7.23	1	0	2.0E-04	0	0	0
H39	6.99	1	0	2.5E-04	0	0	0
H39A	7.06	1	0	2.5E-04	0	0	0
H40	6.89	1	0	3.0E-04	0	0	0
H40A	6.91	1	0	3.0E-04	0	0	0
H43	6.82	0.1	0	3.0E-04	0	0	0
H44	6.42	0.1	0	4.0E-04	0	0	0
H45	6.30	0.1	0	5.0E-04	0	0	0
H46	4.57	0.1	0	5.0E-04	0	0	0
H47	6.31	0.1	0	4.0E-04	0	0	0
H48	7.81	0.1	0	0	1.0E-03	0	0
H48C	7.40	0.1	0	0	5.0E-04	0	0
H49	6.21	0.1	0	5.0E-04	0	0	0
H50	5.98	0.1	0	6.0E-04	0	0	0
H51	4.61	0.11	0	7.0E-04	0	0	0
H52B	7.97	0.1	0	0	0	7.0E-03	0
H53	4.35	0.11	0	7.0E-04	0	0	0
H53A	7.51	0.11	0	0	0	0	0
H55	4.26	0.1	0	1.0E-03	0	0	0
H56	7.69	1	0	0	0	7.0E-03	0
H56A	5.36	1	0	2.5E-03	0	0	0.005
H57	7.24	0.11	0	2.6E-04	0	0	0.01
H58	5.36	0.11	0	1.3E-03	0	0	0.01
H59	6.12	1	0	1.3E-03	0	0	0.01
M1A	7.59	0	0	0	0	1.0E-03	0
M1B	7.78	0	4.871E-04	0	1.3E-03	1.0E-03	0
M2	7.61	0.1	0	0	0	0	0
M2A	7.59	0.1	0	0	0	2.0E-04	0
M2B	7.61	0.1	0	0	0	1.0E-03	0
M2C	7.84	0.1	0	0	0	5.0E-03	0
Mt1-8	7.25	0	0	0	0	0	0
Mt2-7	7.23	0	0	0	0	0	0
Mt4-9	7.47	0.1	0	0	0	0	0
Mt5	7.55	0.1	0	0	0	0	0
Mt5-A	7.47	0.1	0	0	0	2.0E-04	0
Mt5-B	7.63	0.1	0	0	0	1.0E-03	0
Mt5-C	7.90	0.1	0	0	0	5.0E-03	0
Mt5-D	7.55	0.1	0	0	0	0	0
Mt7	7.28	0.1	8.133E-04	0	1.8E-03	0	0

Mixed-flow reactor experiments were run in series on a single magnesite powder sample, each serial experiment consisting of a different fluid flow rate and/or a different composition of the solution flowing through the reactor. Each experimental series is noted by a distinct prefix in the list of experiments of Tables 4 and 5, which report the physico-chemical parameters and the rates of dissolution for all the experiments performed.

Steady state dissolution rates, were indicated by a constant outlet Mg concentration and calculated by using the following equation:

$$\boldsymbol{r}_{\mathrm{d}} = q \cdot \Delta[\mathrm{Mg}]_{\mathrm{tot}}/\boldsymbol{S} \qquad (10)$$

where q represents the fluid flow rate, $\Delta[\mathrm{Mg}]_{\mathrm{tot}}$ stands for the difference between the outlet and inlet solution Mg concentrations (in mol/kg) and $\boldsymbol{S}$ refers to the mineral surface area.

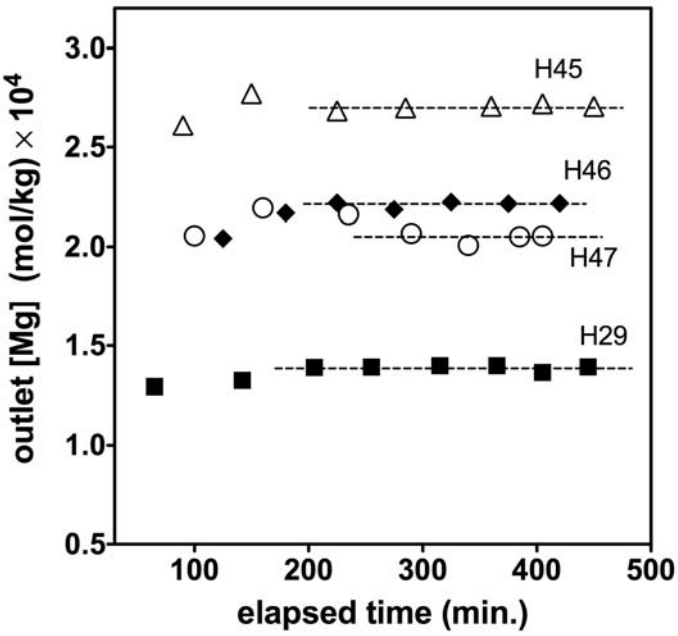

Figure 2. Examples of steady state Mg concentration attained during the indicated dissolution experiments performed at 150 °C.

Constant Mg concentrations in the effluent solution were obtained upon an elapsed time varying from 4 hours to 6 days, depending on the flow rate. Steady-state was verified with a minimum of three constant Mg concentrations of the outlet fluid samples taken over several residence times. Finally, after a steady state Mg concentration had been achieved, inlet fluid composition and/or fluid flow rate were changed to the next chosen experimental conditions. Some examples of attainment of steady state conditions with respect to Mg concentration are shown in Figure 2.

The surface area used to calculate the rates was the BET surface area of unreacted powders. Measurements performed on the same powders after the experiments revealed variations of the surface area generally inferior to 10%.

Analysis of dissolution rates reported in the tables 4 and 5 shows that dissolution reaction occurred even when, according to thermodynamic calculations, some experimental solutions resulted slightly supersaturated with respect to the dissolving phase. This fact is inherent in the uncertainties of the thermodynamic calculations: taking for granted that the solubility product of magnesite is known with a good approximation (see Bénézeth et al., 2009), the inaccuracy which affects, at such temperatures, the constants of formation of the aqueous species implicated in the dissolution reaction, as well as the determination of the corresponding activity coefficients, might increase the uncertainty on the outcome of calculations. Moreover, both pH and alkalinity measured at 25 °C, at least in some cases, may have lead to an imprecise determination of pH and aqueous concentration of carbonate species at experimental conditions.

Table 4. Summary of magnesite dissolution experiments performed in this study at 200 °C.

Run #	pH	NaCl [mol/kg]	$NaHCO_3$ [mol/kg]	Δ [Mg] [mol/kg]	Alk [mol/kg]	BET s. area [cm^2/g]	$MgCO_3$ mass [g]	FFR [g/min]	Ω	r_d [$mol/cm^2/s$]
S2	7.25	0.1	2.5E-04	1.218E-04	4.94E-04	1723	0.915	1.295	0.481	1.67E-12
S2A	7.13	0.1	0	1.808E-04	3.52E-04	1723	0.898	1.595	0.376	3.11E-12
S3	7.53	0.1	1.0E-03	4.021E-05	1.14E-03	1723	0.900	0.892	0.662	3.85E-13
S3A	7.43	0.1	5.0E-04	7.705E-05	6.87E-04	1723	0.900	1.194	0.574	9.89E-13
S4	7.74	0.1	2.5E-03	1.299E-05	2.54E-03	1723	0.957	0.596	0.675	7.82E-14
S4A	7.72	0.1	2.5E-03	1.214E-05	2.51E-03	1723	0.955	1.197	0.613	1.47E-13
S4B	7.72	0.1	2.5E-03	1.086E-05	2.48E-03	1723	0.953	2.197	0.539	2.42E-13
S4C	7.89	0.1	5.0E-03	5.63E-06	4.99E-03	1723	0.952	0.596	0.682	3.41E-14
S4D	7.88	0.1	5.0E-03	5.18E-06	4.94E-03	1723	0.951	1.197	0.614	6.30E-14
S5	7.98	0.1	7.5E-03	3.57E-06	7.45E-03	2007	0.984	0.497	0.682	1.50E-14
S5A	7.97	0.1	7.5E-03	3.38E-06	7.40E-03	2007	0.984	0.997	0.635	2.84E-14
S5B	7.23	0.1	0	1.655E-04	3.66E-04	2007	0.984	2.190	0.386	3.06E-12
S5C	6.88	0.1	0	2.515E-04	2.29E-04	2007	0.959	3.474	0.211	7.56E-12
S5D	6.78	0.1	0	2.260E-04	1.71E-04	2007	0.932	4.997	0.113	1.01E-11
S5E	7.24	0.1	0	1.823E-04	4.26E-04	2007	0.904	1.395	0.546	2.34E-12
S6	8.04	0.1	1.0E-02	2.84E-06	9.87E-03	1791	1.293	0.395	0.733	8.09E-15

Considering the possible faults implied in the calculations, to present and discuss coherently our experimental results a correction to the state of saturation of the solutions, for which the dissolution rates were measured, was made necessary. Knowing that the slowest rates measured should correspond to a solution composition that is at least very close to equilibrium with magnesite, a correction factor of 2.95 has been arbitrarily applied to Ω for the data obtained at 150 °C to make all dissolving solutions undersaturated. This correction introduces a change of the free energy of formation of magnesite equal to -3.82 kJ/mol. The same correction was made for the data at 200 °C, modifying the magnesite free energy of formation of -4.26 kJ/mol. It must be noted that such a correction only rectifies the position of the origin of the graphs presented in this study but doesn't affect the relative position of plotted datapoints at each temperature.

Table 5. Summary of magnesite dissolution experiments performed in this study at 150 °C.
nd = not determined.

Exp. Sol.	**pH**	**NaCl** [mol/kg]	**$NaHCO_3$** [mol/kg]	**Δ [Mg]** [mol/kg]	**Alk** [mol/kg]	**BET s. area** [cm^2/g]	**$MgCO_3$ mass** [g]	**FFR** [g/min]	**Ω**	**r_d** [$mol/cm^2/s$]
H1	8.11	0	1.0E-02	2.46E-06	0.01	1281	0.776	0.797	0.498	3.29E-14
H2A	7.59	0	1.0E-03	2.040E-05	0.0143	1281	1.012	0.605	0.332	1.59E-13
H4	8.09	0	1.0E-02	2.41E-06	0.01	1281	0.812	0.495	0.563	1.91E-14
H6	8.34	0	1.0E-01	1.41E-06	0.1	1281	1.908	0.493	0.993	4.75E-15
H8	8.12	0	1.0E-02	1.55E-06	1.02E-02	1281	1.151	0.291	0.725	5.07E-15
H8A	8.14	0	1.0E-02	1.72E-06	1.02E-02	1281	1.151	0.196	0.776	3.80E-15
H8B	8.11	0	1.0E-02	8.2E-07	1.02E-02	1281	1.151	0.196	0.800	1.81E-15
H9	7.40	0.1	0.0E+00	1.401E-04	2.11E-04	1281	0.700	1.390	0.098	3.62E-12
H9A	7.46	0.1	2.0E-04	1.087E-04	4.17E-04	1281	0.700	1.396	0.142	2.82E-12
H9B	7.55	0.1	1.0E-03	4.022E-05	1.08E-03	1281	0.700	1.396	0.193	1.04E-12
H9C	7.88	0.1	5.0E-03	6.22E-06	5.01E-03	1281	0.700	1.200	0.258	1.39E-13
H10	7.22	0.1	0.0E+00	1.181E-04	1.85E-04	1281	1.000	3.970	0.037	6.10E-12
H11	6.73	0.1	0.0E+00	7.771E-05	1.14E-04	1281	0.888	5.470	0.007	6.23E-12
H17	7.97	0.01	5.0E-03	5.49E-06	5.01E-03	1281	0.719	1.194	0.492	1.19E-13
H17A	7.55	0.01	1.0E-03	2.060E-05	1.04E-03	1281	0.719	1.392	0.214	5.19E-13
H17B	7.30	0.01	2.0E-04	5.941E-05	3.19E-04	1281	0.719	1.390	0.105	1.49E-12
H17C	7.32	0.01	0.0E+00	9.442E-05	1.50E-04	1281	0.719	1.390	0.081	2.38E-12
H25	7.32	0.01	0.0E+00	1.034E-04	1.57E-04	1281	1.007	3.379	0.068	4.52E-12
H25A	7.07	0.01	0.0E+00	1.028E-04	1.05E-04	1281	1.007	4.793	0.031	6.37E-12
H25B	7.33	0.01	0.0E+00	1.025E-04	1.45E-04	1281	1.007	2.956	0.058	3.92E-12
H28	7.73	1	5.0E-03	4.281E-05	5.09E-03	1281	0.718	1.197	0.505	9.29E-13
H29	6.78	0.01	0.0E+00	1.393E-04	1.19E-04	1281	0.695	3.98	0.031	1.04E-11
H29A	6.92	0.01	0.0E+00	1.629E-04	1.66E-04	1281	0.675	1.6916	0.068	5.31E-12
H30	6.44	0.1	0.0E+00	1.015E-04	nd	1281	0.725	3.976	0.001	7.24E-12
H30A	6.71	0.1	0.0E+00	1.313E-04	nd	1281	0.708	1.689	0.010	4.07E-12
H31	7.55	1	1.0E-03	1.490E-04	1.30E-03	1281	0.717	1.403	0.288	3.80E-12

Exp. Sol.	**pH**	**NaCl** [mol/kg]	**$NaHCO_3$** [mol/kg]	**Δ [Mg]** [mol/kg]	**Alk** [mol/kg]	**BET s. area** [cm^2/g]	**$MgCO_3$ mass** [g]	**FFR** [g/min]	**Ω**	**r_d** [$mol/cm^2/s$]
H32	7.51	1	2.0E-04	2.122E-04	6.24E-04	1281	0.658	1.394	0.156	5.85E-12
H32A	7.55	1	0.0E+00	2.281E-04	4.56E-04	1281	0.623	1.397	0.112	6.65E-12
H34	7.51	1	0.0E+00	3.260E-04	6.02E-04	1281	0.724	2.008	0.231	1.18E-11
H34A	7.43	1	0.0E+00	2.772E-04	5.04E-04	1281	0.696	4.021	0.136	2.08E-11
H35	7.34	1	0.0E+00	2.675E-04	4.35E-04	1281	0.884	5.504	0.095	2.17E-11
H35A	7.39	1	0.0E+00	3.056E-04	5.11E-04	1281	0.845	2.509	0.146	1.18E-11
H36	7.08	1	0.0E+00	2.324E-04	3.15E-04	1281	0.739	6.530	0.037	2.67E-11
H36A	7.23	1	0.0E+00	2.650E-04	3.80E-04	1281	0.707	4.481	0.068	2.18E-11
H37	7.29	0.1	0.0E+00	1.969E-04	2.31E-04	1281	1.044	2.842	0.088	6.97E-12
H37A	7.17	0.1	0.0E+00	1.862E-04	1.72E-04	1281	1.002	3.968	0.047	9.60E-12
H38	7.19	1	0.0E+00	2.857E-04	3.71E-04	1281	0.734	6.993	0.064	3.54E-11
H38A	7.23	1	0.0E+00	2.982E-04	3.97E-04	1281	0.693	5.020	0.078	2.81E-11
H39	6.99	1	0.0E+00	2.620E-04	2.74E-04	1281	0.454	7.503	0.031	5.63E-11
H39A	7.06	1	0.0E+00	2.798E-04	3.10E-04	1281	0.416	5.020	0.041	4.39E-11
H40	6.89	1	0.0E+00	2.779E-04	2.56E-04	1281	0.453	8.058	0.024	6.44E-11
H40A	6.91	1	0.0E+00	2.746E-04	2.49E-04	1281	0.413	6.091	0.024	5.27E-11
H43	6.82	0.1	0.0E+00	2.064E-04	nd	1281	0.657	4.983	0.081	2.04E-11
H44	6.42	0.1	0.0E+00	2.199E-04	nd	1281	0.623	5.963	0.037	2.74E-11
H45	6.30	0.1	0.0E+00	2.713E-04	nd	1281	0.654	4.968	0.044	2.68E-11
H46	4.57	0.1	0.0E+00	2.216E-04	nd	1281	0.625	6.429	0.001	2.96E-11
H47	6.31	0.1	0.0E+00	2.053E-04	nd	971	0.634	6.983	0.027	3.88E-11
H48	7.81	0.1	0.0E+00	3.070E-05	1.06E-03	971	0.854	0.795	0.220	4.91E-13
H48C	7.40	0.1	0.0E+00	5.929E-05	6.19E-04	971	0.854	0.995	0.115	1.19E-12
H49	6.21	0.1	0.0E+00	2.527E-04	nd	971	0.646	5.762	0.010	3.87E-11
H50	5.98	0.1	0.0E+00	2.675E-04	nd	971	0.642	5.467	0.020	3.91E-11
H51	4.61	0.11	0.0E+00	3.143E-04	nd	971	0.658	5.433	0.001	4.45E-11
H52B	7.97	0.1	7.0E-03	2.35E-06	0.00703	971	1.421	0.992	0.156	2.81E-14
H53	4.35	0.11	0.0E+00	3.027E-04	nd	971	0.704	5.197	0.001	3.83E-11
H53A	7.51	0.11	0.0E+00	1.199E-04	2.40E-04	971	0.637	2.788	0.064	9.01E-12
H55	4.26	0.1	0.0E+00	2.992E-04	nd	971	0.431	6.015	0.001	7.16E-11
H56	7.69	1	7.0E-03	4.785E-05	7.10E-04	971	1.004	0.801	0.732	6.56E-13
H56A	5.36	1	0.0E+00	7.392E-04	4.21E-03	971	0.993	7.007	0.001	8.95E-11
H57	7.24	0.11	0.0E+00	1.761E-04	1.03E-02	971	0.524	5.922	0.115	3.42E-11
H58	5.36	0.11	0.0E+00	5.020E-04	7.17E-03	971	0.529	6.364	0.001	1.04E-10
H59	6.12	1	0.0E+00	4.574E-04	9.97E-03	971	0.477	7.020	0.010	1.16E-10
M1A	7.59	0	1.0E-03	2.874E-05	1.06E-03	2882	0.539	0.572	0.478	2.11E-15
M2	7.61	0.1	0.0E+00	1.935E-04	3.87E-04	2882	0.620	2.790	0.258	5.03E-12
M2A	7.59	0.1	2.0E-04	1.455E-04	4.91E-04	2882	0.620	2.790	0.281	3.78E-12
M2B	7.61	0.1	1.0E-03	7.539E-05	1.15E-03	2882	0.620	2.786	0.431	1.96E-12
M2C	7.84	0.1	5.0E-03	1.842E-05	5.04E-03	2882	0.620	2.786	0.722	4.78E-13
Mt4	7.47	0.1	0.0E+00	1.387E-04	2.77E-04	1260	0.549	1.360	0.098	4.55E-12
Mt5	7.55	0.1	0.0E+00	1.563E-04	3.30E-04	1260	0.566	1.369	0.156	5.00E-12
Mt5-A	7.47	0.1	2.0E-04	1.145E-04	4.38E-04	1260	0.566	1.417	0.163	3.79E-12
Mt5-B	7.63	0.1	1.0E-03	4.782E-05	1.09E-03	1260	0.566	1.420	0.271	1.59E-12
Mt5-C	7.90	0.1	5.0E-03	1.003E-05	5.10E-03	1260	0.566	1.423	0.441	3.34E-13
Mt5-D	7.55	0.1	0.0E+00	1.545E-04	3.35E-04	1260	0.566	1.454	0.159	5.25E-12
Mt7	7.28	0.1	0.0E+00	4.504E-05	3.01E-04	1260	0.856	0.730	0.475	5.08E-13

4. Results

4.1 Effect of $a_{CO_3^{2-}}$, pH and ionic strength

Magnesite dissolution rates measured at 150 and 200 °C are listed in Table 4-5 and plotted as a function of $a_{CO_3^{2-}}$ and pH in Figure 3. It can be seen that magnesite dissolution rates considerably decrease with increasing activity of both CO_3^{2-} and OH^-. The logarithmic plots of Figure 3a-b illustrate the apparent strong dependence of measured overall dissolution rates on CO_3^{2-} activity: rates decrease approximately by three orders of magnitude for a corresponding increase of $a_{CO_3^{2-}}$ from ~10^{-7} to 10^{-3}. Note, however, that for the strongest CO_3^{2-} activities part of this decrease is due to the effect of chemical affinity, as reacting solutions are close to equilibrium (see the corresponding scale of saturation state reported on the upper part of the plots on Fig. 3 for I = 0.1 M). The linear regressions of datapoints represented by the dashed lines drawn on the plots exhibit a slope close to 1 both at 150 and 200 °C. Inhibition of both magnesite and dolomite dissolution by carbonate species was first observed by Pokrovsky and Schott (1999, 2001) and Pokrovsky et al. (2005, 2009). These authors showed that, for example, at 25 °C and far from equilibrium conditions ($\Omega < 0.005$), inhibition of dissolution starts for $a_{CO_3^{2-}} > 10^{-4.5}$ and $a_{CO_3^{2-}} > 10^{-5.5}$ for magnesite and dolomite respectively. Despite the scatter of data, it can be also seen in Fig. 3a that dissolution rates at 150 °C increase by about one order of magnitude with ionic strength increasing from 0.01 to 1 M, consistently with the dashed lines drawn through the symbols in Fig 3a. Less rate data were obtained at 200 °C (Fig. 3b), but they are less dispersed than the rates determined at 150 °C. This is probably due to the use of pure synthetic magnesite having a quasi-ideal crystal shape for all experiments performed at 200 °C, whereas the presence of impurities and various physical heterogeneities in the natural samples (see Fig. 1b) are likely to be responsible for the pronounced scatter among the data at 150°C.

A similar strong decrease of magnesite dissolution rates is observed when measured rates are plotted as a function of the corresponding solution pH (Fig.3c-d), which suggests inhibition of dissolution by hydroxyl ions. Comparison between Fig. 3a and 3c and 3b and 3d suggests that the impact of pH on magnesite dissolution rates is stronger than that of CO_3^{2-}.

To distinguish the effect of aqueous CO_3^{2-} and OH^- on dissolution rates from that of chemical affinity, magnesite forward dissolution rates (r_+) can be deduced from overall rates

(r_d) using Eqn. 7 with $n = 4$, assuming that magnesite dissolution mechanism does not change with T (Pokrovsky and Schott, 1999, Pokrovsky et al., 2009). Magnesite forward dissolution rates (r_+) thus obtained are plotted as function of $a_{CO_3^{2-}}$ and pH in Figure 4 for an ionic strength of 0.1 M. The plots of Fig. 4 show that dissolution rates decrease with both increasing pH and carbonate activity.

4.2 Effect of temperature on dissolution rates

The plots of Figures 3 and 4 show that both magnesite overall and forward dissolution rates at 200 °C are the same or lower than those measured at 150 °C, which implies negative values (or a value of zero) for the apparent activation energy of magnesite dissolution in this temperature interval. Apparent negative activation energies have been also determined by Pokrovsky et al. (2009) for calcite, dolomite and magnesite in acidic to neutral pH in the 100-150 °C temperature interval. These authors explained the decrease of the apparent activation energy of dissolution with a decreasing enthalpy of surface protonation reaction with increasing T as a result of a successful competition of Na ions against H^+ for sorption on $>CO_3^-$ sites, producing a decrease of the concentration of rate controlling $>CO_3H°$ sites.

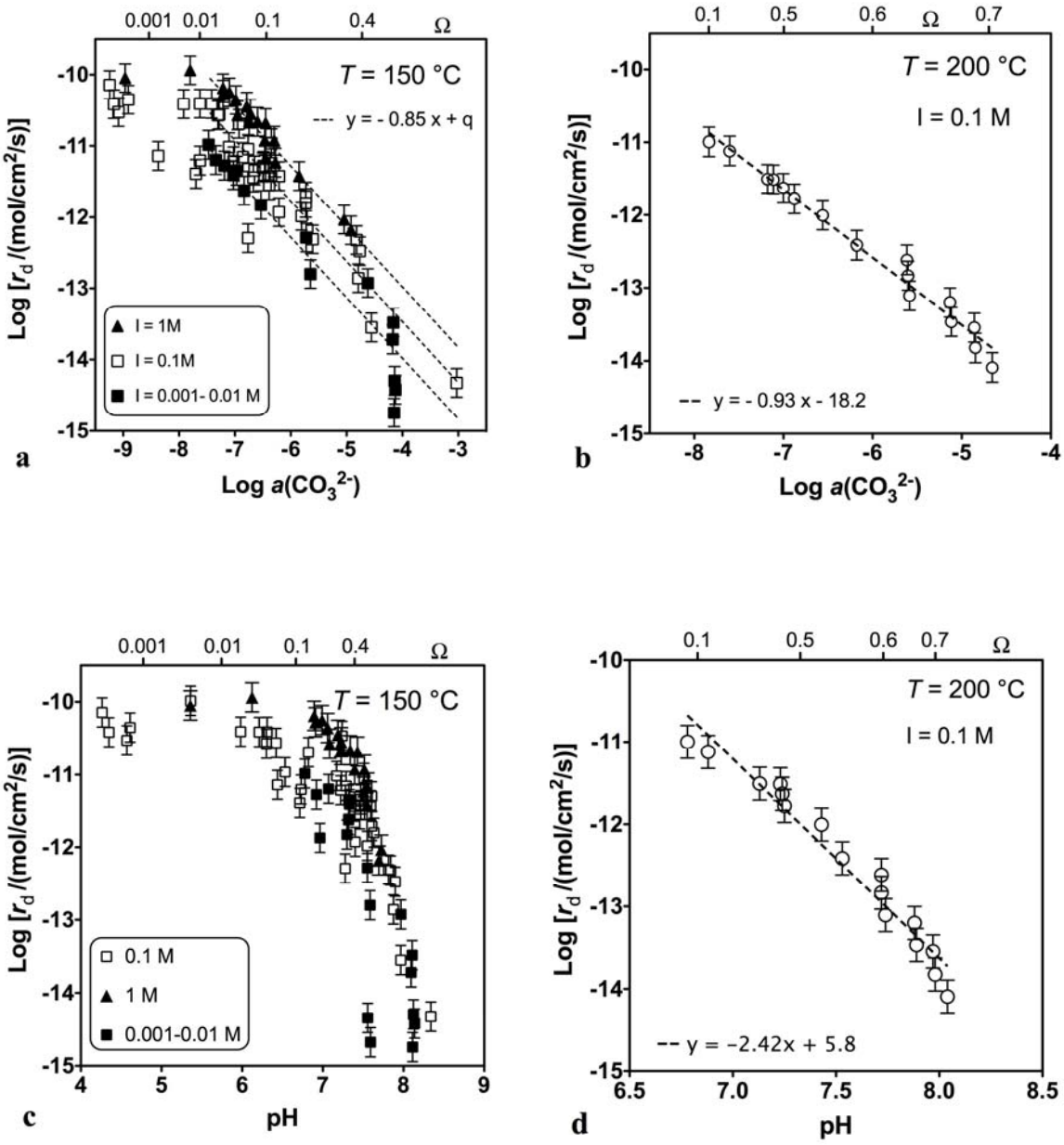

Figure 3. Magnesite dissolution rates plotted against corresponding CO_3^{2-} activity at 150 (**a**) and 200 °C (**b**) and and as a function of the solution pH (**c-d).** At both temperatures rates strongly decrease with increasing CO_3^{2-} activity and increasing pH (OH^- activity), indicating the inhibiting effect of this aqueous species. Plot (a) and (c) also show how dissolution rates tend to increase with increasing ionic strength. Dashed lines represent linear regression lines for the different groups of datapoints. Error bars on symbols correspond to a 0.2 log unit uncertainty in measured rates.

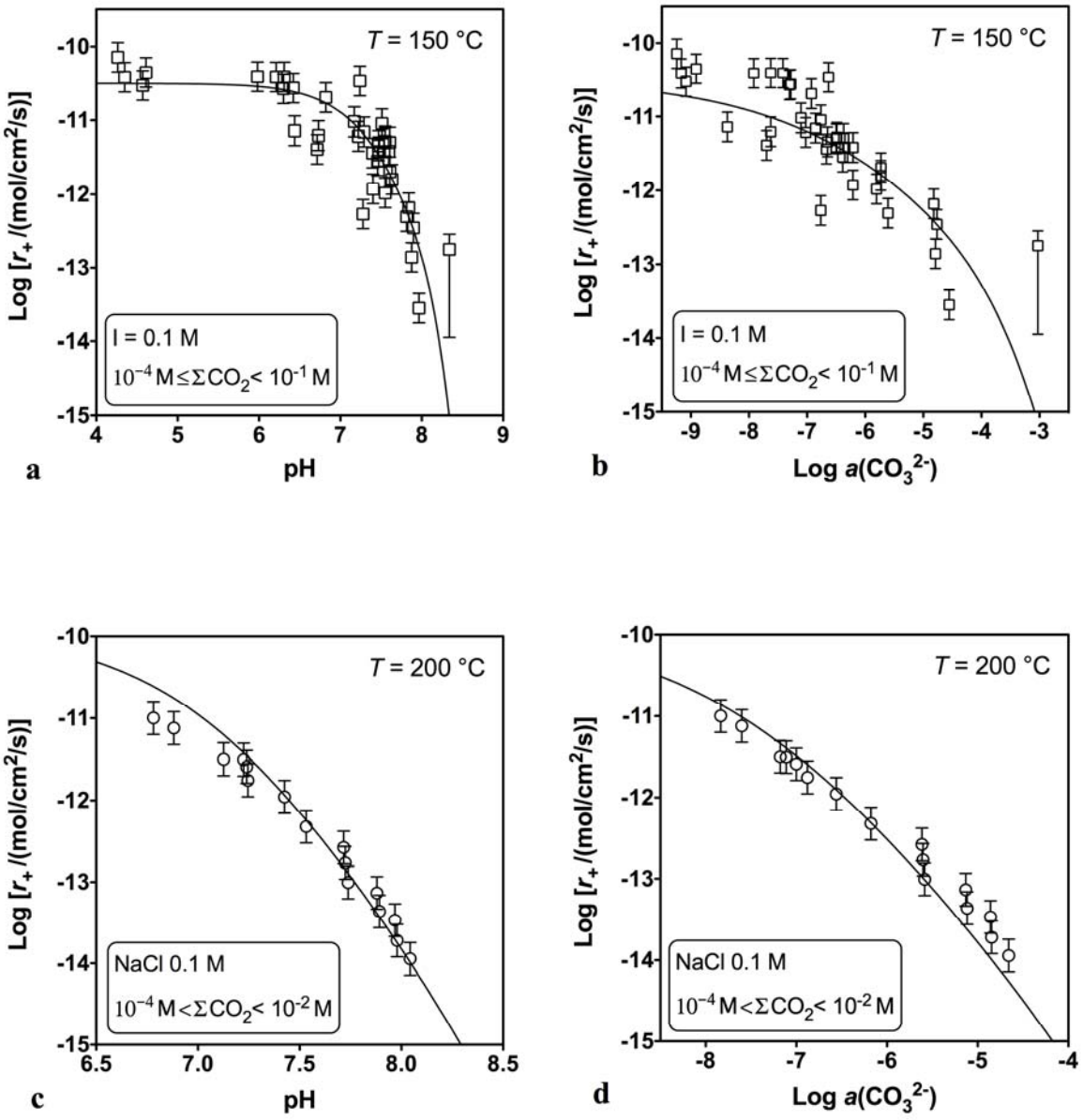

Figure 4. Magnesite forward dissolution rates at 150 (**a-b**) and 200 °C (**c-d**) calculated assuming ***n*** = 4, plotted as a function of carbonate activity and corresponding pH. Solid lines represent the fit of the data obtained with Eqn. (15). The larger error bar relative to the experiment H6 stems from the uncertainty of its saturation state.

4. Modeling of magnesite dissolution as a function of solution composition, chemical affinity and temperature

5.1 Dependence of magnesite dissolution rates on pH and CO_3^{2-} activity

Eqn. (6) implies that in neutral to alkaline conditions magnesite dissolution rate at far from equilibrium conditions is proportional to the concentration of $>MgOH_2^+$ surface sites to the fourth power:

$$r_d = r_+ = k^+_{Mg} \{>MgOH_2^+\}^4 . \qquad (11)$$

In carbonate-bearing solutions both surface carbonation and hydrolysis can lead to a decrease of $>MgOH_2^+$ surface concentration and thus to an inhibition of magnesite dissolution:

$$>MgOH° + H_2O = >MgOH_2^+ + OH^- \quad , \qquad K_{OH} \qquad (12)$$

$$>MgCO_3^- + H_2O = >MgOH_2^+ + CO_3^{2-} , \qquad K_{CO3} \qquad (13)$$

Consequently, magnesite dissolution rates are a function of both CO_3^{2-} and OH^- activities. Determination of the thermodynamic constants of reaction (12) and (13) is necessary to quantify the effect of surface carbonation and hydrolysis on the rates of dissolution. Combining Eqn. (11) with Eqn. (12) and (13) and expressing the conservation of metal sites at magnesite surface:

$$s = \{>MgOH_2^+\} + \{>MgCO_3^-\} + \{>MgOH°\}, \qquad (14)$$

allows to express magnesite far from equilibrium dissolution rates as a function of CO_3^{2-} and OH^- activities, as follows:

$$r_+ = k^+_{Mg} \left(\frac{K_{CO3} K_{OH} a_{H^+}}{K_{CO3} + K_{CO3} K_{OH} a_{H^+} + K_{OH} a_{H^+} a_{CO_3^{2-}}} \right)^n , \qquad (15)$$

where k^+_{Mg} is a rate constant including the total concentration of Mg-sites ($k^+_{Mg} = k^* \cdot s$), K_{OH} and K_{CO3} represent the thermodynamic constants of reaction (12) and (13) respectively, and a_i stands for the activity of subscripted aqueous species.

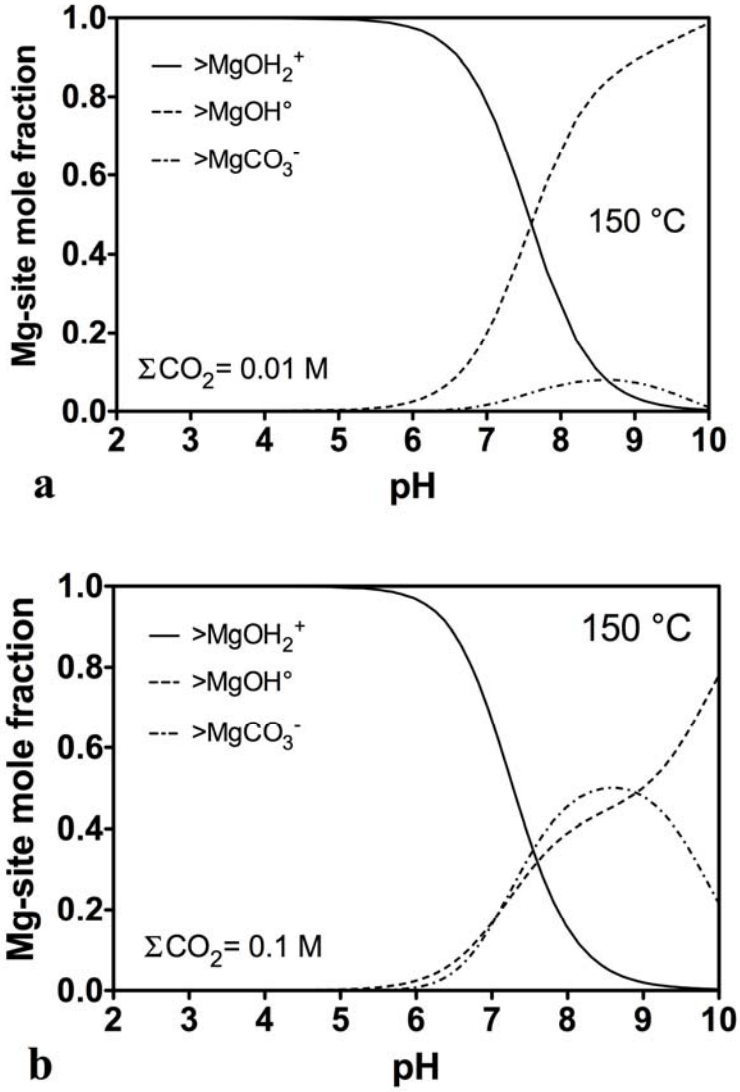

Figure 5. Mg surface species distribution as a function of solution pH at 150 °C, calculated using the formation constants (K_{CO3} and K_{OH}) determined in this study for an ionic strength equal to 0.1 M, a Mg concentration of 10^{-5} mol/kg and for two different contents of dissolved inorganic carbon: a) 0.01 M ; b) 0.1 M.

Modeling the dependence of dissolution rates on CO_3^{2-} activity and pH requires the determination of the equilibrium constants and enthalpies of reaction (12) and (13) at the conditions of interest. Values of the constants K_{OH} and K_{CO3} have been deduced from surface titration and Zeta potential measurements at 25 °C (Pokrovsky et al., 1999a) but are not currently available at higher temperature. Nonetheless values of K_{CO3} and $\Delta H_{r(CO3)}$ have been approximated from magnesite precipitation rates determined as a function of T and CO_3^{2-}

activity by Saldi (2009). At 150 °C k^{+}_{Mg} was deduced from the rates of dissolution at acidic conditions measured in this study (4 < pH < 6), whereas the value of this rate constant at 200 °C was calculated from the value at 150 °C using the Arrhenius equation and assuming a ΔE_a of 46 kJ/mol (Pokrovsky et al., 2009). The values of k^{+}_{Mg} thus obtained are equal to $10^{-10.5}$ and $10^{-9.9}$ mol/cm^2/s, at 150 and 200 °C respectively, and are also in good agreement with the extrapolation which can be obtained from using the corresponding rate constant determined at 25 °C by Pokrovsky and Schott (1999). The only fitting parameter is K_{OH}, whose value was determined from a fit of dissolution rates as a function of temperature and solution composition. The achieved fits of the dissolution rates as a function of pH and $a_{CO_3^{2-}}$ are displayed by solid lines in the plots of Figure 4. A value of Log K_{OH} equal to 7.6 was found to provide the best fit on both pH and CO_3^{2-} plots at 150 °C; an uncertainty of ± 0.3 log units is associated to this value resulting from the important data dispersion. A Log K_{OH} of 7.1 ± 0.1 was instead determined through the fit of the rate data at 200 °C. The values of the constants used to describe the dependence of dissolution rates on solution composition, according to Eqn. (15), are summarized in Table 6. Within the framework of the three Mg-surface-sites model the effect of pH and ΣCO_2 on magnesite surface speciation can be visualized in the plot of Figure 5 where the distribution of these species as a function of pH is illustrated for two different contents of dissolved inorganic carbon at 150 °C. It can be seen that increasing the solution pH from 7 to 8 reduces by 50% the concentration of $>MgOH_2^+$, as a consequence of the formation of >MgOH° in solutions relatively poor in total dissolved carbon ($\Sigma CO_2 \leq 0.01$ M) but also as the result of the formation of $>MgCO_3^-$ sites in carbon rich solutions (ΣCO_2 =0.1 M, Fig. 5b).

Table 6. Summary of the constants used to describe magnesite dissolution rates at 150 and 200 °C at I = 0.1 M.

T (°C)	Log K_{CO3}	Log K_{OH}	Log k^{+}_{Mg} [mol/cm^2/s]
150	-3.9	7.6 ± 0.3	-10.5 ± 0.2
200	-4.4	7.1 ± 0.1	-9.9 ± 0.1

The dependence of measured magnesite dissolution rates on chemical affinity is plotted in Figure 6 for experimental data at 150 °C. The plot shows that the rates significantly

decrease for values of chemical affinity ≤ 15 kJ/mol, approaching 0 for A = 0 kJ/mol. On the same plot have been reported the rates calculated using Eqn. 7, which is derived from the Plummer et al. (1978) model (dashed line), and those obtained from Eqn. (15), for a ΣCO_2 of 10^{-4} and 0.1 M at the same ionic strength of NaCl (0.1 M). For both models a value of rate constant equal to 3.2×10^{-11} mol/cm^2/s was used to draw the rate curves predicted by Eqn. (7) and (15). This value of k^+_{Mg} is also consistent with the rates measured at the same temperature by Pokrovsky et al. (2009) at far from equilibrium conditions, as reported on the graph. It can be noticed that experimental rates are inconsistent with those predicted by Eqn. (7), but are located in the domain defined by Eqn. (15) with $\Sigma CO_2 = 10^{-4}$ and 0.1 M for I = 0.1 M NaCl. This confirms the important impact of solution composition (pH and $a_{CO_3^{2-}}$) on dissolution at near neutral to basic conditions.

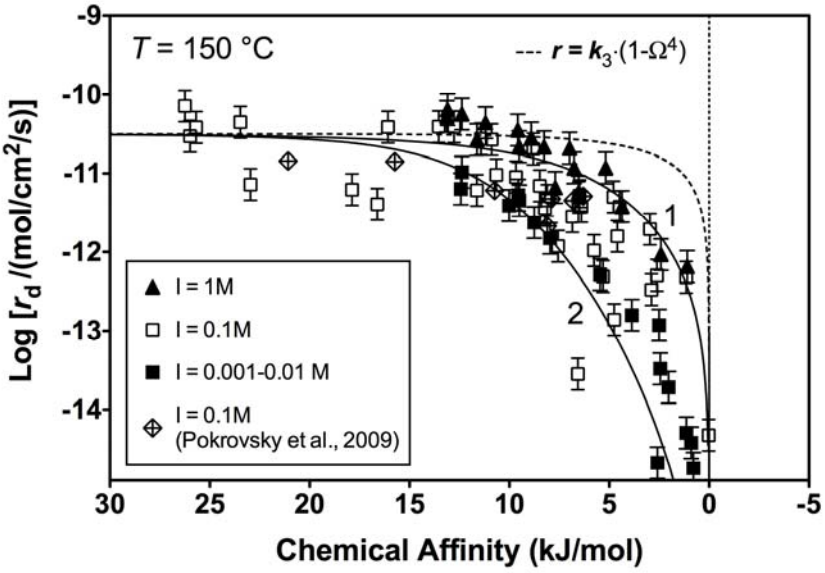

Figure 6. Magnesite steady state dissolution rates as a function of chemical affinity at 150 °C for the different ionic strength investigated. The dashed line and the solid lines represent the dissolution rates predicted by Eqn. (7) and (15) respectively. Rates were calculated using a dissolution rate constant of 3.2×10^{-11} mol/cm^2/s, as obtained from the analysis of rates measured in NaCl 0.1 M medium. Solid line 1 represents the rates calculated according to a total dissolved carbon (ΣCO_2) of 10^{-4} M, whereas solid line 2 is relative to a ΣCO2 equal to 0.1 M. Error bars on data symbols correspond to ± 0.2 log units.

5.2 Effect of temperature on magnesite dissolution rates

Examination of Eqn. (15) shows that magnesite dissolution rates are a function of both $\boldsymbol{E}_a$, the activation energy for the rate constant $\boldsymbol{k}^+_{Mg}$, and $\Delta H_{r(CO3)}$ and $\Delta H_{r(OH)}$, the enthalpies of $>MgCO_3^-$ and >MgOH° formation reactions. Depending on the values of $\boldsymbol{E}_a$, $\Delta H_{r(CO3)}$ and $\Delta H_{r(OH)}$, the apparent activation energy for magnesite dissolution can be positive or negative, and magnesite dissolution can increase, decrease, or remain constant with increasing *T*.

For example, if for sake of simplicity we neglect in a first step the formation of >MgOH° sites, magnesite dissolution rate at a given temperature can be approximated by (see the derivation in the appendix):

$$\boldsymbol{r}_+ = \boldsymbol{k}^*_{Mg} \cdot e^{-\boldsymbol{E}_a / \boldsymbol{RT}} \cdot \left(\frac{\boldsymbol{s} \cdot K^*_{CO3} \cdot e^{-\Delta H_{r(CO3)} / \boldsymbol{RT}}}{\boldsymbol{a}_{CO_3^{2-}}} \right)^{\boldsymbol{n}}, \qquad (16)$$

where $\boldsymbol{k}^*_{Mg}$ and K^*_{CO3} represent respectively the dissolution rate constant and the equilibrium constant of reaction (13) at reference temperature, $\Delta H_{r(CO3)}$ represents the enthalpy of this reaction, $\boldsymbol{n}$ refers to the reaction order of the dissolution reaction and $\boldsymbol{s}$ stands for the total density of metal surface sites. Studying the variation of magnesite dissolution rate using Eqn. (16) together with the enthalpy of reaction (13), conditions at which the rates of dissolution don't change or decrease with increasing temperature can be assessed. In the present study the slight decrease of dissolution rates with increasing temperature is accounted for by the decrease of the constants of Eqns. (12) and (13), which reflects a decrease of the surface density of the rate controlling species ($>MgOH_2^+$). In particular the increasing concentration of >MgOH° at the expenses of $>MgOH_2^+$ results more effective than the formation of $>MgCO_3^-$ in inhibiting dissolution with increasing temperature for low to moderate values of ΣCO_2. The variation of dissolution rates between 150 and 200 °C described by the variation of both K_{CO3} and K_{OH} corresponds to enthalpies of about -33 kJ/mol and -38.3 kJ/mol for reaction (12) and (13) respectively. The absolute values of the enthalpies estimated for these two reactions are lower than the enthalpies of the corresponding reactions involving dissolved species (see Appendix). Nevertheless, analogy with the aqueous solution is helpful to understand direction and *T* dependence of the reactions occurring at the mineral/water interface.

6. Concluding remarks

Magnesite dissolution rates measured at 150 and 200 °C and at neutral to alkaline conditions have been interpreted according to the surface complexation model developed by Pokrovsky et al. (1999), taking account of the dependence of magnesium surface sites distribution on solution composition. Increasing formation of >MgOH° and $>MgCO_3^-$ surface species at the expenses of the rate controlling $>MgOH_2^+$ explains both dissolution rate decrease with increasing T and OH^- and CO_3^{2-} activity, thus resulting in an apparent effect of chemical affinity at far from equilibrium conditions. Description of the rate data within this framework allowed the extension of the magnesite dissolution rate equation, originally developed at 25 °C, to higher temperatures by including in it the increasingly important effect of solution pH. Decrease of magnesite dissolution rates with increasing temperature from 150 to 200 °C can be explained by the decrease of K_{CO3} and K_{OH}, the constants of formation of the rate controlling species, $>MgOH_2^+$.

Alkaline, CO_2 rich solutions together with temperatures ≥ 100 °C represent favorable conditions for CO_2 geological sequestration in deep Mg-rich carbonate aquifers. Achievement of these conditions as a consequence of water-rock interaction during the final stage of the sequestration process may enhance its effectiveness by ensuring a higher stability of the Mg-carbonate phases constituting the sedimentary host reservoir.

Acknowledgements

We would like to thank Jean-Claude Harrichoury and Alain Castillo for the constant technical assistance throughout the duration of the experimental work, Carole Causserand for her generous help during the analytical part of the work, and Philippe de Parseval for providing a sample of the Huaziyu magnesite. We are also grateful to Pascale Bénézeth, Jean-Louis Dandurand,and Robert Gout for helpful discussions during the course of this study. Support from Centre National de la Recherche Scientifique, and the European Community through the MIR Early Stage Training Network (MEST-CT-2005-021120) is gratefully acknowledged.

7. References

Aagaard, P. and Helgeson, H. C. (1982). Thermodynamic and kinetic constraints on reaction-rates among minerals and aqueous solutions: I. Theoretical considerations. *Am. J. Sci.* **282**, 237-285.

Alkattan M., Oelkers E. H., Dandurand J.-L., and Schott J. (1998). An experimental study of calcite and limestone dissolution rates as a function of pH from -1 to 3 and temperature from 25 to 80 °C. *Chem. Geol.* **151**, 199-214.

Brunauer S., Emmet P. H., and Teller E. (1938). Adsorption of gases in multimolecular layers. *J. Am. Chem. Soc.*, **60**, 309-319.

Busenberg, E., Plummer, L.N., 1982. The kinetics of dissolution of dolomite in CO_2-H_2O systems at 1.5 to 65°C and 0 to 1 atm pCO_2. *Amer. J. Sci.* **282**, 45-78.

Chou, L., Garrels, R.M., Wollast, R. (1989). Comparative study of the kinetics and mechanisms of dissolution of carbonate minerals. *Chem. Geo.* **78**, 269-282.

Devidal, J.-L., Schott, J., and Dandurand, J.-L. (1997). An experimental study of kaolinite dissolution and precipitation kinetics as a function of chemical affinity and solution composition at 150°C, 40 bars, and pH 2, 6.8, and 7.8. *Geochim. Cosmochim. Acta* **61**, 5165-5186.

Dove P.M. and Crerar D.A. (1990). Kinetics of quartz dissolution in electrolyte solution using a hydrothermal mixed flow reactor. *Geochim. Cosmochim. Acta* **54**, 955-969.

Eyring, H. (1935). The activated complex in chemical reactions. *J. Chem. Phys.* **3,** 107-115.

Gautier, J.-M., Oelkers, E. H., and Schott, J. (1994). Experimental study of K-feldspar dissolution rates as a function of chemical affinity at 150°C and pH 9. *Geochim. Cosmochim. Acta* **58**, 4549-4560.

Higgins, S. R., Jordan, G., and Eggleston, C. M. (2002). Dissolution kinetics of magnesite in acidic aqueous solution: a hydrothermal atomic force microscopy study assessing step kinetics and dissolution flux. *Geochim. Cosmochim. Acta* **66**, 3201-3210.

Jiang, S. Y., Chen C.X., Jiang Y. H., Dai B. Z., and Ni P. (2004). Geochemistry and genetic model for the giant magnesite deposits in the eastern Liaoning province, China. *Acta Petrol. Sin.* **20 (4)**, 765-772.

Jordan, G., Higgins, S. R., Eggleston, C. M., Knauss, K. G., and Schmahl, W. W. (2001). Dissolution kinetics of magnesite in acidic aqueous solution, a hydrothermal atomic force microscopy (HAFM) study: step orientation and kink dynamics. *Geochim. Cosmochim. Acta* **65**, 4257-4266.

Jordan, G., Pokrovsky, O. S., Guichet, X., and Schmahl, W. W. (2007). Organic and inorganic ligand effects on magnesite dissolution at 100 °C and pH = 5 to 10. *Chem. Geo.* **242**, 484-496.

Lasaga A. C. (1981). Transition State Theory. *Rev. Min.* **8**, 135-169.

Morse, J.W., Arvidson, R.S. (2002). The dissolution kinetics of major sedimentary carbonate minerals. Earth Science Rev. **58**, 51-84.

Oelkers E.H., Schott J., and Devidal J.-L. (1994). The effect of aluminum, pH, and chemical affinity on the rates of alumino-silicate dissolution reactions. *Geochim. Cosmochim. Acta* **58**, 2011-2024.

Palmer D. A. and Wesolowski D. J. (1997). Potentiometric measurements of the first hydrolysis quotient of magnesium (II) to 250 °C and 5 molal ionic strength (NaCl). *J. Sol. Chem.* **26** (2), 217-232).

Parkhurst D. L. and Appelo C. A. J. (1999).User's guide to PHREEQC (version 2) - a computer program for speciation, batch-reaction,one-dimensional transport, and inverse geochemical calculations. U.S. Geological Survey Water-resources Investigation Report 99-4259, pp. 312.

Plummer, L. N., Wigley, T. M. L., and Parkhurst, D. L. (1978). Kinetics of calcite dissolution in CO_2-water system at 5 °C to 60 °C and 0.0 to 1.0 atm CO_2. *Am. J. Sci.* **278**, 179-216.

Pokrovsky, O.S. and Schott, J. (1999). Processes at the magnesium-bearing carbonates solution interface. II Kinetics and mechanism of magnesite dissolution. *Geochim. Cosmochim. Acta* **63**, 881-897.

Pokrovsky O.S., Golubev S. V., Schott J. and Castillo A. (2009). Calcite, dolomite and magnesite dissolution kinetics in aqueous solutions at acid to circumneutral pH, 25 to 150 °C and 1 to 55 atm pCO_2: new constraints on CO_2 sequestration in sedimentary basins. *Chem. Geo.* **In Press, Corrected Proof**.

Pokrovsky O.S., Mielczarski J.A., and Schott J. (2001) Surface speciation of dolomite and

calcite in aqueous solutions, in *Encyclopedia of Surface and Colloid Science.* Ed. A. Hubbard. Marcel Dekker Inc., p. 5081-5095.

Pokrovsky O.S., Mielczarski J.A., and Schott J. (2001) Surface speciation of dolomite and calcite in aqueous solutions, in *Encyclopedia of Surface and Colloid Science.* Ed. A. Hubbard. Marcel Dekker Inc., p. 5081-5095.

Pokrovsky, O. S. and Schott, J. (2001). Kinetics and mechanism of dolomite dissolution in neutral to alkaline solutions revisited. *Am. J. Sci.* **301**, 597-626.

Pokrovsky, O. S., Golubev, S. V., and Jordan, G. (2009a). Effect of organic and inorganic ligands on calcite and magnesite dissolution rates at 60 °C and 30 atm pCO2. *Chem. Geo.* **In Press, Corrected Proof**.

Pokrovsky, O. S., Golubev, S. V., and Schott, J. (2005). Dissolution kinetics of calcite, dolomite and magnesite at 25 °C and 0 to 50 atm pCO2. *Chem. Geo.* **217**, 239-255.

Pokrovsky, O. S., Schott, J., and Thomas, F. (1999a). Processes at the magnesium-bearing carbonates/solution interface. I. A surface speciation model for magnesite. *Geochim. Cosmochim. Acta* **63**, 863-880.

Pokrovsky, O. S., Schott, J., and Thomas, F. (1999b). Dolomite surface speciation and reactivity in aquatic systems. *Geochim. Cosmochim. Acta* **63**, 3133-3143.

Pokrovsky, O.S. and Schott, J. (2002). Surface chemistry and dissolution mechanism of divalent metal carbonates. *Environ. Sci. Technol.* **36**, 426-432.

Saldi, G.D. (2009) Les cinétiques de dissolution et précipitation de la magnesite aux conditions hydrothermales. Thèse de l'Université Paul-Sabatier, Toulouse, 184 p.

Schott J., Pokrovsky O. S., and Oelkers E. H. (2009). The link between mineral dissolution/precipitation kinetics and solution chemistry. In "Thermodynamics and kinetics of water-rock interaction", *Rev. Min.***70**, 207-258.

Shock, E. L., Sassani, D. C., Willis, M., and Sverjensky, D. A. (1997). Inorganic species in geologic fluids: Correlations among standard molal thermodynamic properties of aqueous ions and hydroxide complexes. *Geochim. Cosmochim. Acta* **61**, 907-950.

Sverjensky D. A., Shock E. L., and Helgeson H. C. (1997). Prediction of the thermodynamic properties of aqueous metal complexes to 1000 °C and 5 kb. *Goechim. Cosmochim. Acta* **61**, 1359-1412.

Talman, S.J., Wiwchar, B., Gunter, W.D., Scarge, C.M. , 1990. Dissolution kinetics of calcite in the $H_2O - CO_2$ system along the steam saturation curve to 210°C. In: Spencer, R.J. and Chou, I.M. (Eds.), Fluid-Mineral Interactions: A Tribute to H.P. Eugster. Geochem. Soc. Spec. Publ. Series, 2, 41-55.

Van Cappellen, P., Charlet, L., Stumm, W., and Wersin, P. (1993). A surface complexation model of the carbonate mineral-aqueous solution interface. *Geochim. Cosmochim. Acta* **57**, 3505-3518.

Villegas-Jiménez A., Mucci A., Pokrovsky O. S., and Schott J. (2009). Defining reactives sites on hidrated mineral surfaces: rhombohedral carbonate minerals. *Geochim. Cosmochim. Acta*, in press.

Wollast, R., 1990. Rate and mechanism of dissolution of carbonates in the system $CaCO_3 - MgCO_3$, *in* Stumm, W., editor, Aquatic Chemical Kinetics: Reaction Rates of Processes in Natural Waters: New York, J. Wiley & Sons, p. 431-445.

Zhang, R., Hu, S., Zhang, X., and Yu., W., 2007. Dissolution kinetics of dolomite in water at elevated temperatures. *Aquat. Geochem.* **13**, 309-338.

Appendix: Temperature dependence of magnesite dissolution reactions.

In circumneutral to basic conditions carbonate dissolution is promoted by the hydration of divalent metal sites, according to (Pokrovsky and Schott, 1999a, 2002):

$$r_{+} = k^{+}_{Mg} \{>MeOH_2^{+}\}^{n} \quad \text{(A1)}$$

where, in the case of magnesite, Me is substituted by Mg, n is equal to 4, and the formation of the corresponding hydrated metal sites can be described by the following reactions:

$$>MgOH^{\circ} + H_2O = >MgOH_2^{+} + OH^{-} \quad , \quad \text{(A2)}$$

$$>MgCO_3^{-} + H_2O = >MgOH_2^{+} + CO_3^{2-} \quad , \quad \text{(A3)}$$

whose intrinsic stability constants are given respectively by:

$$K_{OH} = \frac{\{> MgOH_2^{+}\} a_{OH^{-}}}{\{> MgOH^{\circ}\}} \quad \text{and} \quad K_{CO3} = \frac{\{> MgOH_2^{+}\} a_{CO_3^{2-}}}{\{> MgCO_3^{-}\}} \, ,$$

where a_i represents the activity of the sbscripted aqueous species and the curly brackets indicate the surface density of specified surface species. Experimental results obtained at 150 and 200 °C show the inhibiting effect of pH and dissolved CO_3^{2-} on measured dissolution rates in the range of conditions investigated, suggesting the important role of reaction (A2) and (A3) in determining the surface concentration of $>MgOH_2^{+}$ and the resulting rates of dissolution.

If we assume for simplicity that the total surface density of Mg-sites is s = $\{>MgOH_2^{+}\}$+ $\{>MgCO_3^{-}\}$ and that $\{>MgOH_2^{+}\} << \{>MgCO_3^{-}\}$, the following rate equation for forward dissolution rates at reference temperature is provided:

$$r_{+} = k^{+}_{Mg} \cdot \left(\frac{s \cdot K_{CO3}}{a_{CO_3^{2-}}} \right)^{n} \, . \quad \text{(A4)}$$

The rate of dissolution at a given temperature T is thus given by:

$$\boldsymbol{r}_{+}(T) = \boldsymbol{k}^{*}_{Mg} \cdot e^{-\boldsymbol{E}_a / \boldsymbol{R}T} \cdot \left(\frac{\boldsymbol{s} \cdot K^{*}_{CO3} \cdot e^{-\Delta H_r / \boldsymbol{R}T}}{\boldsymbol{a}_{CO_3^{2-}}} \right)^{\boldsymbol{n}}, \qquad \text{(A5)}$$

where $\boldsymbol{k}^{*}_{Mg}$ and K^{*}_{CO3} represent the pre-exponential factors to the dissolution rate constant $\boldsymbol{k}^{+}_{Mg}$ and to the constant K_{CO3} respectively at the temperature T, $\boldsymbol{E}_a$ indicates the activation energy for the dissolution rate constant and $\Delta H_{r(CO3)}$ stands for the enthalpy of reaction (A3).

Assuming that both $\boldsymbol{E}_a$ and $\Delta H_{r(CO3)}$ are constant in the temperature interval of interest, derivation of the natural logarithm of equation (A5) with respect to temperature yields:

$$\frac{\partial \ln \boldsymbol{r}_{+}(T)}{\partial T} = \frac{\boldsymbol{E}_a}{\boldsymbol{R}T^2} + \boldsymbol{n}\frac{\Delta H_{r(CO3)}}{\boldsymbol{R}T^2} + \boldsymbol{n}\frac{\partial(\boldsymbol{a}_{CO_3^{2-}})/\partial T}{\boldsymbol{a}_{CO_3^{2-}}} \qquad \text{(A6)}$$

The variation of dissolution rates with temperature will thus depend on the activity of CO_3^{2-}, other than the enthalpy of reaction (A3) and the activation energy. To analyse the temperature variation of the rates using Eqn. (A6) is necessary to fix the conditions at which dissolution may occur. A solution composition representative of the results reported in this study can be chosen if we want to analyse the variation in dissolution rates between 150 and 200 °C. If for example ΣCO_2 is fixed to 0.05 M in a solution of water containing 0.1 M of NaCl the activity of carbonate ($\boldsymbol{a}_{CO_3^{2-}}$) will decrease from 1.34×10^{-5} at 150 °C to 7.23×10^{-6} at 200 °C, corresponding to an approximately linear variation of $\boldsymbol{a}_{CO_3^{2-}}$ with temperature of -1.32×10^{-7} K^{-1}. The enthalpy of reaction (A3) is not known but its absolute value can be approximated by the enthalpy of formation of the corresponding reaction of formation of aqueous complex $MgCO_3°$:

$$Mg^{2+} + CO_3^{2-} \rightarrow MgCO_3° , \qquad \text{(A7)}$$

which is equal to about +45.7 kJ/mol (Sverjensky et al., 1997) between 150 and 200 °C. For reaction (A3) $\Delta H_{r(CO3)}$ is then in first approximation assumed to be equal to −45.7 kJ/mol.

Integration of Eqn. (A6) between T_1 and T_2 will lead to:

$$\ln\frac{\boldsymbol{r}_{+}(T_2)}{\boldsymbol{r}_{+}(T_1)} = -\frac{\boldsymbol{E}_a}{\boldsymbol{R}}\left(\frac{1}{T_2}-\frac{1}{T_1}\right) - \boldsymbol{n}\frac{\Delta H_{r(CO3)}}{\boldsymbol{R}}\left(\frac{1}{T_2}-\frac{1}{T_1}\right) + \boldsymbol{n}1.32\times10^{-7}\cdot\left[\frac{1}{(\boldsymbol{a}_{CO_3^{2-}})_{T_2}} - \frac{1}{(\boldsymbol{a}_{CO_3^{2-}})_{T_1}}\right]\cdot(T_2 - T_1)$$

(A8)

Solving the equation above for the temperature variation 423.15-473.15 K (150-200 °C), assuming an activation energy of 46 kJ/mol for magnesite dissolution (Pokrovsky et al. 2009), will provide the following results:

$$\frac{\boldsymbol{r}_+(473.15)}{\boldsymbol{r}_+(423.15)} \approx 0.09 \text{ if } \boldsymbol{n} = 4 ; \quad \frac{\boldsymbol{r}_+(473.15)}{\boldsymbol{r}_+(423.15)} \approx 1.5 \text{ if } \boldsymbol{n} = 1.$$

Therefore dissolution rates at 200 °C would roughly be one order of magnitude lower than dissolution rates at 150 °C but if the order of reaction was 1 rates at 150 and 200 °C would be comparable.

In deriving Eqn. (A6) we have excluded the direct effect of pH on the rate variation which is described by Eqn (A2) and that was found to be more important than the one of CO_3^{2-} at the conditions investigated in our study. This effect become stronger with increasing temperature as also suggested by the aqueous association reaction:

$$Mg^{2+} + OH^- \rightarrow MgOH^+ . \qquad \text{(A9)}$$

The constant of formation of $MgOH^+$ increases with temperature according to a $\Delta H_{r(OH)}$ of about 42 kJ/mol (Palmer and Welosowski, 1997) and this complex may become predominant with respect to the other dissolved Mg-species at 200 °C. Calculations made following the same approximations introduced in deriving Eqn. (A6), but considering the pH contribution only, show that the effect of OH^- activity on the rates is in theory less important than the effect of CO_3^{2-} calculated for the same conditions considered above (ΣCO_2 = 0.05 M, NaCl = 0.1 M), giving as a result:

$$\frac{\boldsymbol{r}_+(473.15)}{\boldsymbol{r}_+(423.15)} \approx 0.8 \text{ if } \boldsymbol{n} = 4 ; \quad \frac{\boldsymbol{r}_+(473.15)}{\boldsymbol{r}_+(423.15)} \approx 2.8 \text{ if } \boldsymbol{n} = 1$$

Nevertheless, comparison of dissolution rates at 150 and 200 °C and analysis of the experimental results show that the effect of pH on dissolution rates is stronger or at least comparable with that attributed to carbonate ions, suggesting that the value of $\Delta H_{r(CO3)}$ used above is overestimated.

As shown in this study the combined effect of pH and CO_3^{2-} can adequately explain the slight decrease of the dissolution rates observed from 150 to 200°C, but their integration into an analytic expression to predict the rate variation as a function of *T* requires the knowledge

of the constants of reaction (A2) and (A3) other than the precise determination of the enthalpies of these reaction between the temperatures of interest, together with the variation of the activity of aqueous species implicated (H^+/OH^-, CO_3^{2-}). Consequently we limit ourselves to point out the important role played by reactions (A2) and (A3) in affecting the surface concentration of the rate controlling species. The reduction of $>MgOH_2^+$ concentration with increasing temperature due to these reactions is responsible for the decrease of dissolution rates of magnesite (and possibly other carbonate minerals) with increasing temperature and results in apparent activation energy ($\boldsymbol{E}_a$) that can be ≤ 0.

CHAPITRE 5

Détermination du produit de solubilité de la magnésite

Résumé en français de l'article :

"Solubility product of magnesite as a function of temperature (50- 200 °C)"

1. Introduction

La détermination de la stabilité des phases minérales du système $MgO\text{-}CO_2\text{-}H_2O$ a fait l'objet de nombreuses études, depuis plusieurs dizaine d'années. Bien que la magnésite soit la phase carbonatée la plus stable de ce système (Kittrick and Peryea, 1986 ; Könisberger et al., 1999 ; Hänchen et al., 2008), ce sont des phases hydratées qui ont tendance à se former, particulièrement à température ambiante (hydromagnésite, nesquehonite, artinite (voir Tableau 1). L'analyse des données de la littérature sur la stabilité de la magnésite (par exemple Langmuir, 1965 ; Christ and Hostetler, 1970 ; García et al., 2006) montre une très grande variabilité des valeurs de son produit solubilité ($K_{sp}=\boldsymbol{a}_{Mg^{2+}}\ \boldsymbol{a}_{CO_3^{2-}}$) et de son énergie libre de formation, ce qui reflète les difficultés rencontrées par nombre d'investigateurs dans l'étude de la stabilité de ce minéral. Ainsi, les valeurs du produit de solubilité de la magnésite déduites de mesures de sa solubilité à 25 °C ($K_{sp°\text{-}mgs}$) varient entre 10^{-5} et 10^{-10}. Les mesures de solubilité les plus récentes (Kittrick and Peryea, 1986 ; Pokrovsky and Schott, 1999) et les données thermochimiques impliquent une valeur de K_{sp} à 25 °C comprise entre $10^{-7.5}$ et $10^{-8.1}$. Les valeurs de K_{sp} déterminées aux températures plus élevées ont été essentiellement déduites de mesures calorimétriques et d'équilibres de phases à haute température et pression (par exemple, Harker et Tuttle, 1955 ; Chai et Navrotsky, 1993 ; Koziol et Newton, 1995), alors qu'aucune mesure directe de la solubilité de la magnésite n'a été reportée à ce jour pour des températures supérieures à 90 °C (voir Christ et Hostetler, 1970). Des incertitudes significatives existent donc encore en ce qui concerne les propriétés thermodynamiques de la magnésite (voir Tableau 3) et plus généralement des phases du système carbonaté.

La détermination du produit de solubilité de la magnésite à des températures supérieures à 25 °C est donc fondamentale pour combler le manque de données expérimentales et comparer ensuite les propriétés thermodynamiques ainsi calculées avec celles obtenues à l'aide d'autres méthodes physico-chimiques. Les résultats de cette étude fixeront des

contraintes plus fortes sur la stabilité et les propriétés thermodynamiques de la magnésite aux conditions hydrothermales.

2. Méthodes Expérimentales

Nous avons mesuré la solubilité de la magnésite entre 50 et 200 °C dans des solutions de NaCl (0.1-0.11 mol/kg) et sous des pressions partielles de CO_2 constantes (4-30 bars). Nous avons conduit nos essais en utilisant deux dispositifs expérimentaux différents, un réacteur fermé en titane équipé pour les mesures de pH in situ et une cellule à hydrogène de nouvelle génération, récemment construite au LMTG (cf. Bénézeth et al., 2009). Dans le premier dispositif expérimental le pH a été déterminé avec une précision d'environ 0.02 unités grâce à la mesure en continu du potentiel électrochimique d'un couple d'électrodes à contact solide qui fournit un potentiel constant dans des solutions enrichies en ions Na^+ suivant :

$$E = E° + (2.3\boldsymbol{R}T/F) \, [\text{Log } \boldsymbol{a}_{H^+} + \text{Log } \boldsymbol{a}_{Na^+}], \qquad (1)$$

où E représente le potentiel électrique mesuré, $E°$ le potentiel standard déterminé par la calibration, $\boldsymbol{R}$ est la constante des gaz parfaits, T la température absolue, F la constante de Faraday et $\boldsymbol{a}_i$ indique l'activité de l'ion i en solution. Ce dispositif expérimental nous a permis de mesurer pH et solubilité de la magnésite à 120 et 150 °C, pour des pressions de CO_2 de 15 et 30 bars. Nous avons aussi effectué des mesures à 200 °C, mais sans pouvoir mesurer le pH en raison de la faible stabilité des électrodes à cette température. Dans ce cas, la solubilité a été déterminée à partir des mesures de Mg^{2+} en solution et de la pression de CO_2 dans le réacteur.

La cellule à hydrogène est le dispositif idéal pour les mesures de solubilité dans une vaste gamme de températures en raison de la grande stabilité et précision du système de mesure du pH (~0.002 unité pH). Dans ce dispositif, le pH est déterminé à partir de la différence de potentiel électrochimique entre une solution de référence ayant une concentration d'ions hydrogène connue et la solution étudiée (voir Bénézeth et al. (2009) pour les détails).

Lors d'un essai typique, on laisse s'équilibrer dans la cellule, à la température choisie, la solution de départ avec la poudre de magnésite ; des échantillons de solution sont régulièrement prélevés au cours du temps afin de vérifier l'atteinte de l'équilibre. Le

changement de la température au cours d'une même expérience permet de vérifier la réversibilité de l'équilibre par sous-saturation et sursaturation.

Après chaque prélèvement, les échantillons sont analysés pour déterminer le Mg total dissous et le carbone total inorganique dissous (TDIC). La concentration du Mg a été mesurée par spectroscopie d'absorption atomique (AAS) et le carbone total inorganique a été déterminé soit par mesure de l'alcalinité par titrage acidimétrique à 25 °C, soit à l'aide d'un analyseur de gaz infrarouge non dispersif (NDIR) dont le schéma est illustré sur la Figure 4. Cette dernière méthode fournit une meilleure précision et reproductibilité des résultats par rapport au titrage acidimétrique traditionnel qui est souvent affecté par les échanges de CO_2 entre la solution analysée et l'atmosphère au cours du refroidissement de la solution et du titrage.

3. Résultats expérimentaux

Les valeurs du produit de solubilité apparent ($Q_{sp\text{-}mgs}$) et à dilution infinie ($K_{sp°\text{-}mgs}$) de la magnésite déterminées dans le réacteur fermé en titane sont reportées dans le Tableau 5 (article) avec les valeurs de pH mesurées (ou calculées), les valeurs de la force ionique (I) et les pressions partielles de CO_2 correspondantes. Dans le tableau 6 nous avons listé les résultats expérimentaux des essais conduits dans la cellule à hydrogène, en reportant les valeurs de pH mesurées (pH_m), les concentrations de Mg^{2+} et de TDIC déterminées analytiquement et les concentrations de CO_3^{2-} calculées à partir des constantes apparentes de dissociation de l'acide carbonique (Patterson et al., 1982, 1984). Les valeurs de la force ionique, des coefficients d'activité, de $Q_{sp\text{-}mgs}$ et $K_{sp°\text{-}mgs}$ correspondant à ces essais sont reportées dans le Tableau 7. Les logarithmes des valeurs de $K_{sp°\text{-}mgs}$ obtenues à l'aide des deux dispositifs utilisés dans cette étude sont représentés en fonction de l'inverse de la température absolue dans le diagramme de la Figure 6.

Dans le cas des essais menés avec la cellule à hydrogène, l'état stationnaire a été atteint par sous-saturation à 200 °C et en diminuant successivement la température de 200 à 150 et 100 °C (voir expériences #1-2). Ensuite, l'augmentation de la température nous a permis d'atteindre l'état état stationnaire par sursaturation à 150 °C et ainsi de vérifier la réversibilité de cet équilibre. Dans ces conditions (voir le tableau 6), l'équilibre a été atteint très rapidement (au bout de quelques heures). Par contre, dans le cas de l'expérience #3, menée

sous 4 bars de CO_2, l'équilibre à 50 °C n'a été atteint qu'après environ 26 jours (Fig. 7). Au cours de la même expérience, après augmentation de la température de 50 à 100 °C, nous avons pu verifier la réversibilité de l'équilibre à partir de solutions sursaturées. La variation de la concentration en magnésium de la solution en fonction du temps lors de la réaction de précipitation de la magnésite est reportée sur la Figure 8. L'état stationnaire a été atteint au bout de 30-35 jours.

Parmi toutes les équations que nous avons testées jusqu'à présent pour décrire la variation du produit de solubilité en fonction de la température, l'expression qui permet le meilleur fittage de nos données est de la forme :

$$\log K_{\text{sp°-mgs}} = a + b/T\,(\text{K}) + cT\,(\text{K}). \qquad (2)$$

La régression des données expérimentales à l'aide de l'expression (2) nous a fourni les valeurs suivantes des trois paramètres : a = 4.8603, b = -1115.4171 K and c = -0.0303 K^{-1}. Cette régression est représentée par une ligne continue sur le diagramme de la Figure 6.

L'équation (2) nous a aussi permis de calculer les valeurs d'énergie libre (ΔG_r^o), d'enthalpie (ΔH_r^o), d'entropie ($S_{298.15}^o$) et de capacité calorifique ($\Delta_r C_p^o$) associées à la réaction de dissociation de la magnésite ($MgCO_{3(cr)} = Mg^{2+} + CO_3^{2-}$) à 25 °C. La combinaison de ces valeurs avec les propriétés thermodynamique de Mg^{2+} et CO_3^{2-} proposées par Shock et al. (1997) et reportées dans le Tableau 3 nous a permis de calculer les valeurs correspondantes pour les paramètres thermodynamiques de formation de la magnésite à 25 °C et 1 bar :

$\Delta_f G_{298.15}^o$ = -1027.142 ± 2 kJ·mol^{-1}, $\Delta_f H_{298.15}^o$ = -1110.989 ± 2 kJ·mol^{-1}, $S_{298.15}^o$ = 64.78 ± 2 J·mol^{-1}·K^{-1}, and $C_{p\,298.15}^o$ = 34.61 ± 2 J·mol^{-1}·K^{-1} (l'incertitude correspond à trois fois l'écart-type). Bien que provisoires, ces valeurs sont reportées dans le Tableau 3 afin de les comparer avec les données de la littérature. On peut noter que les valeurs de $\Delta_f G_{298.15}^o$, $\Delta_f H_{298.15}^o$ et $S_{298.15}^o$ sont dans la gamme des valeurs trouvées dans la littérature et en particulier elles sont en bon accord avec celles recommandées par Robie et Hemingway (1995) mais notre valeur $C_{p\,298.15}^o$ est nettement plus faible que celle reportée par ces auteurs (76.09 J·mol^{-1}·K^{-1}). Pour tester l'effet de $C_{p\,298.15}^o$ sur les valeurs des autres paramètres thermodynamiques déduites de nos données expérimentales, nous avons aussi réalisé une deuxième régression en fixant la valeur de $C_{p\,298.15}^o$ (= 76.09 J·mol^{-1}·K^{-1}, Robie et Hemingway (1995)). Bien que cette régression

ne soit pas sensiblement différente de la première, elle implique une valeur d'entropie ($S^{o}_{298.15}$) qui est 15 joules plus faible que celle obtenue dans la première régression. En conséquence, nous avons retenu la première régression de nos données expérimentales, sans fixer la capacité calorifique, sachant que la valeur de $C^{o}_{p\,298.15}$ déduite de ce fit peut-être affectée d'une importante incertitude. Cette régression nous a permis de calculer les valeurs reportées dans le Tableau 3 et de déterminer la valeur de produit de solubilité de la magnésite à 25 °C, log $K_{sp°\text{-}mgs}$ = -7.91.

Les valeurs de $K_{sp°\text{-}mgs}$ obtenues dans cette étude sont aussi en bon accord avec les valeurs utilisées dans la base de données de SUPCRT92 (Johnson et al., 1992) (Figure 7). Enfin, le bon accord entre les valeurs thermodynamiques déduites de nos mesures expérimentales et celles issues de mesures calorimétriques démontre que des données thermodynamiques fiables peuvent être obtenues par mesures de solubilité.

Solubility product of magnesite as a function of temperature (50-200 °C)

Pascale Bénézeth*, Giuseppe D. Saldi, Jean-Louis Dandurand and Jacques Schott and Eric H. Oelkers

Géochimie et Biogéochimie Expérimentale, LMTG – CNRS – OMP – Université de Toulouse, 14, Avenue Edouard Belin, 31400 Toulouse, France

***Corresponding author:**

Tel.: +33 5 61 33 26 32; fax: +33 5 61 33 25 60

E-mail addresses: benezeth@lmtg.obs-mip.fr, saldi@lmtg.obs-mip.fr

Prepared for submission to *Chemical Geology*

Keywords: magnesite solubility product, thermodynamic properties, kinetic of dissolution-precipitation

1. Introduction.

1.1 Stability of carbonates in the system MgO-CO_2-H_2O

The stability of the phases forming in the system MgO-CO_2-H_2O (see Table 1 for a list of names and chemical formulas) has been the object of several studies. Despite the abundance of data concerning the relative stability of the carbonate phases belonging to this system, surprising discrepancies exist between the results of different studies, reflecting the experimental difficulties encountered in studying this system. For instance, some confusion exists in the literature with respect to the exact formula of hydromagnesite, that according to some authors (Baron and Favre, 1958; Kazakov, 1959; Sayles and Fyfe, 1973; Dandurand and Schott, 1977; Könisberger et al., 1999), corresponds to $5MgO{\cdot}4CO_2{\cdot}5H_2O$, whereas Palache et al. (1951), Carpenter (1963) and Langmuir (1965) proposed the chemical formula $4MgO{\cdot}3CO_2{\cdot}4H_2O$ and Takahashi (1927) used $5MgO{\cdot}4CO_2{\cdot}7H_2O$ to indicate the same mineral phase. As a consequence, the different chemical formula generates contradictions between corresponding solubility data. Major discrepancies also exist for the solubility product and free energy of formation of magnesite ($MgCO_3$). Reviews of existing data (e.g., Langmuir, 1965; Christ and Hostetler, 1970, Kittrick and Peryea, 1986; Könisberger et al., 1999; Marion et al., 2001) showed that reported values of the solubility product ranged from $10^{-10.3}$ to $10^{-6.9}$ (and even 10^{-5}) at room temperature. This large variation of magnesite solubility product has deep consequences on the relative stability of the various mineral phases of the system MgO-CO_2-H_2O and different solubility diagrams can be proposed. Langmuir explained the general scarcity of Mg-carbonates in natural environments with their high solubilities and assigned to magnesite a solubility product higher than that of nesquehonite ($MgCO_3{\cdot}3H_2O$) and hydromagnesite ($K_{sp} = 10^{-4.9}$).

However, according to more recent determination of solubility and Gibbs free energy (Kittrick and Peryea, 1986; Könisberger et al., 1999), magnesite is the most stable carbonate phase forming in the system MgO-CO_2-H_2O, under all conditions of temperature and CO_2 partial pressure, as also reported by Marion (2001) and Hänchen et al. (2008). All other hydrated Mg-carbonates are unstable with respect to magnesite but their formation is favored by the slow kinetics of crystallization of magnesite, commonly attributed to the strongly hydrated character of the Mg^{2+} ion (Sayles and Fyfe, 1973; Lippman, 1973). Nesquehonite readily precipitates at 25 °C under moderate CO_2 pressures from solutions that are also supersaturated with respect to hydromagnesite and magnesite (Dell and Weller, 1959; Davies

and Bubela, 1973; Hänchen et al., 2008). Nesquehonite successively transforms into hydromagnesite [$4MgCO_3 \cdot Mg(OH)_2 \cdot 4H_2O$], with appearance of dypingite [$4MgCO_3Mg(OH)_2 \cdot 5H_2O$] as transitory phase, but an increase of temperature to about 50 °C is required to make this process fast (Davies and Bubela, 1973; Hopkinson et al., 2008). Lansfordite ($MgCO_3 \cdot 5H_2O$) forms preferably at temperatures lower than 25 °C and its temperature equilibrium with nesquehonite was estimated to be around 10 °C (Ming and Franklin, 1985). Artinite [$MgCO_3 \cdot Mg(OH)_2 \cdot 3H_2O$] is found at relatively lower pCO_2 conditions with respect to nesquehonite and lansfordite but its field of stability is limited by the presence of the other hydrous phases (Könisberger et al., 1999).

Table 1. List of mineral phases forming in the system MgO-CO_2-H_2O.

Mineral name	Chemical formula
Brucite	$Mg(OH)_2$
Barringtonite	$MgCO_3 \cdot 2H_2O$
Nesquehonite	$MgCO_3 \cdot 3H_2O$
Lansfordite	$MgCO_3 \cdot 5H_2O$
Artinite	$MgCO_3 \cdot Mg(OH)_2 \cdot 3H_2O$
Hydromagnesite	$4MgCO_3 \cdot Mg(OH)_2 \cdot 4H_2O$
Dypingite	$4MgCO_3 \cdot Mg(OH)_2 \cdot 5H_2O$
Magnesite	$MgCO_3$

Magnesite was produced in laboratory at temperatures of 55-100 °C and relatively high CO_2 partial pressures (Gloss, 1938; Baron and Favre, 1958). More recently Deelman (1999) succeeded in synthesizing magnesite at only 40 °C by repeated variations of the solution pH. In low temperature environments magnesite is most often the product of transformation of hydromagnesite, especially at high salinity conditions (Alderman and von der Borch, 1961; Kinsman, 1967; Christ and Hostetler, 1970; Zachmann, 1989), and its direct precipitation from a supersaturated solution, without appearance of any intermediate phase, requires temperatures of the order of 100-150 °C, CO_2 partial pressures of ~ 100 bar and elevated degrees of supersaturation (Hänchen et al., 2008).

In summary, within the system considered here, only the phase transition brucite ↔ magnesite defines a stable equilibrium (see Könisberger et al., 1999), with magnesite being more stable at relatively high CO_2 partial pressures. The stability order among Mg-carbonate

phases can be thus schematized as follows (Marion, 2001): magnesite > hydromagnesite > nesquehonite ($T \geq 8.5$ °C) / lansfordite ($T \leq 8.5$ °C).

The chemical composition of the different phases crystallizing in the system MgO-CO_2-H_2O is illustrated in the ternary plot of Fig. 1. The less stable Mg-carbonate phases are those with a higher content of water and tend to form at low temperature. According to the Ostwald step rule (cf. Morse and Casey, 1988), the metastable phases are progressively replaced by more stable ones, with magnesite thus forming as the final product of transformation from hydromagnesite.

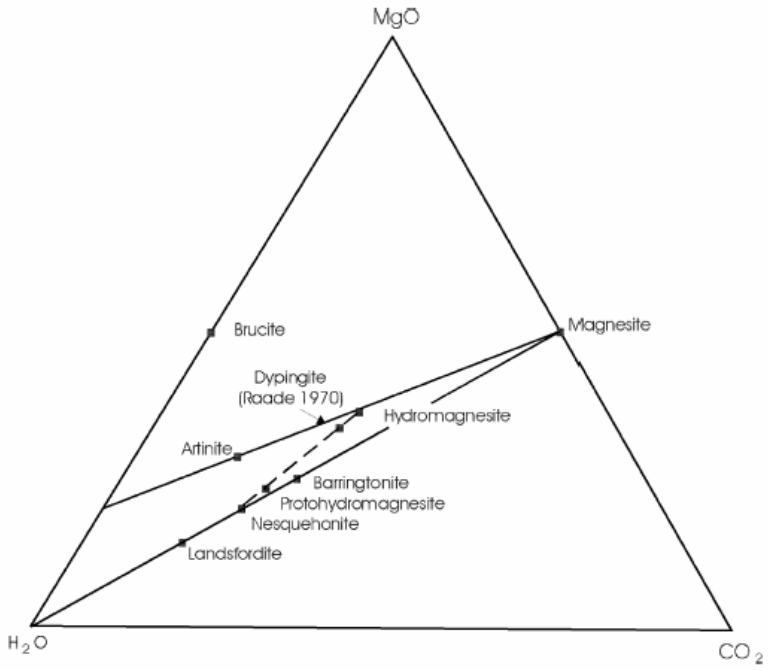

Figure 1. Compositional plot for the phases forming in the MgO-CO_2-H_2O system (from Davies and Bubela, 1973). Note that the less stable Mg-carbonates contain a higher number of water molecules in their chemical formula. The most stable phases forming in the system are either $MgCO_3$ or $Mg(OH)_2$, according to CO_2 fugacity and temperature. In low-T environments magnesite is the product of transformation from metastable hydrated phases (generally hydromagnesite).

1.2 Magnesite solubility and thermodynamics - review of existing data

Magnesite solubility is described by the following reaction:

$$MgCO_{3(cr)} = Mg^{2+} + CO_3^{2-}\ , \qquad (1)$$

whose equilibrium constant defines the magnesite solubility product ($K_{sp°\text{-}mgs}$), according to:

$$K_{sp°\text{-}mgs} = \boldsymbol{a}_{Mg^{2+}}\ \boldsymbol{a}_{CO_3^{2-}} \quad (2)$$

where $\boldsymbol{a}_i$ represents the activity of the i^{th} ion. Magnesite solubility values were reported, at room temperature, by several investigators (e.g., Engel, 1889; Leitmeier, 1915; Wells, 1915; Bär, 1932; Leick, 1932; Halla and Ritter, 1935; Yanat'eva, 1954, 1957; Garrels et al., 1960; Rossini et al., 1952; Morey, 1962; Stout and Robie, 1963; Halla and Van Tassel, 1964; Christ and Hostetler, 1970; Levchenko et al., 1970; Sayles and Fyfe, 1973; Kittrick and Peryea, 1986; Robie and Hemingway, 1995; Könisberger et al., 1999; Marion, 2001). Most of the solubility studies were conducted on natural samples of magnesite and attained chemical equilibrium from undersaturated conditions. The large discrepancies among the experimental results reported by the cited works ($K_{sp°\text{-}mgs}$ varying between $10^{-10.3}$ and $10^{-6.90}$) may be explained by the presence of different impurities in the natural samples employed and by the fact that in some cases, considering the extremely slow kinetics of magnesite dissolution, the equilibrium with respect to magnesite was not attained (Riesen, 1969; García et al., 2006). Furthermore, the reversibility of the equilibrium from supersaturated conditions was not verified in most of the studies and doubts on the real nature of the dissolved phase also arise (cf. Langmuir, 1964).

The existing discordance about magnesite solubility may have led to think that a reliable determination of the solubility product of magnesite by classical solubility experiments was almost impossible, since fewest attempts were made to measure the solubility products of magnesite after the 1965 review by Langmuir. Christ and Hostetler (1970) measured magnesite solubility at 90 °C providing a solubility product of $10^{-9.1}$, from which they calculated a value at 25 °C ($10^{-8.1}$) by using the Van't Hoff equation. No other measurements have been published to date at higher temperatures.

Several log $K_{sp°\text{-}mgs}$ from previous studies are reported in Table 2 and in Figure 2. Note that Chen et al. (2006) provided a value at 150 °C ($10^{-9.04}$), which was calculated from the value at 25°C reported by Smith and Martell (1976) ($10^{-8.1}$) using the Van't Hoff equation. As can be seen in Figure 2, their value disagreed with the trend reported by Christ and Hostetler (1970) or the one that can be calculated from SUPCRT92 (Johnson et al., 2002).

Table 2. Literature values of magnesite solubility product (K_{sp}) obtained from solubility experiments and thermodynamic calculations.

T (°C)	log $K_{sp°\text{-}mgs}$	Reference
17	-10.3	Bär (1932)
25	-9.42	Morey (1962)
25	-8.12	Stout and Robie (1963)
21	-6.90	Halla and Van Tassel (1966)
25	-8.1	Christ and Hostetler (1970) (calculated, Van't Hoff, see text)
25	-7.59	Kittrick and Peryea (1986)
25	-7.93	Langmuir (1997) (recalculated)
25	-8.03	Allison et al. (1991) (MINTEQ)
25	-8.04	Johnson et al. (2002) (SUPCRT92)
25	-7.46	Chen et al. (2006): reported value from Smith and Martell (1976)
25	-7.52	Pokrovsky et al. (1999)
90	-9.1	Christ and Hostetler (1970)
150	-9.04	Chen et al. (2006) (calculated, Van't Hoff, see text)

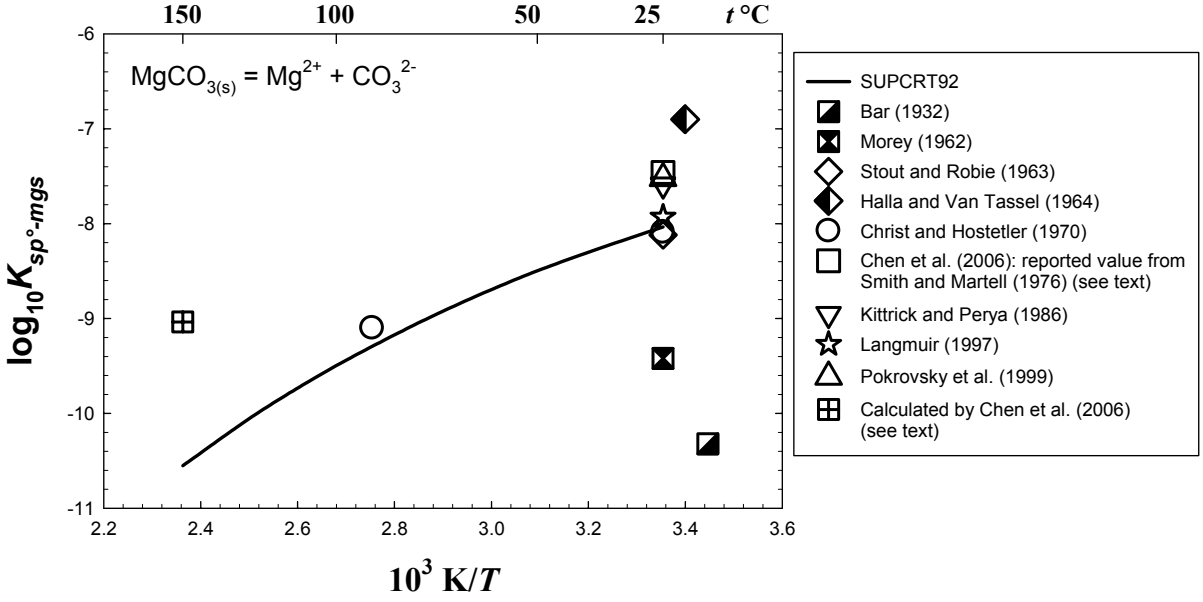

Figure 2: Literature values of the logarithm of magnesite solubility product as a function of the reciprocal temperature compared with the values calculated by SUPCRT 92.

The thermodynamic data of magnesite which are included in the reference databases of several codes for aqueous speciation (e.g., PHREEQC, EQ3/6, MINTEQ, SUPCRT) are based on high temperature calorimetric experiments, high *P*-high *T* phase equilibria studies and successive revision of these data (e.g. Helgeson et al., 1978). The high temperature stability of magnesite is limited by its thermal dissociation which is described by:

$$MgCO_3 \rightarrow MgO + CO_2 \quad (3)$$

This reaction was used to extract the thermodynamic properties of $MgCO_3$, knowing the properties of CO_2 and MgO (Harker and Tuttle, 1955; Chai and Navrotsky 1993; Koziol and Newton, 1995). Nevertheless, also by means of these experimental measurements, the values of Gibbs free energy of formation ($\Delta_f G^o_{298.15}$) and enthalpy of formation ($\Delta_f H^o_{298.15}$) provided for magnesite exhibit sometimes significant discrepancies, leading, for example, to the derivation of geologic phase diagrams that can be in disagreement with field observations (Trommsdorff and Connolly, 1990). A list of the magnesite thermodynamic properties found in literature (along with those determined in this study) is reported in Table 3. The values for $\Delta_f G^o_{298.15}$ of magnesite at reference temperature and pressure vary between -1012 and -1030 kJ/mol. Langmuir (1965) provided a value of -1012.2, which was later corrected by Dandurand and Schott (1977) to -1012.5. A considerable group of works report instead $\Delta_f G^o_{298.15}$ values that ranged between -1026 and -1031 kJ/mol (Rossini et al., 1952; Robie, 1965; Robie and Waldbaum, 1968; Christ and Hostetler, 1970; Helgeson et al., 1978; Sadiq and Lindsay, 1979; Kittrick and Peryea, 1986; Berman, 1988; Chernosky and Berman, 1989; Trommsdorff and Connolly, 1990; Könisberger et al., 1999). Solubility measurements performed by Kittrick and Peryea (1986) both from undersaturated and supersaturated conditions yield an average $\Delta_f G^o_{298.15}$ of -1026.0 ±2.1 kJ/mol, whereas on the basis of a review of thermodynamic data in conjunction with a petrogenetic analysis, Trommsdorff and Connolly provided a value of -1027.4 kJ/mol, which is also in agreement with the value (-1027.8 kJ/mol) calculated by Helgeson et al. (1978). The magnesite standard enthalpy of formation from the elements ($\Delta_f H^o_{298.15}$) available in the literature varies between -1096 and -1118 kJ/mol (Robie et al., 1978; Helgeson et al., 1978; Berman, 1988; Chernosky and Berman, 1989; Holland and Powell, 1990; Chai and Navrotsky, 1993; Koziol and Newton, 1995; Robie and Hemingway, 1995). Heat capacity (C_p) functions used to calculate the thermodynamic properties of magnesite were provided by Robie et al. (1978), Stull and Prophet (1971) and Hemingway et al. (1977) with reported values of the standard entropy ($S^o_{298.15}$) of about 65 J/mol/K (Robie et al., 1978; Wagman et al., 1982; Robie and Hemingway, 1995). From the more recent thermodynamic data, the value of magnesite solubility product originally proposed by Langmuir (1965) at 25 °C has thus to be considered incorrect, in favor of a more widely accepted value range of $\log K_{sp°\text{-}mgs}$ of -7.9 to -8.2.

Table 3. Standard state properties of magnesite and aqueous species involved in Eqn. 1 at 25 °C and 1 bar.

Solid Species	$\Delta G°_f$ kJ/mol	$S°_f$ J/mol/K	$\Delta H°_f$ kJ/mol	$C_p°$ J/mol/K	Reference
$MgCO_{3(cr)}$	-1029.3	65.7	-1112.9	75.5	Rossini et al. (1952)
	-1029.5±1.4				Robie (1965)
	-1026.0±2.1				Kittirick and Peryea (1986)
	-1012.2±2.3				Langmuir (1965)
	-1012.5				Dandurand and Schott (1977)
	-1026.6				Sadiq and Lindsay (1979)
	-1029.48	65.09	-1113.28	76.09	Robie et al. (1978)
	-1027.8		-1111.4		Helgeson et al. (1978)
	-1030.5±0.4		-1117.94±0.4		Könisberger et al. (1999)
	-1029.875	65.210	-1113.636	76.1	Berman (1988)
	-1027.436	65.21			Trommsdorff and Connolly (1990)
	-1030.709	65.09	-1114.505		Chernosky and Berman (1989)
	-1029.7±1.4	65.7			Robie and Waldbaum (1968)
		65.09	-1111.68		Koziol and Newton (1995)
				162.29	Hemingway et al. (1977)
		65.10	-1112.48±0.81	76.02	Holland and Powell (1990)
	-1012.1	65.7	-1095.8	75.52	Wagman et al. (1982)
	-1029.5±1.4	65.1±0.1	-1113.3±1.3	76.09	Robie and Hemingway (1995)
	-1027.1±2.0	**64.8±2.0**	**1110.99±2.0**	**34.61**	**This study**
Aqueous species	$\Delta G°_f$ kJ/mol	$S°_f$ J/mol/K	$\Delta H°_f$ kJ/mol	$C_p°$ J/mol/K	Reference
Mg^{2+}	-454.8	-138	-466.85		Robie et al. (1978)
	-454.8	-138.1	-466.85		Wagman et al. (1982)
		-137±4	-467.0±0.6		Cox et al. (1989)
	-455.6				Robie and Waldbaum (1968)
	-456.0	-118.0	-462.0		Rossini et al. (1952)

Aqueous species	$\Delta G°_f$ kJ/mol	$S°_f$ J/mol/K	$\Delta H°_f$ kJ/mol	$C_p°$ J/mol/K	Reference
Mg^{2+}	-454.0	-138.1	-466.0	-22.3	Shock and Helgeson (1988)/Shock et al. (1997)
				259.4	Criss and Cobble (1964)
CO_3^{2-}	-527.98	-50.00	-675.24	-289.53	Shock and Helgeson (1988)
	-527.90	-50.0±1.0	-675.23±0.25		Cox et al. (1989)
	-527.9	-56.9	-677.140		Robie et al. (1978)
	-528.1	-53.1	-676.3		Rossini et al. (1952)

2. Magnesite solubility experiments

The aim of the present study is to determine the solubility product of magnesite over a wide range of temperatures, assessing the validity of the data obtained by different methods and possibly rehabilitating the role of direct solubility measurements as reliable tool for this kind of determination.

Magnesite solubility product was measured from 50 to 200 °C in 0.1 mol/kg NaCl solutions and in some cases under constant CO_2 partial pressure (4-30 bar) both by means of a hydrogen electrode concentration cell (HECC) and a traditional batch Ti-reactor. Both systems were implemented to provide a continuous measurement of the pH *in situ* during the course of the experiments (see descriptions below). A precise measure of pH is critical for the correct determination of the solution speciation and the consequent computation of the solubility product at a given temperature.

Synthetic magnesite samples were used for the whole experimental study. Description of the synthesis process and of the specimens produced is provided in the magnesite precipitation study by Saldi et al. (2009, chapter 2).

2.1 High temperature Ti-reactor

Batch solubility experiments were carried out in a 400 ml titanium reactor at 120, 150 and 200 °C, under a CO_2 partial pressure of 15 and 30 bar which was kept constant throughout the entire duration of each experiment. The reactor was equipped with a system for the measurement of the electrochemical potential consisting of a solid contact Li-Sn alloy commercial electrode coupled to a Na-selective glass reference electrode, which provides a constant potential in Na^+ rich solutions, according to:

$$E = E° + (2.3\boldsymbol{R}T/F) [\text{Log } \boldsymbol{a}_{H^+} + \text{Log } \boldsymbol{a}_{Na^+}] , \quad (4)$$

where E represents the measured electrical potential of the system, $E°$ stands for the standard potential determined from the calibration curve, $\boldsymbol{R}$ denotes the gas constant, T corresponds to the absolute temperature, F symbolizes the Faraday constant and $\boldsymbol{a}_{H^+}$ and $\boldsymbol{a}_{Na^+}$ designate the activity of the Na^+ and H^+ ions in solution, respectively. At 200 °C, the electrochemical potential was not measured because of the limited stability of these electrodes at this temperature. At the beginning of the experiments between 7 and 9 g of synthetic magnesite powder were put in the reactor which was filled up with 400 ml of 0.1 M NaCl solution (using ultrapure deionized water: resistivity 18.2 MΩ·cm). The reactor vessel was then sealed before addition of either 15 or 30 bar of CO_2 at room temperature. Equilibrium between solution and applied CO_2 pressures maintained the solution pH at values between 4.9 and 5.2, preventing the formation of brucite, which is expected to precipitate at basic pH's. Samples were taken periodically and achievement of equilibrium was verified by the reading of a constant measured potential and analysis of successive solution samples. Once the equilibrium was verified temperature was increased either from 120 to 150 °C or from 150 to 200 °C. Because of the retrograde solubility of carbonate minerals a precipitation reaction was initiated by increasing temperature and conditions were kept constant until the new equilibrium was achieved. This experimental protocol allowed us to reach equilibrium both from undersaturated and supersaturated conditions, attesting in particular the reversibility of equilibrium at 150 °C.

2.2 Hydrogen-electrode concentration cell (HECC)

The design and function of the HECC have been described in numerous publications (*e.g.,* Palmer et al., 2001; Bénézeth et al., 2007) and more recently in the study of siderite (Bénézeth et al., 2009). In most of the experiments, carried out in this study with this cell, the solutions were initially allowed to equilibrate with the solid at a starting pH_m ranging from 3 to 4 and at temperature indicated in Table 4. Once the cell attained thermal equilibrium, solution samples were withdrawn from the test solution over time. During each sampling episode, approximately 1 ml of test solution was withdrawn (and discarded) via an Hastelloy valve, through a platinum dip tube provided at its bottom with a porous Teflon frit (3-5 μm), and then through a 13 mm, 0.2 μm polyvinylidene fluoride filter (PVDF Acrodisc LC13). 2 to 4 ml samples were then collected into sterilized, polypropylene/polyethylene syringes containing a known mass of high purity 0.1 $mol \cdot l^{-1}$ HCl (double distilled HCl) for subsequent analyses of magnesium by flame atomic absorption. Samples ranging from 0.5 to 4 ml were also taken to determine the total dissolved inorganic carbon (TDIC) by either alkalinity measurements or by using a Non-Dispersive Infra-Red (NDIR) CO_2 gas analyzer (see section 2.3). Equilibrium was attained within *ca.* 24 hours (at temperature $t \geq 100$ °C); nevertheless samples were taken at time intervals of several days (see Table 6) whereupon temperature was decreased, approaching then equilibrium from under-saturation. During the course of some runs (#2 and 3), the temperature was raised (from 100 to 150 °C and from 50 to 100 °C, respectively) approaching then equilibrium from over-saturation. Furthermore, during the course of run #3, 4 bars of pure CO_2 at 50 °C have been added to change the pH to more acidic value. The details and discussion of the experimental conditions performed during runs # 2 and 3 (temperature jump, injection of $CO_{2(g)}$) are reported in the results section.

Table 4. Stoichiometric molal compositions ($mol \cdot kg^{-1}$) of starting solutions

Run #	*t* (°C) range investigated	Reference cell		Test cell	
		m(HCl) x10^3	*m*(NaCl)	*m*(HCl) x10^3	*m*(NaCl)
1	200-100	1.9997	0.0980	1.9997	0.0980
2	200-100	2.4925	0.0973	2.4925	0.0973
3	75-100	2.4925	0.0973	2.4925	0.0973

2.3 Solution Analyses

Solution samples were analyzed for Mg, alkalinity and/or total dissolved inorganic carbon (TDIC). Mg was analyzed by flame atomic absorption spectroscopy (AAS) using a range of Mg standard solutions of 0.1 to 0.6 ppm prepared with the same experimental matrix solution. Analytical results were affected by an uncertainty of ± 1% whereas the detection limit was of about 6×10^{-7} mol/kg of Mg.

2.3.1 Alkalinity measurements

For the batch experiments and run#1 performed with the HECC, total alkalinity was determined at 25 °C immediately after sampling by a traditional acidimetric titration on a 2-5 ml sample. Alkalinity was measured using either a Schott automatic volumetric titrator (TA 10plus) or by hand acidimetric titration using the Gran plot method. Total dissolved inorganic carbon (TDIC) and carbonate speciation were calculated at 25 °C from the measured pH and alkalinity at this temperature by using the apparent dissociation constants of water in NaCl media measured by Busey and Mesmer (1978) and the apparent dissociation constants (Q) of the of the following reactions:

$$CO_{2(aq)} + H_2O = HCO_3^- + H^+ \quad (5)$$

$$HCO_3^- = H^+ + CO_3^{2-} \quad (6)$$

at the ionic strength of interest. The values of Q_5 (= $[HCO_3^-][H^+]/[CO_2]_{aq}$) and Q_6 (=$[CO_3^{2-}][H^+]/HCO_3^-$]) were taken from Patterson et al. (1982) and Patterson et al. (1984), respectively. The speciation of carbonates is subsequently recalculated at the temperature of the experiments using the total dissolved inorganic carbon calculated at 25 °C combined with the measured pH and the values of the constants Q_5 and Q_6 taken from the cited references for the temperature of interest. Note that for the experiments performed in the batch reactor at elevated pCO_2, the alkalinity measured at 25 °C by acidimetric titration could not provide a reliable value of TDIC because of the important CO_2 degassing during the sampling procedure and following titration as well. In this case, the solubility product was calculated by assuming that the solution was in equilibrium with the applied CO_2 partial pressure, thus fixing the molality of total dissolved carbon. These calculations were made with the code PHREEQC version 2.15 using the included llnl database (Parkhurst and Appelo, 1999).

2.3.2 Direct determination of TDIC

For runs # 2 and 3 carried out in the HECC, TDIC was analyzed using a LI-820 (LICOR Inc.) non dispersive infra-red (NDIR) CO_2 gas analyzer. This method is based on the measurement of IR energy absorbed by the CO_2 extracted from a sample (by acidification) along an optical path with respect to a reference signal. Development and use of this direct method of TDIC analysis were described by O'Sullivan and Millero (1998), Kaltin et al. (2005), Bandstra et al. (2006) and Cioni et al. (2007). A schematic representation of the analytical system developed at the LMTG is presented in Figure 3. A known volume of sample solution, from 0.5 to 4 ml, depending upon the TDIC concentration, is first injected through a three-way valve in a Savillex® container with a syringe; the following injection of a 0.5 to 1.5 ml of 0.1 to 1 mol/l HCl through the same path converts all aqueous carbonate species into $CO_{2(g)}$, which is stripped out by a gas carrier (synthetic gas, free of CO_2) flowing through the system with a known flow rate as controlled by a flowmeter. The carrier-CO_2 gas stream reaches a four-way valve from which it is directed towards the NDIR gas analyzer. The gas analyzer consists of an optical bench where a broad-band IR source emits a signal that travels along the optical path to a pyroelectric detector. The fraction of source energy absorbed by the gas flow in the optical path corresponds to the concentration of CO_2 stripped from the sample. The measurement of CO_2 concentration is accomplished by the analysis of reference and sample signals passing through narrow band optical filters corresponding to the absorption band of CO_2 (4.24 μm) and the band of energy of the reference signal. The pyroelectric element operates on the basis of the thermal energy received and for this reason it is important to regulate and keep constant the detector temperature. The operating temperature was kept at 50 °C by a thermostat through the optical bench. The resulting signals are then treated by the processing center of the analyzer, which calculates the CO_2 concentrations (ppm) including temperature and pressure corrections. The data acquisition is made with a portable computer connected to the gas analyzer via a digital-to-analog converter. The software used for the acquisition allows the continuous monitoring of the CO_2 concentration in the gas carrier flow. A time plot, as the one shown in Figure 4, displays the peak corresponding to the CO_2 stripped from the system (purge), before the injection of the sample and the acid, and then from the sample itself, whose area integration provides the concentration of TDIC computed on the basis of the calibration curves previously determined as shown in Figures 5a and 5b. These calibrations were performed by analyzing standard

solutions prepared from dried reagent grade Na_2CO_3 and $NaHCO_3$. Different standard solutions were prepared according to the different range of concentration expected from the samples to analyze, as well as according to the optical cell length used. Two optical benches with a different length are available with the LI-820 resulting in different concentration ranges: 14 cm (5.5") optical bench (0 – 1000 ppm or 0 – 2000 ppm) and 5 cm (2") optical bench (0 – 5000 ppm or 0 – 20000 ppm). From these two benches, two calibration curves have been made available as reported in Figures 5a and 5b, showing the peak area versus the moles of CO_2 calculated from the standards concentrations and the amount (in grams) of the standard analyzed.

The efficiency and repeatability of the analyses depend on the flow rate of the carrier gas and the volume of sample to be analyzed (Bandstra et al., 2006). Moreover, if the flow rate of gas is too high CO_2 will be stripped too rapidly and will saturate the optical absorbance path, whereas a too slow stripping may exceed the maximum area that can be integrated (see O'Sullivan and Millero, 1998). For our experimental work an optimum flow rate of carrier gas of 40 ml/min was found for the volumes of sampled solution to analyze. The uncertainty of the analyses performed in this study is generally lower than 5% with a detection limit of ~ 4.5×10^{-3} mol/kg of TDIC with the 14 cm optical bench.

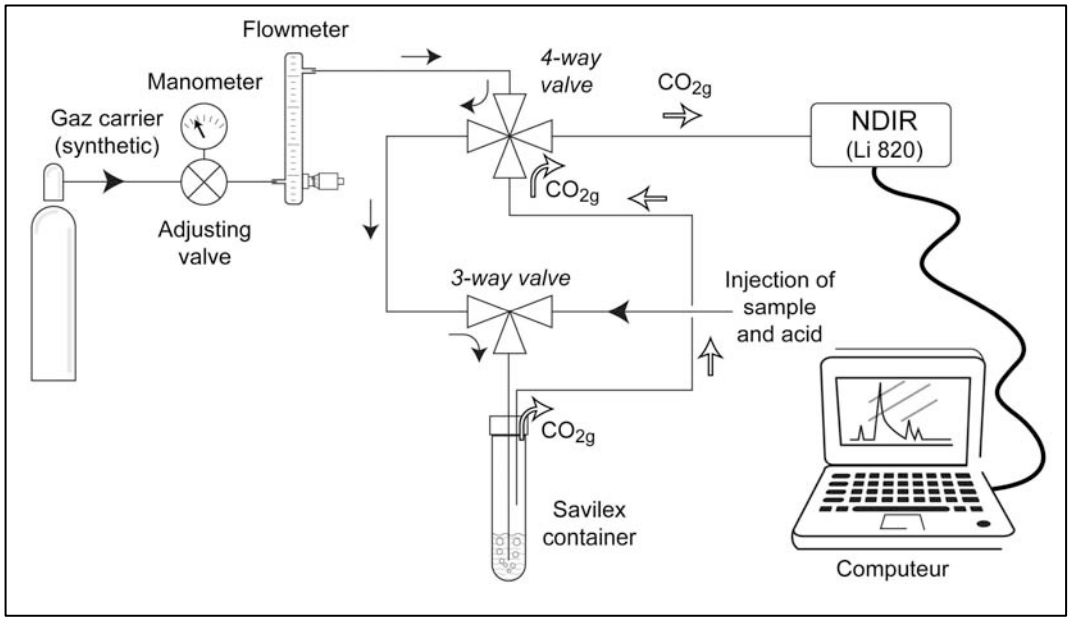

Figure 3. Schematic of the analytical system used for the determination of total dissolved inorganic carbon (TDIC).

Comparison of the analytical data obtained from the method described above with those obtained with the traditional pH-alkalinity method show that analyses performed with the former technique provide a better reproducibility of the results, as also observed by Cioni et al. (2007), whereas the latter method is affected by bigger uncertainties inherent to the pH-alkalinity measurements, which can be liable to a not negligible CO_2 exchange between the sample and the atmospheric air.

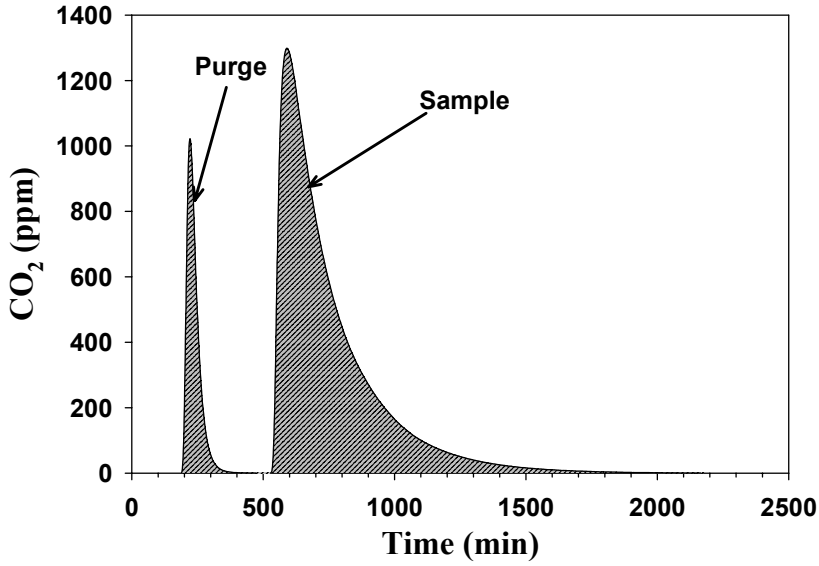

Figure 4. Example of the peaks corresponding to the CO_2 stripped from the system (purge) before the injection of the sample and the acid, which corresponds to the second peak.

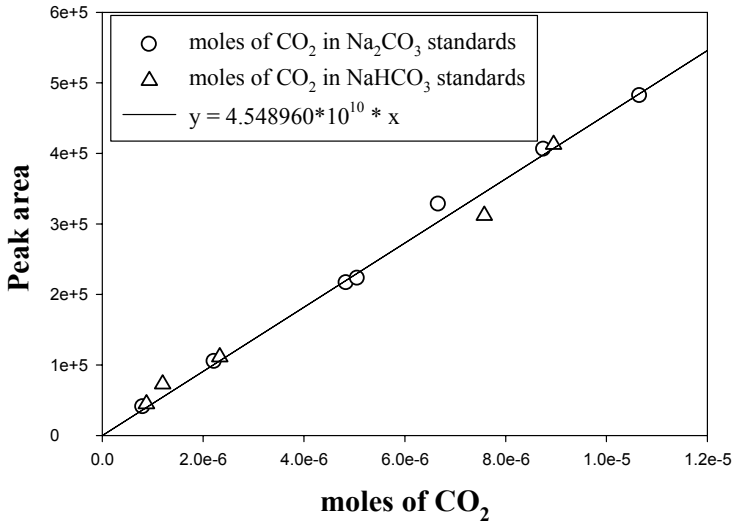

Figure 5a. Calibration curve with the 14 cm optical bench

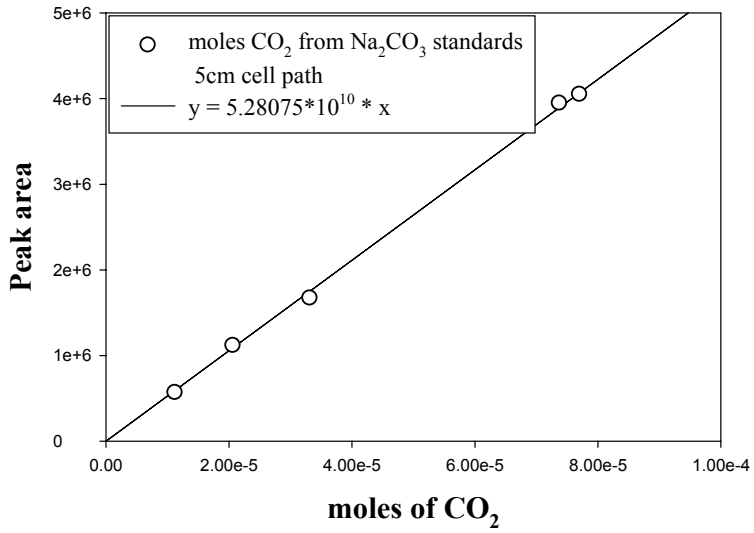

Figure 5b. Calibration with the 5 cm optical bench

3. Experimental results and discussion

The results of the solubility experiments performed in the high-*T* titanium reactor at elevated pCO_2 are summarized in Table 5, which shows the run numbers, the measured or calculated pH and the corresponding values of the solubility products derived from the calculations made with PHREEQC.

Table 5. Summary of the solubility experiments performed in the Ti-batch reactor between 120 and 200 °C and between 15 and 30 bars of CO_2 partial pressure in NaCl media, with the corresponding apparent solubility products ($Q_{sp\text{-}mgs}$) and derived solubility products ($K_{sp°\text{-}mgs}$).

Run #	T (°C)	pCO_2 (bar)	pH	I (mol/kg)	log $Q_{sp\text{-}mgs}$	log $K_{sp°\text{-}mgs}$
Mgs-7-120-eq1	120	25	5.10	0.1266	-8.66	-9.69± 0.3
Mgs-9-120-eq1	120	15	5.27	0.1245	-8.60	-9.61± 0.3
Mgs-4-150-eq1	150	16	5.28	0.1074	-9.11	-10.16± 0.3
Mgs-4-150-eq2	150	30	5.02	0.1079	-9.33	-10.38± 0.3
Mgs-5-150-eq1	150	30	4.96*	0.1161	-9.49	-10.56± 0.3
Mgs-7-150-eq2	150	30	5.12	0.1173	-9.22	-10.30± 0.3
Mgs-8-150-eq1	150	15	5.24*	0.1061	-9.26	-10.31± 0.3
Mgs-8-150-eq3	150	15	5.25*	0.1062	-9.25	-10.29± 0.3
Mgs-9-150-eq2	150	13	5.30	0.1155	-9.20	-10.27± 0.3
Mgs-5-200-eq2	200	30	4.96*	0.0978	-10.74	-11.91± 0.3
Mgs-8-200-eq2	200	15	5.31*	0.0981	-10.30	-11.48± 0.3

*calculated values from equilibrium with measured pCO_2

Table 6 sums up the results of the experiments conducted in the HECC with the run numbers, measured temperature, pH_m ($-\log[H^+]$), the logarithm of the magnesium concentration, the values of TDIC obtained either from pH-alkalinity measurements or from NDIR analysis and the corresponding calculated aqueous CO_3^{2-} concentration (see section 2.3.1 and 2.3.2)

Table 6. Experimental results for magnesite solubility experiments in NaCl media.

Run #	***t* (°C)**	**$-\log[H^+]^a$** measured *in situ*	**$\log[Mg^{2+}]^a_{meas}$**	**[TDIC] ^{a}** from measured alkalinity	**[TDIC]^a** measured by NDIR	**$[CO_3^{2-}]^a$** x10^8	**EquilibriumTime** (hours)
1	199.1	6.208	-2.90	$5.602x10^{-4}$		3.549	216
1	149.6	6.254	-2.846	$1.265x10^{-3}$		23.834	312
1	100.2	6.462	-2.747	$2.320x10^{-3}$		128.581	168
2	199.0	6.289	-2.859		$3.588x10^{-4}$	3.159	168
2	152.4	6.474	-2.830		$5.376x10^{-4}$	21.026	168
2	99.9	6.779	-2.736		$1.251x10^{-3}$	170.781	960
2*	152.2	6.413	-2.822		$6.169x10^{-4}$	19.680	96
3§	*76.6*	*7.504*	*-2.660*		*$1.879x10^{-3}$*	*1490.6*	*744*
3§	*49.8*	*8.040*	*-2.611*		*$2.678x10^{-3}$*	*5886.6*	*480*
3#	49.7	5.720	-1.872		$6.567x10^{-2}$	274.294	788
3*	99.2	5.624	-2.151		$2.644x10^{-2}$	83.239	882

[a] Molal concentrations in the experimental solutions calculated at the temperature of the experiment (see text)
[*] re-increasing temperature, approaching equilibrium from supersaturation
[#] injection of 4 bars of CO_2
[§] values in italic were not considered in the fit (see text)

For the runs carried out with the HECC, the apparent solubility products for reaction (1), defined as $Q_{sp\text{-}mgs} = [Mg^{2+}][CO_3^{2-}]$, are reported in Table 7 with the corresponding ionic strength *I*. The ionic strength and the carbonate speciation were calculated iteratively from the measured pH_m, total Mg and TDIC concentrations, reported in Table 6. The solubility products (at infinite dilution), $K_{sp°\text{-}mgs}$, can then be expressed as:

$$K_{sp°\text{-}mgs} = Q_{sp\text{-}mgs}\,(\gamma_{Mg^{2+}})(\gamma_{CO_3^{2-}}) \qquad (7)$$

where γ_i defines the activity coefficient of the ith aqueous species. The mean stoichiometric

activity coefficients were derived from the Meissner equation (Lindsay, 1989), with the implicit assumption that for an ion of charge z:

$$\gamma_{|z|} = \gamma_{\pm(\mathrm{NaCl})}^{z^2} \qquad (8)$$

where $\gamma_{\pm(\mathrm{NaCl})}$ is the mean molal stoichiometric activity coefficient of NaCl. These latter values were calculated from Archer (1992) and are given in Table 7, together with the ionic strength and the calculated solubility products ($K_{sp°\text{-}mgs}$).

Table 7. Magnesite apparent solubility products, $Q_{sp\text{-}mgs}$, at I ≈ 0.1 molal NaCl, ionic strengths, I, activity coefficients, $\gamma_{\pm(NaCl)}$, and magnesite solubility products, $K_{sp°\text{-}mgs}$, calculated for each run.

Run #	t (°C)	$\log_{10}Q_{sp\text{-}mgs}$	I mol·kg^{-1}	$\gamma_{\pm(NaCl)}$	$^{\S}\log_{10}K_{sp°\text{-}mgs}$
1	199.1	-10.35	0.1010	0.6675	-11.75 ± 0.2
1	149.6	-9.47	0.1012	0.7119	-10.65 ± 0.2
1	100.2	-8.64	0.1012	0.7447	-9.66 ± 0.2
2	199.0	-10.36	0.1006	0.6679	-11.76 ± 0.2
2	152.4	-9.51	0.1005	0.7101	-10.70 ± 0.2
2	99.9	-8.50	0.1010	0.7453	-9.53 ± 0.2
2*	152.2	-9.53	0.1010	0.7099	-10.72 ± 0.2
3§	*76.6*	*-7.49*	*0.1017*	*0.7573*	*-8.45 ± 0.2*
3§	*49.82*	*-6.84*	*0.1022*	*0.7684*	*-7.76 ± 0.2*
3#	49.2	-7.43	0.1375	0.7492	-8.44 ± 0.2
3*	99.18	-8.231	0.1187	0.7345	-9.30 ± 0.2

§ Uncertainties calculated from the combined experimental uncertainties.
*re-increasing temperature, approaching equilibrium from supersaturation
#injection of 4 bars of CO_2
§values in italic were not considered in the fit (see text)

The logarithms of the solubility products taken from Tables 5 and 7 are reported in Figure 6 (associated with the experimental uncertainties reported in these Tables) as a function of reciprocal T.

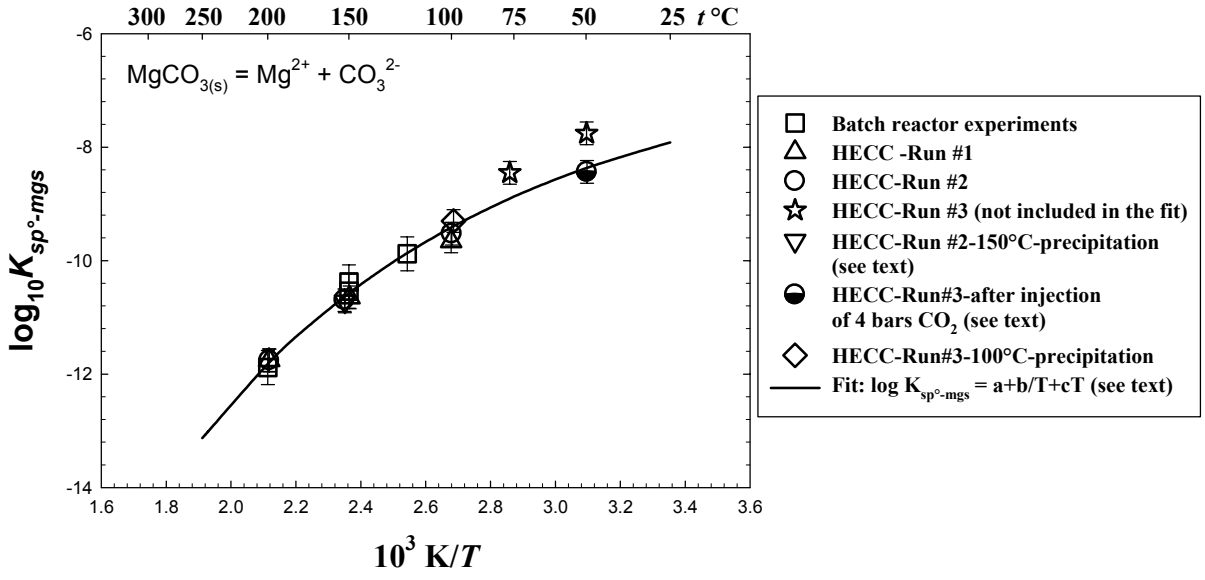

Figure 6. Logarithm of the solubility product of magnesite obtained in this study with the fit of the data (see text).

From tables 5-7 and Figure 6, several observations and discussion can be made, which allowed us to select the runs and data to be used for the regression procedure discussed afterwards. As previously mentioned fast equilibrium is obtained for $t \geq 100$°C, nevertheless samples were taken for additional days to ensure that equilibrium was reached. In Run#1, (triangle symbols, Figure 6) equilibrium was approached only by under-saturation, starting at 200 °C and then decreasing the temperature successively to 150 °C and 100°C, once equilibrium has been reached and verified at each temperature. Note that for this first run, the NDIR analyzer was not available, so TDIC was deduced from measured alkalinity. Once the NDIR method and calibrations has been established, as described in the section 2.3.2, we repeated run #1 at 200, 150 and 100 °C (run#2, circle symbols, Figure 6). When equilibrium has been reached at 100°C, the temperature was raised to 150 °C (temperature jump), approaching then equilibrium from super-saturation (triangle down symbol, Figure 6). At this high temperature the equilibrium was achieved in few hours and, as can be seen in Figure 6, the reversibility of the equilibrium starting from supersaturated conditions was verified. Finally, for run#3, which was initiated at 75°C, solution pH exceeded values of 7 (see table 6) with drifting potential and anomalous higher solubility products (star symbols, Figure 6). At this more basic solution pH's and low CO_2 partial pressure, we suspected that hydrolysis of magnesium and consequently formation of brucite occurred, as previously pointed out in the

introduction. For this reason the data obtained at 75 and 50°C (in italic in tables 6 and 7) were not used in the fitting procedure. To verify our hypothesis, 4 bars of pure $CO_{2(g)}$ has been injected at 50°C to change the pH to more acidic value (from 8.04 to 5.72, see table 6) and a dissolution kinetic was followed as reported in Figure 7. As can be seen from this figure, steady state was reached after about 26 days, from which temperature was increased to 100°C to follow the precipitation kinetic of magnesite as reported in Figure 8.

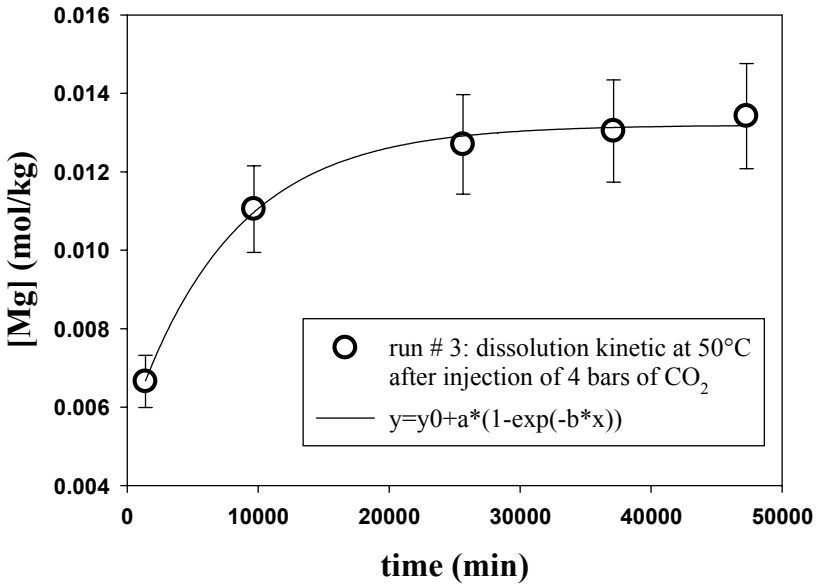

Figure 7. Dissolution kinetics at 50 °C after injection of 4 bars of CO_2(g) (see text). The last sample corresponds to the solubility product reported in Table 6-7 and in Figure 6 as semi-filled circle symbol.

As can be see from Figure 6, the reversibility of the equilibrium has also been verified at 100°C.

Of all the temperature functions tested so far, the simplest equation giving a reliable fit of our data has the form shown in equation (9)

$$\log K_{sp°\text{-mgs}} = a + b/T\,(\text{K}) + cT\,(\text{K}). \qquad (9)$$

A regression then yielded the three variables: a = 4.8603, b = -1115.4171 and c= -0.0303 corresponding to the solid curve shown in Figure 6. This equation yields ΔG_r^o = ($-R$ ln(10){$aT + b + cT^2$})/1000 = 45.177 kJ·mol^{-1}, ΔH_r^o = (R ln(10){$-b+cT^2$})/1000 = -30.211

kJ·mol^{-1}, $\Delta_r C_p^o = R \ln(10)\{2cT\}$ = -345.899 J·mol^{-1}·K^{-1} and consequently ΔS_r^o = -252.851 J·mol^{-1}·K^{-1} at 25°C. Combining these values with the thermodynamic data of Mg^{2+} and CO_3^{2-} from Shock et al. (1997) (reported in Table 3), we obtained for magnesite at 25°C, 1 bar: $\Delta_f G^o_{298.15}$ = -1027.142 ± 2 kJ·mol^{-1} (log $K_{sp°\text{-mgs}}$ = -7.91 ± 0.3), $\Delta_f H^o_{298.15}$ = -1110.989 ± 2 kJ·mol^{-1}, $S^o_{298.15}$ = 64.78 ± 2 J·mol^{-1}·K^{-1} , and $C^o_{p\,298.15}$ = 34.61 ± 2 J·mol^{-1}·K^{-1} (uncertainties are 3σ). These values are reported in Table 3 for comparison with literature data. The values of the Gibbs energy of formation, enthalpy and entropy are in the range of values reported in the literature (Table 3), in particular from the recommended values of Robie and Hemingway (1995). However, our heat capacity value is lower compared to the one given by these authors, which should be preferred over the one we obtained from the second derivative of the fit of the solubility product versus reciprocal of temperature.

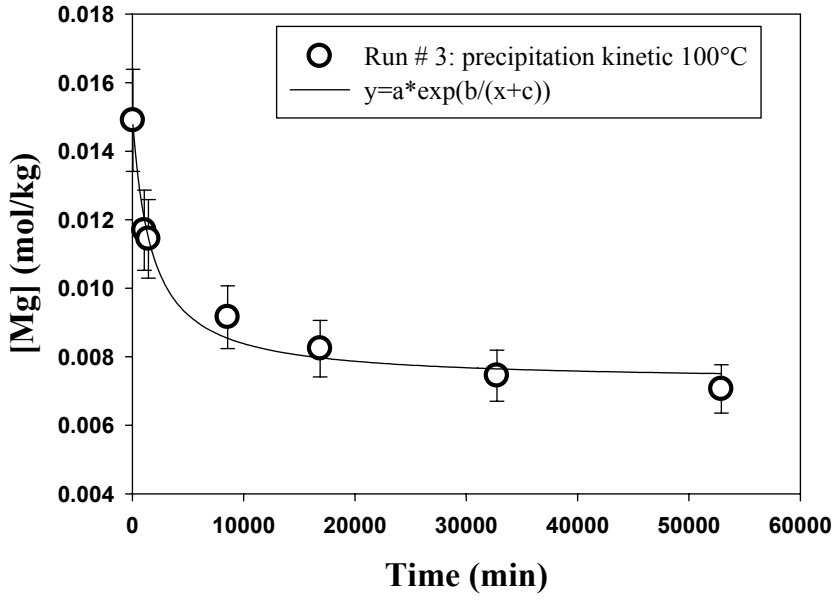

Figure 8. Run #3: Precipitation kinetics at 100 °C from temperature jump (see text). The last sample corresponds to the solubility product reported in Figure 6 as diamond symbol.

4. Conclusion

In this study, the solubility of magnesite has been measured for the first time in a wide range of temperature, from 50 to 200°C. Equilibrium was approached both from under-saturation and super-saturation demonstrating its reversibility. From our preliminary empirical

equation, for the temperature dependence of the magnesite solubility constants (Eq. (9)), the parameters deduced from this regression were used to generate the thermodynamic properties of magnesite as well as the solubility product of magnesite from 25 to 250°C as reported in Figure 9 (solid line) for comparison with the literature values.

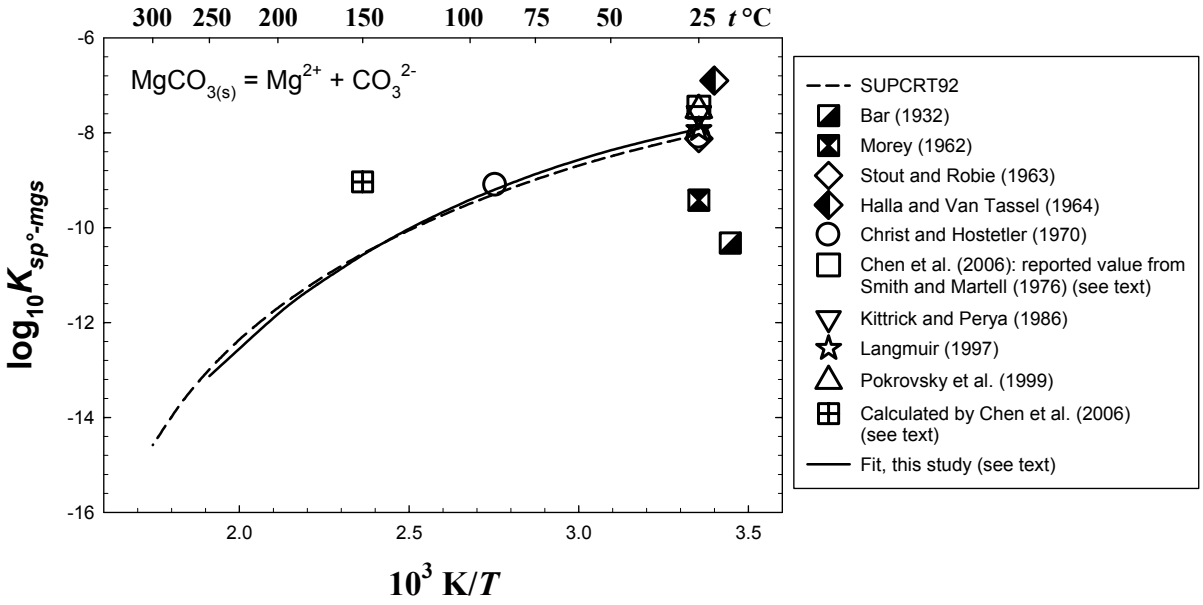

Figure 9. Comparison of our data (fit) with the literature values, including the values calculated by SUPCRT92.

Our data seems in good agreement with the study of Christ and Hostetler (1970), as well as with the temperature dependence of the magnesite solubility constants that can be derived from SUPCRT92 (Johnson et al. 2002). At 25°C, our value (log $K_{sp°\text{-mgs}}$ = -7.91 ± 0.3) is in good agreement with the value calculated by Stout and Robie (1963) as well as the one recalculated by Langmuir (1997). Our close agreement with previous thermodynamic data obtained from calorimetric measurements, proved that reliable thermodynamic data can be obtained from solubility measurements as, for example, recently demonstrated in the case of dawsonite and siderite (Bénézeth et al., 2007, 2009, respectively). However, it should be emphasized here that few additional runs are needed in particular at low temperature to better constrain the fit.

5. References

Alderman A. R., Von der Borch C. C. (1961). Occurrence of magnesite-dolomite sediments in South Australia. *Nature* **192**, 861.

Allison J. D., Brown D. S., and Novo-Gradac K. J. (1991). MINTEQA2/PRODEFA2, a geochemical assessment model for environmental system: version 3.0 user's manual. U.S. EPA. Athens, GA, 106 p.

Archer D.G. (1992). Thermodynamic properties of the NaCl + H2O system. II. Thermodynamic properties of NaCl(aq), NaCl·2H_2O(cr), and phase equilibria. *J. Phys. Chem. Ref. Data* **21**, 793–829.

Bandstra L., Hales B., and Takahashi T. (2006). High-frequency measurements of total CO_2: method development and first oceanographic observations. *Marine Chemistry* **100**, 24-38.

Bär O. (1932). Beitrag zum Thema dolomitentstehung. Zentralblatt für Mineralogie und Paläontologie, pp. 46–62.

Baron G. and Favre I. (1958). État actuel des recherché en direction de la synthèse de la dolomie. Revue de l'Institut Français du Petrole XIII n. 7-8, 1067-1085.

Bénézeth, P., Dandurand J.-L., and Harrichoury J.-C. (2009). Solubility product of siderite ($FeCO_3$) as a function of temperature (25-250 °C). *Chem. Geol.* **265**, 3-12.

Bénézeth, P., Palmer, D.A., Anovitz, L.M., Horita, J., (2007). Dawsonite synthesis and reevaluation of its thermodynamic properties from solubility measurements: implications for mineral trapping of CO_2. *Geochim. Cosmochim. Acta* **71**, 4438-4455.

Berman R. G. (1988). Internally consistent thermodynamic data for minerals in the system Na_2O-K_2O-CaO-MgO-FeO-Fe_2O_3-Al_2O_3-SiO_2-TiO_2-H_2O-CO_2. *Journal of Petrology* **29**, 445-522.

Busey R. H. And Mesmer R. E. (1978). Thermodynamic quantities for the ionization of water in sodium chloride media to 300 °C. *J. Chem. Eng. Data* **23**, 175-176.

Carpenter A. B., 1963. Mineralogy of the system CaO-MgO-CO_2-H_2O at Crestmore, California. Ph.D. dissertation, Harvard University, USA.

Chai, L. and Navrotsky A. (1993). Thermochemistry of carbonate-pyroxene equilibria. *Contributions to Mineralogy and Petrology*, **114**, 139-147.

Chernosky J. V. and Berman R. G. (1989). Experimental reversal of the equilibrium: Clinochlore + 2 magnesite = 3 forsterite + spinel + $2CO_2$ + 4 H_2O and revised thermodynamic properties for magnesite. *Am. J. Sci*. **289**, 249-266.

Christ C. L. and Hostetler P. B. (1970). Studies in the system MgO-SiO_2-CO_2-H_2O (II): the activity product constant of magnesite. *Am. J. Sci.* **268**, 439-453.

Cioni, R., Gambardella, B., and Marini, L., 2007. Field determination of total dissolved inorganic carbon (TDIC) in natural waters using an IR analyzer - I. Preliminary laboratory tests. *Geothermics* **36**, 47-62.

Cox J. D., Wagman D. D., and Medvedev V. A. (1989). CODATA Key Values for Thermodynamics. Hemisphere Publishing Corp., New York.

Criss C. M. and Cobble J. W. (1964). The thermodynamic properties of high temperature aqueous solutions V. The calculation of ionic heat capacities up to 200 °C. entropies and heat capacities above 200 °C. *Am. Chem. Soc. J.* **86**, 5390-5393.

Dandurand J.-L., and Schott J. (1977). Stabilité de la magnésite et de la dolomite; interpretation des resultants de mise en solution et de synthèse par thermodiffusion. *Bull. Soc. Fr. Mineral. Cristallogr.***100**, 94-99.

Davies P.J., Bubela R. (1973). The transformation of nesquehonite into hydromagnesite. *Chem. Geol.* **12**, 289–300.

Deelman, J. C. (1999). Low temperature nucleation of magnesite and dolomite. N. Jb. Miner. Mh. 7, 289-302.

Dell R.M. and Weller S.W. (1959). The thermal decomposition of nesquehonite, $MgCO_3 \cdot 3H_2O$, and magnesium ammonium carbonate $MgCO_3(NH_4)_2CO_3 \cdot 4H_2O$. *Trans. Faraday Soc.* **55**, 2203-2220.

Engel, M., (1889). Sur la solubilité des sels en présence des acides, des bases et de sels. *Ann. Chim. Phys.* **17**, 349-369.

García A. F., Thomsen K., and Stenby E. H. (2006). Prediction of mineral scale formation in geothermal and oilfield operations using the Extended UNIQUAC model. Part II. Carbonate-scaling minerals. *Geothermics* **35**, 239-284.

Garrels R.M., Thompson M.E., and Siever R. (1960). Stability of some carbonates at 25 °C and one atmosphere total pressure. *Am. J. Sci.* **258**, 402-418.

Gloss G. (1938). Über Magnesiumkarbonate und wässrige Salzsysteme mit Magnesium-karbonaten. Thesis, Firedrich-Wilhelmus-Universität Berlin, 87 pp..

Halla, F. and Van Tassel R., (1964). Löslichkeitsanomalien beim magnesit. *Redex Rundschau* **1**, 42-43.

Halla, F. and Van Tassel R., (1966). Dissolution phenomena of alkaline earth carbonates. III. Magnesite, $MgCO_3$. *Redex Rundschau*, 356-362 (from Chem. Abs., 1967, no. 119325n).

Halla, F.and, Ritter, F., (1935). Eine methode zur bestimmung der änderung der freien energie bei reaktionen des typus A(s) + B(s) ↔ AB(s) und ihre anwendung auf das dolomitproblem. *Z. Phys. Chem.* **175A**, 63-82.

Hänchen, M., Prigiobbe, V., Baciocchi, R., and Mazzotti, M. (2008). Precipitation in the Mg-carbonate system – effects of temperature and CO_2 pressure. *Chem. Eng. Sci.,* **63,** 1012-1028.

Harker R.I. and Tuttle O.F. (1955). Studies in the system CaO-MgO-CO2 . Part 1. The thermal dissociation of calcite, dolomite and magnesite. *Am. J. Sci.* **235**, 209-224.

Helgeson H.C., Delany J.M., Nesbitt H.W., and Bird D.K. (1978). Summaryand critique of the thermodynamic properties of rock-forming minerals. *Am. J. Sci.*, **278A**, 1-204.

Hemingway B. S., Robie R. A., Fisher J. R., and Wilson J. H. (1977). The heat capacities of gibbsite, $Al(OH)_3$, between 13 and 480 K, and magnesite, $MgCO_3$, between 13 and 380 K and their standard entropies at 298.15 K and the heat capacities of Calorimetry Conference Benzoic Acid Benzoic Acid between 12 and 316 K. *US Geol. J. Res.* **5**, 797-806.

Holland T. J. B. and Powell R. (1990). An enlarged and updated internally consistent thermodynamic dataset with uncertainties and correlations: the system K_2O-Na_2O-CaO-MgO-MnO-FeO-Fe_2O_3-Al_2O_3-TiO_2-SiO_2-C-H_2-O_2. Joumal of Metamorphic Petrology **8**, 89-124.

Hopkinson L., Rutt K. and Cressey G. (2008). The trnsformation of nesquehonite to hydromagnesite in the system CaO-MgO-H_2O-CO_2: an experimental spectroscopic study. *J. Geol.* **116**, 387-400.

Johnson J., Anderson G. and Parkhurst D. (2007). LLNL: Database from thermo.com.V8.R6.230, prepared by at Lawrence Livermore National Laboratory.

Johnson J. W., Oelkers E. H. and Helgeson H. C. (1992). SUPCRT92 - A software package for calculating the standard molal thermodynamic properties of minerals, gases, aqueous species, and reactions from 1bar to 5000 bar and 0 °C to 1000 °C. *Computers & Geosciences* **18**, 899-947.

Kaltin S., Haraldsson C., and Anderson L. G. (2005). A rapid method for determination of total dissolved inorganic carbon in seawater with high accuracy and precision. *Marine Chemistry* **96**, 53-60.

Kazakov A. V., Tikhomirova M. M., and Plotnikova V. I. (1959). The system of carbonate equilibria. *Int. Geol. Rev.* 1 (10), 1-39.

Kinsman D. J. (1967). Huntite from a carbonate-evaporite environment. *Am. Mineral.* **52**,1332–1340.

Kittrick, J. A. and Peryea, F. J. (1986). Determination of the Gibbs free energy of formation of magnesite by solubility methods. *Soil Science Society of America Journal* **50**, 243-247.

Könisberger E., Könisberger L.-C., and Gamsjager H. (1999). Low temperature thermodynamic model for the system Na_2CO_3-$MgCO_3$-$CaCO_3$-H_2O. *Geochim. Cosmochim. Acta* **63**, 3105-3119.

Koziol A. M. and Newton R. C. (1995). Experimental determination of the reactions magnesite + quartz = enstatite + CO_2 and magnesite = periclase + CO_2, and enthalpies of formation of enstatite and magnesite. *Am. Mineral.* **80**, 1252-1260.

Langmuir D. (1964). Stability of carbonates in the system CaO-MgO-CO_2-H_2O. Ph.D. thesis, Harvard University, USA.

Langmuir D. (1965). Stability of carbonates in the system MgO-CO_2-H_2O. *J. Geol.***73**, 730-750.

Langmuir D. (1997). Aqueous environmental geochemistry. Prentice Hall, pp. 600.

Leick, J. (1932). The solubilities of calcium carbonate and of magnesium carbonate in water that is free from carbonic acid. *Z. Anal. Chem.* **87**, 415-422.

Leitmeier H. (1915). Zur kenntnis der carbonate II. *Neues Jahrb. Mineralog.*, Abt. B, 655–700.

Levchenko V.M., Minkin M.B., and Dukhina T.P. (1970). Magnesium carbonate solubility. *Pochvovedenie* **8**, 144-148.

Lindsay Jr. W.T. (1989). Chemistry of steam cycle solutions: principles. In: Cohen, P. (Ed.), The ASME handbook on water technology for thermal power plants. The American Society of Mechanical Engineers, New York, pp. 341–544. Chapter 7.

Lippmann F. (1973). Sedimentary Carbonate minerals. Springer-Verlag eds., pp. 229.

Marion G. M. (2001) Carbonates mineral solubility at low temperatures in the Na-K-Mg-Ca-H-Cl-SO_4-OH-HCO_3-CO_3-CO_2-H_2O system. *Geochim. Cosmochim. Acta* **65** (12), 1883-1896.

Ming D. W. And Franklin W. T. (1985). Synthesis and chracterization of landsfordite and nesquehonite. *Soil Sci. Soc. Am. J.* **49**, 1303-1308.

Morey, G.W. (1962). The action of water on calcite, magnesite, and dolomite. *Am. Mineral.* **47**, 1456–1460.

Morse J. W. And Casey W. H. (1988). Ostwald process and mineral paragenesis in sediments. *Am. J. Sci.* **288**, 537-560.

O'Sullivan D. W. and Millero F. J. (1998). Continual measurement of the total inorganic carbon in surface seawater. *Marine Chemistry* **60**, 75-83.

Palache C., Berman H., and Frondel C. (1951). The system of mineralogy, vol. 2, 7th ed. John Wiley, New York.

Palmer, D.A., Bénézeth, P., Wesolowski, D.J. (2001). Aqueous high temperature solubility studies. I. The solubility of boehmite at 150 °C as a function of ionic strength and pH as determined by "in situ" measurements. *Geochim. Cosmochim. Acta* **65**, 2081-2095.

Parkhurst D. L. and Appelo C. A. J. (1999).User's guide to PHREEQC (version 2) - a computer program for speciation, batch-reaction,one-dimensional transport, and inverse geochemical calculations. U.S. Geological Survey Water-resources Investigation Report, pp. 99-4259.

Patterson, C.S., Busey, R.H., Mesmer, R.E. (1984). Second ionization of carbonic acid in NaCl media to 250 °C. *J. Solution Chem.* **13**, 647-661.

Patterson, C.S., Slocum, G.H., Busey, R.H., Mesmer, R.E. (1982). Carbonate equilibria in hydrothermal systems: first ionization of carbonic acid in NaCl media to 300 °C. *Geochim. Cosmochim. Acta* **46**, 1653–1663.

Pokrovsky, O. S., Schott, J., and Thomas, F. (1999). Processes at the magnesium-bearing carbonates/solution interface. I. A surface speciation model for magnesite. *Geochim. Cosmochim. Acta* **63**, 863-880.

Riesen, W.F. (1969). Thermodynamische untersuchungen am quatern ären system Ca^{2+}-Mg^{2+}-CO_2-H_2O. Ph.D. Thesis. Universität Bern.

Robie R. A. (1965). Heat and free energy of formation of herzenbergite, troilite, magnesite, and rhodochrosite calculated from equilibrium data. *U.S. Geol. Survey* **525**, 65–72.

Robie R. A. and Waldbaum D. R. (1968) Thermodynamic properties of minerals and related substances at 298.15°K (25.0°C) and one atmosphere (1.013 bars) pressure and at higher temperatures. *U.S. Geol. Survey Bull.* **1259,** 256 p.

Robie R.A., Hemingway B.S., and Fisher J.R. (1978). Thermodynamic properties of minerals and related substances at 298.15 K and 1 bar (105 Pa) pressure and at higher temperatures. *U.S. Geol. Survey Bull.* **1452**. U.S. Government Printing Office, Washington, DC, p. 456.

Robie, R.A. and Hemingway B.S. (1995). Thermodynamic properties of minerals and related substances at 298.15 K and 1 bar (105 Pa) pressure and at higher temperatures. *U.S. Geol. Survey Bull.*, **2131**.

Rossini F.D., Wagman D.D., Evans W.H., Levine S., and Jaffe I. (1952). Selected values of chemical thermodynamic properties. Part I. Tables. *U.S. Natl. Bur. Standard Circ.*, 500.

Sadiq M. and Lindsay W. L. (1979). Selection of standard free energy of formation for use in soil chemistry. *Colorado State Univ. Exp. Sta. Tech. Bull.* **134**.

Sayles, F. L. and Fyfe, W. S. (1973). The crystallization of magnesite from aqueous solution. *Geochim. Cosmochim. Acta* **37**, 87-99.

Shock E. L. and Helgeson H. C. (1988). Calculation of the thermodynamic and transport properties of aqueous species at high pressures and temperatures: correlation algorithms for ionic species and equation of state predictions to 5kb and 1000 °C. *Geochim. Cosmochim. Acta* **52**, 2009-2036.

Shock, E. L., Sassani, D. C., Willis, M., and Sverjensky, D. A. (1997). Inorganic species in geologic fluids: Correlations among standard molal thermodynamic properties of aqueous ions and hydroxide complexes. *Geochim. Cosmochim. Acta* **61**, 907-950.

Smith R. M. and Martell A. E. (1976). Critical Stability Constants. Plenum Press, New York.

Stout J.W. and Robie R.A. (1963). Heat capacity from 11 to 300 K, entropy, and heat of formation of dolomite. *J. Phys. Chem*. **67** (11), 2248-2252.

Stull D. R. and Prophet H. (1971). JANAF thermochemical tables, 2d. edition: Natl. Bur Standards, *Natl. Standards Ref. Data Ser*., NBS37, 1141 pp.

Takahashi G. (1927). Investigation on the synthesis of potassium carbonate by Mr. Engel. *Bull. Imp. Hyg. Lab. (Tokio)* **29**, 165-262.

Trommsdorff V. and Connolly J. A .D. (1990). Constraints on phase diagram topology for the system CaO-MgO-SiO_2-CO_2-H_2O. Contributions to Mineralogy and Petrology **104**, 1-7.

Wagman D. D., Evans W. H., Parker V. B., Schumm R. H., Halow I., Bailey S. M. Churney K. L., and Nuttail R. L. (1982). The NBS tables of chemical thermodynamic properties: selected values for inorganic and C_1 ans C_2 organic substances in SI units. *J. Chem. Ref. Data* **11** supplement n. 2, 392 pp.

Wells, R.C. (1915). Solubility of magnesium carbonate in natural water. *J. Am. Chem. Soc.* **37**, 1704-1707.

Yanat'eva O.K. (1954). Solubility in the system $CaCO_3$-$MgCO_3$-H_2O at different temperatures and pressures of CO_2 . *Doklady Akad. Nauk. SSSR* **96**, 777–779.

Yanat'eva O.K. (1957). Solubility of the system Ca, Mg-CO_3, SO_4-H_2O at 25 °C and PCO_2 of 0.0012 atm. *Zh. Neorgan. Khim.* **2** (9), 2183-2187.

Zachmann D. W. (1989). Mg-carbonates deposits in freshwater environment. In "Magnesite: geology, mineralogy, geochemistry, formation of Mg-carbonates". *Monograph series on Mineral Deposits*, n. 28, pp. 300. Gebrüder Borntraeger, Berlin-Stuttgart.

Conclusion Générale

CONCLUSION GENERALE

Le but de ce travail était de fournir une étude complète des propriétés cinétiques et thermodynamiques de la magnésite en solution aqueuse. Cette étude a été effectuée à dans des conditions de température, pression partielle de CO_2 et composition chimique des solutions aqueuses représentatives des sites potentiels de stockage (bassin sédimentaires profonds et formations de roches ultrabasiques et basaltiques) pour lesquelles les procédés de séquestration minérale du CO_2 *ex situ* peuvent être les plus efficaces.

L'étude des vitesses de précipitation de la magnésite, effectuée entre 100 et 200 °C et sous fortes pression de CO_2, fournit une base de données originale, indispensable pour la compréhension du processus de séquestration minérale et son application à l'échelle industrielle. L'interprétation des résultats expérimentaux à l'aide des modèles de spéciation surfacique couplés à la théorie de l'état transitoire nous a permis d'évaluer rigoureusement l'impact de la composition chimique de la solution sur les vitesses de cristallisation et de quantifier, en particulier, l'effet inhibiteur des espèces carbonatées en fonction de la température. Nos résultats suggèrent la faisabilité du processus de carbonatation minérale *ex situ* sous fortes pressions de CO_2, des conditions qui induisent des pH des solutions faiblement acides ou proche de la neutralité et ainsi permettent d'accélérer les vitesses de dissolution des silicates magnésiens, tout en évitant l'inhibition de la précipitation de la magnésite par les ions CO_3^{2-}. Dans le cas d'injection de fluides enrichis en CO_2 dans des réservoirs de roches basiques et ultrabasiques, par contre, l'augmentation du pH des solutions induite par la dissolution des roches augmente la teneur en CO_3^{2-} et ainsi ralentit notablement la vitesse du processus global de carbonatation. En outre, à cause de la complexité chimique et minéralogique des sites potentiels de stockage et des faibles vitesses de précipitation des carbonates magnésiens, la formation de magnésite ou de carbonates de magnésium hydratés peut être défavorisée par la nucléation de phases silicatées secondaires porteuses de magnésium comme les smectites et les zéolites, qui ainsi réduisent le piégeage minéral de CO_2.

Le travail effectué en utilisant la microscopie à force atomique (AFM) hydrothermale confirme et complète les observations macroscopiques. Les vitesses de cristallisation déduites des mesures microscopiques sont, en effet, comparables à celles mesurées en réacteur à circulation et représentatives d'un mécanisme de croissance spirale. Les images AFM nous

ont permis de constater que ce mécanisme contrôle la croissance cristalline de la magnésite dans un grand intervalle de température et des valeurs d'indices de saturation ($15 \leq \Omega \leq 200$ pour $80 \leq T < 120$ °C). La forte diminution des vitesses de précipitation avec la diminution de température doit être mise en relation avec la forte énergie d'activation de la vitesse d'avancement des marches (~159 kJ/mol) et la forte anisotropie cinétique qui caractérise l'avancement des marches obtuses et aiguës des couches élémentaires ($G_o \approx 12 \times G_a$). Ce résultat fournit une preuve supplémentaire et plus efficace de la difficulté qu'épreuve la magnésite à précipiter à température ambiante.

La détermination des vitesses de dissolution de la magnésite aux pH neutres et alcalins complète les informations récentes sur les cinétiques de dissolution de ce minéral en milieu neutre et acide jusqu'a 150 °C. L'analyse de nos résultats expérimentaux a démontré la validité à 150 et 200 °C du modèle de complexation surfacique initialement développé à 25 °C. L'application de ce modèle a rendu nécessaire l'introduction d'un terme supplémentaire qui prend en compte l'effet inhibiteur du pH (par hydrolyse des sites Mg) dans l'équation qui décrit les vitesses de dissolution aux conditions étudiées et améliore le modèle originel. La diminution des vitesses de dissolution observée avec l'augmentation de température, qui implique des valeurs négatives d'énergie apparente d'activation, est expliquée par l'accroissement de l'hydrolyse et de la carbonatation (dans le cas des solutions enrichies en espèces carbonatées) des sites $>MgOH^{2+}$ qui contrôlent les vitesses de dissolution de la magnésite en milieu neutre et alcalin. Pour quantifier ces effets, nous avons approché les valeurs des enthalpies des réactions d'hydrolyse et de carbonatation des sites magnésiens à partir de nos données expérimentales et des paramètres thermodynamiques des réactions équivalentes en solution. Des températures suffisamment élevées ($T \geq 100$ °C) et des pH neutres et basiques en présence de fluides enrichis en CO_2 représente des conditions favorables à la séquestration de CO_2 sous forme dissoute dans les réservoirs sédimentaires constitués par des carbonates de Mg.

Pour consolider nos données cinétiques et achever la caractérisation physico-chimique de la magnésite, il était essentiel de déterminer son produit de solubilité (K_{sp°) aux températures auxquelles nous avons étudié ses vitesses de dissolution et précipitation. La mise en œuvre d'une cellule hydrothermale à hydrogène nous a permis d'obtenir des déterminations très précises du K_{sp° de la magnésite grâce, surtout, à des mesures in situ particulièrement fiables et précises du pH. Les valeurs des produits de solubilités ainsi mesurées nous ont permis de

générer les propriétés thermodynamiques de cette phase et de les comparer à celles obtenues par mesures calorimétriques et d'équilibre entre phases. La cohérence des nos données thermodynamiques avec celles fournies par Robie et Hemingway (1995) confirment la qualité des nos résultats et rétablit le rôle important des mesures de solubilité à haute température pour la détermination des produits de solubilité et des propriétés thermodynamiques des minéraux.

D'un point de vue plus général, les résultats obtenus dans ce travail améliorent significativement la compréhension et la quantification des cinétiques de réaction des phases carbonatées aux conditions hydrothermales et fournissent une base de données essentielle pour l'étude des réactions de dissolution/précipitation des carbonates dans les systèmes complexes. En particulier, les vitesses de précipitation et dissolution de la magnésite présentées dans ce travail constituent des données indispensables à la modélisation géochimique des processus liés à la séquestration géologique du CO_2 et à la prévision des quantités de CO_2 susceptibles d'être piégées à long terme.

Références Bibliographiques

Aagaard, P. and Helgeson, H. C. (1982). Thermodynamic and kinetic constraints on reaction-rates among minerals and aqueous solutions: I. Theoretical considerations. *Am. J. Sci.* **282**, 237-285.

Adams E. E. and Caldeira K. (2008). Ocean Storage of CO_2. *Elements* **4**, 319-324.

Alderman A. R., Von der Borch C. C. (1961). Occurrence of magnesite-dolomite sediments in South Australia. *Nature* **192**, 861.

Aldushin, K., Jordan, G. & Schmahl, W.W. (2006) Basal plane reactivity of phyllosilicates studied in-situ by hydrothermal atomic force microscopy (HAFM). *Geochim. Cosmochim. Acta.* **70**, 4380-4391.

Aldushin, K., Jordan, G., Aldushina, E. & Schmahl, W.W. (2007) On the kinetics of ion-exchange in phlogopite - an in-situ AFM study. *Clays and Clay Minerals* **55**, 339-347.

Alexander, G., Maroto-Valer, M. M., and Gafarova-Aksoy, P. (2007). Evaluation of reaction variables in the dissolution of serpentine for mineral carbonation. *Fuel* **86**, 273-281.

Alkattan M., Oelkers E. H., Dandurand J.-L., and Schott J. (1998). An experimental study of calcite and limestone dissolution rates as a function of pH from -1 to 3 and temperature from 25 to 80 °C. *Chem. Geol.* **151**, 199-214.

Allison J. D., Brown D. S., and Novo-Gradac K. J. (1991). MINTEQA2/PRODEFA2, a geochemical assessment model for environmental system: version 3.0 user's manual. U.S. EPA. Athens, GA, 106 p.

Anbeek C. (1992). Surface roughness of minerals and implication for dissolution studies. *Geochim. Cosmochim. Acta* **56**, 1461-1469.

Andreani, M., Luquot, L., Gouze, P., Godard, M., Hoise, E., and Gibert, B. (2009). Experimental study of carbon sequestration reactions controlled by the percolation of CO_2-rich brine through peridotites. *Environ. Sci. Technol.* **43**, 1226-1231.

Archer D.G. (1992). Thermodynamic properties of the NaCl + H2O system. II. Thermodynamic properties of NaCl(aq), $NaCl{\cdot}2H_2O$(cr), and phase equilibria. *J. Phys. Chem. Ref. Data* **21**, 793–829.

Arnorsson S.N., Gunnarsson, I., Stefansson, A., and Sveinbjornsdottir A.E. (2002) Major element chemistry of surface and ground waters in basaltic terrain, N-ICeland. I. Primary mineral saturation. *Geochim. Cosmochim. Acta* **66**, 4015-4046.

Arvidson, R. S. and Mackenzie, F. T., 1999. The dolomite problem: Control of precipitation kinetics by temperature and saturation state. *Am. J. Sci.* **299**, 257-288.

Astilleros, J. M., Pina, C. M., Fernndez-Diaz, L., and Putnis, A., (2002) Molecular-scale surface processes during the growth of calcite in the presence of manganese. *Geochim. Cosmochim. Acta* **66**, 3177-3189.

Bachu S. (2000). Sequestration of CO2 in geological media: criteria and approach for site selection in response to climate change. *Energy Conversion and Management* **41**, 953-970.

Bandstra L., Hales B., and Takahashi T. (2006). High-frequency measurements of total CO_2: method development and first oceanographic observations. *Marine Chemistry* **100**, 24-38.

Bär O. (1932). Beitrag zum Thema dolomitentstehung. Zentralblatt für Mineralogie und Paläontologie, pp. 46–62.

Baron G. and Favre I. (1958). État actuel des recherché en direction de la synthèse de la dolomie. Revue de l'Institut Français du Petrole XIII n. 7-8, 1067-1085.

Béarat, H., McKelvy, M. J., Chizmeshya, A. V. G., Gormley, D., Nunez, R., Carpenter, R. W., Squires, K., and Wolf, G. H. (2006). Carbon sequestration via aqueous olivine mineral carbonation: Role of passivating layer formation. *Environ. Sci. Technol.* **40**, 4802-4808.

Bénézeth P., Palmer D. A., Wesolowski D. J. (1997). The aqueous chemistry of aluminum. A new approach to high-temperature solubility measurements. *Geothermics* **26**, 465-481.

Bénézeth, P., Palmer D. A., Anovitz L. M., and Horita J. (2007). Dawsonite synthesis and reevaluation of its thermodynamic properties from solubility measurements: implications for mineral trapping of CO_2. *Geochim. Cosmochim. Acta* **71**, 4438-4455.

Bénézeth P., Palmer D. A., and Wesolowski D. J. (2008). Dissolution/precipitation kinetics of boehmite and gibbsite: Application of a pH-relaxation technique to study near-equilibrium rates. *Geochim. Cosmochim. Acta* **72**, 2429-2453.

Bénézeth P., Dandurand J. L., and Harrichoury J. C. (2009). Solubility product of siderite ($FeCO_3$) as a function of temperature (25-250 °C). *Chem. Geol.* **In Press, Corrected Proof**.

Benson S. M. and Cole D. R. (2008). CO_2 Sequestration in Deep Sedimentary Formations. *Elements* **4**, 325-331.

Berger G., Cadore E., Schott J., and Dove P.M. (1994). Dissolution rate of quartz in lead and sodium electrolyte solutions between 25 and 300 °C: effect of the nature of surface complexes and reaction affinity. *Geochim. Cosmochim. Acta* **58**, 541-551.

Berman R. G. (1988). Internally consistent thermodynamic data for minerals in the system Na_2O-K_2O-CaO-MgO-FeO-Fe_2O_3-Al_2O_3-SiO_2-TiO_2-H_2O-CO_2. *Journal of Petrology* **29**, 445-522.

Berner, R. A., Lasaga, A. C., and Garrels, R. M. (1983). The carbonate-silicate geochemical cycle and its effect on atmospheric carbon-dioxide over the past 100 million years. *Am. J. Sci.* **283**, 641-683.

Binning G., Quate G. F., and Gerber Ch. (1986). Atomic force microscope. *Phys. Rev. Lett.* **56**, 930-934.

Bjorlykke, K. and Egeberg, P.K. (1993) Quartz cementation in sedimentary basins. *AAPG Bull.* **77**, 1538-1546.

Bosbach, D., Hall, C., and Putnis, A. (1998) Mineral precipitation and dissolution in aqueous solution: in-situ microscopic observations on barite (001) with atomic force microscopy. *Chem. Geo.* **151**, 143-160.

Brandt, F., Bosbach, D., Krawczyk-Barsch, E., Arnold, T., and Bernhard. G. (2003) Chlorite dissolution in the acid pH-range: A combined microscopoc and macroscopic approach. *Geochim. Cosmochim. Acta* **67**, 1451-1461.

Brunauer S., Emmet P. H., and Teller E. (1938) Adsorption of gases in multimolecular layers. *J. Am. Chem. Soc.*, **60**, 309-319.

Burton W. K., Cabrera N., and Frank F. C. (1951). The growth of crystals and the equilibrium structure of their surfaces. *Phil. Trans. Royal Soc. London* **A243**, 299–358.

Busenberg, E., and Plummer, L. N. (1986). A comparative study of the dissolution and crystal growth kinetics of calcite and aragonite, *in* Mumpton, F. A., editor, Studies in Diagenesis: U. S. Geological Survey Bulletin B 1578, pp. 139–168.

Busenberg, E., Plummer, L.N. (1982). The kinetics of dissolution of dolomite in CO_2-H_2O systems at 1.5 to 65°C and 0 to 1 atm pCO_2. *Amer. J. Sci.* **282**, 45-78.

Busey R. H. And Mesmer R. E. (1978). Thermodynamic quantities for the ionization of water in sodium chloride media to 300 °C. *J. Chem. Eng. Data* **23**, 175-176.

Cabrera N. and Vermilyea D. A. (1958) The growth of crystals from solution. In *Growth and Perfection of Crystals* (ed. R. H. Doremus, B. W. Roberts, and D. Turnbull), pp. 393–410. John Wiley & Sons.

Carpenter A. B., 1963. Mineralogy of the system CaO-MgO-CO_2-H_2O at Crestmore, California. Ph.D. dissertation, Harvard University, USA.

Castaing M., Kraus J.-L., Beaufils P. and Ricard J. (1991). Temperature-jump method for studying the fast transport of Na^+ by (221)C10-crptand across lipid membranes. *Biophys. Chem.* **41**, 203–215.

Chai, L. and Navrotsky A. (1993). Thermochemistry of carbonate-pyroxene equilibria. *Contributions to Mineralogy and Petrology*, **114**, 139-147.

Chen, Z. Y., O'Connor, W. K., and Gerdemann, S. J. (2006). Chemistry of aqueous mineral carbonation for carbon sequestration and explanation of experimental results. *Environ. Prog.* **25**, 161-166.

Chernosky J. V. and Berman R. G. (1989). Experimental reversal of the equilibrium: Clinochlore + 2 magnesite = 3 forsterite + spinel + $2CO_2$ + 4 H_2O and revised thermodynamic properties for magnesite. *Am. J. Sci*. **289**, 249-266.

Chernov A. A. (1961) The spiral growth of crystals. *Soviet Phys. Usp.* **4**, 116–148.

Chernov, A. A. and Rashkovich, L. N. (1987) Spiral crystal growth with nonlinear dependence of step growth rate on supersaturation; the {110} faces of KH2PO4 crystals in aqueous solution. *Journal of Crystal Growth* **84**, 389-393.

Chou, L., Garrels, R.M., Wollast, R. (1989). Comparative study of the kinetics and mechanisms of dissolution of carbonate minerals. *Chem. Geo.* **78**, 269-282.

Chou L. and Wollast R. (1984). Study of the weathering of albite at room temperature and pressure with a fluidized bed reactor. *Geochim. Cosmochim. Acta* **48**, 2205-2217.

Christ C. L. and Hostetler P. B. (1970) Studies in the system MgO-SiO_2-CO_2-H_2O (II): the activity product constant of magnesite. *Am. J. Sci.* **268**, 439-453.

Christoffersen, J. and Christoffersen, M. R. (1981). Kinetics of dissolution of calcium hydroxyapatite : IV. The effect of some biologically important inhibitors. *Journal of Crystal Growth* **53**, 42-54.

Cioni, R., Gambardella, B., and Marini, L. (2007). Field determination of total dissolved inorganic carbon (TDIC) in natural waters using an IR analyzer - I. Preliminary laboratory tests. *Geothermics* **36**, 47-62.

Cox J. D., Wagman D. D., and Medvedev V. A. (1989). CODATA Key Values for Thermodynamics. Hemisphere Publishing Corp., New York.

Criss C. M. and Cobble J. W. (1964). The thermodynamic properties of high temperature aqueous solutions V. The calculation of ionic heat capacities up to 200 °C: entropies and heat capacities above 200 °C. *Am. Chem. Soc. J.* **86**, 5390-5393.

Dandurand J.-L., and Schott J. (1977). Stabilité de la magnésite et de la dolomite; interpretation des resultants de mise en solution et de synthèse par thermodiffusion. *Bull. Soc. Fr. Mineral. Cristallogr.***100**, 94-99.

Dangles O., Elhabiri M. and Brouillard R. (1994) Kinetic and thermodynamic investigation of the aluminum–anthocyanin complexation in aqueous solution. *J. Chem. Soc. Perkin Trans.* **2**, 2587-2596.

Davies P.J., Bubela R. (1973). The transformation of nesquehonite into hydromagnesite. *Chem. Geol.* **12**, 289–300.

Davis K. J., Dove P. M., and De Joreo J. J. (2000) The role of Mg^{2+} as an impurity in calcite growth. *Science* **290**, 1134-1137.

Deelman, J. C. (1999). Low temperature nucleation of magnesite and dolomite. *N. Jb. Miner. Mh.* **7**, 289-302.

Deelman, J. C. (2003). Note on magnesite formation (studies on irreversible geochemical reactions **9**). *Carnets de Géologie/Notebooks on Geology*, Maintenon, Letter 2003/03.

Dell R.M. and Weller S.W. (1959). The thermal decomposition of nesquehonite, $MgCO_3 \cdot 3H_2O$, and magnesium ammonium carbonate $MgCO_3(NH_4)_2CO_3 \cdot 4H_2O$. *Trans. Faraday Soc.* **55**, 2203-2220.

Devidal, J.-L., Schott, J., and Dandurand, J.-L. (1997). An experimental study of kaolinite dissolution and precipitation kinetics as a function of chemical affinity and solution composition at 150°C, 40 bars, and pH 2, 6.8, and 7.8. *Geochim. Cosmochim. Acta* **61**, 5165-5186.

Di Tommaso D. and de Leeuw N. H. (2009). Theoretical study of the dimerization of calcium carbonate in aqueous solution under natural water conditions. *Geochim. Cosmochim. Acta* **In Press** (doi:10.1016/j.gca.2009.06.003).

Dove P. M. and Rimstidt D. J. (1994). Silica - Water Interactions. *Rev. Min.* **29,** 259-308.

Dove P.M. and Crerar D.A. (1990) Kinetics of quartz dissolution in electrolyte solution using a hydrothermal mixed flow reactor. *Geochim. Cosmochim. Acta* **54**, 955-969.

Dove, P. M. and Hochella Jr, M. F., (1993) Calcite precipitation mechanisms and inhibition by orthophosphate: In situ observations by Scanning Force Microscopy. *Geochim. Cosmochim. Acta* **57**, 705-714.

Duckworth, O. W. and Martin, S. T., (2003). Connections between surface complexation and geometric models of mineral dissolution investigated for rhodochrosite. *Geochim. Cosmochim. Acta* **67**, 1787-1801.

Eigen M. and de Maeyer L. (1963). In "Thechnique of Organic Chemistry" vol. VIIIb. A. Weissenberger Ed.; Wiley, New York, pp. 895

Engel, M. (1889). Sur la solubilité des sels en présence des acides, des bases et de sels. *Ann. Chim. Phys.* **17**, 349-369.

Eyring, H. (1935). The activated complex in chemical reactions. *J. Chem. Phys.* **3,** 107-115.

García A. F., Thomsen K., and Stenby E. H. (2006). Prediction of mineral scale formation in geothermal and oilfield operations using the Extended UNIQUAC model. Part II. Carbonate-scaling minerals. *Geothermics* **35**, 239-284.

Garrels R.M., Thompson M.E., and Siever R. (1960). Stability of some carbonates at 25 °C and one atmosphere total pressure. *Am. J. Sci.* **258**, 402-418.

Gautelier, M., Schott, J., and Oelkers, E. H. (2007). An experimental study of dolomite dissolution rates at 80 degrees C as a function of chemical affinity and solution composition. *Chem. Geo.* **242**, 509-517.

Gautier J.-M. (1999). Etude expérimental et modélisation de la cinétique de dissolution et de cristallisation des silicates en milieu hydrothermal: cas du quartz et du feldspath potassique. PhD thesis, Université Paul Sabatier, p. 175.

Gautier, J.-M., Oelkers, E. H., and Schott, J. (1994). Experimental study of K-feldspar dissolution rates as a function of chemical affinity at 150°C and pH 9. *Geochim. Cosmochim. Acta* **58**, 4549-4560.

Gautier, J.-M., Oelkers, E. H., and Schott, J. (2001). Are quartz dissolution rates proportional to B.E.T. surface areas? *Geochim. Cosmochim. Acta* **65**, 1059-1070.

Gautier Q., Saldi G. D., Bénézeth P., Oelkers E. H. and Schott J. (2009). Effects of organic ligands on magnesite precipitation rates. *Geochim. Cosmochim. Acta* **73** (13), A419.

Georgiou, D. K. and Vekilov, P. G. (2006) A fast response mechanism for insulin storage in crystals may involve kink generation by association of 2D clusters. *Proc. Natl. Acad. Sci. U. S. A.* **103**, 1681-1686.

Gerdemann, S. J., O'Connor, W. K., Dahlin, D. C., Penner, L. R., and Rush, H. (2007). Ex situ aqueous mineral carbonation. *Environ. Sci. Technol.* **41**, 2587-2593.

Giammar D.E., Bruant R.G. and Peters, C.A. (2005). Forsterite dissolution and magnesite precipitation at conditions relevent for deep saline aquifer storage and sequestration of carbon-dioxide. *Chem. Geo.* **217,** 257-276.

Gislason, S.R., Arnórsson, S., and Ármannsson, H. (1996) Chemical weathering of basalt in Southwest Iceland: Effects of runoff, age of rocks and vegetative/glacial cover. *Am. J. Sci.* **296,** 837-907.

Gloss G. (1938). Über Magnesiumkarbonate und wässrige Salzsysteme mit Magnesium-karbonaten. Thesis, Firedrich-Wilhelmus-Universität Berlin, 87 pp..

Goldberg P., Chen Z.-Y., O' Connor W., Walters R., and Ziock H. (2001). CO_2 mineral sequestration studies in U. S.. *Presented at the First National Conference on Carbon Sequestration*. Washington DC, May 14-17, 2001.

Gratz A. J., Hillner P. E., and Hansma P. K. (1993) Step dynamics and spiral growth on calcite. *Geochim. Cosmochim. Acta* **57**, 491–495.

Gysi, A. P. and Stefánsson, A. (2008). Numerical modeling of CO_2-water-basalt interaction. *Mineralogical Magazine* **72**, 55-59.

Halla, F. and Van Tassel R., (1964). Löslichkeitsanomalien beim magnesit. *Redex Rundschau* **1**, 42-43.

Halla, F. and Van Tassel R., (1966). Dissolution phenomena of alkaline earth carbonates. III. Magnesite, $MgCO_3$. *Redex Rundschau*, 356-362 (from Chem. Abs., 1967, no. 119325n).

Halla, F.and, Ritter, F., (1935). Eine methode zur bestimmung der änderung der freien energie bei reaktionen des typus A(s) + B(s) ↔ AB(s) und ihre anwendung auf das dolomitproblem. *Z. Phys. Chem.* **175A**, 63-82.

Hänchen, M., Prigiobbe, V., Baciocchi, R., and Mazzotti, M. (2008). Precipitation in the Mg-carbonate system – effects of temperature and CO_2 pressure. *Chem. Eng. Sci.,* **63,** 1012-1028.

Hänchen, M., Prigiobbe, V., Storti, G., Seward, T. M., and Mazzotti, M. (2006). Dissolution kinetics of fosteritic olivine at 90-150 °C including effects of the presence of CO2. *Geochim. Cosmochim. Acta* **70**, 4403-4416.

Harker R.I. and Tuttle O.F. (1955). Studies in the system CaO-MgO-CO2 . Part 1. The thermal dissociation of calcite, dolomite and magnesite. *Am. J. Sci.* **235**, 209-224.

Helgeson H.C., Delany J.M., Nesbitt H.W., and Bird D.K. (1978). Summaryand critique of the thermodynamic properties of rock-forming minerals. *Am. J. Sci.*, **278A**, 1-204.

Hemingway B. S., Robie R. A., Fisher J. R., and Wilson J. H. (1977). The heat capacities of gibbsite, $Al(OH)_3$, between 13 and 480 K, and magnesite, $MgCO_3$, between 13 and 380 K and their

standard entropies at 298.15 K and the heat capacities of Calorimetry Conference Benzoic Acid Benzoic Acid between 12 and 316 K. *US Geol. J. Res.* **5**, 797-806.

Higgins S. R., Bosbach D., Eggleston C. M., and Knauss K. (2000). Kink dynamics and step growth on barium sulfate (001): a hydrothermal scanning probe microscopy study. *J. Phys. Chem. B* **104**, 6978-6982.

Higgins S. R., Eggleston C. M., Knauss K. G., and Boro C. O. (1998). A hydrothermal atomic force microscope for imaging in aqueous solution up to 150°C. *Rev. Sci. Instrum.* **69,** 2994–2998.

Higgins S.R. and Hu X. (2006). Near molecular-scale growth of natural minerals: Experimental methods and errors in length-dependent step speeds with scanning probe microscopy. *Journal of Electron Spectroscopy and Related Phenomena* **150**, 235–247.

Higgins, S. R., Jordan, G., and Eggleston, C. M. (2002) Dissolution kinetics of magnesite in acidic aqueous solution: a hydrothermal atomic force microscopy study assessing step kinetics and dissolution flux. *Geochim. Cosmochim. Acta* **66**, 3201-3210.

Hitchon, B., Gunter, W. D., Gentzis, T., and Bailey, R. T. (1999). Sedimentary basins and greenhouse gases: a serendipitous association. *Energy Conversion and Management* **40**, 825-843.

Holland T. J. B. and Powell R. (1990). An enlarged and updated internally consistent thermodynamic dataset with uncertainties and correlations: the system K_2O-Na_2O-CaO-MgO-MnO-FeO-Fe_2O_3-Al_2O_3-TiO_2-SiO_2-C-H_2-O_2. Joumal of Metamorphic Petrology **8**, 89-124.

Hopkinson L., Rutt K. and Cressey G. (2008). The transformation of nesquehonite to hydromagnesite in the system CaO-MgO-H_2O-CO_2: an experimental spectroscopic study. *J. Geol.* **116**, 387-400.

Hribar, B., Southall, N. T., Vlachy, V., and Dill, K. A. (2002). How ions affect the structure of water. *Journal of the American Chemical Society* **124**, 12302-12311.

Inskeep, W. P. and Bloom, P. R., 1985. An evaluation of rate equations for calcite precipitation kinetics at pCO2 less than 0.01 atm and pH greater than 8. *Geochim. Cosmochim. Acta* **49**, 2165-2180.

IPCC (2005). Underground geological storage. In: Metz B., Davidson O., de Coninck H. C., Loos M., Meyer L. A. (eds.). IPCC special report on carbon dioxide capture and storage, prepared by Working Group III of the Intergovernmental Panel on Climate Change. Cambridge University Press, Cambridge, UK, and New York, USA, pp. 195-276.

Jiang, S. Y., Chen C.X., Jiang Y. H., Dai B. Z., and Ni P. (2004). Geochemistry and genetic model for the giant magnesite deposits in the eastern Liaoning province, China. *Acta Petrol. Sin.* **20 (4)**, 765-772.

Johnson J., Anderson G. and Parkhurst D. (2007). LLNL: Database from thermo.com.V8.R6.230, prepared by at Lawrence Livermore National Laboratory.

Johnson J. W., Oelkers E. H. and Helgeson H. C. (1992). SUPCRT92 - A software package for calculating the standard molal thermodynamic properties of minerals, gases, aqueous species, and reactions from 1bar to 5000 bar and 0 °C to 1000 °C. *Computers & Geosciences* **18**, 899-947.

Jordan, G., Higgins, S. R., Eggleston, C. M., Knauss, K. G., and Schmahl, W. W. (2001). Dissolution kinetics of magnesite in acidic aqueous solution, a hydrothermal atomic force microscopy (HAFM) study: step orientation and kink dynamics. *Geochim. Cosmochim. Acta* **65**, 4257-4266.

Jordan, G., Pokrovsky, O. S., Guichet, X., and Schmahl, W. W. (2007). Organic and inorganic ligand effects on magnesite dissolution at 100 °C and pH = 5 to 10. *Chem. Geo.* **242**, 484-496.

Kaltin S., Haraldsson C., and Anderson L. G. (2005). A rapid method for determination of total dissolved inorganic carbon in seawater with high accuracy and precision. *Marine Chemistry* **96**, 53-60.

Kaszuba J.P., Janecky, D.R., and Snow, M.G. (2003). Carbon dioxide reaction process in a model brine aquifer at 200º C and 200 bars: Implications for geologic sequestration of carbon. *App. Geochem.,* **18,** 1065-1080.

Kazakov A. V., Tikhomirova M. M., and Plotnikova V. I., 1959. The system of carbonate equilibria. *Int. Geol. Rev.* 1 (10), 1-39.

Kinsman D. J. (1967). Huntite from a carbonate-evaporite environment. *Am. Mineral.* **52**,1332–1340.

Kittrick, J. A. and Peryea, F. J. (1986). Determination of the Gibbs free energy of formation of magnesite by solubility methods. *Soil Sci. Soc. Am. J.* **50**, 243-247.

Kojima T., Nagamine A., Ueno N., and Uemiya S. (1997). Absorption and fixation of carbon dioxide by rock weathering. *Energy Convers. Manage.* **38**, S461-S466.

Könisberger E., Könisberger L.-C., and Gamsjager H. (1999). Low temperature thermodynamic model for the system Na_2CO_3-$MgCO_3$-$CaCO_3$-H_2O. *Geochim. Cosmochim. Acta* **63**, 3105-3119.

Kowacz, M. and Putnis, A. (2008). The effect of specific background electrolytes on water structure and solute hydration: Consequences for crystal dissolution and growth. *Geochim. Cosmochim. Acta* **72**, 4476-4487.

Kowacz, M., Putnis, C., and Putnis, A. (2007). The effect of cation/anion ratio in solution on the mechanism of barite growth at constant supersaturation: Role of the desolvation process on the growth kinetics. *Geochim. Cosmochim. Acta* **71**, 5168-5179.

Koziol A. M. and Newton R. C. (1995). Experimental determination of the reactions magnesite + quartz = enstatite + CO_2 and magnesite = periclase + CO_2, and enthalpies of formation of enstatite and magnesite. *Am. Mineral.* **80**, 1252-1260.

Kubota, N. and Mullin, J. W. (1995) A kinetic model for crystal growth from aqueous solution in the presence of impurity. *J. Crystal Growth* **152**, 203-208.

Lackner, K. S., Butt, D. P., and Wendt, C. H. (1997). Progress on binding CO2 in mineral substrates. *Energy Conversion and Management* **38**, S259-S264.

Lackner, K. S., Wendt, C. H., Butt, D. P., Joyce, E. L., and Sharp, D. H. (1995). Carbon dioxide disposal in carbonate minerals. *Energy* **20**, 1153-1170.

Langmuir D., (1964). Stability of carbonates in the system CaO-MgO-CO_2-H_2O. Ph.D. thesis, Harvard University, USA.

Langmuir D. (1997). Aqueous environmental geochemistry. Prentice Hall, pp. 600.

Langmuir D., (1965). Stability of carbonates in the system MgO-CO_2-H_2O. *J. Geol.***73**, 730-750.

Langmuir I. (1918). The adsorption of gases on plane surfaces of glass, mica and platinum. *J. Am. Chem. Soc.* **40**, 1361-1403.

Lasaga A. C. (1981). Transition State Theory. *Rev. Min.* **8**, 135-169.

Leick, J. (1932). The solubilities of calcium carbonate and of magnesium carbonate in water that is free from carbonic acid. *Z. Anal. Chem.* **87**, 415-422.

Leitmeier H. (1915). Zur kenntnis der carbonate II. *Neues Jahrb. Mineralog.*, Abt. B, 655–700.

Levchenko V.M., Minkin M.B., and Dukhina T.P. (1970). Magnesium carbonate solubility. *Pochvovedenie* **8**, 144-148.

Lin F.-C., and Cemency C. V. (1981) The dissolution kinetics of brucite, antigorite, talc and phlogopite at room temperature and pressure. *Am. Min.* **66**, 801–806.

Lincoln S. F. and Merbach A. E. (1995). Substitution reactions of solvated metal cations. In *Advances in inorganic chemistry*, vol. 42, pp. 1-88. Academic Press.

Lindsay Jr. W.T. (1989). Chemistry of steam cycle solutions: principles. In: Cohen, P. (Ed.), The ASME handbook on water technology for thermal power plants. The American Society of Mechanical Engineers, New York, pp. 341–544. Chapter 7.

Lippmann F. (1973) Sedimentary Carbonate minerals. Springer-Verlag, pp. 229.

Luce R. W., Bartlett W. B., and Parks G. A. (1972). Dissolution kinetics of magnesium silicates. *Geochim. Cosmochim. Acta* **36**, 35–50.

Marini L. (2007). Geological sequestration of carbon dioxide: Thrmodynamics, kinetics and reaction path modeling. *Developments in Geochemistry* **11**. Elsevier, pp. 470.

Marion G. M. (2001) Carbonates mineral solubility at low temperatures in the Na-K-Mg-Ca-H-Cl-SO_4-OH-HCO_3-CO_3-CO_2-H_2O system. *Geochim. Cosmochim. Acta* **65** (12), 1883-1896.

Maroto-Valer, M. M., Fauth, D. J., Kuchta, M. E., Zhang, Y., and Andresen, J. M. (2005). Activation of magnesium rich minerals as carbonation feedstock materials for CO2 sequestration. *Fuel Processing Technology* **86**, 1627-1645.

Matter J. M., Takahashi T., and Goldberg D. (2007). Experimental evaluation of CO_2-water-rock reactions during CO2 injection in basaltic rocks. Implications for CO2 geological sequestration. *Geochemistry, Geophysics, Geosystems* **8**: doi:10.1029/2006GC001427.

McGrail, B. P., Schaef, H. T., Ho, A. M., Chien, Y. J., Dooley, J. J., and Davidson, C. L. (2006). Potential for carbon dioxide sequestration in flood basalts. *J. Geophys. Res.-Solid Earth* **111**, 13.

Ming D. W. And Franklin W. T. (1985). Synthesis and chracterization of landsfordite and nesquehonite. *Soil Sci. Soc. Am. J.* **49**, 1303-1308.

Möller P. (1989) Magnesite: geology, mineralogy, geochemistry, formation of Mg-carbonates. *Monograph series on Mineral Deposits*, n. 28, pp. 300. Gebrüder Borntraeger, Berlin-Stuttgart.

Morey, G.W. (1962). The action of water on calcite, magnesite, and dolomite. *Am. Mineral.* **47**, 1456–1460.

Morse J. W. And Casey W. H. (1988). Ostwald process and mineral paragenesis in sediments. *Am. J. Sci.* **288**, 537-560.

Morse, J.W., Arvidson, R.S. (2002). The dissolution kinetics of major sedimentary carbonate minerals. Earth Science Rev. **58**, 51-84.

Morse, J.W., Arvidson, R.S. and Luttge, A. (2007) Calcite formation and dissolution. *Chem. Revs.* **107,** 342-381.

Mucci, A. (1986). Growth kinetics and composition of magnesian calcite overgrowths precipitated from seawater: Quantitative influence of orthophosphate ions. *Geochim. Cosmochim. Acta* **50**, 2255-2265.

Mucci, A. and Morse, J. W. (1983). The incorporation of Mg^{2+} and Sr^{2+} into calcite overgrowths: influences of growth rate and solution composition. *Geochim. Cosmochim. Acta* **47**, 217-233.

Nancollas, G. H. and Reddy, M. M. (1971). The crystallization of calcium carbonate. II. Calcite growth mechanism. *Journal of Colloid and Interface Science* **37**, 824-830.

Nielsen, A. E. (1964). Kinetics of precipitation. Pergamon Press, pp. 151

Nielsen A. E. (1984). Electrolyte crystal growth mechanism. *J. Crystal Growth* **67**, 289-310.

O'Connor W.K., Dahlin D.C., Nilsen D.N., Rush G.E., Walters R.P., and Turner P.C. (2000). CO_2 Storage in Solid Form: A study of direct mineral carbonation. *Fifth International Conference on Greenhouse Gas Control Technologies,* Cairns, Australia, August 13 - August 16, 2000.

Oelkers E.H., and Cole D.R. (2008) Carbon dioxide sequestration: A solution to a global problem. *Elements* **4**, 305-310.

Oelkers E.H., and Schott J. (2005). Geochemical Aspects of CO_2 Sequestration. *Chem. Geo.* **217,** 183-186.

Oelkers E.H., Bjorkum, P.A., and Murphy W.M. (1996) A petrographic and computational investigation of quartz cementation and porosity reduction in North Sea sandstones. *Am. J. Sci.,* **296,** 420-452.

Oelkers E.H., Schott J., and Devidal J.-L. (1994). The effect of aluminum, pH, and chemical affinity on the rates of alumino-silicate dissolution reactions. *Geochim. Cosmochim. Acta* **58**, 2011-2024.

Oelkers, E. H. (2001). An experimental study of forsterite dissolution rates as a function of temperature and aqueous Mg and Si concentrations. *Chem. Geo.* **175**, 485-494.

Oelkers, E. H. and Schott, J. (1995) Experimental study of anorthite dissolution rates and the relative mechanism of feldspar hydrolysis. *Geochim. Cosmochim. Acta* **59**, 5039-5053.

Oelkers, E. H. and Schott, J. (1999) Experimental study of kyanite dissolution rates as a function of chemical affinity and solution composition. *Geochim. Cosmochim. Acta* **63**, 785-797.

Oelkers, E. H. and Schott, J. (2001). An experimental study of enstatite dissolution rates as a function of pH, temperature, and aqueous Mg and Si concentration, and the mechanism of pyroxene/pyroxenoid dissolution. *Geochim. Cosmochim. Acta* **65**, 1219-1231.

Oelkers, E.H., Gislason, S.R., and Matter, J. (2008) Mineral carbonation of CO_2. *Elements* **4**, 333-337.

Ohara M. and Reid R.C. (1973) Modeling crystal growth rates from solution. Prentice Hall, Inc., London, pp. 272.

O'Sullivan D. W. and Millero F. J. (1998). Continual measurement of the total inorganic carbon in surface seawater. *Marine Chemistry* **60**, 75-83.

Pacala S. and Socolow R. (2004). Stabilization wedges: Solving the climate problem for the next 50 years with current technologies. *Science* **305**, 968-972.

Palache C., Berman H., and Frondel C., 1951. The system of mineralogy, vol. 2, 7th ed. John Wiley, New York.

Palmer D. A. and Wesolowski D. J. (1997). Potentiometric measurements of the first hydrolysis quotient of magnesium (II) to 250 °C and 5 molal ionic strength (NaCl). *J. Sol. Chem.* **26** (2), 217-232).

Palmer, D.A., Bénézeth, P., Wesolowski, D.J. (2001). Aqueous high temperature solubility studies. I. The solubility of boehmite at 150 °C as a function of ionic strength and pH as determined by "in situ" measurements. *Geochim. Cosmochim. Acta* **65**, 2081-2095.

Paquette, J. and Reeder, R. J. (1995) Relationship between surface structure, growth mechanism, and trace element incorporation in calcite. *Geochim. Cosmochim. Acta* **59**, 735-749.

Parkhurst D. L. and Appelo C. A. J. (1999) User's guide to PHREEQC (version 2) - a computer program for speciation, batch-reaction,one-dimensional transport, and inverse geochemical calculations. U.S. Geological Survey Water-resources Investigation Report 99-4259, pp. 312

Patterson, C.S., Busey, R.H., Mesmer, R.E. (1984). Second ionization of carbonic acid in NaCl media to 250 °C. *J. Solution Chem.* **13**, 647-661.

Patterson, C.S., Slocum, G.H., Busey, R.H., and Mesmer, R.E. (1982). Carbonate equilibria in hydrothermal systems: first ionization of carbonic acid in NaCl media to 300 °C. *Geochim. Cosmochim. Acta* **46**, 1653–1663.

Piana, S., Jones, F., and Gale, J. D. (2006). Assisted desolvation as a key kinetic step for crystal growth. *J. American Chemical Society* **128**, 13568-13574.

Pina C. M. and Jordan G. (2009) Reactivity of mineral surfaces at nano-scale: kinetics and mechanisms of growth and dissolution. EMU-notes in Mineralogy 8, accepted.

Pina, C. M., Becker, U., Risthaus, P., Bosbach, D., and Putnis, A. (1998) Molecular-scale mechanisms of crystal growth in barite. *Nature* **395**, 483-486.

Pina, C. M., Fernández-Díaz, L., Prieto, M., and Putnis, A. (2000). In situ atomic force microscope observations of a dissolution-crystallisation reaction: the phosgenite-cerussite transformation. *Geochim. Cosmochim. Acta* **64**, 215-221.

Pines E. and Huppert D. (1983). pH jump: a relaxation approach. *J. Phys. Chem.* **87**, 4471-4478.

Plummer, L. N., Wigley, T. M. L., and Parkhurst, D. L. (1978). Kinetics of calcite dissolution in CO_2-water system at 5 °C to 60 °C and 0.0 to 1.0 atm CO_2. *Am. J. Sci.* **278**, 179-216.

Pokrovski, G. S., Schott, J., and Sergeyev, A. S. (1995). Experimental determination of the stability constants of NaSO4- and NaB (OH)40 in hydrothermal solutions using a new high-temperature

sodium-selective glass electrode -- Implications for boron isotopic fractionation. *Chem. Geo.* **124**, 253-265.

Pokrovsky O.S. and Schott J. (1999) Processes at the magnesium-bearing carbonates solution interface. II. Kinetics and mechanism of magnesite dissolution. *Geochim. Cosmochim. Acta* **63**, 881-897.

Pokrovsky O. S. and Schott J. (2000). Kinetics and mechanism of forsterite dissolution at 25°C and pH from 1 to 12. *Geochim. Cosmochim. Acta* **64**, 3313-3325.

Pokrovsky O. S. and Schott J. (2001). Kinetics and mechanism of dolomite dissolution in neutral to alkaline solutions revisited. *Am. J. Sci.* **301**, 597-626.

Pokrovsky, O. S. and Schott J. (2002). Surface chemistry and dissolution kinetics of divalent metal carbonates. *Environ. Sci. Technol.* **36**, 426-432.

Pokrovsky, O.S. and Schott J. (2004). Experimental study of brucite dissolution and precipitation in aqueous solution: surface speciation and chemical affinity control. *Geochim. Cosmochim. Acta* **68**, 31-45.

Pokrovsky O.S., Golubev S. V., Schott J. and Castillo A. (2009). Calcite, dolomite and magnesite dissolution kinetics in aqueous solutions at acid to circumneutral pH, 25 to 150 °C and 1 to 55 atm pCO_2: new constraints on CO_2 sequestration in sedimentary basins. *Chem. Geo.* **In press, corrected proof.**

Pokrovsky O. S., Golubev S. V. and Jordan G. (2009a). Effect of organic and inorganic ligands on calcite and magnesite dissolution rates at 60 °C and 30 atm pCO2. *Chem. Geo.* **In Press, Corrected Proof**.

Pokrovsky O. S., Golubev S. V. and Schott J. (2005). Dissolution kinetics of calcite, dolomite and magnesite at 25 °C and 0 to 50 atm pCO2. *Chem. Geo.* **217**, 239-255.

Pokrovsky O.S., Mielczarski J.A., and Schott J. (2001) Surface speciation of dolomite and calcite in aqueous solutions, in *Encyclopedia of Surface and Colloid Science.* Ed. A. Hubbard. Marcel Dekker Inc., p. 5081-5095.

Pokrovsky O. S., Schott J. and Thomas F. (1999a). Processes at the magnesium-bearing carbonates/solution interface. I. A surface speciation model for magnesite. *Geochim. Cosmochim. Acta* **63**, 863-880.

Pokrovsky O. S., Schott J. and Thomas F. (1999b). Dolomite surface speciation and reactivity in aquatic systems. *Geochim. Cosmochim. Acta* **63**, 3133-3143.

Potapenko, S. Y. (1993) Moving of step through impurity fence. *J. Crystal Growth* **133**, 147-154.

Prabhananda B. S., Rittger E. and Grell E. (1987). Kinetics and mechanism of anionic ligand binding to carbonic anhydrase. *Biophys. Chem.* **26**, 217-224.

Prigogine I. (1967). Introduction to Thermodynamics of Irreversible Processes. Wiley, New York, pp. 147.

Reddy, M. M. and Gaillard, W. D. (1981). Kinetics of calcium carbonate (calcite)-seeded crystallization: Influence of solid/solution ratio on the reaction rate constant. *Journal of Colloid and Interface Science* **80**, 171-178.

Reddy, M. M. and Nancollas, G. H. (1976). The crystallization of calcium carbonate : IV. The effect of magnesium, strontium and sulfate ions. *J. Crystal Growth* **35**, 33-38.

Reddy, M. M., Plummer, L. N., and Busenberg, E. (1981). Crystal growth of calcite from calcium bicarbonate solutions at constant PCO_2 and 25 °C: a test of calcite dissolution model. *Geochim. Cosmochim. Acta* **45**, 1281-1289.

Reeder, R. J. (1996) Interaction of divalent cobalt, zinc, cadmium, and barium with the calcite surface during layer growth. *Geochim. Cosmochim. Acta* **60**, 1543-1552.

Riesen, W.F. (1969). Thermodynamische untersuchungen am quatern ären system Ca^{2+}-Mg^{2+}-CO_2-H_2O. Ph.D. Thesis. Universität Bern.

Rimstidt J. D. and Barnes H. L. (1980). The kinetics of silica-water reactions. *Geochim. Cosmochim. Acta* **44**, 1683-1699.

Rimstidt J. D. and Dove P. M. (1986). Mineral/solution reaction rates in a mixed flow reactor: wollastonite hydrolisis. *Geochim. Cosmochim. Acta* **50**, 2509-2516.

Robie R. A. (1965). Heat and free energy of formation of herzenbergite, troilite, magnesite, and rhodochrosite calculated from equilibrium data. *U.S. Geol. Survey* **525**, 65–72.

Robie R. A. and Waldbaum D. R. (1968) Thermodynamic properties of minerals and related substances at 298.15°K (25.0°C) and one atmosphere (1.013 bars) pressure and at higher temperatures. *U.S. Geol. Survey Bull.* **1259,** 256 p.

Robie R.A., Hemingway B.S., and Fisher J.R. (1978). Thermodynamic properties of minerals and related substances at 298.15 K and 1 bar (105 Pa) pressure and at higher temperatures. *U.S. Geol. Survey Bull.* **1452**. U.S. Government Printing Office, Washington, DC, p. 456.

Robie, R.A. and Hemingway B.S. (1995). Thermodynamic properties of minerals and related substances at 298.15 K and 1 bar (105 Pa) pressure and at higher temperatures. *U.S. Geol. Survey Bull.*, **2131**.

Rossini F.D., Wagman D.D., Evans W.H., Levine S., and Jaffe I. (1961). Selected values of chemical

thermodynamic properties. Part I. Tables. *U.S. Natl. Bur. Standard Circ*., 500.

Rosso, J. J. and Rimstidt, J. D. (2000). A high resolution study of forsterite dissolution rates. *Geochim. Cosmochim. Acta* **64**, 797-811.

Sadiq M. and Lindsay W. L. (1979). Selection of standard free energy of formation for use in soil chemistry. *Colorado State Univ. Exp. Sta. Tech. Bull.* **134**.

Saldi, G. D., Köhler, S. J., Marty, N., and Oelkers, E. H. (2007). Dissolution rates of talc as a function of solution composition, pH and temperature. *Geochim. Cosmochim. Acta* **71**, 3446-3457.

Sánchez-Pastor, N., Pina, C. M., Astilleros, J. M., Fernandez-Diaz, L., and Putnis, A. (2005) Epitaxial growth of celestite on barite (001) face at a molecular scale. *Surf. Sci.* **581**, 225-235.

Sangwal, K. (1998) Growth kinetics and surface morphology of crystals grown from solutions: Recent observations and their interpretations. *Progress in Crystal Growth and Characterization of Materials* **36**, 163-248.

Sayles, F. L. and Fyfe, W. S. (1973) The crystallization of magnesite from aqueous solution. *Geochim. Cosmochim. Acta* **37**, 87-99.

Schlinder P. W. and Stumm W. (1987). The surface chemistry of oxides, hydroxides and oxide minerals. *In*: Aquatic surface chemistry. Stumm W. (ed.) John Wiley, New York, p. 83-110.

Schott J., Berner R. A., and Sjoberg E. L. (1981). Mechanism of pyroxene and amphibole weathering —I. Experimental studies of iron-free minerals. *Geochim. Cosmochim. Acta* **45**, 2123-2135.

Schott J., Pokrovsky O. S., and Oelkers E. H. (2009). The link between mineral dissolution/precipitation kinetics and solution chemistry. In "Thermodynamics and kinetics of water-rock interaction", *Rev. Min.***70**, 207-258.

Seifritz W. (1990). CO_2 disposal by means of silicates. *Nature* **345**, 486-486.

Shiraki, R. and Brantley, S. L. (1995) Kinetics of near-equilibrium calcite precipitation at 100°C: An evaluation of elementary reaction-based and affinity-based rate laws. *Geochim. Cosmochim. Acta* **59**, 1457-1471.

Shock E. L. and Helgeson H. C. (1988). Calculation of the thermodynamic and transport properties of aqueous species at high pressures and temperatures: correlation algorithms for ionic species and equation of state predictions to 5kb and 1000 °C. *Geochim. Cosmochim. Acta* **52**, 2009-2036.

Shock, E. L., Sassani, D. C., Willis, M., and Sverjensky, D. A. (1997) Inorganic species in geologic fluids: Correlations among standard molal thermodynamic properties of aqueous ions and hydroxide complexes. *Geochim. Cosmochim. Acta* **61**, 907-950.

Shvarov, Y. V. (1999). Algorithmization of the numerical equilibrium modelling of dynamic

geochemical processes. *Geochemistry International* **37**, 571-576.

Shvarov, Y., Bastrakov, E. (1999). A software package for geochemical equilibrium modeling. User's Guide. Australian Geological Survey Organization, Department of Industry, Science and Resources.

Smith R. M. and Martell A. E. (1976). Critical Stability Constants. Plenum Press, New York.

Staudt, W. J., Reeder, R. J., and Schoonen, M. A. A. (1994) Surface structural controls on compositional zoning of SO_2^{-4} and SeO_2^{-4} in synthetic calcite single crystals. *Geochim. Cosmochim. Acta* **58**, 2087-2098.

Steefel, C. I. and Van Cappellen P. (1990). A new kinetic approach to modeling water-rock interaction. The role of nucleation, precursors and Ostwald ripening. *Geochim. Cosmochim. Acta* **54**, 2657-2677.

Stipp, S. L. and Hochella, M. F. (1991). Structure and bonding environments at the calcite surface as observed with X-ray photoelectron spectroscopy (XPS) and low energy electron diffraction (LEED). *Geochim. Cosmochim. Acta* **55**, 1723-1736.

Stout J.W. and Robie R.A. (1963). Heat capacity from 11 to 300 K, entropy, and heat of formation of dolomite. *J. Phys. Chem*. **67** (11), 2248-2252.

Stull D. R. and Prophet H. (1971). JANAF thermochemical tables, 2d. edition: Natl. Bur Standards, *Natl. Standards Ref. Data Ser*., NBS37, 1141 pp.

Stumm W. and Morgan J. J. (1996). Aquatic chemistry: chemical equilibria and rates in natural waters. John Wiley & Sons Inc., p. 1022.

Sverjensky D. A., Shock E. L., and Helgeson H. C. (1997). Prediction of the thermodynamic properties of aqueous metal complexes to 1000 °C and 5 kb. *Goechim. Cosmochim. Acta* **61**, 1359-1412.

Takahashi G., 1927. Investigation on the synthesis of potassium carbonate by Mr. Engel. *Bull. Imp. Hyg. Lab. (Tokio)* **29**, 165-262.

Talman, S.J., Wiwchar, B., Gunter, W.D., Scarge, C.M. (1990). Dissolution kinetics of calcite in the $H_2O - CO_2$ system along the steam saturation curve to 210°C. In: Spencer, R.J. and Chou, I.M. (Eds.), Fluid-Mineral Interactions: A Tribute to H.P. Eugster. Geochem. Soc. Spec. Publ. Series, 2, 41-55.

Teng H. H., Dove P. M., Orme C. A., and De Yoreo, J. J. (1998). The thermodynamics of calcite growth: A baseline for understanding biomineral formation. *Science* **282,** 724–727.

Teng, H. H., Dove, P. M., and De Yoreo, J. J. (2000). Kinetics of calcite growth: surface processes and relationships to macroscopic rate laws. *Geochim. Cosmochim. Acta* **64**, 2255-2266.

Teng, H. H., Dove, P. M., and DeYoreo, J. J. (1999). Reversed calcite morphologies induced by microscopic growth kinetics: insight into biomineralization. *Geochim. Cosmochim. Acta* **63**, 2507-2512.

Torrent, J., Font, J., Herberhold, H., Marchal, S., Ribó, M., Ruan, K., Winter, R., Vilanova, M., and Lange, R. (2006). The use of pressure-jump relaxation kinetics to study protein folding landscapes. *Biochim. Biophys. Acta (BBA) - Proteins & Proteomics* **1764**, 489-496.

Trommsdorff V. and Connolly J. A .D. (1990). Constraints on phase diagram topology for the system CaO-MgO-SiO_2-CO_2-H_2O. Contributions to Mineralogy and Petrology **104**, 1-7.

Usdowski E. (1989). Synthesis of dolomite and magnesite at 60 °C in the system Ca^{2+}-Mg^{2+}-CO_3^{2-} - Cl_2^{2}-H_2O. *Naturwissenschaften* **76**, 374-375.

Van Cappellen, P. and Berner, R. A., (1991). Fluorapatite crystal growth from modified seawater solutions. *Geochim. Cosmochim. Acta* **55**, 1219-1234.

Van Cappellen, P., Charlet, L., Stumm, W., and Wersin, P. (1993). A surface complexation model of the carbonate mineral-aqueous solution interface. *Geochim. Cosmochim. Acta* **57**, 3505-3518.

van Enckevort, W. J. P. and van den Berg, A. C. J. F. (1998) Impurity blocking of crystal growth: a Monte Carlo study. *J. Crystal Growth* **183**, 441-455.

Vasconcelos C., McKenzie J. A., Bernasconi S., Grujic D., and Tien A. J. (1995). Microbial mediationas a possible mechanism for natural dolomite formationat low temperatures: *Nature* **377**, 220–222.

Vavouraki, A. I., Putnis, C. V., Putnis, A., and Koutsoukos, P. G. (2008). An Atomic Force Microscopy study of the growth of calcite in the presence of sodium sulfate. *Chem. Geo.* **253**, 243-251.

Vekilov, P. G. (2007). What determines the rate of growth of crystals from solution? *Cryst. Growth Des.* **7**, 2796-2810.

Villegas-Jiménez A., Mucci A., Pokrovsky O. S., and Schott J. (2009). Defining reactives sites on hidrated mineral surfaces: rhombohedral carbonate minerals. *Geochim. Cosmochim. Acta*, in press.

Voronkov V. V. and Rashkovich L. N. (1992) Influence of a mobile adsorbed impurity on the motion of steps. *Sov. Phys. Crystallogr.* **37(3)**, 289–295.

Wagman D. D., Evans W. H., Parker V. B., Schumm R. H., Halow I., Bailey S. M. Churney K. L., and

Nuttail R. L. (1982). The NBS tables of chemical thermodynamic properties: selected values for inorganic and C_1 ans C_2 organic substances in SI units. *J. Chem. Ref. Data* **11** supplement n. 2, 392 pp.

Wasylenki, L. E., Dove, P. M., Wilson, D. S., and De Yoreo, J. J. (2005) Nanoscale effects of strontium on calcite growth: An in situ AFM study in the absence of vital effects. *Geochim. Cosmochim. Acta* **69**, 3017-3027.

Wells, R.C. (1915). Solubility of magnesium carbonate in natural waters. *J. Am. Chem. Soc.* **37**, 1704-1707.

Wilson E. J. and Gerard D. (2007). Carbon capture and sequestration: integrating technology, monitoring and regulation. Blackwell Publishing. Ames (IA), USA. p. 269.

Wogelius, R. A. and Walther, J. V. (1991). Olivine dissolution at 25 °C: effects of pH, CO_2 and organic acids. *Geochim. Cosmochim. Acta* **55**, 943-954.

Wolf, G.H., Chizmeshya A.V.G., Diefenbacher, J., and McKelvy, M.J., (2004). In-situ observationof CO_2 sequestration reactions using a novel microreaction system. *Env. Sci. Tech.,* **38,** 932-936.

Wolff-Boenisch, D., Gislason, S. R., and Oelkers, E. H. (2006). The effect of crystallinity on dissolution rates and CO_2 consumption capacity of silicates. *Geochim. Cosmochim. Acta* **70**, 858-870.

Wollast, R. (1990). Rate and mechanism of dissolution of carbonates in the system $CaCO_3$ – $MgCO_3$, *in* Stumm, W., editor, Aquatic Chemical Kinetics: Reaction Rates of Processes in Natural Waters: New York, J. Wiley & Sons, p. 431-445.

Yanat'eva O.K. (1954). Solubility in the system $CaCO_3$-$MgCO_3$-H_2O at different temperatures and pressures of CO_2 . *Doklady Akad. Nauk. SSSR* **96**, 777–779.

Yanat'eva O.K. (1957). Solubility of the system Ca, Mg-CO_3, SO_4-H_2O at 25 °C and PCO_2 of 0.0012 atm. *Zh. Neorgan. Khim.* **2** (9), 2183-2187.

Yeghicheyan, D. (1996). Etude expérimentale du partage des terres rares entre carbonates de calcium et solutions aqueuses: influence de la cinétique de cristallisation et de la spéciation des terres rares en solution. *PhD Thesis*, Université Paul Sabatier, pp. 167.

Zachmann D. W. (1989). Mg-carbonates deposits in freshwater environment. In "Magnesite: geology, mineralogy, geochemistry, formation of Mg-carbonates". *Monograph series on Mineral Deposits*, n. 28, pp. 300. Gebrüder Borntraeger, Berlin-Stuttgart.

Zhang, J. and Nancollas, G. H. (1998) Kink Density and Rate of Step Movement during Growth and Dissolution of an ABCrystal in a Nonstoichiometric Solution. *Journal of Colloid and Interface Science* **200**, 131-145.

Zhang, R., Hu, S., Zhang, X., and Yu., W. (2007). Dissolution kinetics of dolomite in water at elevated temperatures. *Aquat. Geochem.* **13**, 309-338.

ANNEXE

Dissolution rates of talc as a function of solution composition, pH and temperature

Available online at www.sciencedirect.com
ScienceDirect
Geochimica et Cosmochimica Acta 71 (2007) 3446–3457
Geochimica et Cosmochimica Acta
www.elsevier.com/locate/gca

Dissolution rates of talc as a function of solution composition, pH and temperature

Giuseppe D. Saldi [a], Stephan J. Köhler [b], Nicholas Marty [c], Eric H. Oelkers [a,*]

[a] *Geochimie et Biogéochimie Experimentale, LMTG, Université de Toulouse, CNRS, IRD, OMP. 14 ave Edouard Belin, F-31400 Toulouse, France*
[b] *Institute of Applied Geosciences, Graz University of Technology, Rechbauerstraße 12, A-8010 Graz, Austria*
[c] *CGS/EOST UMR 7517, 1 rue Blessig, 67084 Strasbourg Cedex, France*

Received 7 June 2006; accepted in revised form 5 April 2007; available online 3 May 2007

Abstract

Steady-state talc dissolution rates, at far-from-equilibrium conditions, were measured as a function of aqueous silica and magnesium activity, pH from 1 to 10.6, and temperature from 25 to 150 °C. All rates were measured in mixed flow reactors and exhibited stoichiometric or close to stoichiometric dissolution. All measured rates at pH > 2 obtained at a fixed ionic strength of 0.02 M can be described to within experimental uncertainty using

$$r_+ = s_{\mathrm{BET}}\left(A_{\mathrm{A}}\left(\frac{a_{\mathrm{H}^+}^2}{a_{\mathrm{Mg}^{2+}}}\right)^{1/4} + A_{\mathrm{B}}\right)\exp(-E_{\mathrm{A}}/RT)$$

where r_+ signifies the BET surface area normalized forward talc steady-state dissolution rate, s_{BET} denotes the BET surface area of talc present in the reactor, A_{A} and A_{B} refer to pre-exponential factors equal to 5.0×10^{-9} and 0.8×10^{-9} mol/cm^2/s, respectively, E_{A} designates an activation energy equal to 45 kJ mol^{-1}, R represents the gas constant, T denotes absolute temperature, and a_i refers to the activity of the subscripted aqueous species. The first term of this rate expression is consistent with talc dissolution rates at acidic pH being controlled by the detachment of partially liberated silica tetrahedral formed at talc edge surfaces from the exchange of Mg^{2+} for two protons. Corresponding atomic force microscopic observations confirms that dissolution proceeds by the removal of T-O-T sheets from talc edges. At pH ⩽ 2, the Mg^{2+} for proton exchange is so extensive that talc T-O-T sheets break apart leading to increased surface area and accelerated rates, whereas rates appear to be pH independent at pH ⩾ 7.

1. INTRODUCTION

This study of talc dissolution rates is motivated for two major reasons:

(1) Magnesium silicates are a potential source of the divalent cations necessary for the sequestering of CO_2 in carbonate minerals; magnesium silicate dissolution rates, together with corresponding magnesium carbonate precipitation rates, allow the quantitative modeling and assessment of various CO_2 sequestration scenarios (e.g. Bergman and Winter, 1995).
(2) Talc is a well crystallized sheet silicate having a simple composition; it consists of T-O-T sheets with only magnesium in the octahedral and only silica in the tetrahedral layer. It is anticipated that studies of the dissolution behavior of simple compositioned sheets silicates, such as talc, will illuminate the dissolution behavior of sheet silicates, including clay minerals as a whole.

* Corresponding author. Fax: +33 561 33 25 60.
E-mail address: oelkers@lmtg.obs-mip.fr (E.H. Oelkers).

0016-7037/$ - see front matter © 2007 Published by Elsevier Ltd.
doi:10.1016/j.gca.2007.04.015

Towards the improved understanding of talc dissolution kinetics, its dissolution rates have been measured as a function of solution composition and temperature. The goal of this communication is to report the results of this experimental study.

To date relatively few studies have focused on the dissolution behavior of talc. Hemley et al. (1977) equilibrated talc together with chrysotile, forsterite, and brucite at elevated pressures and temperatures to determine their phase relationships. Lin and Cemency (1981) measured the dissolution behavior of talc at 25 °C and pH ~ 5 in a closed-system reactor. They observed that Mg from octahedral sheets was released more rapidly than Si from tetrahedral sheets, and suggested that talc dissolution rates are controlled by the destruction of these tetrahedral silica sheets. Jurinski and Rimstidt (2001) measured the dissolution rates of talc at 37 °C in mixed-flow reactors at $2 < pH < 8$. These authors observed little to no pH dependence of their talc dissolution rates.

2. THEORETICAL BACKGROUND

The standard state adopted in this study is that of unit activity for pure minerals and H_2O at any temperature and pressure. For aqueous species other than H_2O, the standard state is unit activity of the species in a hypothetical 1 molal solution referenced to infinite dilution at any temperature and pressure. Talc dissolution can be described according to

$$Mg_3Si_4O_{10}(OH)_2 + 6H^+ = 3Mg^{2+} + 4SiO_2(aq) + 4H_2O \quad (1)$$

Note that $SiO_2(aq)$ in reaction (1) represents the H_4SiO_4 aqueous species rather than total dissolved Si. Taking account of the standard state, the law of mass action for reaction (1) can be written

$$K_{talc} = a^3_{Mg^{+2}} a^4_{SiO_2(aq)} a^{-6}_{H^+} \quad (2)$$

where K_{talc} stands for the equilibrium constant of reaction (1), and a_i represents the activity of the subscripted aqueous species. The chemical affinity (A) for reaction (1) can be expressed as

$$A = RT \ln \left(\frac{K_{talc}\ a^6_{H^+}}{a^3_{Mg^{+2}}\ a^4_{SiO_2(aq)}} \right). \quad (3)$$

where R designates the gas constant, and T represents absolute temperature. It follows from Eq. (3) that talc is undersaturated when A is positive, and supersaturated when negative. All thermodynamic calculations reported in the present study were performed using the PHREEQC 2.6 computer code (Parkhurst and Appelo, 1999) together with its llnl database (Johnson et al., 2000). It is assumed in all thermodynamic calculations that the solid used in the dissolution experiments was pure stoichiometric talc. Although surface complexation theory suggests that the activities of charged particles on charged surfaces may differ somewhat from unity (Davis and Kent, 1990), the activities of species at the talc surface are assumed to be equal to their mole fraction. This latter assumption is shown below to be consistent with measured rate data.

Within the context of Transition State Theory, surface reaction controlled dissolution rates can be considered to be the difference between the forward rate (r_+) and the reverse rate (r_-) such that

$$r = r_+ - r_- = r_+ \left(1 - \frac{r_-}{r_+} \right). \quad (4)$$

Taking account of the law of detailed balancing it can be shown that Eq. (4) is equivalent to (Aagaard and Helgeson, 1977, 1982; Lasaga, 1981; Helgeson et al., 1984; Murphy and Helgeson, 1987, 1989; Oelkers, 2001a)

$$r = r_+(1 - \exp(-A/\sigma RT)), \quad (5)$$

where σ stands for Temkin's average stoichiometric number equal to the ratio of the rate of destruction of the activated or precursor complex relative to the overall rate. Experimental evidence suggests that the value of σ in Eq. (2) is 1 for quartz (Berger et al., 1994) and 3 for the alkali-feldspars (Gautier et al., 1994). The form of Eq. (5) is such that overall rates (r) equal forward rates (r_+) when $A \gg \sigma RT$. The majority of dissolution rates measured in the present study were performed at far-from-equilibrium conditions, such that $A \gg \sigma RT$. At these conditions $r_- \ll r_+$ and thus $r \approx r_+$. Talc dissolution rates in this study are thus symbolized r_+. Such experimental results can be used to assess the effect of aqueous solution composition on forward dissolution rates independently from the effects of chemical affinity.

Within the formalism of Transition State Theory, r_+ is proportional to the concentration of a rate controlling 'precursor' complex in accord with (Wieland et al., 1988)

$$r_+ = k_+ s[P^\bullet]. \quad (6)$$

k_+ in Eq. (6) refers to a rate constant, s stands for the mineral/fluid interfacial surface area and $[P^\bullet]$ designates the concentration of the 'precursor' complex which itself is proportional to the concentration of the activated complex. The variation of r_+ with aqueous composition, therefore, can be deduced from the law of mass action for the reaction forming the 'precursor' complex from the original mineral (c.f. Oelkers, 2001a).

The identity and variation with aqueous solution composition of the rate controlling precursor complex $P^\bullet$, can be deduced from a mineral's dissolution mechanism. The dissolution of multi-component silicate minerals such as talc occurs through the breaking of metal–oxygen bonds (e.g. Mg–O and Si–O bonds). Each metal–oxygen bond within a silicate structure breaks at a distinct rate, which may be orders of magnitude different from that of other metal–oxygen bonds. Dissolution proceeds by the sequential removal of metals from the mineral structure; the order of the removal of each metal is dictated by the relative rates of breaking each metal oxygen bond. The breaking of these bonds is coupled to the formation of hydrogen–oxygen bonds to maintain charge balance, via metal for proton exchange reactions (Oelkers, 2001a). The slowest breaking metal–oxygen bond holding the mineral structure together controls the overall dissolution rate and can be

designated as the rate controlling bond. It follows that only processes that accelerate destruction of this rate controlling bond will accelerate the overall dissolution rate. One such process is the removal of metals adjacent to the rate controlling bonds from the mineral structure (Gratz et al., 1991; Gratz and Bird, 1993; Gautier et al., 2001). For example, the breaking of Si–O bonds is faster if the Si is attached to the mineral surface by two rather than three bridging oxygens. Note that not all metal–oxygen bonds need to be broken to dissolve a mineral. For example, Si–O bonds need not be broken for the dissolution of either forsterite or anorthite; Mg–O bonds are rate controlling for forsterite dissolution and Al–O bonds are rate controlling for anorthite dissolution (Oelkers and Schott, 1995; Oelkers, 2001b).

The talc structure consists of octahedral Mg–O bonds and tetrahedral Si–O bonds. Mg is situated in octahedral sites that are bound via oxygen bridges to 4 Si tetrehedra and 2 protons. A variety of evidence suggests that octahedral Mg–O bonds break more rapidly than tetrahedral Si–O bonds. Luce et al. (1972) observed that Mg was released faster than Si during the initial dissolution of serpertine, forsterite, and enstatite at $1.6 < \mathrm{pH} < 9$. They also observed that the initial Mg release was due to a stoichiometric exchange of one Mg^{2+} for two H^+. Similarly, Lin and Cemency (1981) observed the preferential initial release of Mg during the acid dissolution of antigorite, talc, and phlogopite. This observation lead these authors to conclude that breaking of the slower Si–O bonds were rate controlling for the dissolution of these minerals. The relatively rapid release rate of Mg versus Si from silicate minerals is also supported by the formation of Mg-leached layers during the acid dissolution of surfaces of dissolved enstatite and other pyroxenes (Luce et al., 1972; Schott et al., 1981; Berner and Schott, 1982; Schott and Berner, 1985; Petit et al., 1987; Schott and Petit, 1987; Peck et al., 1988; Ferruzzi, 1993). These conclusions are in agreement with that of Schott et al. (1981) who, based on the concurrence of XPS adsorption band positions in fresh and acid leached enstatite, postulated that H^+ replaces Mg in the enstatite structure during hydrolysis without rearranging the silica bonding network. These observations suggest the talc dissolution mechanism outlined in Fig. 1, where talc dissolution is initiated by the relatively rapid removal of Mg atoms at edge positions via Mg–H exchange reactions. This exchange reaction can be expressed as (e.g. Oelkers and Schott, 2001)

$$> \mathrm{Mg} + 2\mathrm{H}^+ = \mathrm{Mg}^{2+} + 2 > \mathrm{H} \tag{7}$$

where >Mg designates an Mg atom in the talc structure. This exchange reaction partially liberates Si–O tetrahedra, which are subsequently released to solution completing the dissolution process. In accord with transition state theory, far-from-equilibrium talc dissolution rates will therefore be proportional to the concentration of partially detached Si tetrahedra. The concentration of these partially detached Si tetrahedra can be estimated from the law of mass action for reaction (7) which when combined with Eq. (6) yields (c.f. Oelkers, 2001a)

$$r_+ = k_+ s \lfloor > \mathrm{Si}^* \rfloor = k_+ s \left(\frac{\left(\frac{a^2_{\mathrm{H}^+}}{a_{\mathrm{Mg}^{2+}}} \right)^{1/n}}{1 + K_7 \left(\frac{a^2_{\mathrm{H}^+}}{a_{\mathrm{Mg}^{2+}}} \right)^{1/n}} \right) \tag{8}$$

where $\lfloor > \mathrm{Si}^* \rfloor$ represents the concentration of partially detached Si tetrahedra at the talc edges, a_i again refers to the activity of the subscripted aqueous species, n denotes a stoichiometric coefficient equal to the number of partially detached Si tetrahedra formed by the removal of each Mg, and K_7 designates the equilibrium constant for reaction (7). As there are 4 Si tetrahedra attached to each Mg octahedra, it seems likely that $n \sim 4$. When there is still substantial Mg remaining at the talc edge surface, Eq. (8) reduces to

$$r_+ \approx k_+ s \left(\frac{a^2_{\mathrm{H}^+}}{a_{\mathrm{Mg}^{2+}}} \right)^{1/n} \tag{9}$$

These equations suggest that increasing aqueous hydrogen ion activity and decreasing aqueous Mg activity will increase far-from-equilibrium talc dissolution rates, and these rates will be independent of aqueous Si activity. The degree to which (1) this mechanism is applicable to talc and (2) Eqs. (8) and (9) can describe talc dissolution rates is assessed below.

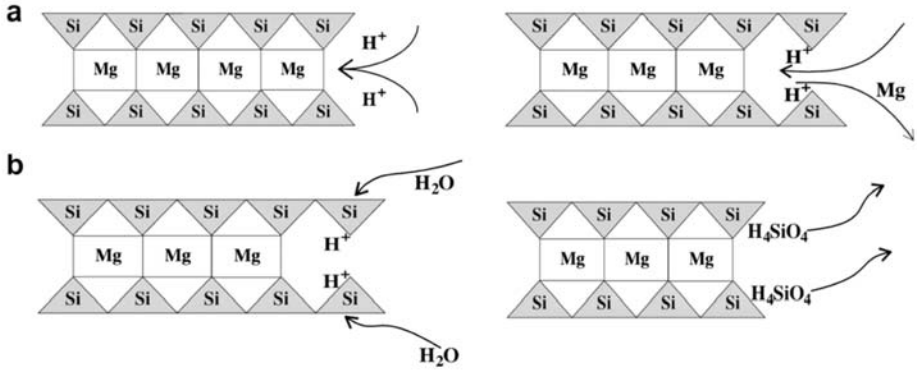

Fig. 1. Schematic illustration of the talc dissolution mechanism consisting of (a) the exchange of Mg atoms with 2 protons near the talc edge surfaces, followed by (b) the liberation of Si.

3. MATERIALS AND METHODS

Talc originating from the Trimouns mine in Ariege, France, has been chosen for this study due to its high purity and crystallinity. This material has already been extensively characterized (Martin et al., 1999a,b,c). This sample was first ground with an agate mortar and pestle. The size fraction between 50 and 200 μm was obtained by sieving; this fraction was then ultrasonically cleaned using acetone. The specific surface area of the cleaned powder is 0.603 ± 0.009 m^2/g as determined by krypton absorption using the Brunauer et al. (1938, B.E.T.) method. The chemical composition of the talc determined by fusion analysis yields a Si/Mg atomic ratio of 1.27 ± 0.06 which is consistent with the theoretical value of 1.33. Photomicrographs of this initial talc powder are shown in Fig. 2a and b. It can be seen that these grains are clean, and no fine particles are apparent.

Dissolution experiments were performed in mixed flow reactors as described by Oelkers and Schott (2001) using sealed Azalon plastic beakers with a 0.45 μm outlet filter at 25 and 80 °C and Parr reactors with a 10 μm outlet filter at 135 and 150 °C. Fluid is injected into the reactors using Gilson peristaltic pumps, which allow fluid flow rates from 0.01 to 10 g/min. Steady-state dissolution rates, as indicated by constant outlet Mg and Si concentration, was obtained after an elapsed time ranging from 0.5 to 45 days, depending on flow rate and temperature. Dissolution experiments were performed in fluids comprised of demineralised H_2O, and Merck reagent grade HCl, NaOH, NaCl, NH_4Cl, NH_4OH, NaH_2PO_4, KH_2PO_4, and $MgCl_2$. All inlet fluids had stoichiometric ionic strengths of 0.02 mol kg^{-1}. The compositions of all inlet solutions are listed in Table 1. Magnesium compositions of the inlet and outlet fluids were determined using a Perkin Elmer Zeeman 5000 atomic absorption spectrometer; silica compositions were measured using the Molybdate Blue method (Koroleff, 1976). The reproducibility of chemical analyses was ±4% for Si and Mg concentrations greater than 0.5 and 0.1 ppm, respectively, but higher at lower concentrations.

Outlet fluid pH was measured at 25 °C immediately after sampling, pH values at the elevated experimental temperatures were computed using PHREEQC (Parkhurst and Appelo, 1999) using its llnl database. Outlet solutions were undersaturated with respect to all possible secondary phases other than for the solutions having pH > 8, which were slightly supersaturated with respect to chrysotile, brucite, and/or anthophillite.

Steady-state dissolution rates (r) were computed from the measured steady-state solution compositions using

$$r = \frac{\Delta m_i F}{\nu_i \bar{s}_{BET} M} \tag{10}$$

where Δm_i stands for the concentration difference between the inlet and outlet of the ith element in solution, F represents the fluid mass flow rate, ν_i refers to the stoichiometric number of moles of the ith element in one mole of talc, and $\bar{s}_{BET}$ denotes the BET specific surface area of the initial talc, and M signifies the initial mass of talc in the reactor.

One additional experiment was performed to determine talc dissolution rates directly at 25 ± 2 °C using a Digital Instruments Nanoscope IIIa Multimode Atomic Force Microscope (AFM) (c.f. Bickmore et al., 1999). This experiment was performed by submerging a single talc grain into

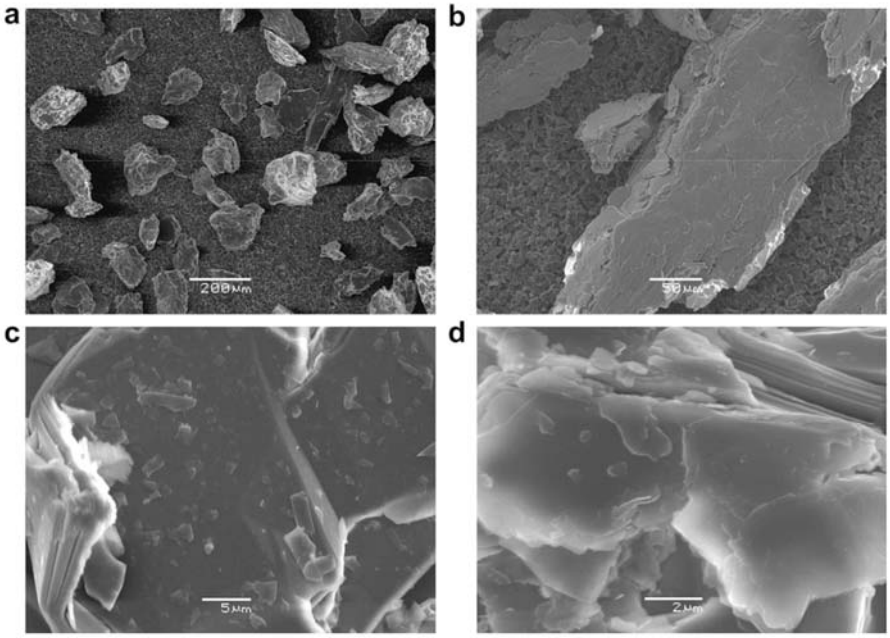

Fig. 2. Scanning electron microscope photomicrographs of talc surfaces. (a) and (b) talc surfaces before their dissolution, (c) and (d) talc surfaces after their dissolution at 150 °C in a pH 2 solution.

Table 1
Compositions of inlet solutions used in the present study

pH (25 °C)	1 M $HCl_{(l)}$, g/kg[a]	$NaCl_{(s)}$, g/kg	$KH_2PO_{4(s)}$, g/kg	$NH_4Cl_{(s)}$, g/kg	$NaH_2PO_{4(s)}2H_2O$, g/kg	28% NH_3, g/kg	1 M $NaOH_{(l)}$, g/kg
1.7	19.9525	0.0025	—	—	—	—	—
2	10	0.5844	—	—	—	—	—
2.3	5.0125	0.875	—	—	—	—	—
2.7	1.995	1.0525	—	—	—	—	—
3.3	0.5	1.1375	—	—	—	—	—
4	0.1	1.1688	—	—	—	—	—
4.3	0.05	1.165	—	—	—	—	—
5.5	—	1.165	—	—	—	—	—
7	—	—	—	—	2.0718	—	7.056
7.3	—	—	6.805	—	—	—	17.35
7.5	—	—	—	1.0538	—	0.0182	—
8	—	—	—	1.0201	—	0.0566	—
8.55	—	—	—	0.9115	—	0.18	—
9.25	—	—	—	0.855	—	—	6.665
9.7	5.65	—	—	—	—	1.29	—
10	—	—	—	0.1654	—	1.0282	—
12	5.575	—	—	—	—	—	10

[a] Mass of each solid or solution added to each kg of inlet solution.

0.15 g of a NaCl–HCl solution with an ionic strength of 0.02 and a pH of 2. An additional 0.05 g of this solution was added to the system every 45 min in an attempt to counteract the effects of evaporation and acid consumption. Talc dissolution was observed by regularly scanning a 2.6 by 2.6 micron part of its surface at a 0.8 Hz scan rate and a 512 sampling resolution per scan line. The mass of talc dissolved was determined by measuring the volume of distinct features on its surface using the Nanotec WSxM 2.1 computer code.

4. RESULTS AND DISCUSSION

Representative examples of the temporal evolution of solution composition during talc dissolution experiments performed in acid and basic solutions are illustrated in Fig. 3. At acid pH Mg is initially preferentially removed from the talc surface but at basic pH it is preferentially retained in agreement with the relative fast equilibration of the Mg for proton exchange reaction. After a short initial elapsed time, the system attains a steady-state and the outlet solution composition becomes constant.

Steady-state outlet solution concentrations of Mg and Si were used to compute talc dissolution rates using Eq. (10). Rates were measured at a variety of aqueous silica and magnesium activities, pH from 1.7 to 10.6, and temperature from 25 to 150 °C. All measured steady-state talc dissolution rates are listed in Table 2. Also listed in this table are the steady-state outlet solution compositions and the chemical affinity of these solutions with respect to brucite, anthophyllite, chrysotile, sepiolite, and talc. All experiments performed at pH < 8 were highly undersaturated with respect to talc; for all of these experiments the talc chemical affinity is greater than 17 kcal/mol. These solutions are also undersaturated with respect to other potential precipitating phases. In contrast, calculations suggest that some of the experiments performed at basic conditions were supersaturated with respect to one or more secondary phase and in one case supersaturated with respect to talc itself. As talc was the only phase placed into the reactor, this calculation suggests that the thermodynamic data for talc incorporated into the database is somewhat uncertain.

The difference between the inlet and outlet solution concentration of Si are plotted as a function of the corresponding Mg concentration difference in Fig. 4. The ratio of this difference, $\Delta Si/\Delta Mg$, ranges from 0.8 to 1.5 for 41 of the 48 measured steady-state outlet solution concentrations compared with a molar Si/Mg ratio of 1.27 for the dissolving talc. Seven steady-state solution concentrations had either higher or lower $\Delta Si/\Delta Mg$ ratios. Of these, 4 were performed in basic solutions that were supersaturated with respect to brucite and potentially other Mg-rich phases. The high Si/Mg atomic ratio of these solutions are consistent with the precipitation of Mg-rich secondary phases. Two other steady-state outlet solutions had $\Delta Si/\Delta Mg$ ratios of 2.64 and 0.6 likely because their Mg or Si concentrations were close to the analytical detection limit, and one steady-state outlet solution had a $\Delta Si/\Delta Mg$ ratio of 0.13. The $\Delta Si/\Delta Mg$ ratio of this steady-state outlet solution has a high uncertainty because of the high inlet Mg concentration during this experiment.

Logarithms of BET surface area normalized steady-state talc dissolution rates are illustrated as a function of pH in Fig. 5. Rates based on changes in both reactive fluid Mg and Si concentration are listed in Table 2; only those based on Si are shown in the figures. Rates obtained in both phosphate and ammonia bearing buffer solutions appear to be consistent with those obtained in buffer-free inlet solutions. Measured constant temperature steady-state talc dissolution rates decrease with increasing pH up to pH ~ 7; the dashed lines drawn through the data at pH > 7 in Fig. 5 are consistent with $r_+ \propto pH^{-0.5}$. Rates at pH > 7 appear to be pH independent to within experimental uncertainty. These pH > 7 rates exhibit some scatter; this scatter may

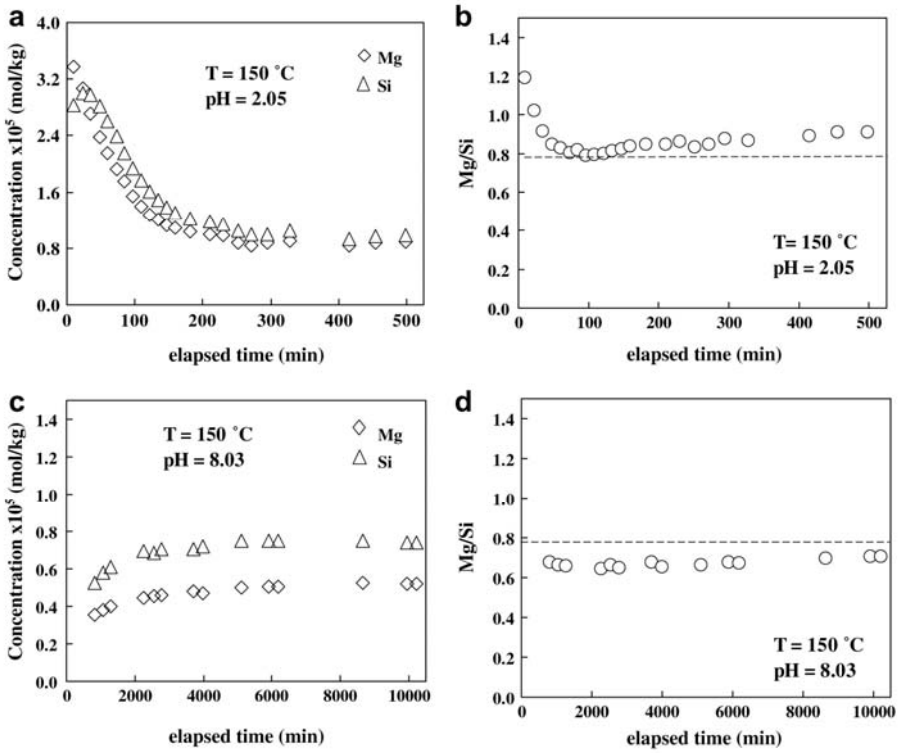

Fig. 3. Temporal evolution of outlet solution aqueous Mg and Si concentration and Mg/Si ratio during talc dissolution experiments: (a) aqueous Mg and Si concentrations during the dissolution of talc at 150 °C and pH 2.05. (b) the atomic Mg/Si ratio of the fluids shown in a. (c) aqueous Mg and Si concentrations during the dissolution of talc at 150 °C and pH 8.03. (d) the atomic Mg/Si ratio of the fluids shown in (c). The dashed lines represent the atomic Mg/Si ratio of the talc.

be due to the effects of secondary phase precipitation in these solutions that are supersaturated with respect to one or more secondary phases. No clear minimum of talc dissolution rates at intermediate pH is observed. This observation similar to that of other Mg–silicate phases (e.g. enstatite and olivine; Pokrovsky and Schott, 2000; Oelkers and Schott, 2001), but in contrast to many Al–silicates (e.g. Gislason and Oelkers, 2003).

Logarithms of 150 °C steady-state talc dissolution rates at pH ~ 4.6 and ~5.3 are illustrated as a function of the corresponding logarithms of aqueous Mg activity in Fig. 6. Constant pH rates decrease with increasing aqueous magnesium activity; The lines drawn through the data in Fig. 6 is consistent with $r_+ \propto a_{Mg^{2+}}{}^{-0.25}$. To within experimental uncertainty the variation of measured constant temperature talc dissolution rates with aqueous magnesium activity at pH < 7 is equal to the reciprocal square root of its dependence on aqueous hydrogen activity. This observation is consistent with the concept that talc dissolution rates are controlled by the destruction of partially detached Si tetrahedra formed by the exchange of two protons for one Mg near the talc surface. Moreover, the slopes of the lines drawn in Figs. 5 and 6 are consistent with $n = 4$. This value of n suggests that 4 Si-rich precursor complexes are formed by the removal of each Mg, which is in agreement with the talc structure, as described above.

An equation describing talc dissolution rates over the full range of pH can be generated by combining the Mg/H exchange rate equation Eq. (9) with a parallel pH independent rate equation yielding

$$r_+ = s\left(k_+\left(\frac{a_{H^+}^2}{a_{Mg^{2+}}}\right)^{1/4} + k_b\right) \tag{11}$$

where k_b designates a rate constant describing pH independent rates at basic pH. To generate a fit of measured talc dissolution rates as a function of both temperature and solution compositions, Eq. (11) was combined with an Arrhenius equation describing the variation of talc rate constants as a function of temperature to yield (c.f. Oelkers, 2001a):

$$r_+ = s\left(A_A\left(\frac{a_{H^+}^2}{a_{Mg^{2+}}}\right)^{1/4}\exp(-E_{A,A}/RT) + A_B\exp(-E_{A,B}/RT)\right) \tag{12}$$

where A_A and A_B refer to pre-exponential factors, $E_{A,A}$ and $E_{A,B}$ designate activation energies, R represents the gas constant, T denotes absolute temperature, and a_i refers to the activity of the subscripted aqueous species. Regression of all rate data excluding those obtained at pH below 2 at 135 and 150 °C shows talc dissolution rates to be consistent

Table 2
Measured steady-state talc dissolution rates and corresponding solution compositions including chemical affinities of potential secondary phases

	pH	Surface area, cm^2	Inlet $Mg \times 10^5$, mol/kg	Inlet $Si \times 10^5$, mol/kg	Outlet $Mg \times 10^5$, mol/kg	Outlet $Si \times 10^5$, mol/kg	ΔSi/ΔMg	Fluid flow rate, g/min	log r(Mg), $mol/cm^2/s$	log r(Si), $mol/cm^2/s$	Brucite[a] affinity, kcal/mol	Anthophillite[a] affinity, kcal/mol	Chrysotile[a] affinity, kcal/mol	Sepiolite[a] affinity, kcal/mol	Talc[a] affinity, kcal/mol
$T = 150$ °C															
	1.72	7439	0	0	12.3	15.5	1.26	3.86	−12.40	−12.42	22.24	145.42	56.99	90.65	57.53
	2.02	6629	0	0	2.66	3.72	1.40	0.99	−13.57	−13.55	22.35	155.81	59.72	98.30	62.66
	2.04	6629	0	0	1.06	1.43	1.36	4.61	−13.31	−13.32	23.05	167.09	63.41	105.89	67.96
	2.05	6629	0	0	0.889	0.977	1.10	9.42	−13.15	−13.24	23.15	170.39	64.37	108.23	69.55
	2.75	7439	0	0	3.52	3.95	1.12	0.61	−13.78	−13.86	19.28	133.88	50.40	85.69	53.24
	3.34	7439	0	0	1.43	1.84	1.29	1.96	−13.60	−13.63	17.59	127.21	46.62	82.80	50.74
	3.51	13387	0	0	2.53	3.22	1.27	0.70	n.d.	−14.18	16.44	115.44	42.25	75.40	45.43
	3.95	6126	0	0	0.870	1.19	1.37	0.98	−14.12	−14.11	16.14	119.97	42.99	79.20	47.85
	4.56	13387	0	0	3.41	4.34	1.27	0.40	n.d.	−14.31	12.25	84.09	29.17	57.13	31.86
	4.58	13387	0	0	3.99	5.06	1.27	0.40	n.d.	−14.25	12.05	81.61	28.29	55.53	30.72
	4.76	6126	0	0	0.405	0.632	1.56	0.92	−14.43	−14.36	13.64	106.74	36.57	72.40	42.49
	5.35	7420	0	0	1.77	2.20	1.24	0.31	−14.27	−14.30	9.76	71.24	22.85	50.60	26.67
	5.55	7439	0	0	1.89	2.34	1.24	0.40	−14.38	−14.38	8.96	65.20	20.33	47.08	24.06
	5.96	6126	0	0	0.085	0.221	2.61	0.96	−15.11	−14.82	10.32	90.56	28.37	64.41	36.06
	8.03	6126	0	0	0.532	0.745	1.40	0.47	−14.62	−14.60	0.39	14.02	−3.18	19.41	2.75
	9.09	6126	0	0	0.267	0.685	2.56	0.40	−15.01	−14.72	−3.12	−3.44	−11.93	10.70	−4.22
	2.04	6629	52	0	53.6	3.52	1.43	1.00	−13.67	−13.55	19.76	138.02	52.03	88.20	55.07
	2.06	6629	11	0	12.9	3.39	1.41	1.00	−13.60	−13.58	20.86	146.01	55.41	92.81	58.51
	4.69	13387	205	0	208	3.42	0.91	0.36	n.d.	−14.41	8.34	58.30	17.83	42.68	20.91
	4.70	13387	20.5	0	25.3	4.82	0.99	0.36	n.d	−14.27	10.04	67.86	22.34	47.73	24.85
	4.78	13387	82	0	86.0	3.91	0.97	0.36	n.d	−14.36	8.71	60.00	18.72	43.49	21.58
	5.26	7420	205	0	212	0.854	0.13	0.33	n.d	−14.80	6.13	52.18	13.54	40.85	18.96
	5.56	7420	62	0	63.4	1.14	0.82	0.33	n.d	−14.68	5.98	49.19	12.61	38.80	17.54
	2.00	6136	0	31	3.28	34.9	1.19	0.98	−13.54	−13.59	22.26	140.08	55.67	86.62	54.85
	2.05	6136	0	6	3.33	10.6	1.36	0.97	−13.54	−13.53	22.04	146.57	57.02	91.76	58.20
$T = 135$ °C	1.70	6054	0	0	6.14	7.24	1.18	2.4	−13.10	−12.91	22.93	154.11	59.91	95.17	61.33
	2.69	6054	0	0	0.463	0.515	1.11	2.4	−14.22	−14.07	21.31	159.90	59.32	101.54	65.03
	5.15	6054	0	0	1.10	1.42	1.29	0.29	−14.77	−14.55	11.43	84.18	28.05	57.09	32.11
$T = 80$ °C	1.71	6569	0	0	2.28	2.41	1.06	0.084	−14.70	−14.64	23.04	148.08	58.10	86.63	57.56
	1.67	6653	0	0	9.38	9.21	0.98	0.267	−14.13	−14.27	23.89	161.55	62.53	95.67	63.87
	2.31	6052	0	0	5.23	5.71	1.09	0.082	−14.63	−14.67	21.36	138.97	53.72	81.90	53.85
	2.71	9065	0	0	4.42	4.98	1.13	0.088	−14.80	−14.89	20.15	131.28	50.28	77.64	50.60
	3.45	12066	0	0	4.29	4.74	1.11	0.037	−15.33	−15.38	17.77	114.93	43.23	68.35	43.62

4.40	10986	0	0	1.49	1.44	0.96	0.045	−15.58	−15.65	15.47	105.50	37.99	64.16	40.06
7.15	22249	0	0	1.44	n.d	n.d	0.06	−15.69	n.d.	n.d	n.d	n.d	n.d	n.d
9.66	23494	0	0	3.55	5.72	1.61	0.045	−15.28	−15.14	−2.34	−20.98	−15.90	−8.44	−14.28
10.20	12508	0	0	0.968	1.24	1.28	0.061	−15.70	−15.63	−3.06	−10.06	−14.06	0.65	−8.46
10.18	11223	0	0	0.107	0.881	8.20	0.065	−16.56	−15.74	−1.47	4.18	−8.52	9.34	−2.14
$T = 25$ °C														
1.74	6042	0	0	0.407	0.344	0.85	0.045	−15.6	−15.93	25.28	171.35	66.32	97.90	67.43
1.80	10148	0	0	1.780	1.92	1.08	0.0251	−15.8	−15.78	24.07	155.19	60.78	87.28	59.95
2.01	6012	0	0	0.389	0.428	1.10	0.0238	−16.07	−16.15	24.41	164.65	63.57	93.96	64.51
2.36	6126	0	0	0.537	0.324	0.60	0.066	−15.5	−15.78	23.26	157.93	60.45	90.35	61.73
2.36	6126	0	0	1.41	1.13	0.80	0.0247	−15.5	−15.78	22.69	148.01	57.26	83.63	57.05
2.76	12084	0	0	0.199	0.175	0.88	0.222	−15.8	−15.88	22.76	157.32	59.67	90.53	61.68
2.76	12084	0	0	0.566	0.652	1.15	0.0266	−16.3	−16.18	22.14	146.76	56.26	83.38	56.70
3.33	14465	0	0	0.876	0.823	0.94	0.0266	−16.1	−16.18	20.33	132.96	50.54	75.29	50.71
4.06	6018	0	0	0.133	0.196	1.47	0.0236	−16.54	−16.49	19.45	133.62	49.61	76.88	51.48
6.97	6026	0	0	0.069	n.d	n.d	0.0125	−17.00	n.d	n.d	n.d	n.d	n.d	n.d
7.52	6130	0	0	0.083	0.103	1.24	0.0129	−16.96	−16.95	10.28	72.52	22.87	42.52	25.51
9.67	6512	0	0	0.070	0.235	3.36	0.0127	−17.09	−16.72	4.39	29.51	4.76	17.63	6.95

[a] Listed affinities are for mineral dissolution reactions, such that A is positive for undersaturation and negative for supersaturation.

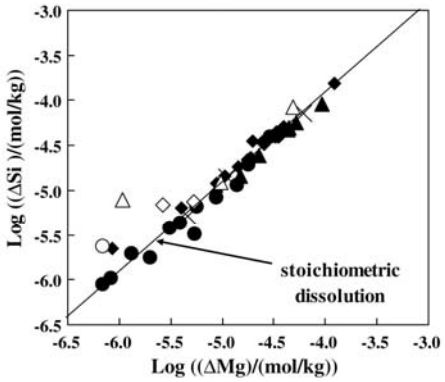

Fig. 4. The difference between the inlet and outlet solution Si concentration (ΔSi) plotted as a function of the corresponding Mg concentration difference (ΔMg) for all steady-state solutions. The filled circles, triangles, crosses, and diamonds represent rates measured at 25, 80, 135, and 150 °C, respectively. Open symbols correspond to experiments performed at pH > 8 whereas filled symbols correspond to experiments performed at pH < 8. The solid curve is consistent with stoichiometric talc dissolution.

with $A_A = 5.0 \times 10^{-9}$ mol/cm^2/s and $A_B = 0.8 \times 10^{-9}$ mol/cm^2/s and $E_{A,A} = E_{A,B} = 45$ kJ/mol. Because within the uncertainty of the data $E_{A,A} = E_{A,B}$ and BET surface areas were used to normalize rates, Eq. (12) can be reduced to:

$$r_+ = s_{BET}\left(A_A\left(\frac{a_{H^+}^2}{a_{Mg^{2+}}}\right)^{1/4} + A_B\right)\exp(-E_A/RT) \qquad (13)$$

where $E_A = E_{A,A} = E_{A,B}$ and s_{BET} corresponds to the BET surface area of talc in the system. The quality of this regression can be gauged with the aid of Figs. 7 and 8, which compares rates calculated with Eq. (13) with their measured

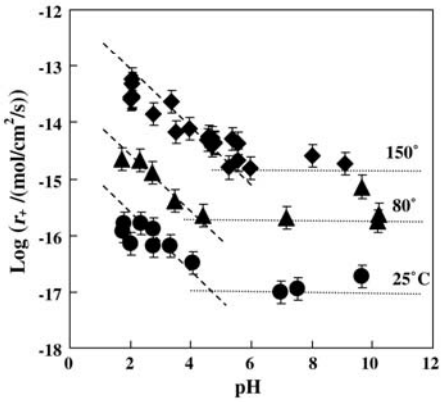

Fig. 5. Variation of the logarithm of measured steady-state talc dissolution rates as a function of pH. The filled circles, triangles, and diamonds represent rates measured at 25, 80, and 150 °C, respectively. The slopes of the dashed curves drawn through the symbols at pH < 6 correspond to $r_+ \propto pH^{0.5}$, whereas the dotted lines are consistent with rates being independent of pH at pH > 6. Error bars on the symbols correspond to a ±0.2 log unit uncertainty on the measured rates.

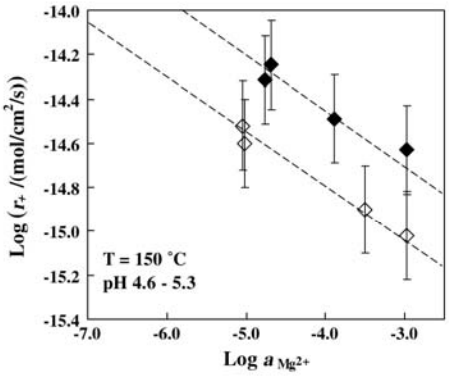

Fig. 6. Log–log plots showing the variation of measured talc dissolution rates at 150 °C as a function of the aqueous activity of Mg^{2+}. The filled and open symbols correspond to measured rates at pH ~ 4.6 and ~5.4, respectively; the dashed curves are consistent with $r_+ \propto a_{Mg^{2+}}{}^{-0.25}$. Error bars on the symbols correspond to a ±0.2 log unit uncertainty on the measured rates.

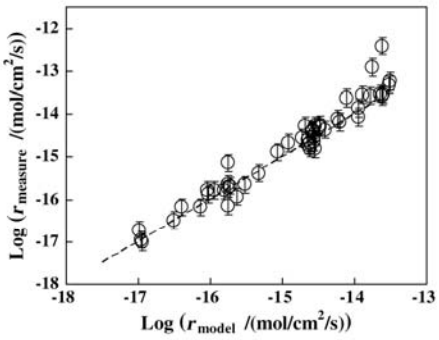

Fig. 8. Comparison of measured talc dissolution rates with corresponding rates calculated using Eq. (13) together with consistent with $A_A = 5.0 \times 10^{-9}$ mol/cm^2/s, $A_B = 0.8 \times 10^{-9}$ mol/cm^2/s, and $E_A = 45$ kJ/mol. Symbols correspond to the measured and calculated rates; error bars on the symbols correspond to a ±0.2 log unit uncertainty on the measured rates. The dashed line represents equal values for these two rates.

counterparts. It can be seen that all measured rates are within 0.4 log units of corresponding computed rates, other than for the experiments measured at pH ⩽ 2 at 135 and 150 °C. Insight into the origin of the distinct rate behavior of rate measured at pH ⩽ 2 at 135 and 150 °C can be obtained from the surface morphology of talc grains after their dissolution at these conditions.

Photomicrographs of several talc grains following their dissolution at pH 2 and 150 °C are shown in Fig. 2c and d. It can be seen that several talc edges have fanned out, exposing a large amount of talc edge surface area to dissolution. As a result the surface area of these powders, as measured by BET techniques, reacted at pH 2 increased from 0.60 to ~1.65 m^2/g during the experiments. It seems

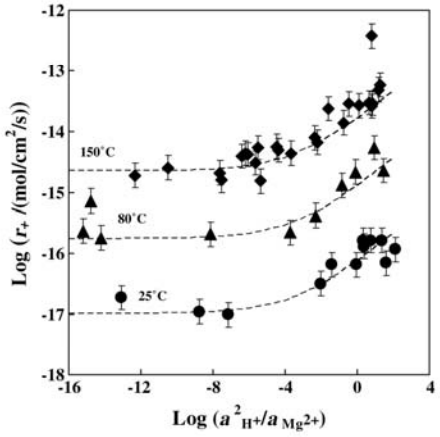

Fig. 7. Logarithms of steady-state talc dissolution rates plotted as a function of log $\left(\frac{a^2_{H^+}}{a_{Mg^{2+}}}\right)$. Symbols correspond to measured rates; error bars on the symbols correspond to a ±0.2 log unit uncertainty on the measured rates. The dashed curves were calculated using Eq. (13) together with consistent with $A_A = 5.0 \times 10^{-9}$ mol/cm^2/s, $A_B = 0.8 \times 10^{-9}$ mol/cm^2/s, and $E_A = 45$ kJ/mol.

likely therefore that, at these highly acidic conditions, the exchange of Mg for protons is so extensive that the T-O-T sheets break apart at the talc edges leading to increased surface area and accelerated dissolution rates. Similar observations have been reported for other clay minerals when leached in strongly acidic solutions (Kaviratna and Pinnavaia, 1994; Aldushin et al., 2004, 2006). This observation is also consistent with estimates of the average depth of Mg removal during the initial dissolution of talc in these low pH experiments. Taking account of the relative release rate of Mg versus Si during the first 10 h of the talc dissolution experiment performed at pH 2.05 and 150 °C and mass balance calculations it is estimated that an average of 19 Mg atoms were preferentially released from each mn^2 of talc surface prior to attaining a stoichiometric steady state. Assuming that only 1/10 of the talc surface area are edges and that there are ~3–4 Mg atoms per mn^2 on the talc edges, an average of ~60 unit cells of Mg were removed on average from these edges surfaces at 150 °C and pH 2. In accord with Eq. (8) it seems likely that that aqueous Mg will have little effect on talc dissolution rates at such conditions. In contrast, similar mass balance calculations performed for experiments performed at pH ~ 4 and 150 °C suggest an average Mg leaching of less than 0.4 Mg atoms per mn^2 of talc surface. Again assuming that only 1/10 of the talc surface area are edges and that there are ~3–4 Mg atoms per mn^2 on the talc edges, no more than the surface Mg atoms are removed from the talc, consistent with an influence of aqueous Mg on talc dissolution rates at these higher pH.

The close connection between measured talc dissolution rates and those calculated with Eq. (13) support a talc dissolution mechanism at acidic pH consisting of the initial relatively rapid exchange of Mg for protons at talc edges followed by the relatively slow rate controlling depolymerization and hydration/protonation of SiO_4 tetrahedrons. Similarly, it has also been postulated that the dissolution rates of montmorillonite (Zysset and Schindler, 1996), kaolinite (Oelkers et al., 1994; Devidal et al., 1997), and

muscovite (Oelkers et al., 2000) are controlled by the destruction of partially detached Si tetrahedra sheets, formed by proton/metal exchange reactions. Results on talc presented above support the possibility that a single general mechanism can be developed describing the dissolution of the sheet silicates including the clay minerals.

The results of the single talc dissolution rate determined directly by AFM observations are presented in Fig. 9. An overview of one part of the scanned talc surface is shown in Fig. 9a. Rates were determined by the change in mass of the surface feature seen in the upper right hand part of this image. Fig. 9b shows the height of this feature as determined by an AFM scan over the white bar shown in the inset of this figure. It can be seen that the height of this feature is ~1 nm, which corresponds to the height of a single talc T-O-T layer. The total surface area of the basal plane of this feature as a function of elapsed time is presented in Fig. 9c. Similar to observations reported by Bickmore et al. (2001), scans performed regularly during this experiment show that this feature dissolved by decreasing the basal plane surface area; the edge height of this feature remained constant throughout the experiment. This observation supports the dissolution mechanism described above, which indicates that only talc edge surfaces are reactive and its basal plane surfaces are inert.

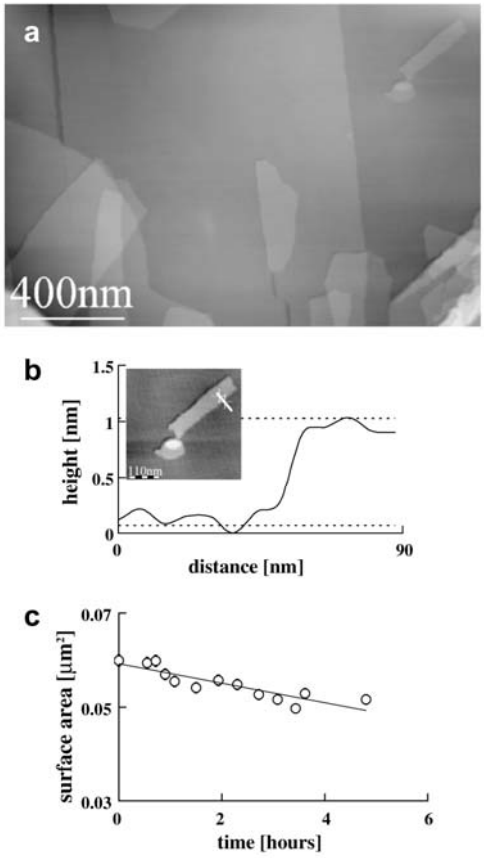

Fig. 9. In situ tapping mode AFM dissolution experiment of talc de Trimouns in a pH 2 HCl solution containing 0.01 mol/kg NaCl and at 25 °C: (a) large scale image of talc surface at the beginning of the experiments, (b) a height profile of the feature located in the upper right side of (a), and an enlargement of the upper right corner of (a), and (c) variation of the surface area of this feature as a function of elapsed time during the experiment.

One challenge in using AFM observations to generate dissolution and growth rates is how to normalize rates to mineral surface area. If the talc dissolution observed in the AFM experiment performed in the present study is normalized to the total surface area of the analyzed surface feature, one obtains a dissolution rate of $1.6 \pm 0.6 \times 10^{-14}$ mol/cm^2/s. In contrast, if this observed dissolution is normalized to just the surface area of the surface feature's edges, one obtains a dissolution rate of $8 \pm 3 \times 10^{-13}$ mol/cm^2/s. In either case these rates are approximately two orders of magnitude faster than that of the corresponding bulk powder listed in Table 2. A similar difference between edge surface area normalized rates and bulk surface area normalized rates of phlogopite has been reported by Rufe and Hochella (1999). These differences stem from the differences in surface area used to normalize the observed dissolution to quantify rates. Bulk rates are an average rate of the whole talc powder, which contain a large percentage of uncreative surfaces, whereas rates generated from the AFM observations presented above are based on the relatively small surface of a reactive surface feature. One consequence of the reactive heterogeneity of sheet silicate mineral surfaces is that their bulk dissolution rates are observed to vary significantly as a function of time during laboratory experiments and by analogy in the field (c.f. Köhler et al., 2005; Hodson, 2006). Note, that the AFM rates determined in this study are close to the lower limit compatible with AFM measurements (Dove and Platt, 1996) and all AFM rates can be influenced by artifacts including frictional effects of the scanning tip and laser induced temperature changes (Park et al., 1996). As such there is a high degree of uncertainty in the talc AFM-based rates reported above.

The dissolution rates of a number of clay minerals when normalized to their edge surface area are remarkably similar to one another. Brandt et al. (2003) reported a pH 2, 25 °C AFM-based edge surface area normalized chlorite dissolution rate of 2.5×10^{-13} mol/cm^2/s. Similarly, Bosbach et al. (2000) reported a pH 2, 25 °C AFM-based edge surface area normalized hectorite dissolution rate of 6×10^{-13} mol cm^2/s. The similarity of sheet silicate edge surface area normalized dissolution rates suggests (1) that the rate limiting step of the dissolution of these minerals is identical for all sheet silicates, which based on this study is likely the breaking of Si–O bonds, and (2) as suggested by Metz et al. (2005), edge surface area normalized sheet silicate dissolution rates may be a more consistent than those normalized to the total surface area.

5. CONCLUSIONS

Steady-state talc dissolution rates have been found to be consistent with their control by two parallel mechanisms. At acidic pH rates are proportional to both proton and magnesium activity consistent with $r_+ \propto \mathrm{pH}^{-0.5}$ and

$r_+ \propto a_{Mg^{2+}}{}^{-0.25}$. This observation suggests that talc dissolution at acid pH follows a mechanism similar to that of enstatite; the dissolution of both minerals at low pH is apparently controlled by the slow detachment of partially liberated Si tetrahedral sheets formed by the exchange of two protons for one magnesium near the mineral surface. At basic pH rates appear to be pH independent. In addition, due to the similarity of the structures of the sheet silicates and the AFM observations presented above, it seems likely that metal for proton exchange reactions also play a role in the dissolution mechanism of sheet silicate minerals.

ACKNOWLEDGMENTS

We thank Francois Martin for providing the talc dissolved during this study, Dirk Bosbach for his assistance and for hosting S.J.K. while performing AFM experiments and the INE Forschungszentrum in Karlsruhe for supplying lab space for these experiments. We are grateful to Oleg Pokrovsky, Jacques Schott, Jean-Louis Dandurand, Robert Gout, Siggi Gislason, Domenik Wolf-Boenisch, and Stacey Callahan for helpful discussions during the course of this study. Alian Castillo, Jean-Claude Harrichoury and Carole Causser- and provided technical assistance. Support from Centre National de la Recherche Scientifique, the Petroleum Research Fund of the American Chemical Society (PRF #41765-AC2), and the European Community through the MIR Early Stage Training Network (MEST-CT-2005-021120) is gratefully acknowledged.

REFERENCES

Aagaard P., and Helgeson H. C. (1977) Thermodynamic and kinetic constraints on the dissolution of feldspars. *Geol. Soc. Amer. Abstr. Program.* **9**, 873.

Aagaard P., and Helgeson H. C. (1982) Thermodynamic and kinetic constraints on reaction rates among minerals and aqueous solutions: I. Theoretical considerations. *Am. J. Sci.* **282**, 237–285.

Aldushin K., Jordan G., Fechtelkord M., Schmahl W. W., Becker H., and Rammensee W. (2004) On the mechanisms of apophyllite alteration in aqueous solutions. A combined AFM, XPS and MAS NMR study. *Clays Clay Miner.* **52**, 432–442.

Aldushin K., Jordan G., and Schmahl W. W. (2006) Kinematics of apophyllite leaching—A terrace-ledge-kink process within phyllosilicate interlayers. *J. Crystal Growth* **297**, 161–168.

Berger G., Cadoré E., Schott J., and Dove P. M. (1994) Dissolution rate of quartz in Pb and Na electrolyte solutions. Effect of the nature of surface complexes and reaction affinity. *Geochim. Cosmochim. Acta* **58**, 541–551.

Bergman P. D., and Winter E. M. (1995) Disposal of carbon dioxide in aquifers in the US. *Energy Convers. Manag.* **36**, 523–526.

Berner R. A., and Schott J. (1982) Mechanisms of pyroxene and amphibole weathering; II. Observations of soil grains. *Am. J. Sci.* **282**, 1214–1231.

Bickmore B. R., Hochella M. F., Bosbach D., and Charlet L. (1999) Methods for performing atomic force microscopy imaging of clay minerals in aqueous solutions. *Clays Clay Miner.* **47**, 573–581.

Bickmore B. R., Bosbach D., Hochella M. F., Charlet L., and Rufe E. (2001) In situ atomic force microscopy study of hectorite and nontronite dissolution: implications for phyllosilicate edge surface structures and dissolution mechanisms. *Am. Min.* **86**, 411–423.

Bosbach D., Charlet L., Bickmore B., and Hochella M. F. (2000) The dissolution of hectorite; in situ, real-time observations using atomic force microscopy. *Am. Min.* **85**, 1209–1216.

Brandt F., Bosbach D., Krawczyk-Barsch E., Arnold T., and Bernhard G. (2003) Chlorite dissolution in the acid pH range: a combined microscopic and macroscopic approach. *Geochim. Cosmochim. Acta* **67**, 1451–1461.

Brunauer S., Emmett P. H., and Teller E. (1938) Adsorption of gases in multimolecular layers. *J. Am. Chem. Soc.* **60**, 309–319.

Davis J. A., and Kent D. B. (1990) Surface complexation modelling in aqueous geochemistry. *Rev. Min.* **23**, 177–260.

Devidal J.-L., Schott J., and Dandurand J.-L. (1997) An experimental study of kaolinite dissolution and precipitation kinetics as a function of chemical affinity and solution composition at 150 °C, 40 bars, and pH 2, 6.8, and 7.8. *Geochim. Cosmochim. Acta* **61**, 5165–5186.

Dove P. M., and Platt F. M. (1996) Compatible real-time rates of minerals dissolution by Atomic Force Microscopy. *Chem. Geol.* **127**, 331–338.

Ferruzzi, G.G., 1993. The character and rates of dissolution of pyroxenes and pyroxenoids. MS Thesis, University of California, Davis, CA.

Gautier J.-M., Oelkers E. H., and Schott J. (1994) Experimental study of K-feldspar dissolution rates as a function of chemical affinity at 150 °C and pH 9. *Geochim. Cosmochim. Acta* **58**, 4549–4560.

Gautier J.-M., Oelkers E. H., and Schott J. (2001) Are quartz dissolution rates proportional to BET surface areas? *Geochim. Cosmochim. Acta* **65**, 1059–1070.

Gislason S. R., and Oelkers E. H. (2003) The mechanism, rates, and consequences of basaltic glass dissolution. II. An experimental study of the dissolution rates of basaltic glass as a function of pH at temperatures from 6 °C to 150 °C. *Geochim. Cosmochim. Acta* **67**, 3817–3832.

Gratz A. J., and Bird P. (1993) Quartz dissolution: negative crystal experiments and a rate law. *Geochim. Cosmochim. Acta* **57**, 965–976.

Gratz A. J., Manne S., and Hansma P. (1991) Atomic Force Microscopy of atomic-scale ledges and etch pits formed during dissolution of quartz. *Science* **251**, 1343–1346.

Helgeson H. C., Murphy W. M., and Aagaard P. (1984) Thermodynamic and kinetic constraints on reaction rates among minerals and aqueous solutions: II. Rate constants, effective surface area, and the hydrolysis of feldspar. *Geochim. Cosmochim. Acta* **48**, 2405–2432.

Hemley J. J., Montoya J. W., Christ J. L., and Hostetler P. B. (1977) Mineral equilibria in the MgO–SiO_2–H_2O system: talc–chrysotile–forsterite–brucite stability relations. *Am. J. Sci.* **277**, 322–351.

Hodson M. E. (2006) Does reactive surface area depend on grain size? Results from pH 3, 25 °C far-from-equilibrium flow-through dissolution experiments on anorthite and biotite. *Geochim. Cosmochim. Acta* **70**, 1655–1667.

Johnson, J., Anderson, G. and Parkhurst, D. (2000) Database from thermo.com.V8.R6.230 prepared by at Lawrence Livermore National Laboratory, (Revision: 1.11).

Jurinski J. B., and Rimstidt J. D. (2001) Biodurability of talc. *Am. Min.* **86**, 392–399.

Kaviratna H., and Pinnavaia T. (1994) Acid hydrolysis of octahedral Mg^{2+} sites in 2:1 layered silicates: an assessment of edge attack and gallery access mechanisms. *Clays Clay Miner.* **42**, 717–723.

Köhler S. J., Bosbach D., and Oelkers E. H. (2005) Do clay mineral dissolution rates reach steady state? *Geochim. Cosmochim Acta* **69**, 1997–2006.

Koroleff F. 1976 Determination of silicon. In *Methods of Seawater Analysis* (ed., K. Grasshoff). Springer Verlag, New York, pp. 149–158.

Lasaga A. C. (1981) Transition state theory. *Rev. Min.* **8**, 135–169.

Lin F.-C., and Cemency C. V. (1981) The dissolution kinetics of brucite, antigorite, talc and phlogopite at room temperature and pressure. *Am. Min.* **66**, 801–806.

Luce R. W., Bartlett W. B., and Parks G. A. (1972) Dissolution kinetics of magnesium silicates. *Geochim. Cosmochim. Acta* **36**, 35–50.

Martin F., Micoud P., Delmotte L., Marechal C., LeDred R., deParseval Ph., Mari A., Fortune J. P., Salvi S., Beziat D., Grauby O., and Ferret J. (1999a) The structural formula of talc from the Trimouns deposit, Pyrénées, France. *Can. Mineral.* **37**(4), 976–1006.

Martin F., de Parseval, Ph., Micoud, P., Ferret J. 1999b Mössbauer study of chlorite and talc from the Trimouns deposit (Pyrénées, France): evidence for systematic presence of Fe^{3+} In *Clays for our Future* (ed., H. Kodama), Ottawa, Canada, pp. 259–264.

Martin F., Petit S., Grauby O., and Lavie M. P. (1999c) Gradual H/D substitution in synthetic germinium bearing talcs: a method for infrared assignment. *Clay Miner.* **34**, 365–374.

Metz V., Amram K., and Ganor J. (2005) Stoichiometry of smectite dissolution reaction. *Geochim. Cosmochim. Acta* **69**, 1755–1772.

Murphy W. M., and Helgeson H. C. (1987) Thermodynamic and kinetic constraints on reaction rates among minerals and aqueous solutions. III. Activated complexes and the pH-dependence of the rates of feldspar, pyroxene, wollastonite, and olivine hydrolysis. *Geochim. Cosmochim. Acta* **51**, 3137–3153.

Murphy W. M., and Helgeson H. C. (1989) Thermodynamic and kinetic constraints on reaction rates among minerals and aqueous solutions. IV. Retrieval of rate constants and activation parameters for the hydrolysis of pyroxene, wollastonite, olivine, andalusite, quartz and nepheline. *Am. J. Sci.* **289**, 17–101.

Oelkers E. H. (2001a) General kinetic description of multioxide silicate mineral and glass dissolution. *Geochim. Cosmochim. Acta* **65**, 3703–3719.

Oelkers E. H. (2001b) An experimental study of forsterite dissolution rates as a function of temperature and aqueous Mg and Si concentration. *Chem. Geol.* **175**, 485–494.

Oelkers E. H., Schott J., and Devidal J.-L. (1994) The effect of aluminum, pH and chemical affinity on the rates of aluminosilicate dissolution reactions. *Geochim. Cosmochim. Acta* **58**, 2011–2024.

Oelkers E. H., and Schott J. (1995) Experimental study of anorthite dissolution and the relative mechanism of feldspar hydrolysis. *Geochim. Cosmochim. Acta* **59**, 5039–5053.

Oelkers E. H., Gauthier J.-M., Schott J. 2000 An experimental study of the mechanism and dissolution rates of muscovite. In *2000 Goldschmidt Conference*, Oxford, England, Journal of Conference Abstracts **5**, 749.

Oelkers E. H., and Schott J. (2001) An experimental study of enstatite dissolution rates as a function of pH, temperature, and aqueous Mg and Si concentration, and the mechanism of pyroxene/pyroxenoid dissolution. *Geochim. Cosmochim. Acta* **65**, 1219–1231.

Park N., Kim M., Langford S. C., and Dickinson J. T. (1996) Atomic layer wear of single-crystal calcite in aqueous solution using scanning force microscopy. *J. Appl. Phys.* **80**, 2680–2686.

Parkhurst D. L., Appelo C. A. J. 1999 User's guide to PHREEQC (Version 2)—a computer program for speciation, batch-reaction, one-dimensional transport, and inverse geochemical calculations US Geol. Surv. Water Resour. Inv. Report 99-4259.

Peck J. A., Farnan I., and Stebbins J. F. (1988) Disordering and the progress of hydration at the surface of diopside; a cross-polarisation MAS NMR study. *Geochim. Cosmochim. Acta* **52**, 3017–3021.

Petit J. C., Della M. G., Dran J. C., Schott J., and Berner R. A. (1987) Mechanism of diopside dissolution from hydrogen depth profiling. *Nature* **325**, 705–707.

Pokrovsky O. S., and Schott J. (2000) Kinetics and mechanisms of forsterite dissolution at 25 °C and pH from 1 to 12. *Geochim. Cosmochim. Acta* **64**, 3313–3325.

Rufe E., and Hochella M. F. (1999) Quantitative assessment of reactive surface area of phlogopite during acid dissolution. *Science* **285**, 874–876.

Schott J., Berner R. A., and Sjoberg E. L. (1981) Mechanism of pyroxene and amphibole weathering—I. Experimental studies of iron-free minerals. *Geochim. Cosmochim. Acta* **45**, 2123–2135.

Schott, J., Berner, R. A. 1985 Dissolution mechanisms of pyroxenes and olivines during weathering. In: *The chemistry of weathering*, vol. 149 (ed., J. I. Drever), NATO ASI series C; Mathematical and Physical Sciences, pp. 35–53.

Schott, J., Petit, J. C. 1987 New evidence for the mechanisms of dissolution of silicate minerals. In: *Aquatic Surface Chemistry: Chemical processes at the Mineral-Surface Interface* (ed., W. Stumm) Swiss Federal Institute of Technology Zurich, Switzerland, pp. 293–315.

Wieland E., Werhli B., and Stumm W. (1988) The coordination chemistry of weathering: III. A potential generalization on dissolution rates of minerals. *Geochim. Cosmochim. Acta* **52**, 1969–1981.

Zysset M., and Schindler P. W. (1996) The proton promoted dissolution kinetics of K-montmorillonite. *Geochim. Cosmochim. Acta* **60**, 921–931.

Associate editor: Liane G. Benning

TITLE: Magnesite dissolution and precipitation rates at hydrothermal conditions

---

ABSTRACT

Magnesite ($MgCO_3$) is the stable anhydrous member of a series of Mg-carbonates with different degrees of hydration. Despite its relative scarcity in the natural environments, it constitutes an important mineral phase for the permanent sequestration of CO_2 as carbonate minerals. Experimental determination of magnesite precipitation and dissolution rates at conditions representative of the storage sites is therefore fundamental for the assessment of magnesite sequestration potential in basaltic and ultramafic rocks and the optimization of the techniques of CO_2 storage.

Magnesite precipitation rates have been measured using mixed-flow and batch reactors as a function of temperature ($100 \leq T \leq 200$ °C), solution composition and CO_2 partial pressure (up to 30 bar). Rates were found to be independent of aqueous solution ionic strength at 0.1 M $< I <$ 1.1 M but decrease significantly with increasing aqueous CO_3^{2-} activity at pH > 8. All rates obtained from mixed flow reactor experiments were found to be consistent with the model of Pokrovsky et al. (1999) where magnesite precipitation rates are proportional to the concentration of the $>MgOH_2^+$ surface species. The study of magnesite crystallization using hydrothermal atomic force microscopy (HAFM) demonstrated the consistency of the rates derived from microscopic measurements with those obtained from bulk experiments and showed that these rates are also consistent with a spiral growth mechanism. According to AFM observations this mechanism controls magnesite growth over a wide range of temperatures and saturation states ($15 \leq \Omega \leq 200$ for $80 \leq T < 120$ °C). Precipitation rates dependence on solution composition recommends the use of relatively high pCO_2 to accelerate the rate of the overall carbonation process, avoiding the inhibiting effect of carbonate ions on magnesite precipitation and increasing the rates of Mg-silicate dissolution via acidification of reacting solutions.

Determination of magnesite dissolution rates by mixed flow reactor at 150 and 200 °C and at neutral to alkaline conditions allowed us to improve and extend to high temperatures the surface complexation model originally developed at 25 °C. The decrease of dissolution rates observed from 150 to 200 °C can be explained by the increasing carbonation and hydrolysis of the rate controlling $>MgOH_2^+$ sites. As a result of the decreasing rates of dissolution, the achievement of alkaline conditions and temperatures higher than 100 °C by CO_2-rich fluids represents a favorable condition for CO_2 sequestration as dissolved alkalinity in deep aquifers where carbonate minerals are major constituting phases.

The use of a hydrogen electrode concentration cell (HECC) corroborates the kinetic data obtained at close to equilibrium conditions by the precise determination of magnesite solubility product as a function of temperature (50-200°C). These measurements allowed generating the thermodynamic properties of this phase and comparing them with those obtained from calorimetric measurements and phase equilibria experiments.

The results of this study significantly improve our understanding of the kinetic behaviour of carbonate minerals in hydrothermal systems and provide an essential database for the future study of dissolution/precipitation reactions of carbonate minerals in complex systems. This work also provides important kinetic constraints for the geochemical modeling of CO_2 sequestration processes and will help the evaluation of impact and risks connected to a long-term storage.

AUTEUR : Giuseppe SALDI

TITRE : Les cinétiques de dissolution et précipitation de la magnésite aux conditions hydrothermales

DIRECTEURS DE THESE : Eric H. Oelkers

LIEU ET DATE DE SOUTENANCE : Toulouse, le 24 Septembre 2009

RESUME

La magnésite ($MgCO_3$) est la forme anhydre la plus stable d'une série de carbonates de magnésium qui présentent différents degrés d'hydratation. Malgré sa rareté dans les environnements naturels, elle constitue une phase minérale fondamentale pour le piégeage minéral permanent du CO_2. La détermination expérimentale des vitesses de précipitation et de dissolution de la magnésite dans des conditions représentatives de la séquestration géologique est donc fondamentale pour l'estimation du potentiel de séquestration de CO_2 par cette phase dans les basaltes et dans les roches ultrabasiques et pour l'optimisation des procédés de stockage du CO_2.

Nous avons mesuré les vitesses de précipitation de la magnésite en utilisant des réacteurs à circulation et des réacteurs fermés, en fonction de la température ($100 \leq T \leq 200$ °C), de la composition de la solution aqueuse et de la pression partielle de CO_2 (de 0 à 30 bar). Les vitesses mésurées sont indépendantes de la force ionique de la solution pour 0.1 M $< I <$ 1.1 M, mais elles diminuent significativement avec l'augmentation de l'activité des ions CO_3^{2-} pour des pH supérieures à 8. Les vitesses mesurées dans les réacteurs à circulation sont cohérentes avec le modèle de coordination chimique surfacique de Pokrovsky et al. (1999) selon lequel les vitesses de précipitation de la magnésite sont proportionnelles à la concentration des sites surfaciques $>MgOH_2^+$. L'étude des vitesses de cristallisation conduite par microscopie à force atomique hydrothermale (HAFM) a montré un bon accord entre les vitesses déduites de mesures microscopiques et les vitesses macroscopiques et a aussi démontré que la précipitation de la magnésite s'effectue selon un mécanisme de croissance spirale. Suivant les observations effectuées par AFM, ce mécanisme contrôle la vitesse de croissance de la magnésite dans un grand intervalle de température et d'indice de saturation ($15 \leq \Omega \leq 200$ pour $80 \leq T < 120$ °C). En raison de l'inhibition de la précipitation de la magnésite par les ions carbonates, il est recommandé d'opérer sous des pressions partielles de CO_2 assez élevées, ce qui présente en outre l'avantage d'accélérer la cinétique de dissolution des silicates magnésiens, grâce à l'acidification de la solution par le CO_2.

La détermination des vitesses de dissolution de la magnésite dans des réacteurs à circulation à 150 et 200 °C et en milieu neutre à alcalin nous a permis d'améliorer le modèle de complexation de surface et d'étendre son application aux températures considérées. La diminution des vitesses de dissolution observée de 150 à 200 °C peut être expliquée par l'augmentation, en fonction de la température, de la carbonatation et de l'hydrolyse des sites $>MgOH_2^+$ qui contrôlent la vitesse de dissolution de la magnésite. Des températures supérieures à 100 °C qui entrainent une diminution de la vitesse de dissolution de la magnésite et des autres carbonates sont donc favorables au stockage de CO_2 sous forme dissoute dans les aquifères profonds riches en minéraux carbonatés.

L'utilisation d'une cellule à électrodes d'hydrogène (HECC) nous a permis de préciser les données cinétiques à proximité de l'équilibre grâce à la détermination précise du produit

de solubilité de la magnésite en fonction de la température (50-200 °C). De plus, ces mesures nous ont permis de générer les propriétés thermodynamiques de la magnésite et de les comparer à celles obtenues par mesures calorimétriques et par équilibres de phases.

Les résultats de cette étude représentent une importante contribution à la compréhension des cinétiques de réaction des minéraux carbonatés dans les systèmes hydrothermaux et permettent de proposer une base de données essentielle pour la quantification des réactions de dissolution/précipitation des carbonates dans les systèmes complexes. En outre, ce travail fournit des contraintes cinétiques pour la modélisation géochimique des processus de séquestration du CO_2 et sera utile à l'évaluation de l'impact et des risques liés au stockage de CO_2 à long terme.

MOTS-CLEFS: minéraux carbonatés ; cinétiques de dissolution et précipitation de la magnésite; séquestration géologique du CO_2 ; produit de solubilité; conditions hydrothermales.

DISCIPLINE ADMINISTRATIVE

Sciences de la Terre et Environnement

INTITULE ET ADRESSE DU LABORATOIRE

Laboratoire des Mécanismes et Transferts en Géologie (LMTG)
14 av. Edouard Belin
31 400 Toulouse
France